7-1-2016

Experimental Investigation into the Thermal and Magmatic Evolution of Mercury

Kathleen Vander Kaaden

Kathleen Elyse Vander Kaaden
Candidate

Earth and Planetary Science
Department

This dissertation is approved, and it is acceptable in quality and form for publication:

Approved by the Dissertation Committee:

Francis McCubbin, Chairperson

Carl Agee

Nancy Chabot

Tobias Fischer

Karen Ziegler

EXPERIMENTAL INVESTIGATION INTO THE THERMAL AND MAGMATIC EVOLUTION OF MERCURY

by

KATHLEEN E. VANDER KAADEN

B.Sc., Geological Sciences, Salem State University, 2010

M.Sc., Earth and Planetary Sciences, University of New Mexico, 2012

DISSERTATION

Submitted in Partial Fulfillment of the
Requirements for the Degree of

Doctor of Philosophy

Earth and Planetary Sciences

The University of New Mexico
Albuquerque, New Mexico

July, 2016

Dedication

To my nephew, Lorenzo Jayden Vanderkaaden, and my niece, Elsie Marie McCubbin. May your imaginations always run wild, your creativity never be restricted, and your desire to experiment and explore grow with each and every day.

"Most people say that it is the intellect which makes a great scientist. They are wrong: it is character."

- Albert Einstein

Acknowledgements

First and foremost, I would like to thank my pops and my madre for always pushing me to be my best, instilling the “Vander Kaaden Way” in me from a young age, and throwing me a few bucks over the years. I would also like to thank my sissy Kiki for being my rock not just these last ten years that I’ve been in college, but for the entirety of my life, and my brothers Gerrit and Jono for the constant reminder of how ridiculous my life choice was to “look at rocks”. Of course, my family wouldn’t be complete without my in-laws Zack Flanders, Jocelyn Vander Kaaden, and Yu Vanderkaaden who have kept me and my siblings grounded for many many years. Thank you all for your love and support, I would definitely not even be close to where I am today if it wasn’t for all of you!

To my massholes, thanks for being such great friends, making long trips to visit me over these last 6 years of graduate school, and always being there for my late night panic phone calls, last minute trip planning to work around my ridiculous graduate student schedule, and countless pizza and beer nights at my parentals while trying to pack my suitcase for the journey back to school. You all have made me a better person for knowing you and being surrounded by you for the majority of my life. Special thanks to my better half Kailbop Pratt, Chantal Joy, Justin Tavares, Meaghan Callahan, Steve Mueller, Sammie Stone, Salina Duggan, Kristen Cuthberton, Alysa Harris, Sarah Amaral, Janelle Howard, all of my pookies, and my Aussie girls. I definitely wouldn’t have had the courage to move away from home to start this crazy journey if I didn’t know that I had all of your support back home.

Throughout graduate school I’ve had the pleasure to work with some amazing people at the University of New Mexico. I would not have made it through this graduate program without the support of all my fellow graduate students. Specifically, I want to thank Alison Santos for making me realize back at Salem State that geology is actually really cool and completely derailing (in a good way) the entire course of my life, Laura Burkemper and Steve Elardo for taking me under their experimental wings and showing me the ways of grad school and experimental petrology, Poorna Srinivasan and Lindsay Ross for their constant support both in an out of school and for working out all of our grad school frustrations at those late night gym classes, Scott Jasechko and Kevin Hobbs for the countless beers and long life talks and research discussions, and my PRG crowd for making sure I kept up with the literature, even if some of our topics were excruciatingly painful.

A special thanks goes to the woman behind all of the paperwork, reimbursements, and countless forms that I’ve been required to fill out over the last 6 years. I definitely would not have managed all of the paperwork required with getting a Ph.D. if it wasn’t for Shannon Clark, Lee Ann Lloyd, Cindy Jaramillo, and Paula Pascetti. I would also like to thank all of the faculty, staff, and research scientists in EPS and the IOM that have taught me so much over the course of my degree. I would like to personally thank Mike Spilde for his endless hours of helping me use the microprobe, Horton Newsom and Jayne Aubele for getting me involved in education and publication outreach, Chip Shearer for always being willing to help no matter how big or small my problem, for always providing much needed career advice, and for being a fellow Patriots fan and watching games with me when everyone else was against our team, and Paul Burger and Aaron Bell for always providing help in the laboratories and advice on my research.

All of the research for my dissertation would not have been possible without the incredible advancement in knowledge about Mercury from the MESSENGER mission. I would like to thank the PI, Sean Solomon, for allowing me to be an honorary member of the science team and allowing me to participate in team meetings, Nancy Chabot for not only serving as my external examiner but for reviewing multiple manuscripts before publication, and the entire GcDG for their constant collaborations, in depth discussions, and thought provoking questions about my work. Without the entire MESSENGER science team and the tremendous efforts they

put into making sure the mission was more than successful, the subject matter of my dissertation would not be anything close to what it is.

I would like to thank my committee members for supporting me throughout the course of this process and for always being willing to help out, even when I had questions on things completely unrelated to my project. A special thanks to Karen Ziegler for advising me on my second project, teaching me about stable isotopes, and providing guidance both in science and in life over the years, Carl Agee for all of his support during my masters degree and continued support throughout my PhD, and Tobias Fischer for stepping in towards the end without question and his willingness to help me complete this lengthy process.

Moving to Texas for the last year of my degree was far from easy. I would like to thank everyone at Johnson Space Center who welcomed me with open arms into Building 31, made sure I had everything I needed so my degree was not delayed, and helped make the transition much easier. Specifically, thanks to my high pressure weirdos Lisa Danielson, Jenny Rapp, and Kellye Pando for taking me in without thinking twice about it, helping me get comfortable with all of the different experimental equipment, and making my work a priority so I could graduate on time.

Of course with research comes expenses so I would like to thank everyone who has contributed to my graduate degree. I would like to thank the following funding sources for their generous grants/scholarships that helped me substantially over the years paying for tuition, fees, health insurance, experimental and analytical costs, as well as travel to numerous conferences to present this research: the New Mexico Space Grant Consortium, the NASA Earth and Space Sciences Fellowship, the NASA Cosmochemistry program, and the department of Earth and Planetary sciences as well as accompanying summer scholarship funds.

Last, but certainly not least, I would like to thank the three people who, without their continued support, there is no way I would have made it through this program: Lisa McCubbin, Francis McCubbin, and Lauren Vargo. Lisa, thank you for being my family away from home, constantly encouraging me over the past 6 years, providing the love and support necessary to get me through some of the hardest years of my life, and putting up with mine and Francis' ridiculousness. Francis, thank you for being the best advisor any graduate student could ever have the pleasure of working with. Thank you so much for making my career what it is, getting me so involved in the planetary community, teaching me really terrible puns that I can't help but use, informing me about the four squares of success and always making sure I was in the right one, pushing me to my limits, picking me up after the many times I fell (physically, mentally, and emotionally), and being one of the most influential people in my entire life. Lauren, thank you for being the most amazing girlfriend in the entire world. The last year of my PhD was, by far, the hardest one and there is no way I would have made it through it in one piece if it wasn't for you supporting me, making sure I had everything I needed to get through this process, and dealing with my ridiculous stressed and crazy states. I can only hope I will be as supportive throughout your PhD as you were for me. And to all those reading this, and anyone else whom I may have forgotten, thank you!

Table of Contents

Chapter 1: *Mineralogy, Petrology, and Geochemistry of Mercury's Mantle Revealed by Surface Compositions*

Chapter 2: *Exotic crust formation on Mercury: Consequences of a shallow, FeO-poor mantle*

Chapter 3: *The origin of boninites on Mercury: An experimental study of the northern volcanic plains lavas*

Chapter 4: *Sulfur Solubility in Silicate Melts Under Highly Reducing Conditions as Seen on Mercury*

Chapter 5: *Carbon Solubility in Si-Fe-Bearing Metals During Core Formation on Mercury*

Chapter 1

Mineralogy, Petrology, and Geochemistry of Mercury's Mantle Revealed by Surface Compositions

In collaboration with

Francis M. McCubbin[1,2]
Larry R. Nittler[3]
Patrick N. Peplowski[4]
Shoshana Z. Weider[3]
Larry G. Evans[5]
Elizabeth A. Frank[3]
Timothy McCoy[6]

[1]Institute of Meteoritics, Department of Earth & Planetary Sciences, University of New Mexico, Albuquerque, NM 87131, USA. [2]NASA Johnson Space Center, Mailcode XI2, 2101 NASA Parkway, Houston, TX 77058, USA. [3]Department of Terrestrial Magnetism, Carnegie Institution of Washington, DC 20015, USA. [4]The Johns Hopkins University Applied Physics Laboratory, Laurel, MD 20723, USA. [5]Computer Science Corporation, Lanham-Seabrook, MD 20706, USA. [6]Department of Mineral Sciences, National Museum of Natural History, 10th and Constitution Aves. NW, Smithsonian Institution, Washington, DC 20560, USA.

Abstract

During the time that the MErcury Surface, Space ENvironment, GEochemistry, and Ranging spacecraft was in orbit around the innermost planet, new and exciting results regarding the planets structure, chemical makeup, and diverse surface were revealed, confirming that Mercury is an endmember among the terrestrial planets. Using the most recent results from the X-Ray Spectrometer and Gamma-Ray and Neutron Spectrometer, in conjunction with the Mercury Dual Imaging System, nine distinct geochemical regions were identified on Mercury. Using a variation on the classical CIPW normative mineralogy calculation, Mercury's silicate mineralogy is dominated by plagioclase, pyroxene (both orthopyroxene and clinopyroxene), and olivine, with lesser amounts of quartz. In terms of petrologic classification, the rocks on the surface of Mercury are

highly diverse and span the region from komatiitic to boninitic. The high abundances of alkalis lend to many of these regions being classified as alkali-rich komatiites and/or boninites. When compared to other terrestrial planetary bodies, including the Moon, Earth, Mars, and Vesta, mercurian compositions span a wide range in SiO_2 space that is greater than the Moon, Mars, and Vesta and is more similar to the wide range seen on Earth. However, although the compositions of Mercury look chemically evolved, the high SiO_2 content is a primitive feature and a direct result of the low oxygen fugacity on the planet.

Keywords: Mercury, Petrologic Classification, IUGS, Boninites, Komatiites

1. Introduction

Prior to the return of data from the MErcury Surface, Space ENvironment, GEochemistry, and Ranging (MESSENGER) spacecraft, information regarding the planet Mercury was limited. The success of the Mariner 10 flybys in 1974 and 1975 resulted in imaging of ~45 % of the planet, detecting a magnetic field, measuring H, He, and O in the exosphere, as well as determining other physical and chemical characteristics of the planet (Broadfoot et al., 1974; Broadfoot et al., 1976; Chase et al., 1974; Murray, 1975; Ness et al., 1975; Ness et al., 1974; Solomon et al., 2001). However, with this limited data, much was to be inferred about Mercury. Given its proximity to the sun, it was expected that Mercury would be volatile depleted. Furthermore, Mercury was frequently compared to the Moon with its high density of craters, abundant smooth plains (perhaps similar in origin to the lunar mare), and its similar surface reflectance spectra (Blewett et al., 2002; Taylor and Scott, 2004). Reflectance spectra of Mercury were thought to be

similar to the lunar highlands, although more sodic in nature and more variable than what is seen on the Moon (Sprague and Roush, 1998). Additionally, although FeO and TiO_2 abundances on Mercury were suggested to be much lower than that of the Moon (Blewett et al., 1997; Blewett et al., 2009; McClintock et al., 2008; McCord and Clark, 1979; Riner et al., 2010; Robinson and Lucey, 1997; Robinson et al., 2008; Vilas, 1988), the idea of formation from a magma ocean event (Brown and Elkins-Tanton, 2009; Riner et al., 2010) resulting in a plagioclase floatation crust was suggested (Taylor and McLennan, 2009). Based on earlier evidence, it was not clear if the bulk surface of Mercury was a primary crust that had been modified substantially by the late heavy bombardment, or secondary crust produced by volcanism on the planet (Taylor and McLennan, 2009). With a partial dataset and lack of chemical analyses of the surface, there was much left to interpretation regarding the evolution of Mercury.

During the time that the MESSENGER spacecraft was in orbit around the innermost planet, new and exciting results regarding the planets structure, chemical makeup, and diverse surface were revealed, confirming that Mercury is an endmember among the terrestrial planets (Solomon et al., 2001). The X-Ray Spectrometer (XRS) and Gamma-Ray and Neutron Spectrometer (GRNS) on board the MESSENGER spacecraft provided the first detailed chemical analyses of Mercury's surface (Evans et al., 2012; Nittler et al., 2011; Nittler et al., 2014; Peplowski et al., 2014; Peplowski et al., 2015a; Peplowski et al., 2012a; Peplowski et al., 2012b; Weider et al., 2015; Weider et al., 2014; Weider et al., 2012). The XRS was a 7.5 pound instrument designed to map elements in the top millimeter of Mercury's crust with emissions in the 1–10 keV range (i.e. Mg, Al, Si, S, Ca, Ti, Fe) (Nittler et al., 2011; Solomon et al., 2001; Weider et al., 2015; Weider

et al., 2014; Weider et al., 2012). The gamma-ray spectrometer (GRS) was a larger instrument (20.3 pounds) designed to measure gamma rays from naturally radioactive elements (i.e. K, Th, U) and gamma rays that were emitted by the nuclei of atoms (e.g. H, C, O, Na, Mg, Al, Si, Cl, Ca, Ti, Fe,) in the upper 10–100 cm of Mercury's surface once the planet was struck by cosmic rays (Evans et al., 2012; Peplowski et al., 2014; Peplowski et al., 2015a; Peplowski et al., 2012a; Peplowski et al., 2012b; Solomon et al., 2001). The neutron spectrometer (NS), intended to look at the H content of Mercury's polar deposits, accompanied the GRNS package, and was designed to map differences in epithermal, fast, and thermal neutrons emitted from Mercury's surface after being struck by cosmic rays (Lawrence et al., 2016; Solomon et al., 2001).

These geochemical instruments, in conjunction with the Mercury Dual Imaging System (MDIS) were used to identify numerous geological and geochemical features on the surface of Mercury that were previously unknown. Furthermore, they were used to identify several surprising characteristics about the surface of Mercury, including elevated S abundances (up to 4 wt%) and low Fe abundances (less than 2 wt%) (Nittler et al., 2011; Weider et al., 2014). The S and Fe abundances were used to confirm the highly reducing nature of Mercury, which has been estimated to be between 2.6 and 7.3 $\log_{10}$ units below the Iron-Wüstite (IW) buffer (McCubbin et al., 2012; Zolotov et al., 2013), lower than any of the other terrestrial planets in the inner Solar System (Herd, 2008; Sharp et al., 2013; Wadhwa, 2008). This highly reducing nature has important consequences for the thermal and magmatic evolution of Mercury, its surface mineralogy and geochemistry, and the petrogenesis of mercurian magmas (Brown and Elkins-Tanton, 2009; Charlier et al., 2013; McCubbin et al., 2012; Namur et al., 2016; Nittler et al.,

2011; Stockstill-Cahill et al., 2012; Vander Kaaden and McCubbin, 2015, 2016). To date, there has not been a systematic effort to understand the mineralogy and petrology of the surface of Mercury, so that is one of the aims of the present study. Furthermore, we will use the insights gained here to understand the mineralogy, petrology, and geochemistry of Mercury's mantle.

1.1 Identification of Distinct Geochemical Regions

Several geochemical regions have been identified on the surface of Mercury (Peplowski et al., 2015b; Weider et al., 2015). These regions were identified based on their composition as measured by the XRS and GRS instruments as well as variations of neutrons detected by the NS. The oxide compositions of the various geochemical regions were calculated in the same manner as Vander Kaaden and McCubbin (2016). By following these procedures, a variable Si abundance is calculated across Mercury's surface, which could mean that a diverse set of rocks and minerals were analyzed by the geochemical instruments onboard MESSENGER. Currently, the surface compositions of Mercury have been likened to terrestrial komatiites due to similarities in values of Al/Si versus Mg/Si (Nittler et al., 2011; Weider et al., 2015) as well as terrestrial boninites, given the high calculated SiO_2 abundances of some regions (e.g., Vander Kaaden and McCubbin, 2016). To investigate the potential mineralogical and petrologic diversity on the innermost planet, we focus our study on nine regions with characteristic major element compositions (Weider et al., 2015): (i) the high-Mg region (HMR), (ii) a sub-region of the HMR with the planet's highest Ca and S contents (HMR-CaS), (iii) a subset of the northern volcanic plains (NP) with relatively high Mg content (NP-HMg) distinguished by low-fast neutrons (Lawrence et al., 2016), (iv) a subset of the NP with

relatively low Mg content (NP-LMg), (v) the Rachmaninoff basin (RB), (vi) the planet's largest pyroclastic deposit, located northeast of the Rachmaninoff basin (PD), (vii) the high-Al regions southwest and southeast of the NP (HAl), (viii) the smooth plains within the Caloris basin (CB), and (ix) the intermediate terrane (IT) on the mercurian surface, made up of intercratered plains and highly-cratered terrain. The goal of this study is to determine an average composition for each of these nine distinct geochemical regions. These compositions will be used to infer mineralogical, petrologic, and geochemical identifications for the materials that constitute Mercury's surface. These data will provide insight into the mineralogy of the mercurian mantle, the petrologic diversity of rocks on the planet, as well as the range in Si (or SiO_2) abundances across the surface and the interior.

2. Determination of compositions

XRS (Nittler et al., 2011; Nittler et al., 2014; Weider et al., 2015) and GRS (Peplowski et al., 2014; Peplowski et al., 2012a) analyses were used to determine the average compositions for nine geochemical regions on the surface of Mercury (Tables 1–2). XRS measurements of the nine geochemical regions were revisited using the most recent MESSENGER analyses including the low altitude campaign data acquired towards the end of the mission. Elemental data obtained from XRS include Mg/Si, Ca/Si, Al/Si, Fe/Si, and S/Si. Due to varying pixel sizes with latitude, the two NP regions were calculated using area-weighted averages to avoid over interpretation of any single pixel. The NP-HMg region (Figure 1) was defined as Mg/Si > 0.4 and confined to the center longitude regions consistent with the "low fast neutron" region described in Lawrence et al. (2016), which exhibited distinct neutron absorption characteristics compared to other

portions of the NP. The NP-LMg (Figure 1) was defined as Mg/Si < 0.35 and consists of the majority of smooth plains towards the northern pole of the planet. The IT region was calculated as the remainder of the planet, excluding previously defined regions and includes the southern hemisphere, intercratered plains, and highly-cratered terrain. Importantly, the abundances of Ti, Mn, and Cr have not been reported for most of these units; therefore, two average compositions for each geochemical region were calculated. The first composition for each individual geochemical region (Table 1) only considers reported values of Ti, Mn, and Cr. The second composition (Table 2) used the XRS detection limits for Ti, Mn, and Cr (Nittler et al., 2011; Weider et al., 2015) as the concentrations of these elements when they were below detection for a given region. Final elemental ratios that were used for all calculations are given in Table S1.

Alkali abundances in these regions were determined by GRS. The most recent modeling of the Na data (Peplowski et al., 2014) supports a consistent Na value across the planet of 2.6 wt%, with the exception of the NP-LMg region that has a Na value of 4.8 wt%. In terms of potassium, the location of each region on Mercury was used to assign a suitable K_2O value from previously published data (Peplowski et al., 2012a). The K value assigned to the HMR, HMR-CaS, RB, HAl, and PD was defined by the "All 2012" region in Peplowski et al. (2012a). The K value for CB was defined by "CB" in Peplowski et al., (2012a) and the IT K value was defined by the "ICP/HCT/SP" region defined in Peplowski et al. (2012a). The K values for the NP-HMg and NP-LMg were redefined, 0.2 wt% and 0.15 wt%, respectively, based on the most recent GRS maps that have been produced.

Similar to the approach taken in Vander Kaaden and McCubbin (2016), to determine the composition of each distinct geochemical region, the valence of each element was first assigned (i.e., Si^{4+}, Ti^{4+}, Al^{3+}, Cr^{2+}, Fe^{2+}, Mn^{2+}, Mg^{2+}, Ca^{2+}, Na^{+}, K^{+}, S^{2-}). A corresponding abundance of O^{2-} was then calculated so that the resulting composition for each specific region was charge balanced. Finally, assuming no major constituent elements have been excluded, the resulting sum of oxides/sulfides should be ~100 wt%. Therefore, the composition for each region was normalized to 100 wt%, while maintaining the measured element/Si ratios. From these calculations, the resulting O/Si values ranged from 1.58–1.91, which are higher than the O/Si values measured by MESSENGER GRS (1.20±0.1 reported in McCubbin et al. (2016)). However, McCubbin et al. (2016) has shown that the O/Si value at the surface is likely related to secondary degassing processes at the Mercurian surface and was not inherited as a primary feature, so the compositions we have computed likely reflect the state of the melts prior to secondary processes. Consequently, we use the results herein to understand the mercurian interior as opposed to the actual rocks and minerals on the surface, which were likely modified by secondary processes (McCubbin et al., 2016).

3. Inferred Mineralogy and Petrology of Mercury's Surface Compositions

Based on the compositions of the nine geochemical regions, considering those with both measured and upper limit values for Cr, Mn, and Ti, there is a range of ~5.3 wt% Si, which corresponds to a range of ~11.4 wt% SiO_2 across the nine geochemical regions. This range is consistent with the GRS measurements of Si (Peplowski et al., 2012a). After normalization, taking into account both sets of analyses for each composition, SiO_2 (11.43 wt% range), MgO (13.01 wt% range), and Al_2O_3 (7.74 wt%

range) exhibit the largest range in values across the mercurian surface. Sulfides and all other oxides vary by less than 3 wt%.

Although each geochemical region may not represent a single rock type or a specific set of minerals that can be easily deduced by bulk normative mineralogical calculations, the results of these calculations can be useful when trying to understand the geochemistry, mineralogy, and petrology of the surface of a planet, especially from the standpoint of comparative planetary geochemistry. Consequently, we have calculated a CIPW norm (Cross et al., 1903) and have petrologically classified each of the nine geochemical regions according to International Union of Geological Sciences (IUGS) classification protocols (Le Bas, 2000 and references therein; Le Maitre et al., 2002). We caution the reader that the classifications determined here are based solely on the chemical composition for each unit and they should not be used, *a priori*, to infer geologic processes or settings.

3.1 Normative Mineralogy

Due to the high amount of sulfur in mercurian compositions, the CIPW normative mineralogy calculations could not be conducted in the conventional manner. Instead, we first calculated the sulfides that would be present in each composition using the partition coefficients calculated from the experimental results of Vander Kaaden and McCubbin (2016). This method, based on experiments run at conditions similar to those on Mercury, preferentially makes FeS, CrS, TiS_2, and MnS. If S remains after Fe, Cr, Ti, and Mn are consumed then MgS, and CaS are produced using a sulfide-melt Ca-Mg exchange coefficient of 1.97 as determined by Vander Kaaden and McCubbin (2016) until all S is consumed. Once all of the sulfur in each composition was consumed as sulfides, the

remaining composition was renormalized to 100%, resulting in a sulfur-free composition. Using this sulfur-free composition, the normative mineralogy of each geochemical region was calculated using the steps of Johannsen (1931). A modification that we made to this classical calculation is the treatment of MnO. Typically, MnO is assumed to act like FeO and is included in the calculation of an ilmenite component. However, given the highly reducing nature of Mercury (McCubbin et al., 2012; Zolotov et al., 2013), as well as the low amount of Fe and Ti on the surface (Nittler et al., 2011; Weider et al., 2014), it is unlikely that ilmenite will be present. Therefore, any MnO that was left over after making MnS has been put into a manganosite (MnO) component, although it is likely consumed by olivine and/or pyroxene in the actual surface compositions. The results of the normative mineralogy calculations are given in Figure 2, Figure S1, Table S2, and Table S3.

For the purposes of this discussion, we consider both the compositions with only measured Cr, Mn, and Ti (Figure 2, Table S2), as well as those that were computed using the detection limits of Cr, Mn, and Ti from Nittler et al. (2011) as upper limit estimates for these elements (Figure S1, Table S3). All of the regions considered in this study are hypersthene normative, with the exception of the HMR-CaS. However, the HMR-CaS only has ~0.7–3.1 wt% nepheline, which is likely within the error of our calculations, so we do not place too much weight on this result. In terms of silica saturation, CB is consistently quartz-normative, whereas all of geochemical regions, with the exception of HAl are consistently olivine-normative. Depending on the amount of Cr, Mn, and Ti present, the HAl region is either olivine-normative (containing ~7 wt% olivine) or quartz-normative (containing ~0.4 wt% quartz). Although it is near the boundary, the value of

quartz is extremely low and likely within the resolution of our calculations, so we will consider the HAl olivine-normative.

The normative mineralogy of the surface compositions calculated herein represent the mineralogy of mercurian surface materials prior to or in the absence of any secondary degassing processes that could have caused the loss of O^{2-} (i.e., McCubbin et al., 2016). The major minerals present on the surface of Mercury includes plagioclase, olivine, pyroxene (both orthopyroxene (opx) and clinopyroxene (cpx)), and quartz. Albitic plagioclase ($NaAlSi_3O_8$) consistently dominates all regions (32.42–58.35 wt%), lending to the alkali-rich nature of Mercury. Olivine (0–34.59 wt%) is much more dominant in the HMR, HMR-CaS, RB, and PD representing ≥ ~30 wt% of the normative calculation than in the NP regions, HAl, and IT where it only makes up ≤ ~16 wt% of the bulk composition. As stated previously, CB is consistently olivine-free. In terms of pyroxene, both orthopyroxene (i.e. hypersthene 0–37.13 wt%) and clinopyroxene (i.e. diopside 0–22.43 wt%) are present in these geochemical regions. Orthopyroxene is the dominant pyroxene present in the NP-HMg, HAl, CB, and IT regions whereas clinopyroxene is the dominant pyroxene present in the HMR, HMR-CaS, RB, and the PD. The NP-LMg has almost equal proportions of opx and cpx present. Furthermore, although quartz is present only in the CB region (≤ 8 wt%), it is a dominant major mineral of that region.

Figure 2 shows the mineralogy of the HMR and HMR-CaS are extremely similar, with the main difference being in the amount of opx present. The NP regions are similar in their mineralogy with the NP-HMg containing ~10 wt% more olivine than the NP-LMg, which contains ~10 wt% more cpx. The RB and PD regions have similar mineralogy with the PD having slightly less sulfides (~4 wt%) and opx (~5.5 wt%), but

greater abundances of plagioclase (~3 wt%) and olivine (~5 wt%). Interestingly, the HAl and CB regions have extremely similar mineralogy with the main difference being that the HAl has ~7 wt% greater abundances of opx whereas the CB has ~8 wt% greater abundances of quartz. These two regions are also similar in composition to the IT, suggesting these three regions may represent the bulk composition of Mercury, dominated by plagioclase, opx, and sulfides. Importantly, it is not possible to distinguish a homogenous surface that is dominated by opx and a heterogeneous one that has opx and subequal amounts of olivine and silica.

The modal abundances of the major silicate minerals calculated here can also be used to classify plutonic rocks according to IUGS standards. Figure 3 shows the classification of melt compositions exposed at the surface (NP-HMg, NP-LMg, and PD) as well as the HMR and HMR-CaS. Figure 3A shows a cpx-opx-ol ternary where the NP regions are classified as either websterite or olivine websterites, mainly due to the amount of sodium present in these compositions. The PD is classified as a lherzolite. The HMR-CaS is classified as a wehrlite and the HMR is either a lherzolite or wehrlite, depending on the amount of Cr, Mn, and Ti present. Alternatively, if these regions are classified using an ol-plag-pyx ternary (Figure 3B), all regions are classified as olivine gabbronorites. The only exception is the NP-LMg region without Cr, Mn, and Ti, which falls in the gabbronorite field.

Sulfides are the next major mineral present in the CIPW normative calculations. In Figures 2 and S1, the sulfides are considered only as a single, multi-component phase making up ~1.6 to 6.5 wt% of the normative mineralogy. Sulfides are most abundant in the HMR-CaS, which is consistent with this region containing the highest S abundances

on the planet. The HMR and RB both contain over 5 wt% sulfides, whereas the NP, IT, and HAl regions contain ~4 wt% sulfides. The PD, which is consistent with some of the lowest S abundances on the planet, also contains the least amount of sulfides. Figure S2 and S3 show the various sulfide components present in each region. When considered as individual sulfide components, the surface of mercury is composed of FeS (1.16 – 3.98 wt%), CrS (0–0.89 wt%), TiS_2 (0–1.77 wt%), MnS (0–0.86 wt%), MgS (0–3.23 wt%), and CaS (0–0.33 wt%). FeS is consistently the dominant sulfide mineral across all regions. Using only the measured values of Cr, Mn, and Ti, TiS_2 is present only in the CB (~0.6 wt%). MgS and CaS are present in all regions with the exception of the PD and MgS is consistently more dominant than CaS, a direct result of the sulfide-melt Ca-Mg exchange coefficient used in this study.

The remaining minerals have modeled abundances that are too low to make a definitive assessment of whether or not they are present. These minerals include orthoclase (0.53–1.42 wt%), nepheline (0–3.10 wt%), corundum (0–0.80 wt%), titanite (0–1.35 wt%), and MnO (0–0.71 wt%). By including the detection limit of Cr, Mn, and Ti into the oxide composition, CrS, MnS, titanite, and MnO are produced, which were not present when only the measured values of these elements were included. Orthoclase is present across all regions in small amounts and, similar to albite, reflects the alkali-rich nature of Mercury. Nepheline is only present in the HMR-CaS region, but again it is most likely within error of the reported values, so it is not significant in terms of mercurian mineralogy. Corundum is present in the HAl, as expected, and in the CB regions.

3.2 Petrologic Classification

Using the SiO_2 and total alkali (Na_2O + K_2O) contents, the petrologic classification of each composition is shown on a total alkali vs. silica (TAS) diagram in Figure 4. The NP-LMg is the most alkali rich of the regions studied and is classified as a trachyandesite (Figure 4). The NP-HMg, HAl, and IT are consistently basaltic andesites. The CB rocks are classified as andesites on this diagram, whereas the HMR compositions all fall in the basalt field. The remaining regions (RB and PD) span across the basalt-basaltic andesite boundary on a TAS diagram depending on the amount of Cr, Mn, and Ti present. However, this diagram is not applicable to compositions with high MgO abundances (MgO > 8 wt%, Le Bas, 2000) like those on Mercury (MgO: 12.13–25.14 wt%). Consequently, the High-Mg classification diagram (Figure 2 in Le Bas, 2000) was employed to place further constraints on the petrologic classifications. The High-Mg classification diagram has been superimposed on the TAS diagram in Figure 4 to illustrate further the chemical boundaries and how they affect nomenclature.

With this further classification, the NP regions, as well as the CB, Hal, and IT, are classified as boninites since their SiO_2 and MgO contents are >52 wt% and 8 wt%, respectively. However, since the total alkali content for the NP-LMg extends beyond the upper bounds of this classification (≥4 wt% total alkalis), we use the term ‘alkali-rich boninite’ for this composition , consistent with the classification in Vander Kaaden and McCubbin (2016). Both of the HMR regions are classified as komatiitic since their SiO_2 contents are <52 wt% and their MgO contents are >18 wt%, although they may be alkali-rich komatiites, if future targeted analyses from subsequent missions are in agreement with the latitudinally-averaged alkali data (Peplowski et al., 2014) that suggests the HMR regions have 3.51 wt% Na_2O (i.e., komatiites are defined as having ≤1 wt% Na_2O). Both

RB and the PD span these two distinct compositions and can be classified as either boninitic or komatiitic, depending on the amount of SiO_2 present. Whether or not the composition of RB and PD is on the boninites or komatiite side of the boundary is a direct result of the actual abundances of Cr, Mn, and Ti that are present in these compositions.

4. Discussion

4.1. Insights into Mercury's mantle from geochemical regions on its surface

Many of the chemical compositions initially reported for Mercury's surface span a wide range of terrane types. This study has focused on determining the chemical composition and petrologic classification of distinct geochemical units on mercury. This section focuses on geochemically significant regions that can provide insight into the mantle of Mercury and various igneous processes (i.e. NP, PD, HMR,and HMR-CaS).

4.1.1 Melt compositions exposed at the surface

Out of the nine geochemical regions considered in the present study, the northern volcanic plains and the pyroclastic deposit located to the NE of Rachmaninoff Basin, which both appear to be volcanic in origin and have targeted analyses available (Denevi et al., 2013; Head et al., 2011; Kerber et al., 2011; Nittler et al., 2014; Ostrach et al., 2015; Weider et al., 2015), are the best candidates for melt compositions resulting from partial melting of the mercurian interior exposed on Mercury's surface. The NP covers more than 12% of the surface area of the northern hemisphere of Mercury (Head et al., 2011; Ostrach et al., 2015). This geologic unit is less cratered than its surroundings and believed to be the product of at least two episodes of flood volcanism that were emplaced

over a relatively short period of geologic time (e.g. 100 My or less, Head et al., 2011; Ostrach et al., 2015). Absolute model ages for the NP range from ~2.5–3.7 Ga (Le Feuvre and Wieczorek, 2011; Marchi et al., 2009; Neukum et al., 2001; Ostrach et al., 2015). The lack of an impact basin near the NP region favors a volcanic origin of these lavas. In fact, the NP lavas are the most likely example of an actual melt composition that can be compositionally assessed from orbit (Vander Kaaden and McCubbin, 2015). Although not a homogenous unit, targeted XRS analyses (Weider et al., 2015) are now available, which show two distinct terranes within the NP region, one with higher Mg and one with lower Mg (Tables 1–2).

The PD northeast of Rachmaninoff Basin is the largest pyroclastic deposit on Mercury (Kerber et al., 2011) that has spatially resolved, targeted, XRS measurements used to determine its composition (Nittler et al., 2014). It is not contained within a known impact crater, which can be said for only 5 out of the 51 pyroclastic deposits identified on Mercury thus far (Kerber et al., 2011; Nittler et al., 2014), making it a likely example of partially melted mantle material on the surface of the planet (as opposed to a crustal impact melt). Since it is a pyroclastic deposit, it is likely that some volatiles were lost through the explosive volcanism that produced the PD (Nittler et al., 2014; Weider et al., 2016). Possible magmatic volatile abundances required to emplace this deposit on the surface of Mercury can be found in Kerber et al. (2011).

Because these two units likely represent melt compositions, additional information regarding the geochemical properties of these melts are provided in Table 3. The NP-HMg composition is peraluminous (i.e., $Na_2O+K_2O+CaO < Al_2O_3$) and the NP-LMg and PD compositions are metaluminous (i.e., $Al_2O_3 < (CaO + Na_2O + K_2O)$ and

Al_2O_3 > (Na_2O + K_2O)). The low iron on Mercury lends to high Mg#'s (molar (Mg/Mg+Fe)*100) for these three compositions ranging from 93.23–95.15. Furthermore, the range in non-bridging oxygen's to tetrahedrally coordinated cations in the melt (NBO/T) (Table 3) shows the NP lavas are typically polymerized (NBO/T<1) melts and therefore more viscous than the PD, which is less polymerized than the NP (NBOT/T>1). The NBO/T values for the NP-LMg are consistent with the experimental results from Sehlke and Whittington (2015). Furthermore, given this similarity, it also suggests that the NP lavas are more viscous than Hawaiian basalts erupted at the same temperature (Sehlke and Whittington, 2015; Sehlke et al., 2014).

The normative mineralogy for the NP regions is dominated by plagioclase, diopside, hypersthene, and olivine with lesser amounts of orthoclase, sulfides, and MnO. The albite content of the plagioclase in the NP-HMg is ~ 63.9–65.0 whereas the albite content of the plagioclase in the NP-LMg is ~94.2–95.7, lending to the sodium rich nature of the NP-LMg compared to the NP-HMg. The dominant mineralogy of this region is consistent with the experimental results of Vander Kaaden and McCubbin (2016). They reported that the NP boninites were derived by high degrees of partial melting of an olivine-dominant, pyroxene- and plagioclase-bearing mantle source region.

The normative mineralogy for the PD is dominated by plagioclase (albite content ~67), olivine, and diopside with lesser amounts of orthoclase, hypersthene, MnO, and sulfides. The formation of MnO in both compositions is due to a deficit in sulfur, possibly from the loss of sulfur during the volcanic eruptions (Weider et al., 2016). Figure 3 shows that the PD consistently plots away from the NP regions in terms of normative mineralogy and rock type. Either this suggests a heterogeneous mantle on

Mercury or that the PD was erupted from depths greater than the NP where less plagioclase was present in the source. In order to place constraints on the thermal and magmatic evolution of Mercury as well as physical and chemical properties of the planet (e.g. determination of surface and mantle mineralogy; Charlier et al., 2013; Namur et al., 2016; Vander Kaaden and McCubbin, 2015, 2016) that cannot be resolved by the MESSENGER spacecraft, these unique geochemical units, representative of melt compositions, warrant further experimental investigation.

4.1.2 High-Mg Region

The HMR, centered at ~30°N, 290°E, is a large (>$5x10^6$ km^2) region with the highest S/Si and Ca/Si ratios on the planet (HMR-CaS), relatively low Al/Si values, lower elevations, and thinner than average mercurian crust (Weider et al., 2015). Our classification of the HMR as a komatiite is consistent with the classification by Maturilli et al. (2014) who have suggested this region is most similar to Commondale, a terrestrial komatiite dominated by orthopyroxene instead of clinopyroxene (Wilson, 2003). The Commondale lavas have high SiO_2, low Fe, and high CaO/Al_2O_3 (Wilson, 2003), similar to the chemical composition of the HMR region. However, the formation of the HMR is still debated. Weider et al. (2015) have proposed that the komatiitic composition of the HMR could be indicative of high-degree partial melting of a lherzolitic mantle source. Alternatively, Weider et al. (2015) has suggested that the HMR is related to an impact feature and the high Mg/Si is due to mantle excavation during this large impact event more than 4.1 Ga. Given the lack of impact-like features in the HMR, if it is representative of an impact feature, it must have been at least partially resurfaced by volcanic activity post impact (Weider et al., 2015).

CIPW norm calculations of the HMR and HMR-CaS result in hypersthene and nepheline normative compositions, respectively. These normative compositions hold true regardless of the presence or absence of Cr, Mn, and Ti. When these elements are excluded, the HMR contains 7.46 wt% hypersthene and the HMR-CaS contains 0.67 wt% nepheline, which is too low to be considered definitive. However, when the detection limits from Nittler et al. (2011) are included for Cr, Mn, and Ti, the amount of hypersthene in the HMR decreases to 0.28 wt% and the amount of nepheline in the HMR-CaS increases to 3.10 wt%. If this difference in hypersthene vs. nepheline normative mineralogy is correct, it could provide important information regarding the mineralogical heterogeneity within the mercurian interior However, once the error from these calculations is taken into account for the XRS measurements, the small amounts of hypersthene in the HMR and nepheline in the HMR-CaS are no longer significant, so we will not consider this possibility further. Until higher precision measurements are attained, this difference in mineralogy cannot be accurately quantified and inferences about the heterogeneous nature of the mantle of Mercury or petrogenesis of these two particular regions are highly speculative.

Figure 3 shows the HMR and HMR-CaS can be classified as either lherzolites/wehrlites or olivine gabbronorites if they are representative of plutonic rocks. Furthermore, the HMR regions consistently plot close to the PD in both Figure 3A and Figure 3B. Therefore, it is possible that the HMR regions were produced in a similar manner as the PD, possibly from a deeper source region or higher degrees of partial melting than the NP was produced. These results are consistent with Frank et al. (2016) that a mantle excavation origin by impact is highly unlikely for this region. Based on our

results, it is clear that the HMR regions are volcanic in origin; however, whether or not the volcanism was impact related cannot be determined from this study.

4.2. Comparative planetary geochemistry

In order to determine the extent of petrologic diversity on Mercury, we have compared our data to other terrestrial bodies including Earth (Lebas et al., 1986), Moon (Lodders and Fegley, 1998), Mars (Gellert et al., 2006; McSween et al., 2009; Stolper et al., 2013), and Vesta (Barrat et al., 2009; Lodders and Fegley, 1998; Mittlefehldt, 2015). Although the mercurian compositions have been correctly classified above using the High-Mg diagram (Le Bas, 2000), we have included the compositions from each body on the TAS diagram in Figure 5 for direct comparison. As expected, rocks from Earth span the entire range of the TAS diagram since these are the rocks on which the classification scheme was originally based. With the exception of lunar granites (i.e., 12032,366-19 Seddio et al., 2013), lunar rocks have, on average, less than 0.5 wt% total alkalis. Although they span a relatively wide range in SiO_2 content (~20 wt% SiO_2), the consistently low amount of $Na_2O + K_2O$ constrains the lunar rocks to a small field on the TAS diagram (Figure 5). Data from Vesta was compiled using eucrite basalt samples and impact glasses from howardites (Barrat et al., 2009; Lodders and Fegley, 1998). With the exception of two impact glasses containing high alkalis and high SiO_2 contents (shown as small purple circles in the dacite field on Figure 5), igneous rocks from Vesta span a very small range in total alkali contents (≤3 wt%) and SiO_2 (≤9 wt%). For martian samples, data has been compiled using orbital data (Mars Odyssey), rover data (MER, MSL), as well as data from meteorite samples (NWA 7034, SNC's). From Figure 5, one can see that despite all of the data we have for Mars, there is a very small field spanning ≤6 wt%

in total alkali contents and ≤16 wt% in SiO_2. One exception to this dataset is the rock called Jake M, which plots in the phono-tephrite field and has been classified as a mugearite by Stolper et al. (2013). This rock is significantly different from other martian meteorites and rocks analyzed from rovers and orbital missions, but it supports the presence of alkaline magmas on Mars (McSween et al., 2006; Nekvasil et al., 2007; Nekvasil et al., 2009; Stolper et al., 2013). With the planetary bodies included in this comparison, Mercury is currently the only body that does not have an identifiable hand sample available for analysis on Earth. The range in alkali content as well as SiO_2 content of mercurian rocks based solely on orbital data from one mission is remarkable. Although it is possible that there could be a sample biasing issue in the current dataset for other planetary bodies, our petrologic classification of the nine geochemical regions indicates that Mercury's surface is chemically evolved relative to those of the Moon, Mars, and Vesta and is similar in diversity (with respect to range in SiO_2 content) to Earth (Taylor and McLennan, 2009).

4.2.1 Igneous rocks

The most likely examples of silicate melts on the surface of Mercury, represented by the NP-HMg, NP-LMg, and PD, share similar characteristics to terrestrial silicate melts with some very important differences. Boninites on Earth typically require arc magmatism and hydrous conditions to induce melting (e.g., Cameron et al., 1983; Polat et al., 2002). However, Vander Kaaden and McCubbin (2016) have shown eruption scenarios for the NP that invoke high degrees of partial melting from a shallow source region, similar to flood volcanism on Earth, in the absence of arc magmatism and hydrous conditions to produce the large volume of boninitic lava on the surface of the

planet observed in the NP. Furthermore, Figure 6 demonstrates that the compositions of most of the geochemical regions investigated here fall within a forsterite, enstatite, albite triangle on the TAS diagram. Therefore, the composition of mercury's interior is likely similar to major rock-forming minerals that compose other planetary mantles. Moreover, no exotic petrogenetic scenarios are required to get these mercurian melts to the surface, albeit they may differ from typical petrogenetic scenarios observed on other planetary bodies.

4.2.2 Regolith

Regolith is considered to be "a general term for the layer or mantle of fragmental and unconsolidated rock material, whether residual or transported and of highly varied character, that nearly everywhere forms the surface of the land and overlies or covers bedrock" (Bates and Jackson, 1980). Regolith is typically the product of mixing on a planetary surface and likely represents an average surface composition. This unconsolidated, fragmented material is abundant across the surface of Mercury and defines the IT geochemical region in this study. As stated previously, the IT falls very close to the komatiite-boninite boundary using the IUGS classification scheme. The mineralogy of this regolith, based on CIPW normative calculations, includes over 50 wt% plagioclase (~59 Ab), over 30 wt% hypersthene, and variable amounts of diopside (~4 wt%) and olivine (~2-5 wt%). Minor components present in the regolith include sulfides and orthoclase with possible MnO depending on the amount of Cr, Mn, and Ti present in this region. The IT is most similar in normative mineralogy to the HAl and CB regions. In comparison with the other geochemical regions we have defined in this study, the IT is hypersthene and olivine normative, consistent with the majority of these regions.

However, the IT contains more opx than any other region on Mercury and typically contains more plagioclase with the exception of the NP-LMg, HAl, and CB regions. This regolith component also has a similar amount of sulfides to the other geochemical regions defined in this study (Figures S2 and S3) suggesting an even distribution of sulfur across the planet. Since the IT region in this study composes the majority of the mercurian surface, plagioclase and opx likely dominate the surface of Mercury with lesser amounts of cpx, sulfides, olivine, and silica. Given the olivine normative nature of this material, silica exists in the mercurian regolith at subordinate abundances to olivine. This is consistent with the models of Stockstill-Cahill et al. (2012) that suggested the surface of Mercury is mainly composed of Mg-rich orthopyroxene and plagioclase.

Table 4 compares the composition of the lunar regolith, martian regolith, the Earth's regolith, and the regolith of Vesta with that of Mercury (i.e. crosses in Figure 5). The lunar regolith was determined using lunar meteorite data from Korotev et al. (2003) which takes into account the composition of the feldspathic highlands terrane, which is significantly far away from the lunar mare and procellarum KREEP terrane, and representative of the average lunar crust. The martian regolith composition was determined using the bulk matrix composition from the martian regolith breccia NWA 7034 (Santos et al., 2015), which is the most representative sample of the martian crust (i.e., Agee et al., 2013). For Earth's upper crust composition, we used the suggested composition in Rudnick and Gao (2003), which takes into account numerous analyses of loess and previously published values for the Earth's upper continental crust. The reader is referred to Table 3 in Rudnick and Gao (2003) for a full description on how this composition was determined. The regolith of Vesta was calculated by averaging only the

howardites classified as being regolithic: Bholghati, Bununu, Jodzie, Kapoeta, and Malvern classified by Warren et al. (2009), and EET 87513, GRO 95535, GRO 95602, LEW 85313, and MET 00423 classified by Mittlefehldt et al. (2013) from the compositions provided in Mittlefehldt (2015) and references therein. In comparison to these other terrestrial regolith's, the regolith on Mercury, represented by the IT (Table 4), has the highest MgO, Na_2O, and S, and the lowest FeO. The other oxides (e.g. SiO_2, CaO, Al_2O_3, and K2O) are intermediate among terrestrial planetary regoliths.

Normative mineralogy of these planetary regoliths (Table S4) show similar minerals present on the surface of these planetary bodies including plagioclase, orthoclase, diopside, and hypersthene. However, ilmenite and apatite are present on these planetary bodies and likely excluded from surface mineralogy of Mercury (Evans et al., 2015, Riner et al., 2010; Figure 2). The high SiO_2 of the IT, which is greater than all terrestrial bodies considered in Table 4 with the exception of the Earth, gives the impression that Mercury is a more evolved planetary body. The Earth is believed to have reached its Si-rich surface composition through plate tectonics and processes involving liquid water (Campbell and Taylor, 1983), but Mercury is "evolved" without such processes. However, the high SiO_2 on Mercury is a primitive signature and a direct consequence of the low oxygen fugacity of the planet. Under such highly reducing conditions, the majority of the Fe in the planet will partition into the core (Hauck et al., 2013). This results in very low abundances of iron in the silicate portion of the planet. When a major oxide component is removed from the silicate, in this case, FeO, all other components increase proportionally, and SiO_2 is most affected because it is the most abundant oxide component. Importantly, some Si is also lost to the core due to the highly

reducing conditions, but this process primarily affects the Mg/Si ratio of the bulk silicate and is likely an explanation for the primary mantle mineral in Mercury being forsterite instead of enstatite (Vander Kaaden and McCubbin, 2016). Table 5 shows all of the compositions of Table 4 renormalized after FeO has been removed to better illustrate this point. When this calculation is done, Mercury now only has higher SiO_2 contents than the Moon and is average among the terrestrial planets. From this comparison, it is clear that Mercury is an endmember among the terrestrial planetary bodies and although similar processes have operated on Mercury to produce the IT that have produced the regolith on the Moon, Earth, Mars, and Vesta, the low oxygen fugacity of Mercury has resulted in a vastly different regolith composition than what is typically seen in the inner Solar System.

5. Conclusion

The results from this study indicate that Mercury has a diverse set of rocks on its surface, especially when compared with other terrestrial bodies. From this investigation, we infer a wide range of SiO_2 content, alkali content, and major element compositions across Mercury's surface. CIPW normative calculations of nine geochemical regions on the surface of Mercury allow us to gain insight into the mineralogy of the planet, which is likely dominated by plagioclase, pyroxene, and olivine, with minor amounts of quartz. Although these minerals are similar to those found on other planetary bodies, their chemical compositions are vastly different, most notably the low abundance of iron and high abundance of sodium and magnesium in mercurian compositions. Our petrologic classification of the nine geochemical regions as komatiites or boninites indicates that Mercury's surface is more diverse relative to those of the Moon, Mars, and Vesta, and is

similar (with respect to range in SiO_2 content) to Earth (Taylor and McLennan, 2009). In fact, Mercury may represent the only other example of a planet in our Solar System with vast amounts of andesitic crust exposed at the surface. The formation of Earth's evolved crust is normally associated with plate tectonics and the presence of water. These two factors, however, were likely not involved with the formation of Mercury's crust, and the high SiO_2 content is primitive in nature. The study of Mercury's crustal compositions may therefore provide important new insights into crustal evolution mechanisms. The results of this investigation into the mineralogical, petrological, and geochemical compositions of the mercurian surface, yet again, support the endmember nature of this planet.

Acknowledgements

We thank the MESSENGER Science Team, with special thanks to the MESSENGER Geochemistry Discipline Group, for dynamic discussions regarding the interpretation of MESSENGER data and preparation of this manuscript. We also thank Ryan Zeigler, Randy Korotev, Alison Santos, and Duck Mittlefehldt for helpful discussions regarding lunar, martian, and vestan chemical compositions. This work was funded by a NASA Solar System Workings Grant to FMM. This work was also supported by NASA Headquarters under the NASA Earth and Space Science Fellowship Program-Grant NNX15AQ80H awarded to KEVK.

References

Agee, C.B., Wilson, N.V., McCubbin, F.M., Ziegler, K., Polyak, V.J., Sharp, Z.D., Asmerom, Y., Nunn, M.H., Shaheen, R., Thiemens, M.H., Steele, A., Fogel, M.L., Bowden, R., Glamoclija, M., Zhang, Z., and Elardo, S.M. (2013) Unique Meteorite from Early Amazonian Mars: Water-Rich Basaltic Breccia Northwest Africa 7034. Science 339, 780-785.

Barrat, J.A., Bohn, M., Gillet, P. and Yamaguchi, A. (2009) Evidence for K-rich terranes on Vesta from impact spherules. Meteoritics & Planetary Science 44, 359-374.

Bates, R.L. and Jackson, J.A. (1980) Glossary of geology, in: Bates, R.L., Jackson, J.A. (Eds.), Glossary of geology, 2nd ed. American Geological Institute, Falls Church, Virginia.

Blewett, D.T., Hawke, B.R. and Lucey, P.G. (2002) Lunar pure anorthosite as a spectral analog for Mercury. Meteoritics & Planetary Science 37, 1255-1268.

Blewett, D.T., Lucey, P.G., Hawke, B.R., Ling, G.G. and Robinson, M.S. (1997) A comparison of Mercurian reflectance and spectral quantities with those of the Moon. Icarus 129, 217-231.

Blewett, D.T., Robinson, M.S., Denevi, B.W., Gillis-Davis, J.J., Head, J.W., Solomon, S.C., Holsclaw, G.M. and McClintock, W.E. (2009) Multispectral images of Mercury from the first MESSENGER flyby: Analysis of global and regional color trends. Earth and Planetary Science Letters 285, 272-282.

Broadfoot, A.L., Kumar, S., Blelton, M.J.S. and McElroy, M.B. (1974) Mercury's atmosphere from Mariner 10: preliminary results. Science 185, 166-169.

Broadfoot, A.L., Shemansky, D.E. and Kumar, S. (1976) Mariner 10: Mercury atmosphere. Geophysical Research Letters 3, 577-580.

Brown, S.M. and Elkins-Tanton, L.T. (2009) Compositions of Mercury's earliest crust from magma ocean models. Earth and Planetary Science Letters 286, 446-455.

Cameron, W.E., McCulloch, M.T. and Walker, D.A. (1983) Boninite Petrogenesis: Chemical and Nd-Sr isotopic constraints. Earth and Planetary Science Letters 65, 75-89.

Campbell, I.H. and Taylor, S.R. (1983) No water, no granites - No oceans, no continents. Geophysical Research Letters 10(11), 1061-1064.

Charlier, B., Grove, T.L. and Zuber, M.T. (2013) Phase equilibria of ultramafic compositions on Mercury and the origin of the compositional dichotomy. . Earth and Planetary Science Letters 363, 50-60.

Chase, S.C., Miner, E.D., Morrison, D., Munch, G., Neugebauer, G. and Schroeder, M. (1974) Preliminary infrared radiometry of the night side of Mercury from Mariner 10. Science 185, 142-145.

Cross, W., Iddings, J.P., Pirsson, L.V. and Washington, H.S. (1903) Quantitative Classification of Igneous Rocks. University of Chicago Press.

Denevi, B.W., Ernst, C.M., Meyer, H.M., Robinson, M.S., Murchie, S.L., Whitten, J.L., Head, J.W., Watters, T.R., Solomon, S.C., Ostrach, L.R., Chapman, C.R., Byrne, P.K., Klimczak, C. and Peplowski, P.N. (2013) The distribution and origin of smooth plains on Mercury. Journal of Geophysical Research-Planets 118, 891-907.

Evans, L.G., Peplowski, P.N., McCubbin, F.M., McCoy, T.J., Nittler, L.R., Zolotov, M.Y., Ebel, D.S., Lawrence, D.J., Starr, R.D., Weider, S.Z. and Solomon, S.C.

(2015) Chlorine on the surface of Mercury: MESSENGER Gamma-Ray measurements and implications for the planet's formation and evolution. Icarus 257, 417-427.

Evans, L.G., Peplowski, P.N., Rhodes, E.A., Lawrence, D.J., McCoy, T.J., Nittler, L.R., Solomon, S.C., Sprague, A.L., Stockstill-Cahill, K.R., Starr, R.D., Weider, S.Z., Boynton, W.V., Hamara, D.K. and Goldsten, J.O. (2012) Major-element abundances on the surface of Mercury: Results from the MESSENGER Gamma-Ray Spectrometer. Journal of Geophysical Research-Planets 117, E00L07.

Frank, E.A., Potter, R.W.K., Abramov, O., Mojzsis, S.J. and Nittler, L.R. (2016) Investigations into the origin of Mercury's high-magnesium region, 47th Lunar and Planetary Science Conference, The Woodlands, TX, p. 1270.

Gellert, R., Rieder, R., Bruckner, J., Clark, B.C., Dreibus, G., Klingelhofer, G., Lugmair, G., Ming, D.W., Wanke, H., Yen, A., Zipfel, J. and Squyres, S.W. (2006) Alpha particle X-ray spectrometer (APXS): Results from Gusev crater and calibration report. Journal of Geophysical Research-Planets 111.

Head, J.W., Chapman, C.R., Strom, R.G., Fassett, C.I., Denevi, B.W., Blewett, D.T., Ernst, C.M., Watters, T.R., Solomon, S.C., Murchie, S.L., Prockter, L.M., Chabot, N.L., Gillis-Davis, J.J., Whitten, J.L., Goudge, T.A., Baker, D.M.H., Hurwitz, D.M., Ostrach, L.R., Xiao, Z., Merline, W.J., Kerber, L., Dickson, J.L., Oberst, J., Byrne, P.K., Klimczak, C. and Nittler, L.R. (2011) Flood Volcanism in the Northern High Latitudes of Mercury Revealed by MESSENGER. Science 333, 1853-1856.

Herd, C.D.K. (2008) Basalts as probes of planetary interior redox state. Oxygen in the Solar System 68, 527-553.

Johannsen, A. (1931) A descriptive petrography of the igneous rocks, University of Chicago Press, pp. 88-92.

Kerber, L., Head, J.W., Blewett, D.T., Solomon, S.C., Wilson, L., Murchie, S.L., Robinson, M.S., Denevi, B.W. and Domingue, D.L. (2011) The global distribution of pyroclastic deposits on Mercury: The view from MESSENGER flybys 1-3. Planetary and Space Science 59, 1895-1909.

Korotev, R.L., Jolliff, B.L., Zeigler, R.A., Gillis, J.J. and Haskin, L.A. (2003) Feldspathic lunar meteorites and their implications for compositional remote sensing of the lunar surface and the composition of the lunar crust. Geochimica Et Cosmochimica Acta 67, 4895-4923.

Lawrence, D.J., Peplowski, P.N., Beck, A.W., Feldman, W.C., Frank, E.A., McCoy, T.J., Nittler, L.R., Chabot, N.L., Ernst, C.M. and Solomon, S.C. (2016) Compositional Terranes on Mercury Derived from Measurements of Fast Neutrons, 47th Lunar and Planetary Science Conference, The Woodlands, TX, p. # 1253.

Le Bas, M.J. (2000) IUGS Reclassification of the High-Mg and Picritic Volcanic Rocks. Journal of Petrology 41, 1467-1470.

Le Feuvre, M. and Wieczorek, M.A. (2011) Nonuniform cratering of the Moon and a revised crater chronology of the inner Solar System. Icarus 214, 1-20.

Le Maitre, R.W., Streckeisen, A., Zanettin, B., Le Bas, M.J., Bonin, B., Bateman, P., Bellieni, G., Dudek, A., Efremova, S., Keller, J., Lameyre, J., Sabine, P.A., Schmid, R., Sorensen, H. and Woolley, A.R. (2002) Igneous Rocks: A Classification and Glossary of Terms. Cambridge University Press, New York.

Lebas, M.J., Lemaitre, R.W., Streckeisen, A. and Zanettin, B. (1986) A Chemical Classification of Volcanic-Rocks Based on the Total Alkali Silica Diagram. Journal of Petrology 27, 745-750.

Lodders, K. and Fegley, B. (1998) The Planetary Scientist's Companion. Oxford University Press, New York.

Marchi, S., Mottola, S., Cremonese, G., Massironi, M. and Martellato, E. (2009) A new chronology for the Moon and Mercury. The Astronomical Journal 137, 4936-4948.

Maturilli, A., Helbert, J., St. John, J.M., Head, J.W.I., Vaughan, W.M., D'Amore, M., Gottschalk, M. and Ferrari, S. (2014) Komatiites as Mercury surface analogues: Spectral measurements at PEL. Earth and Planetary Science Letters 398, 58-65.

McClintock, W.E., Izenberg, N.R., Holsclaw, G.M., Blewett, D.T., Domingue, D.L., Head, J.W., III, Helbert, J., McCoy, T.J., Murchie, S.L., Robinson, M.S., Solomon, S.C., Sprague, A.L. and Vilas, F. (2008) Spectroscopic observations of Mercury's surface reflectance during MESSENGER's first mercury flyby. Science 321, 62-65.

McCord, T.B. and Clark, R.N. (1979) Mercury soil: Presence of Fe^{2+}. Journal of Geophysical Research 84, 7664-7668.

McCubbin, F.M., Riner, M.A., Vander Kaaden, K.E. and Burkemper, L.K. (2012) Is Mercury a volatile-rich planet? Geophysical Research Letters 39.

McCubbin, F.M., Vander Kaaden, K.E., Peplowski, P.N., Evans, L.G., Nittler, L.R., (2016) Is there an oxygen problem on Mercury? Icarus in prep.

McSween, H.Y., Ruff, S.W., Morris, R.V., Bell, J.F., Herkenhoff, K.E., Gellert, R., Stockstill, K.R., Tornabene, L.L., Squyres, S.W., Crisp, J.A., Christensen, P.R., McCoy, T.J., Mittlefehldt, D.W. and Schmidt, M. (2006) Alkaline volcanic rocks from the Columbia Hills, Gusev crater, Mars. Journal of Geophysical Research - Planets 111, 15.

McSween, H.Y., Taylor, G.J. and Wyatt, M.B. (2009) Elemental Composition of the Martian Crust. Science 324, 736-739.

Mittlefehldt, D.W. (2015) Asteroid (4) Vesta: I. The howardite-eucrite-diogenite (HED) clan of meteorites. Chemi der Erde 75, 155-183.

Mittlefehldt, D.W., Herrin, J.S., Quinn, J.E., Mertzman, S.A., Cartwright, J.A., Mertzman, K.R. and Peng, Z.X. (2013) Composition and petrology of HED polymict breccias: The regolith of (4) Vesta. Meteoritics & Planetary Science 48, 2105-2134.

Murray, B.C. (1975) The Mariner 10 pictures of Mercury: an overview. Journal of Geophysical Research 80, 2342-2344.

Namur, O., Collinet, M., Charlier, B., Grove, T.L., Holtz, F. and McCammon, C. (2016) Melting processes and mantle sources of surface lavas on Mercury. Earth and Planetary Science Letters 439.

Nekvasil, H., Filiberto, J., McCubbin, F.M. and Lindsley, D.H. (2007) Alkalic parental magmas for the chassignites? Meteoritics & Planetary Science 42, 979-992.

Nekvasil, H., McCubbin, F.M., Harrington, A., Elardo, S. and Lindsley, D.H. (2009) Linking the Chassigny meteorite and the martian surface rock Backstay: Insights into igneous crustal differentiation processes on Mars. Meteoritics & Planetary Science 44, 853-869.

Ness, N.F., Behannon, K.W., Lepping, R.P. and Whang, Y.C. (1975) The magnetic field of Mercury. Journal of Geophysical Research 80, 2708-2716.

Ness, N.F., Behannon, K.W., Lepping, R.P., Whang, Y.C. and Schatten, K.H. (1974) Magnetic field observations near Mercury: preliminary results from Mariner 10. Science 185, 151-160.

Neukum, G., Oberst, J., Hoffmann, H., Wagner, R. and Ivanov, B.A. (2001) Geologic evolution and cratering history of Mercury. Planetary and Space Science 49, 1507-1521.

Nittler, L.R., Starr, R.D., Weider, S.Z., McCoy, T.J., Boynton, W.V., Ebel, D.S., Ernst, C.M., Evans, L.G., Goldsten, J.O., Hamara, D.K., Lawrence, D.J., McNutt, R.L., Schlemm, C.E., Solomon, S.C. and Sprague, A.L. (2011) The Major-Element Composition of Mercury's Surface from MESSENGER X-ray Spectrometry. Science 333, 1847-1850.

Nittler, L.R., Weider, S.Z., Starr, R.D., Chabot, N.L., Denevi, B.W., Ernst, C.M., Goudge, T.A., Head, J.W., Helbert, J., Klima, R.L., McCoy, T.J. and Solomon, S.C. (2014) Sulfur-depleted composition of Mercury's largest pyroclastic deposit: Implications for explosive volcanism and surface reflectance on the innermost planet., 45th Lunar and Planetary Science Conference, The Woodlands, TX, p. # 1391.

Ostrach, L.R., Robinson, M.S., Whitten, J.L., Fassett, C.I., Strom, R.G., Head, J.W. and Solomon, S.C. (2015) Extent, age, and resurfacing history of the northern smooth plains on Mercury from MESSENGER observations. Icarus 250, 602-622.

Peplowski, P.N., Evans, L.G., Stockstill-Cahill, K.R., Lawrence, D.J., Goldsten, J.O., McCoy, T.J., Nittler, L.R., Solomon, S.C., Sprague, A.L., Starr, R.D. and Weider, S.Z. (2014) Enhanced sodium abundance in Mercury's north polar region revealed by the MESSENGER Gamma-Ray Spectrometer. Icarus 228, 86-95.

Peplowski, P.N., Lawrence, D.J., Evans, L.G., Klima, R.L., Blewett, D.T., Goldsten, J.O., Murchie, S.L., McCoy, T.J., Nittler, L.R., Solomon, S.C., Starr, R.D. and Weider, S.Z. (2015a) Constraints on the abundance of carbon in near-surface materials on Mercury: Results from the MESSENGER Gamma-Ray Spectrometer. Planetary and Space Science.

Peplowski, P.N., Lawrence, D.J., Feldman, W.C., Goldsten, J.O., Bazell, D., Evans, L.G., Head, J.W., Nittler, L.R., Solomon, S.C. and Weider, S.Z. (2015b) Geochemical terranes of Mercury's northern hemisphere as revealed by MESSENGER neutron measurements. Icarus 253, 346-363.

Peplowski, P.N., Lawrence, D.J., Rhodes, E.A., Sprague, A.L., McCoy, T.J., Denevi, B.W., Evans, L.G., Head, J.W., Nittler, L.R., Solomon, S.C., Stockstill-Cahill, K.R. and Weider, S.Z. (2012a) Variations in the abundances of potassium and thorium on the surface of Mercury: Results from the MESSENGER Gamma-Ray Spectrometer. Journal of Geophysical Research - Planets 117.

Peplowski, P.N., Rhodes, E.A., Hamara, D.K., Lawrence, D.J., Evans, L.G., Nittler, L.R. and Solomon, S.C. (2012b) Aluminum abundance on the surface of Mercury: Applications of a new background-reduction technique for the analysis of gamma-ray spectroscopy data. Journal of Geophysical Research 117, E00L10.

Polat, A., Hofmann, A.W. and Rosing, M.T. (2002) Boninite-like volcanic rocks in the 3.7-3.8 Ga Isua greenstone belt, West Greenland: geochemical evidence for intra-oceanic subduction zone processes in the early Earth. Chemical Geology 184.

Riner, M.A., McCubbin, F.M., Lucey, P.G., Talyor, G.J. and Gillis-Davis, J.J. (2010) Mercury surface composition: Integrating petrologic modeling and remote sensing data to place constraints on FeO abundance. Icarus 209, 301-313.

Robinson, M.S. and Lucey, P.G. (1997) Recalibrated Mariner 10 color mosaics: Implications for Mercurian volcanism. Science 275, 197-200.

Robinson, M.S., Murchie, S.L., Blewett, D.T., Domingue, D.L., Hawkins, S.E., III, Head, J.W., Holsclaw, G.M., McClintock, W.E., McCoy, T.J., McNutt, R.L., Jr., Prockter, L.M., Solomon, S.C. and Watters, T.R. (2008) Reflectance and color variations on Mercury: Regolith processes and compositional heterogeneity. Science 321, 66-69.

Rudnick, R.L. and Gao, S. (2003) Composition of the Continental Crust. Treatise on Geochemistry 3, 1-64.

Santos, A.R., Agee, C.B., McCubbin, F.M., Shearer, C.K., Burger, P.V., Tartese, R. and Anand, M. (2015) Petrology of igneous clasts in Northwest Africa 7034: Implications for the petrologic diversity of the martian crust. Geochimica Et Cosmochimica Acta 157, 56-85.

Seddio, S.M., Jolliff, B.L., Korotev, R.L. and Zeigler, R.A. (2013) Petrology and geochemistry of lunar granite 12032,366-19 and implications for lunar granite petrogenesis. American Mineralogist 98, 1697-1713.

Sehlke, A. and Whittington, A.G. (2015) Rheology of lava flows on Mercury: An analog experimental study. Journal of Geophysical Research-Planets 120, 1924-1955.

Sehlke, A., Whittington, A.G., Robert, B., Harris, A., Gurioli, L. and Medard, E. (2014) Pahoehoe to 'a'a transition of Hawaiian lavas: an experimental study. Bull Volcanol 76, 879.

Sharp, Z.D., McCubbin, F.M. and Shearer, C.K. (2013) A hydrogen-based oxidation mechanism relevant to planetary formation. Earth and Planetary Science Letters 380, 88-97.

Solomon, S.C., McNutt Jr., R.L., Gold, R.E., Acu˜na, M.H., Baker, D.N., Boynton, W.V., Chapman, C.R., Cheng, A.F., Gloeckler, G., Head, J.W., Krimigis, S.M., McClintock, W.E., Murchie, S.L., Peale, S.J., Phillips, R.J., Robinson, M.S., Slavin, J.A., Smith, D.E., Strom, R.G., Trombka, J.I. and Zuber, M.T. (2001) The MESSENGER mission to Mercury: scientific objectives and implementation. Planetary and Space Science 49, 1445-1465.

Sprague, A.L. and Roush, T.L. (1998) Comparison of laboratory emission spectra with Mercury telescopic data. Icarus 133, 174-183.

Stockstill-Cahill, K.R., McCoy, T.J., Nittler, L.R., Weider, S.Z. and Hauck II, S.A. (2012) Magnesium-rich crustal compositions on Mercury: Implications for magmatism from petrologic modeling. Journal of Geophysical Research 117, E00L15.

Stolper, E.M., Baker, M.B., Newcombe, M.E., Schmidt, M.E., Treiman, A.H., Cousin, A., Dyar, M.D., Fisk, M.R., Gellert, R., King, P.L., Leshin, L., Maurice, S., McLennan, S.M., Minitti, M.E., Perrett, G., Rowland, S., Sautter, V., Wiens, R.C. and Team, M.S. (2013) The Petrochemistry of Jake_M: A Martian Mugearite. Science 341.

Taylor, G.J. and Scott, E.R.D. (2004) Mercury, in: Davis, A.M. (Ed.), Treatise on Geochemistry: Meteorites, Comets and Planets. Elsevier, Amsterdam, The Netherlands, pp. 477-485.

Taylor, S.R. and McLennan, S.M. (2009) Planetary Crusts: Their Composition, Origin and Evolution. Cambridge University Press.

Vander Kaaden, K.E. and McCubbin, F.M. (2015) Exotic Crust Formation on Mercury: Consequences of a Shallow, FeO-poor Mantle. Journal of Geophysical Research - Planets 120, 195-209.

Vander Kaaden, K.E. and McCubbin, F.M. (2016) The origin of boninites on Mercury: An experimental study of the northern volcanic plains lavas. Geochimica Et Cosmochimica Acta 173, 246-263.

Vilas, F. (1988) Surface composition of Mercury from reflectance spectrophotometry in: Vilas, F., Chapman, C.R., Matthews, M.S. (Eds.), Mercury. The University of Arizona Press, Tucson, AZ, pp. 59-76.

Wadhwa, M. (2008) Redox conditions on small bodies, the Moon, and Mars. Oxygen in the Solar System 68, 493-510.

Warren, P.H., Kallemeyn, G.W., Huber, H., Ulff-Møller, F. and Choe, W. (2009) Siderophile and other geochemical constraints on mixing relationships among HED-meteoritic breccias. Geochimica Et Cosmochimica Acta 73, 5918-5943.

Weider, S.Z., Nittler, L.R., Murchie, S.L., Peplowski, P.N., McCoy, T.J., Kerber, L., Klimczak, C., Ernst, C.M., Goudge, T.A., Starr, R.D., Izenberg, N.R., Klima, R.L. and Solomon, S.C. (2016) Evidence from MESSENGER fro sulfur- and carbon-driven explosive volcanism on Mercury. Geophysical Research Letters In press.

Weider, S.Z., Nittler, L.R., Starr, R.D., Crapster-Pregont, E.J., Peplowski, P.N., Denevi, B.W., Head, J.W., Byrne, P.K., Hauck II, S.A. and Solomon, S.C. (2015) Evidence for geochemical terranes on Mercury: The first global mapping of major elements on the surface of the innermost planet. Earth and Planetary Science Letters.

Weider, S.Z., Nittler, L.R., Starr, R.D., McCoy, T.J. and Solomon, S.C. (2014) Variations in the abundance of iron on Mercury's surface from MESSENGER X-Ray Spectrometer observations. Icarus 235, 170-186.

Weider, S.Z., Nittler, L.R., Starr, R.D., McCoy, T.J., Stockstill-Cahill, K.R., Byrne, P.K., Denevi, B.W., Head, J.W. and Solomon, S.C. (2012) Chemical heterogeneity on Mercury's surface revealed by the MESSENGER X-Ray Spectrometer. Journal of Geophysical Research - Planets 117.

Wilson, A.H. (2003) A new class of silica enriched, highly depleted komatiites in the southern Kaapvaal Craton, South Africa. Precambrian Research 127, 125-141.

Zolotov, M.Y., Sprague, A.L., Hauck, S.A., Nittler, L.R., Solomon, S.C. and Weider, S.Z. (2013) The redox state, FeO content, and origin of sulfur-rich magmas on Mercury. Journal of Geophysical Research-Planets 118.

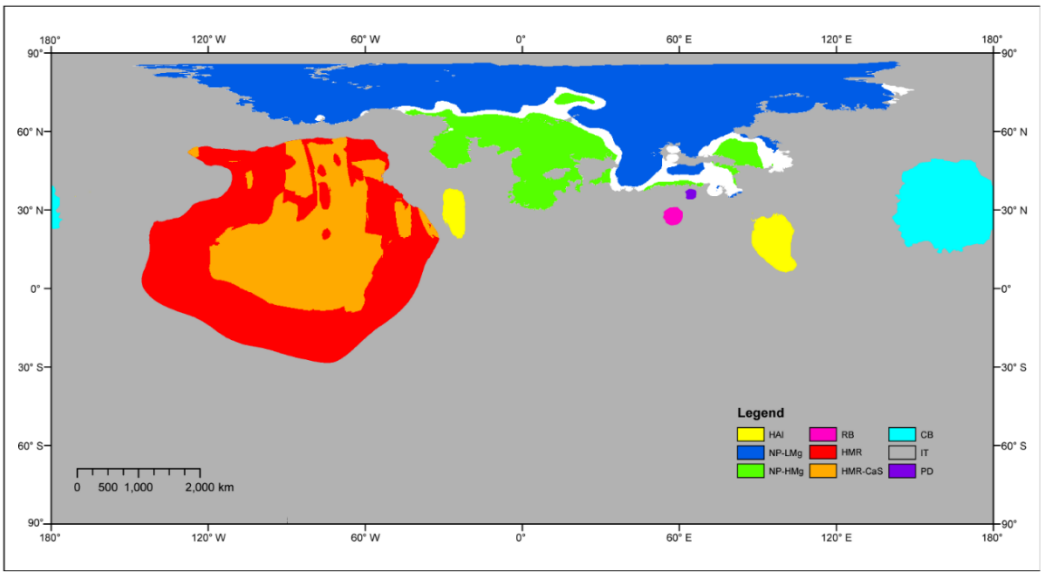

Figure 1. Identification of geochemical regions defined by XRS. White areas indicate regions not considered in our calculations.

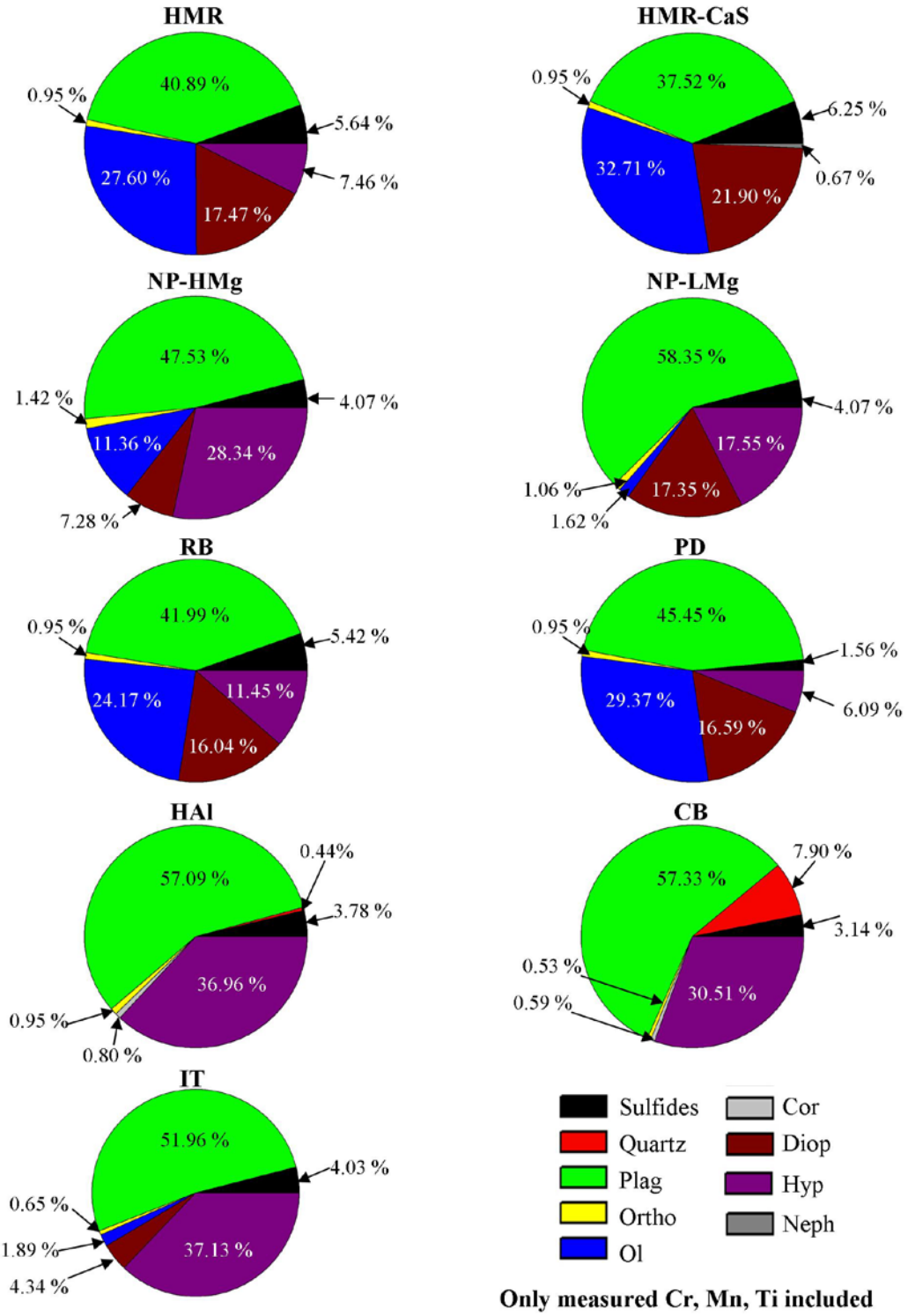

Figure 2. Pie charts reflecting the CIPW normative calculations of the nine geochemical regions using only the measured values of Cr, Mn, and Ti. Plag-plagioclase, ortho-orthopyroxene, ol-olivine, cor-corundum, diop-diopside, hyp-hypersthene, neph-nepheline.

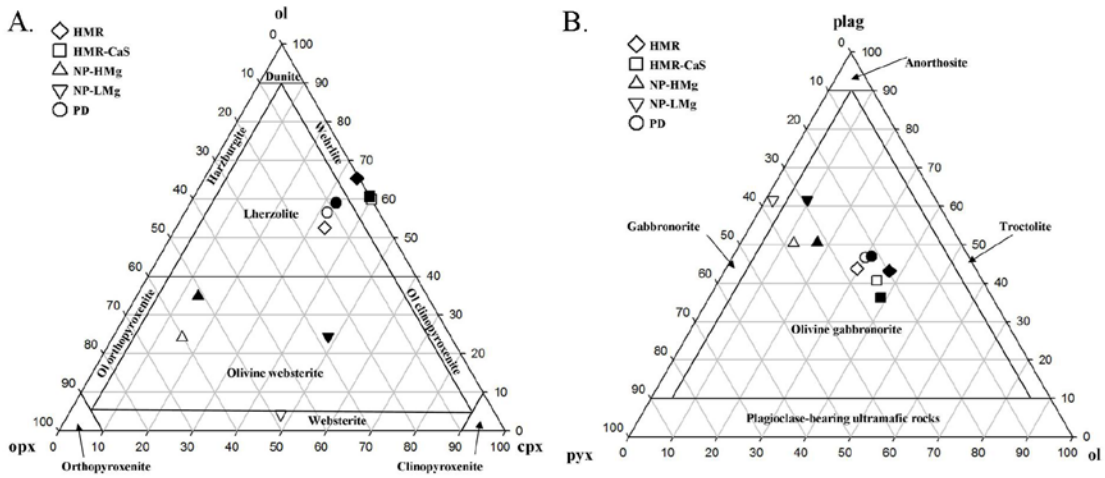

Figure 3. IUGS rock classification diagrams for plutonic rocks. CIPW normative calculations of silicate mineralogies for the HMR, HMR-CaS, NP-HMg, NP-LMg, and PD displayed on (A) clinopyroxene (cpx) – olivine (ol) – orthopyroxene (opx) ternary diagram and (B) olivine – plagioclase (plag) – pyroxene (pyx) ternary diagram. Clinopyroxene is defined as the diopside in the CIPW normative mineralogy calculations and opx is defined as the hypersthene in the CIPW normative mineralogy calculations. The pyx in Figure 3B is the sum of these values.

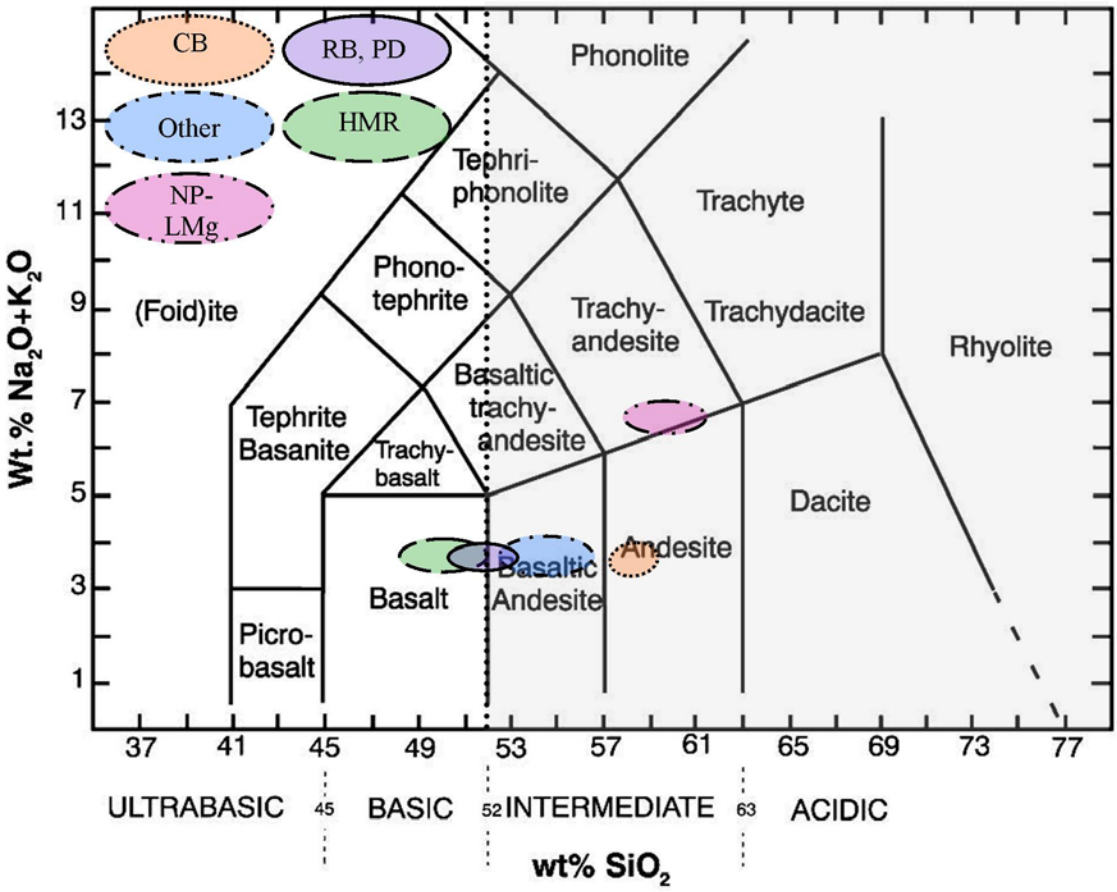

Figure 4. Total alkali versus silica diagram for nine distinct geochemical units on Mercury. Dashed line is at 52 wt% SiO_2. Shaded region >52 wt% SiO_2 represents boninites. Unshaded region <52 wt% SiO_2 represents komatiitic compositions.

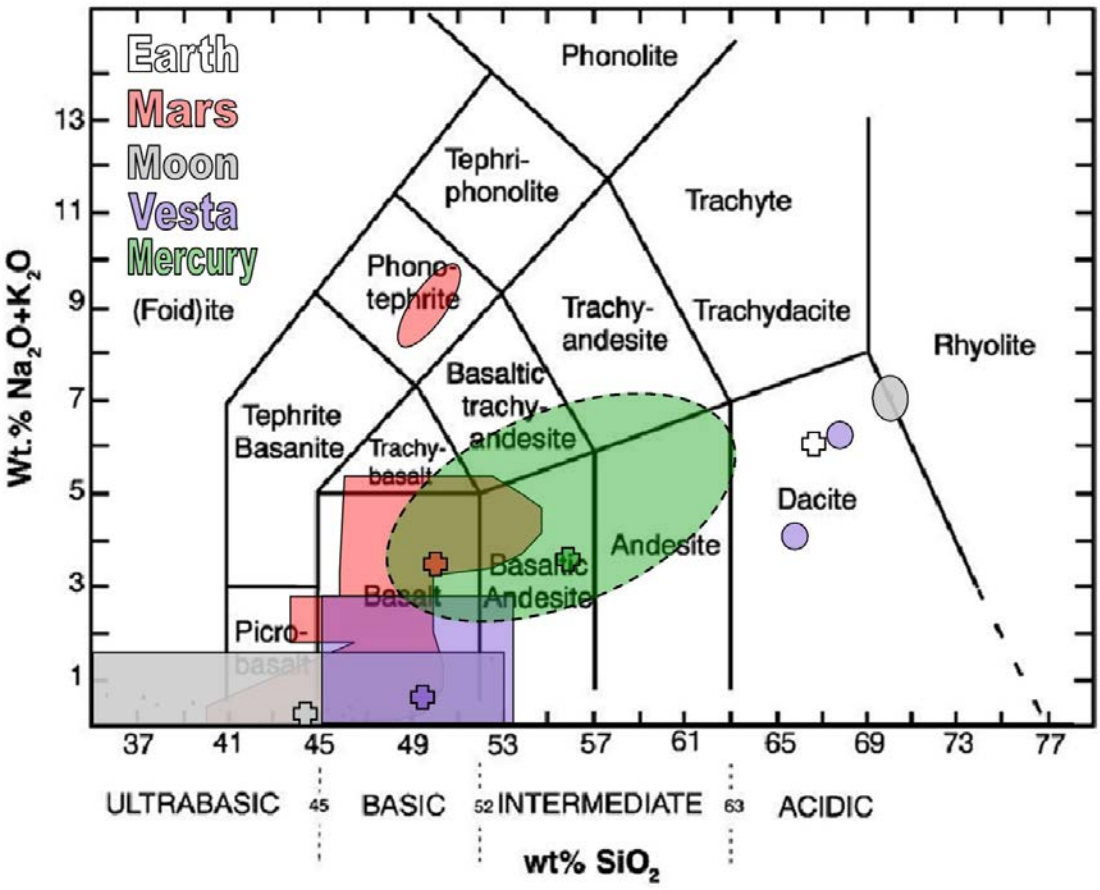

Figure 5. Total alkali versus silica diagram for rocks on Earth, Mars, Moon, Vesta, and Mercury. The shaded region for Mercury was determined by enclosing the nine distinct geochemical units represented in Figure 4. Data for Mars, Moon, and Vesta are from (Barrat et al., 2009; Gellert et al., 2006; Lodders and Fegley, 1998; McSween et al., 2009; Stolper et al., 2013). Crosses represent the average regolith compositions given in Table 4.

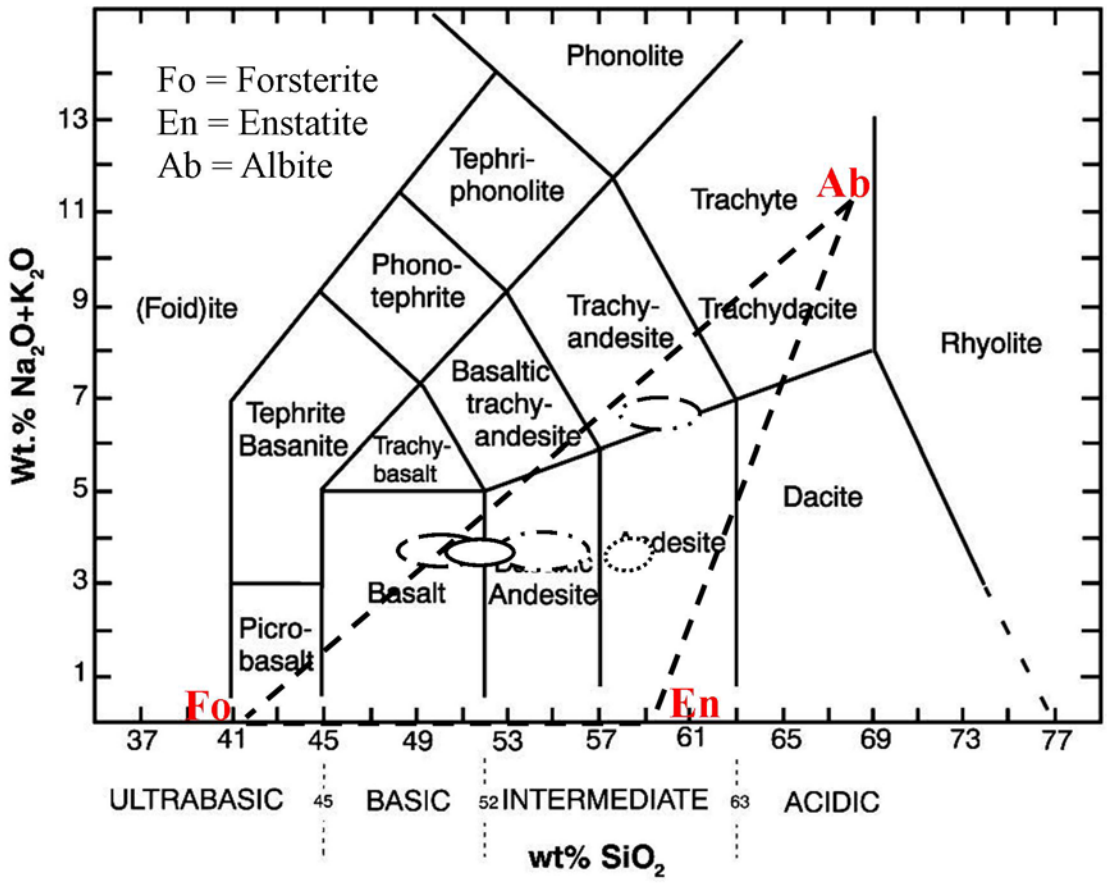

Figure 6. Total alkali versus silica diagram containing endmember minerals forsterite (Fo), enstatite (En), and Albite (Ab). Fields for mercurian geochemical regions are the same as those in Figure 4.

Table 1. Average compositions (wt%) for nine distinct geochemical units on Mercury using only reported values for Ti, Mn, and Cr.

	HMR	HMR-CaS	NP-HMg	NP-LMg	RB	PD	HAl	CB	IT
SiO_2	51.81	50.50	54.89	60.70	52.40	53.08	55.42	58.86	55.89
MgO	24.15	25.14	20.28	12.50	23.42	21.81	16.50	13.05	17.94
CaO	7.00	7.76	5.58	5.43	6.84	7.46	5.73	5.70	5.74
Al_2O_3	10.05	9.27	12.57	12.16	10.45	11.72	16.78	16.59	14.06
K_2O	0.16	0.16	0.24	0.18	0.16	0.16	0.16	0.09	0.11
Na_2O	3.51	3.51	3.51	6.47	3.51	3.51	3.51	3.51	3.51
FeO	1.99	2.19	2.02	1.62	1.94	1.98	0.97	0.99	1.84
TiO_2	0.00	0.00	0.00	0.00	0.00	0.00	0.00	0.46	0.00
CrO	0.00	0.00	0.00	0.00	0.00	0.00	0.00	0.00	0.00
MnO	0.00	0.00	0.00	0.00	0.00	0.00	0.00	0.00	0.00
S	2.67	2.96	1.80	1.88	2.57	0.57	1.88	1.52	1.81
-O=S	1.33	1.48	0.90	0.94	1.28	0.28	0.94	0.76	0.90
Total	100.00	100.00	100.00	100.00	100.00	100.00	100.00	100.00	100.00
Wt% Si	24.22	23.61	25.66	28.37	24.50	24.81	25.90	27.51	26.13
Total Alkalis	3.66	3.66	3.75	6.65	3.66	3.66	3.66	3.60	3.62

Table 2. Average compositions (wt%) for nine distinct geochemical units on Mercury using the detection limit of Ti, Mn, and Cr from Nittler et al. (2011) and Weider et al. (2015) as an upper limit if these elements were not reported.

	HMR	HMR-CaS	NP-HMg	NP-LMg	RB	PD	HAl	CB	IT
SiO_2	50.52	49.27	53.44	58.87	51.08	51.72	53.94	58.00	55.41
MgO	23.54	24.52	19.75	12.13	22.82	21.25	16.06	12.86	17.79
CaO	6.82	7.57	5.43	5.27	6.66	7.27	5.58	5.62	5.70
Al_2O_3	9.80	9.04	12.24	11.79	10.19	11.42	16.34	16.35	13.93
K_2O	0.16	0.16	0.24	0.18	0.16	0.16	0.16	0.09	0.11
Na_2O	3.51	3.51	3.51	6.47	3.51	3.51	3.51	3.51	3.51
FeO	1.94	2.14	1.97	1.57	1.89	1.93	0.94	0.97	1.83
TiO_2	1.18	1.15	1.25	1.38	1.20	1.21	1.26	0.45	0.52
CrO	0.62	0.60	0.65	0.72	0.62	0.63	0.66	0.71	0.17
MnO	0.61	0.59	0.65	0.71	0.62	0.62	0.65	0.70	0.13
S	2.60	2.89	1.75	1.82	2.50	0.56	1.83	1.50	1.79
-O=S	1.30	1.44	0.87	0.91	1.25	0.28	0.91	0.75	0.90
Total	100.00	100.00	100.00	100.00	100.00	100.00	100.00	100.00	100.00
Wt% Si	23.61	23.03	24.98	27.52	23.88	24.18	25.21	27.11	25.90
Total Alkalis	3.66	3.66	3.75	6.65	3.66	3.66	3.66	3.60	3.62

Table 3. Silicate melt parameters for three distinct volcanic units. M: Metaluminous (Al_2O_3 < (CaO + Na_2O + K_2O) and Al_2O_3 > (Na_2O + K_2O)). P: Peraluminous ($Na_2O+K_2O+CaO < Al_2O_3$). NBO/T: Nonbridging oxygen per tetrahedrally coordinated cation.

	NP-HMg	**NP-LMg**	**PD**
Alumina Saturation	P	M	M
Mg # (molar $\left(\frac{Mg}{Mg+Fe}\right) * 100$)	94.70	93.23	95.15
Alkalinity Index	0.48–0.49	0.89–0.94	0.51–0.58
NBO/T	0.98–1.0	0.67–0.71	1.16–1.30

Table 4. Composition of regolith for the Moon (Korotev et al., 2003), Mars (Santos et al., 2015), Earth (Rudnick and Gao, 2003), Vesta (Mittlefehldt, 2015; Mittlefehldt et al., 2013; Warren et al., 2009) and Mercury (this study).

Oxide	Moon	Mars	Earth	Vesta	Mercury
SiO_2	44.80	50.40	66.45	49.62	55.89
MgO	5.41	12.19	2.47	13.79	17.94
CaO	16.34	5.73	3.58	7.14	5.74
Al_2O_3	28.26	11.10	15.36	8.69	14.06
K_2O	0.03	0.54	2.79	0.30	0.11
Na_2O	0.35	3.03	3.26	0.31	3.51
FeO	4.41	14.94	5.03	18.34	1.84
TiO_2	0.22	0.70	0.64	0.44	0
Cr_2O_3	0.10	0.00	0.13	0.63	0
MnO	0.06	0.35	0.10	0.53	0
P_2O_5	0.03	1.01	0.15	0.06	0
S	0.00	0.00	0.06	0.29	1.81
-O=S	0.00	0.00	0.03	0.14	0.9
Total	100.00	100.00	100.00	100.00	100.00

Table 5. Composition of regolith for the Moon (Korotev et al., 2003), Mars (Santos et al., 2015), Earth (Rudnick and Gao, 2003), Vesta (Mittlefehldt, 2015; Mittlefehldt et al., 2013; Warren et al., 2009) and Mercury (this study) renormalized once all FeO is removed.

Oxide	Moon	Mars	Earth	Vesta	Mercury
SiO_2	46.86	59.26	69.98	60.76	56.94
MgO	5.66	14.33	2.60	16.89	18.28
CaO	17.09	6.74	3.77	8.74	5.85
Al_2O_3	29.56	13.05	16.18	10.65	14.32
K_2O	0.03	0.63	2.94	0.37	0.11
Na_2O	0.37	3.56	3.43	0.38	3.58
FeO	*0.00*	*0.00*	*0.00*	*0.00*	*0.00*
TiO_2	0.23	0.82	0.67	0.53	0.00
Cr_2O_3	0.10	0.00	0.14	0.77	0.00
MnO	0.06	0.41	0.11	0.65	0.00
P_2O_5	0.03	1.19	0.16	0.07	0.00
S	0.00	0.00	0.06	0.36	1.84
-O=S	0.00	0.00	0.03	0.18	0.92
Total	100.00	100.00	100.00	100.00	100.00

Supplementary Figures
Figure S1.

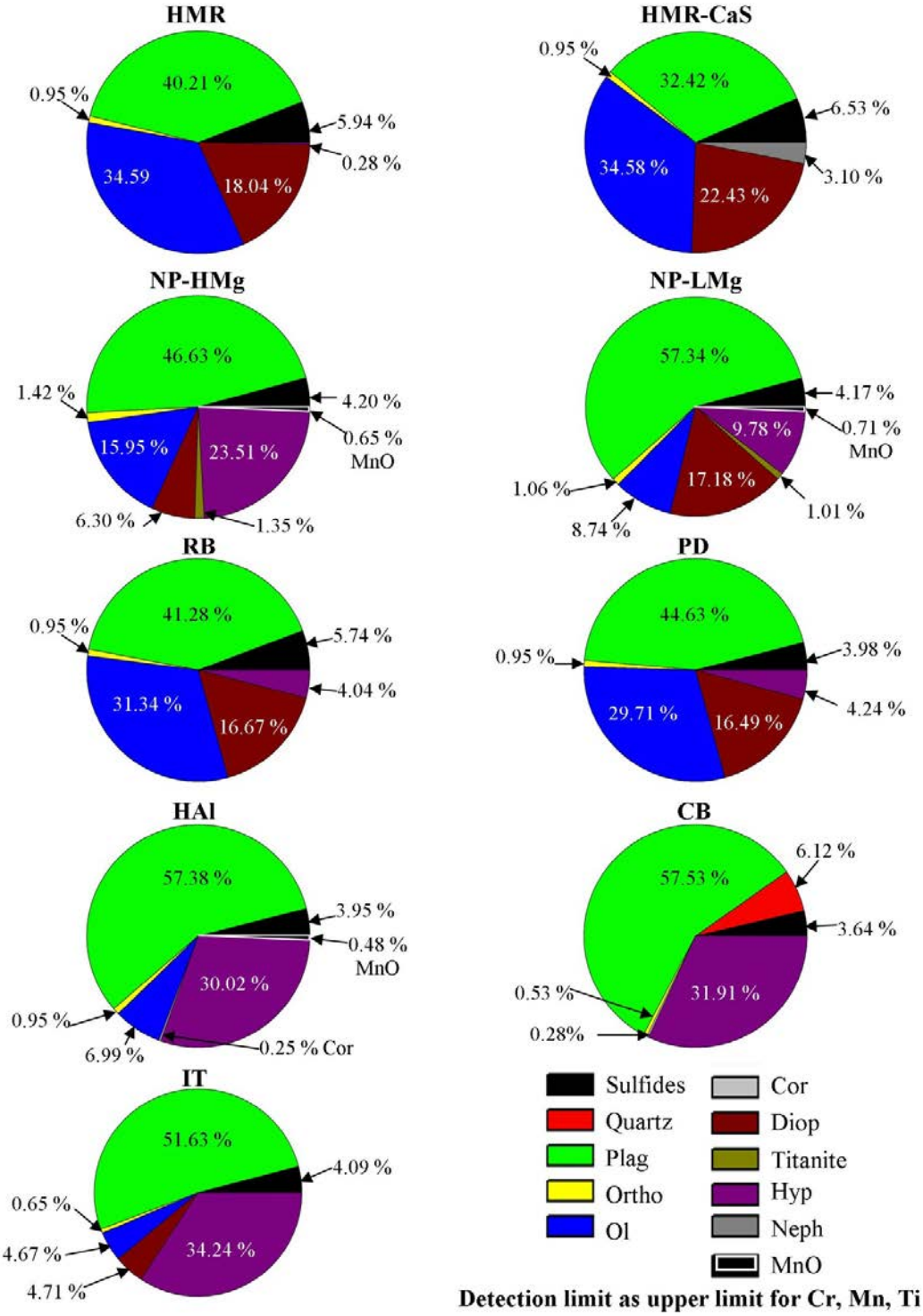

Figure S1. Pie charts reflecting the CIPW normative calculations of the nine geochemical regions using the detection limits from Nittler et al. (2011) and Weider et al. (2015) as upper limit values for Cr, Mn, and Ti. Abbreviations are the same as Figure 2.

Figure S2.

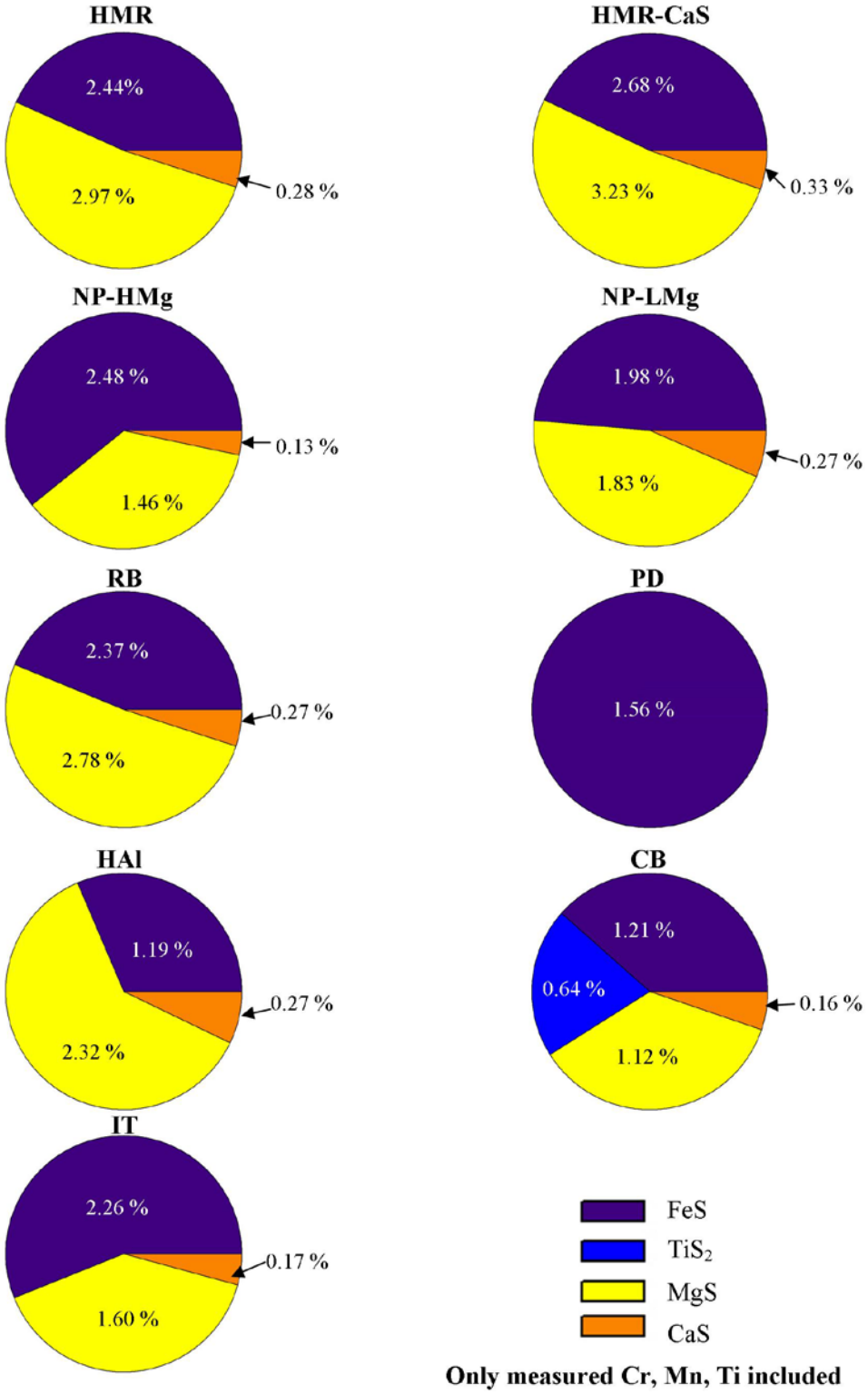

Figure S2. Pie charts reflecting the CIPW normative sulfide calculations of the nine geochemical regions using only the measured values for Cr, Mn, and Ti.

Figure S3.

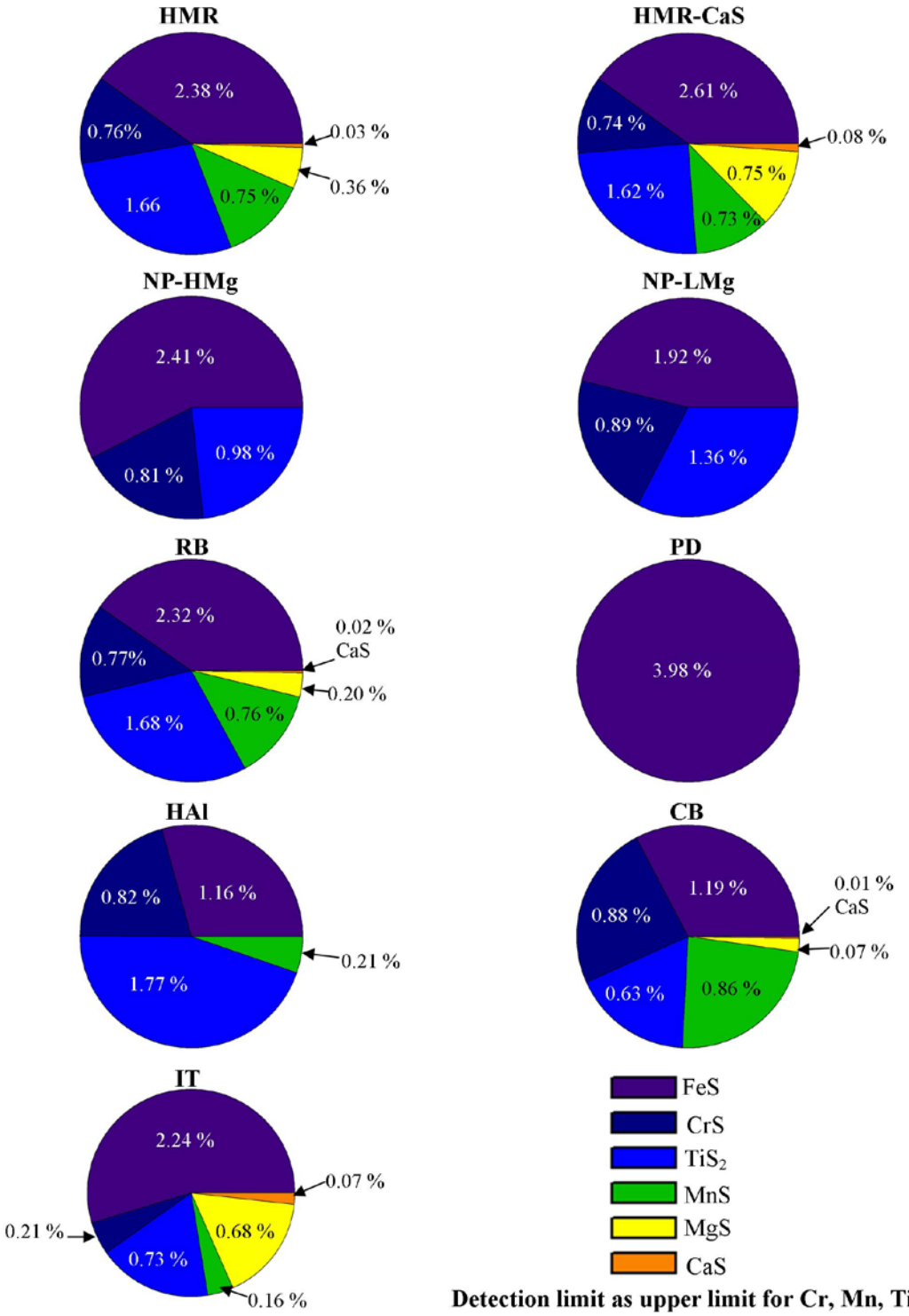

Figure S3. Pie charts reflecting the CIPW normative sulfide calculations of the nine geochemical regions using the detection limits from Nittler et al. (2011) and Weider et al. (2015) as upper limit values for Cr, Mn, and Ti.

Supplementary Tables

Table S1. Elemental Ratios used for Calculations (wt. ratios)

	HMR	HMR-CaS	NP-HMg	NP-LMg	RB	PD	HAl	CB	IT
Mg/Si	0.6012042	0.642157	0.476752	0.265733	0.576471	0.53	0.3841037	0.2859992	0.4141567
Ca/Si	0.2064233	0.234819	0.155493	0.136732	0.1994595	0.215	0.1580525	0.1480682	0.157152
Al/Si	0.2196857	0.2078469	0.259292	0.226804	0.2258526	0.25	0.3429304	0.3191265	0.2847306
K (wt %)	0.1288	0.1288	0.2	0.15	0.1288	0.1288	0.1288	0.0754	0.0952
Na (wt %)	2.6	2.6	2.6	4.8	2.6	2.6	2.6	2.6	2.6
Fe/Si	0.0639778 3	0.0720696 8	0.061337	0.044339	0.0615867 9	0.062	0.0291139 2	0.0278740 2	0.0548836 7
Ti/Si	0.03	0.03	0.03	0.03	0.03	0.03	0.03	0.01	0.03
Cr/Si	0.02	0.02	0.02	0.02	0.02	0.02	0.02	0.02	0.02
Mn/Si	0.02	0.02	0.02	0.02	0.02	0.02	0.02	0.02	0.02
S/Si	0.1102334	0.1255058	0.070045	0.066179	0.1047928	0.023	0.0724751 4	0.0551706 3	0.0692685

Table S2. CIPW Norm Calculations (wt%) for Each Geochemical Region*
*Compositions contain only the measured amounts of Cr, Mn, and Ti. H=Hypersthene, Ol=Olivine, Qtz=Quartz

	HMR	**HMR-CaS**	**NP-HMg**	**NP-LMg**	**RB**	**PD**	**HAl**	**CB**	**IT**
FeS	2.44	2.68	2.48	1.98	2.37	1.56	1.19	1.21	2.26
TiS_2	0.00	0.00	0.00	0.00	0.00	0.00	0.00	0.64	0.00
MgS	2.91	3.23	1.46	1.83	2.78	0.00	2.32	1.12	1.60
CaS	0.28	0.33	0.13	0.27	0.27	0.00	0.27	0.16	0.17
Quartz	0.00	0.00	0.00	0.00	0.00	0.00	0.44	7.90	0.00
Plagioclase	40.89	37.52	47.53	58.35	41.99	45.45	57.09	57.33	51.96
Orthoclase	0.95	0.95	1.42	1.06	0.95	0.95	0.95	0.53	0.65
Nepheline	0.00	0.67	0.00	0.00	0.00	0.00	0.00	0.00	0.00
Corundum	0.00	0.00	0.00	0.00	0.00	0.00	0.80	0.59	0.00
Diopside	17.47	21.90	7.28	17.35	16.04	16.59	0.00	0.00	4.34
Hypersthene	7.46	0.00	28.34	17.55	11.45	6.09	36.96	30.51	37.13
Olivine	27.60	32.71	11.36	1.62	24.17	29.37	0.00	0.00	1.89
Total	100.0	100.0	100.0	100.0	100.0	100.0	100.0	100.0	100.0
Sulfides	5.64	6.25	4.07	4.07	5.42	1.56	3.78	3.14	4.03
Normative	H	N	H	H	H	H	H	H	H
	Ol	Ol	Ol	Ol	Ol	Ol	Qtz	Qtz	Ol

Table S3. CIPW Norm Calculations (wt%) for Each Geochemical Region*
*Compositions contain the detection limit of Cr, Mn, and Ti from Nittler et al., (2011) as upper limit estimate. H=Hypersthene, Ol=Olivine, Qtz=Quartz

	HMR	**HMR -CaS**	**NP-HMg**	**NP-LMg**	**RB**	**PD**	**HAl**	**CB**	**IT**
FeS	2.38	2.61	2.41	1.92	2.32	3.98	1.16	1.19	2.24
CrS	0.76	0.74	0.81	0.89	0.77	0.00	0.82	0.88	0.21
TiS_2	1.66	1.62	0.98	1.36	1.68	0.00	1.77	0.63	0.73
MnS	0.75	0.73	0.00	0.00	0.76	0.00	0.21	0.86	0.16
MgS	0.36	0.75	0.00	0.00	0.20	0.00	0.00	0.07	0.68
CaS	0.03	0.08	0.00	0.00	0.02	0.00	0.00	0.01	0.07
Quartz	0.00	0.00	0.00	0.00	0.00	0.00	0.00	6.12	0.00
Plagioclase	40.21	32.42	46.63	57.34	41.28	44.63	57.38	57.53	51.63
Orthoclase	0.95	0.95	1.42	1.06	0.95	0.95	0.95	0.53	0.65
Nepheline	0.00	3.10	0.00	0.00	0.00	0.00	0.00	0.00	0.00
Corundum	0.00	0.00	0.00	0.00	0.00	0.00	0.25	0.28	0.00
Diopside	18.04	22.43	6.30	17.18	16.67	16.49	0.00	0.00	4.71
Hypersthene	0.28	0.00	23.51	9.78	4.04	4.24	30.02	31.91	34.24
Olivine	34.59	34.58	15.95	8.74	31.34	29.71	6.99	0.00	4.67
Sphene	0.00	0.00	1.35	1.01	0.00	0.00	0.00	0.00	0.00
MnO	0.00	0.00	0.65	0.71	0.00	0.00	0.48	0.00	0.00
Total	100.0	100.0	100.0	100.0	100.0	100.0	100.0	100.0	100.0
Sulfides	5.94	6.53	4.20	4.17	5.74	3.98	3.95	3.64	4.09
Normative	H	N	H	H	H	H	H	H	H
	Ol	Ol	Ol	Ol	Ol	Ol	Ol	Qtz	Ol

Table S4. CIPW Norm Regolith Compositions (wt%)

	Moon	**Mars**	**Earth**	**Vesta**
Quartz	0.00	0.00	22.15	0.00
Plagioclase	78.48	40.73	44.41	24.18
Orthoclase	0.18	3.19	16.50	1.78
Diopside	4.40	5.55	0.00	11.29
Hypersthene	9.12	25.56	14.40	57.61
Olivine	7.33	21.29	0.00	3.55
Ilmenite	0.42	1.33	1.22	0.84
Apatite	0.07	2.34	0.35	0.14
Pyrite	0.00	0.00	0.13	0.61
Total	100.00	100.00	100.00	100.00

Chapter 2

Exotic crust formation on Mercury: Consequences of a shallow, FeO-poor mantle

In collaboration with

Francis M. McCubbin[1,2]

[1]Institute of Meteoritics, Department of Earth & Planetary Sciences, University of New Mexico, Albuquerque, NM 87131, USA. [2]NASA Johnson Space Center, Mailcode XI2, 2101 NASA Parkway, Houston, TX 77058, USA.

Citation: Vander Kaaden, K.E., and McCubbin, F.M. (2015) Exotic crust formation on Mercury: consequences of a shallow, FeO-poor mantle. *Journal of Geophysical Research: Planets*, **120**, 195-209, doi: 10.1002/2014JE004733

Abstract:

The range in density and compressibility of mercurian melt compositions was determined to better understand the products of a possible mercurian magma ocean and subsequent volcanism. Our experiments indicate that the only mineral to remain buoyant with respect to melts of the mercurian mantle is graphite; consequently, it is the only candidate mineral to have composed a primary floatation crust during a global magma ocean. This exotic result is further supported by Mercury's volatile-rich nature and inexplicably darkened surface. Additionally, our experiments illustrate that partial melts of the mercurian mantle that compose the secondary crust were buoyant over the entire mantle depth and could have come from as deep as the core-mantle boundary. Furthermore, Mercury could have erupted higher percentages of its partial melts compared to other terrestrial planets because magmas would not have stalled during ascent due to gravitational forces. These findings stem from the FeO-poor composition and shallow depth of Mercury's mantle, which has resulted in both low melt density and

a very limited range in melt density responsible for Mercury's primary and secondary crusts. The enigmatically darkened, yet low-FeO surface, which is observed today can be explained by secondary volcanism and impact processes that have since mixed the primary and secondary crustal materials.

Keywords: Mercury, Graphite floatation crust, sink-float

1. Introduction

The terrestrial planets that comprise our inner solar system, including the Moon, are all rocky bodies that have differentiated into a crust, mantle, and core. Furthermore, all of these bodies have undergone various igneous processes since their time of primary crust formation. These processes have resurfaced each of these bodies, at least in part, resulting in the production of a secondary crust. Mercury, however, exhibits evidence that it may differ from this typical structure. Since its first flyby encounter with Mercury on January 14, 2008, the MErcury Surface, Space ENvironment, GEochemistry and Ranging (MESSENGER) spacecraft has been collecting data on the structure, chemical makeup, and density of the planet among other important characteristics [*Solomon et al.*, 2001]. Recent MESSENGER-based observations have suggested that Mercury is made up of a crust, mantle, iron sulfide (FeS) layer, and core [*Hauck et al.*, 2013; *Smith et al.*, 2012]. The core of Mercury is likely dominated by iron; however, the high metal-silicate ratio of Mercury, along with the low inferred abundance of FeO [≤4 wt%; *Nittler et al.*, 2011; *Weider et al.*, 2012] in the silicate portion of Mercury further supports it as an end-member among the terrestrial planets and as a unique case of planetary differentiation.

If present, the solid FeS layer is at the top of the liquid outer core where this component would be buoyant relative to the Fe-rich metal core beneath it [*Hauck et al.*, 2013]. The potential existence of this layer has important implications for the distribution of heat-producing elements in the planet's interior [*McCubbin et al.*, 2012], the impact on partitioning of Si and other light elements into the core [*Chabot et al.*, 2014; *Gessmann et al.*, 2001; *Javoy et al.*, 2010; *Li and Agee*, 2001; *Malavergne et al.*, 2010; *Ricolleau et al.*, 2011; *Tsuno et al.*, 2013], and the general thermal and magmatic evolution of the planet [*Hauck et al.*, 2013]. Above this possible layer is the mantle of Mercury. On Earth, the mantle extends to about ~3480 km depth (~135 GPa) [*Dziewonski and Anderson*, 1981]. The metal-silicate ratio of the Earth is similar to the other terrestrial planets, as exemplified by the similarity in the normalized mean moment of inertia (I/mr^2) values [*Ramsey and Blackett*, 1948]. On Mercury, the boundary between the silicate portion of the planet and this metal portion beneath it has been estimated to be approximately 4–7 GPa (420 ± 30 km) [*Hauck et al.*, 2013]. This shallow mantle depth places restrictions on the depth of origin of magmatic materials, as well as the mantle mineralogy. Another interesting feature discovered with data from the MESSENGER spacecraft is the low iron and high sulfur (both approximately 1 to 4 wt%) on the surface of Mercury [*Evans et al.*, 2012; *Nittler et al.*, 2011; *Weider et al.*, 2012; *Weider et al.*, 2014b]. These constraints lead to estimates of very low computed oxygen fugacity between 2.6 and 7.3 $\log_{10}$ units below the Iron-Wüstite buffer [*McCubbin et al.*, 2012; *Zolotov et al.*, 2013], which is the lowest oxygen fugacity yet estimated for the terrestrial planets, representing yet another end-member characteristic of the innermost planet.

With the recent estimates of Mercury's surface composition from the X-Ray Spectrometer (XRS) and Gamma-Ray Spectrometer (GRS) onboard MESSENGER, we now have our first opportunity to directly investigate the compositions of lavas on the planet, and indirectly investigate the chemical make-up of its interior, as well as its thermal and magmatic evolution [*Evans et al.*, 2012; *Evans et al.*, 2014; *Nittler et al.*, 2011; *Peplowski et al.*, 2011; *Peplowski et al.*, 2012a; *Peplowski et al.*, 2012b; *Peplowski et al.*, 2014; *Weider et al.*, 2012; *Weider et al.*, 2014a; *Weider et al.*, 2014b]. One particular region of interest on Mercury is the northern volcanic plains (NVP). The NVP are smooth plains [*Denevi et al.*, 2013] of reported volcanic origin that cover more than 6% of the surface area of Mercury [*Head et al.*, 2011]. Spanning a 4.7×10^6 km^2 region of Mercury, this distinct geologic unit is less cratered than surrounding areas and the largest product of flood volcanism that has been assessed from orbit by MESSENGER [*Head et al.*, 2011]. The NVP region is similar in composition to flood basalts and komatiites on Earth, as demonstrated by similar Mg/Si, Al/Si, and Ca/Si ratios [*Weider et al.*, 2012], although FeO abundances in the mercurian lavas are substantially lower [*Weider et al.*, 2012]. Flood volcanism on Earth is generally produced by partial melting of mantle material that is erupted onto the surface of the planet. By inference, the NVP lavas are the most likely example of melt compositions derived from the mercurian interior that can be assessed compositionally from orbit. Therefore, they represent the best candidate for experimental examination.

Knowledge of the density, compressibility, and other physical properties of magmas is required to understand the differentiation of planetary interiors, and subsequent primary and secondary crust formation. In this study, we performed sink-float

experiments on a NVP melt composition (Table 1) in order to determine the density of secondary magmas from Mercury. Although there is some evidence that suggests this unit is not completely homogeneous [*Peplowski et al.*, 2012a; *Weider et al.*, 2015], the composition assessed from orbit is still broadly representative of mercurian melts. Therefore, given that these experiments represent the first experimental investigation of a suspected mercurian lava composition, these data will be able to provide first-order estimates of the density of melts on Mercury. The density of this melt was then compared with the density and compressibility of primitive low-FeO peridotite and komatiite melt compositions to constrain the full range of mercurian melt densities that span from an analog for the mercurian magma ocean liquid (Fe-free peridotite) to partial melts of the mantle (NVP lavas). The densities of these liquids were subsequently compared to densities of a number of rock-forming minerals over the pressure range of the mercurian mantle (up to 7 GPa) to better constrain the thermal and magmatic evolution of Mercury.

2. Experimental Methods

Experiments were conducted using the sink-float technique [*Agee and Walker*, 1988] to generate a full compression curve for a NVP melt composition (Table 1). We have experimentally investigated a melt with substantially more FeO than is found as the global average on the surface of Mercury and by inference, substantially higher than the bulk FeO content of the mercurian mantle. Consequently, the melt density we report is an upper estimate for mercurian melt compositions. Furthermore, the result of each experiment does not provide a direct measurement of the density of the liquid at the experimental conditions but rather gives an open ended bracket on the density. Sinking spheres, referred to as a “sink”, indicate the density markers are denser than the melt

whereas floating spheres, referred to as a "float", are inferred to be less dense than the melt. However, if there is no movement of the spheres (a "neutral buoyancy"), this observation is interpreted to indicate the density of the spheres is equivalent to that of the melt. Using this technique, the precise density of the liquid is best defined by a neutral buoyancy bracketed by a sink at slightly lower pressures and a float at slightly higher pressures. This method has been used to successfully bracket the density of silicate liquids at high-pressures [*Agee and Walker*, 1993; *Agee*, 1998; *Circone and Agee*, 1996; *Knoche and Luth*, 1996; *Smith and Agee*, 1997; *Suzuki et al.*, 1998; *van Kan Parker et al.*, 2011; *Vander Kaaden et al.*, 2015].

All experiments were conducted at the Institute of Meteoritics (IOM), University of New Mexico (UNM). A Walker-style multi-anvil (MA) device was used for all experiments. Density markers were crystals of well-characterized minerals with a diameter of 330–700 μm, ground to spheres using a Bond Air Mill. For all our sink-float experiments (2.5–6 GPa), forsterite-rich olivine spheres were used.

2.1 Starting Materials

The synthetic starting material for the northern volcanic plains melt composition was prepared at the IOM using high-purity reagent grade powdered oxides and silicates, which were mixed sequentially by volume and ground under ethanol using an automated agate mortar and pestle. All Fe in the mixtures was added as FeO in the form of synthetic fayalite. The reader is referred to *Vander Kaaden et al.* [2015] for details on the preparation of the synthetic fayalite. A super-liquidus experiment was run on the synthetic composition to check that the mixture was of the appropriate bulk composition and to ensure homogeneity was maintained throughout the mixing process. The bulk

composition for the synthetic melt as well as the targeted composition can be found in Table 1. Our NVP melt composition is free of volatile components (S, Na_2O, and K_2O) and has a higher value of FeO than reported by *Nittler et al.* [2011] and *Weider et al.* [2014b]. The volatile components have been left out of the starting material to ensure homogenization of our experimental charge under the short run conditions required for sink-float experiments (30 seconds). In addition, S was excluded from the experiments because S solubility is highly dependent on oxygen fugacity in silicate melts [*Berthet et al.*, 2009], and it is unlikely that the experimental charge would have reached redox equilibrium and incorporate the appropriate amount of S in the silicate melt structure within the 30 second run of the sink-float experiments. The higher concentration of FeO allows us to investigate an upper limit in terms of density for mercurian magmas. Although we excluded S, Na, and K from our starting composition, all three components would decrease the density of the NVP melt (Figure 1) [i.e. *Agee*, 2008]. Consequently, the addition of S, Na, and K, which are present in significant quantities on the mercurian surface [*Nittler et al.*, 2011; *Peplowski et al.*, 2012a; *Weider et al.*, 2012], would cause this melt to become less dense than reported here, so our experiments are truly exploring an upper limit melt density for the NVP lavas.

2.2. Sink-Float Experiments

Each experiment was set up by packing the starting material into a Mo^0 or graphite capsule and placing two mineral spheres, which served as density markers, at the top and bottom of the capsule. A ceramic octahedron made from Ceramcast-584 was used as the pressure medium. Rhenium foil was used as a heater and Type C ($W_5Re_{95}/W_{26}Re_{74}$) thermocouple was located on the center of the outer surface of the

heater. Two Al_2O_3 spacers were placed in the heater with an aluminum sheath surrounding the capsule so it sat directly in the center of the octahedron. The octahedron was surrounded with 8 tungsten carbide cubes each with a truncation-edge-length of 8 mm and placed in the hat-box of the MA. The reader is referred to *Agee et al.* [1995] for pressure calibrations of our MA device.

The sample was then pressurized and rapidly heated at 200–300 °C per minute to super-liquidus temperatures (approximately 1700–2050 °C depending on desired pressure). The experiments were held at the elevated *P*-*T* conditions for 30–60 seconds to allow the synthetic powder adequate time to melt and for the spheres to be driven up or down in the capsule by buoyancy forces. The longer run durations (60 seconds) were typically repeat experiments to ensure a neutral buoyancy was in fact neutral and the lack of movement was not due to sluggish buoyancy reactions. Experiments were limited to these short run durations to prevent dissolution of the spheres into the melt, which would drive the melt composition from the target composition being investigated. The sample was quenched by shutting off the power to the furnace and allowing the run to decompress gradually. The average rate of cooling was approximately 285 °C/s.

3. Analytical Techniques

All run products were set in epoxy and then ground using sand paper with various grit sizes (53.5 µm, 36 µm, 23.6 µm, and 16 µm) until the mineral spheres were exposed. Once exposed, the samples were polished to 0.3 µm before subsequent micro-beam analysis.

3.1. Electron Probe Microanalysis

The polished run products, including quenched materials and mineral spheres, were carbon coated and analyzed at UNM using a JEOL 8200 Electron Probe Microanalyzer (EPMA). Samples were analyzed using an accelerating voltage of 15 KeV and a beam current of 20 nA. A broad beam (10–20 μm) was used for glass analyses whereas a focused 1 μm beam was used for the analysis of mineral density markers. The quenched melt was analyzed to determine the composition and to assess for any melt/capsule or melt/sphere interactions. The spheres were analyzed around the center to confirm composition and near the edges to ensure there was no sphere/melt interaction. Standards used for analysis include natural olivine from the Taylor standard reference block (Type 202-52; produced by the C. M. Taylor Corporation, Sunnyvale, CA) for the olivine spheres, as well as almandine (analyzed for Al, Fe, Si), augite (Si, Al, Ca, Mg), chromite (Cr), olivine (Mg, Si, Fe), orthoclase (Si), pyrope (Cr, Mg, Ca, Si), titanite (Ti), and spessartine (Mn). A synthetic $CaMoO_4$ was used to determine the amount of MoO_2 contamination in the glasses from the capsule material for all runs. Peak and background count times were 20 seconds and 10 seconds, respectively for major elements and 30 seconds and 15 seconds, respectively for minor elements.

3.2. Micro-Fourier Transform Infrared Spectroscopy

To determine the amount of H_2O in our "nominally dry" runs, 2 experimental charges from MA experiments on the same composition were removed from their epoxy, mounted, and doubly polished for quantitative micro-Fourier transform infrared (micro-FTIR) spectroscopic measurements. Micro-FTIR measurements were conducted on the experimental glass products at room temperature in transmittance mode with a Nicolet Nexus 670 Fourier Transform Infrared Spectrometer in the IOM at UNM following

procedures similar to *McCubbin et al.* [2008]. The interior of the IR unit was in an atmosphere purged of H_2O and CO_2, which eliminated atmospheric absorption features. Prior to each analysis, all spots were first assessed using an optical microscope to make certain only glass was being measured during any given analysis. Transmittance IR spectra were collected over the mid-IR range (400–4000 cm^{-1}) from doubly polished thin sections of the run products using a Continuum microscope with a Globar source, XT-KBr beamsplitter, and a MCT/A detector over a 100 × 100 μm area with a 4 cm^{-1} resolution. Thicknesses for each sample were obtained by focusing a reflected aperture on the top surface of the sample and then the bottom surface of the sample and recording the z-axis position of the mapping stage in the Atlus software. These arbitrary units were converted to micrometers using an empirical calibration determined specifically for our instrument [*Berger*, 2012]. Background spectra were collected under the same conditions before each analysis. Total dissolved water concentrations were determined for each glass using the calculation scheme of *Mandeville et al.* [2002] as well as the intensity of the broad OH band at 3570 cm^{-1}. 1024 scans were performed for each IR spectrum that we acquired.

4. Density Calculations

A well-defined equation of state is needed to determine the density of the spheres at the experimental pressure and temperature conditions. Additionally, in order to assess the density of this NVP melt, equation of states were used to determine the densities of many common rock-forming minerals that could be present within the mercurian interior. The densities of the mineral markers in each experiment (olivine), as well as common

rock-forming minerals, were calculated using the 3rd-order Birch-Murnaghan equations of state [*Birch*, 1947]:

$$P = \frac{3}{2} K_T \left[\left(\frac{\rho_{T,P}}{\rho_{T,0}} \right)^{7/3} - \left(\frac{\rho_{T,P}}{\rho_{T,0}} \right)^{5/3} \right] * \left[1 - \frac{3}{4} \left(4 - K' \right) \left(\left(\frac{\rho_{T,P}}{\rho_{T,0}} \right)^{2/3} - 1 \right) \right] \quad (1)$$

where K_T is the isothermal bulk modulus defined as:

$$K_T = K_{298} + {}^{dK}/_{dT} (T - 298) \quad (2)$$

For these equations, K_T is in GPa and T is in Kelvin. In equation (1) P is pressure, K' is the pressure derivative, and $\rho_{T,0}$ and $\rho_{T,P}$ are the densities of the spheres at temperature T and ambient pressure (10^5 Pa) and high pressure, respectively. The density at 10^5 Pa is given by:

$$\rho_{T,0} = \rho_{298}(T) \exp \int_{298}^{T} \alpha(T) dT \quad (3)$$

in which α is the thermal expansion and defined as:

$$\alpha(T) = \alpha_0 + \alpha_1 T + \frac{\alpha_2}{T^2} \quad (4)$$

Parameters used for each mineral are found in Table 2. The main uncertainty of the sink/float method is the calculation of sphere density through use of these equations, which is estimated at ±0.03 g/cm^3 [*Circone and Agee*, 1996].

5. Results

5.1. EPMA and FTIR Results

EPMA analyses of each run product are given in Table 3. The compositions of the melts from experiment to experiment are consistent. The Al_2O_3 content is slightly higher

than our starting material (Table 1) most likely due to slight contamination from the Al_2O_3 ceramic inner parts of the octahedron assembly. The higher MgO content of our final melt compositions may be the result of partial dissolution of the olivine spheres into our melt at the high temperatures of these experiments. The high MoO_2 analyses in NVP-4 and NVP-11 is likely due to the presence of small, unavoidable, molybdenum metal blebs interspersed through the experimental charges and do not likely reflect Mo dissolved in the silicate melt [e.g., *Burkemper et al.*, 2012].

Once the composition of the melts were assessed, our data were normalized to 1450 °C in order to relate the density of our experiments to each other using an isothermal Birch-Murnaghan equation of state. This was done by first taking the difference between the 1-bar density of the experimental charge at the *P*-*T* conditions of the run (ρ_{liq}) and the 1-bar density of the ideal starting composition if no interactions occurred during the experiment between the melt, capsule, and density markers ($\rho_{ideal\ liq}$) at this temperature. The density of each data point was then shifted by this difference assuming the shape of the density curve would be the same regardless of temperature (i.e., shifted either up or down). The same procedure is used to correct for compositional differences between the ideal starting composition (Table 1) and the actual composition of the melt during the run determined by EPMA. The normalized values are given in Table 3. Additionally, the two MA experiments that were used to determine the amount of H_2O present in our "dry" experiments ranged in thicknesses from 48–120 μm. Micro-FTIR analyses of the glasses in these experiments indicates consistent water contents of ~0.3 wt% H_2O.

5.2. Sink-Float Results

Results from our sink-float experiments are shown in Figure 2. Fo_{100} spheres sank in this melt at 2.5 GPa, 3.0 GPa, 3.5 GPa, and 5 GPa and temperatures of 1700 °C, 1775 °C, 1775 °C, and 1950 °C, respectively. These same Fo_{100} spheres floated in this melt at 6 GPa and 2050 °C indicating forsterite is more dense than the mercurian melt up to 5 GPa. A straight line has been fit to the data, instead of an equation of state, to define the maximum compressibility of this melt at 0.08 g/cm^3/GPa, although we acknowledge that the true compression curve is likely represented by a curved line. This line indicates that the NVP lavas are slightly more compressible than a terrestrial komatiite (0.075 g/cm^3/GPa) or peridotite (0.065 g/cm^3/GPa) melt [*Agee and Walker*, 1988; 1993], although a more realistic compression curve would essentially match terrestrial komatiite and peridotite.

6. Discussion

6.1. Range of Mercurian Melt Density

Due to the high amount of FeO and absence of light elements like Na, K, and S in our experimental starting composition, the melt density we report is an upper bound on that of mercurian melt compositions. In an attempt to span the entire range of mercurian melts, we have computed the density of an FeO-free end-member NVP composition to determine the lower limit of mercurian melt density (Figure 3). Since we do not have any primitive samples of the mercurian interior, and subsequently do not know if the NVP composition is representative of all mercurian melts, we have considered common terrestrial materials that may be similar to mercurian mantle melts, including a peridotite and komatiite. However, these terrestrial liquids typically range in FeO content from ~5–11 wt% FeO [*Agee and Walker*, 1993], which exceeds the FeO abundances of mercurian

surface materials [*Chabot et al.*, 2014; *Charlier et al.*, 2013; *Nittler et al.*, 2011; *Weider et al.*, 2012; *Weider et al.*, 2014b]. Therefore, it is more realistic to consider an FeO-free peridotite and an FeO-free komatiite as possible terrestrial analogs for mercurian melts. As a result, the total range of mercurian melt densities can be constrained by the density of Fe-free peridotite, Fe-free komatiite, and both Fe-bearing and Fe-free NVP lavas. This calculation was performed by first subtracting all of the iron out of the peridotite and komatiite compositions from *Agee and Walker* [1993] and renormalizing the compositions. A 1-bar density was then calculated from *Lange and Carmichael* [1987]. These FeO-free 1-bar densities, along with the bulk modulus and pressure derivative values from *Agee and Walker* [1993] for a peridotite and komatiite, respectively were used along with the 3rd-order Birch-Murnaghan equation of state [*Birch*, 1947] to calculate the density of each FeO-free composition. The computation of the FeO-free end-member NVP composition was conducted in a similar fashion.

These melts demonstrate a very narrow range of melt density for the silicate portion of the planet Mercury. Furthermore, the melt density is much lower than melts from other planetary bodies (Table 4) [*Agee and Walker*, 1993; *Agee*, 1998; *Bertka and Fei*, 1997; *Misawa*, 2004; *Vander Kaaden et al.*, 2015; *Warren et al.*, 1996]. The limited melt density range and overall low melt density has important implications for the internal structure of Mercury's mantle and for the formation of primary and secondary crustal materials discussed below.

6.2. How easily can mercurian melts rise through the mantle?

In the Earth's mantle, there is a region where partial melts of the mantle are no longer buoyant with respect to surrounding mantle minerals due to the higher

compressibility of silicate liquids as a function of pressure compared to most common mantle minerals. The depth at which this occurs is referred to as a density crossover. This depth within a planetary interior has important implications for the ability and likelihood of silicate melts to eventually erupting onto the surface of the planet. To determine where these crossovers exist in the mercurian mantle, we compared the range in melt density for Mercury (Section 6.1) with the densities of many common rock-forming minerals that could be present within the mercurian interior (Figure 4). Pertinent equations and parameters are given in Section 4 and Table 2. Due to the low expected FeO in Mercury's interior, Mg-rich end-members were chosen as they will be the least dense form of each mineral solid-solution series. Upon examination of common rock-forming minerals, we found that there is a density crossover at ~6.8 GPa with our melt and Fo_{100}. Given the range of core-mantle boundary conditions from *Hauck et al.* [2013], however, this crossover should occur near the base of the mantle, or in the core of the planet, and would not inhibit the rise of any mercurian magmas through the mantle. Furthermore, there is no density crossover between the NVP melt and Mg-rich pyroxenes, garnet, or spinel, which are all common minerals in other terrestrial planetary mantles [*Bertka and Fei*, 1997; *Neal*, 2001; *Ringwood*, 1966; 1975; *Smith et al.*, 1970; *Wood et al.*, 1970] and therefore candidate minerals for Mercury's mantle.

It is also possible that plagioclase and quartz are present in the mercurian mantle [*Brown and Elkins-Tanton*, 2009], so they were also included among the minerals we investigated. There is a density crossover with the NVP melt and An_{50} at ~1.9 GPa. Consequently, if this melt originated from deeper than ~1.9 GPa in a plagioclase dominated source region, it would sink into the interior of Mercury. However,

plagioclase is not stable at pressures greater than ~1 GPa [i.e. *Green and Hibberson*, 1970], so this density crossover would not inhibit the eruption of mercurian melts. Additionally, Figure 4 shows that this mercurian melt would be buoyant in a mantle consisting of quartz, since SiO_2 is consistently denser than the NVP melt. As a result of the locations of each density crossover, our data indicate partial melts of the mercurian mantle are buoyant in a mantle consisting of olivine, pyroxene, garnet, spinel, anorthite, and quartz in any proportions. This illustrates the extreme buoyancy conditions of mercurian melts, and it indicates that partial melts of Mercury's mantle could rise and eventually erupt from depths as deep as the core-mantle boundary of the planet. Furthermore, partial melts of the mercurian interior would be less likely to stall during ascent, indicating Mercury may have erupted a greater percentage of its partial melts in comparison to other terrestrial planets, although other geophysical factors may have impeded magmatic eruptions on Mercury [e.g., *Byrne et al.*, 2014]. On Earth, the depth at which density crossovers occur for peridotite and mantle olivine are at much greater pressure [~10 GPa; *Agee and Walker*, 1993] that are not reached in the mercurian mantle. Importantly, Mercury represents the first terrestrial planet in our Solar System that does not contain regions within its mantle where partial melts would be more dense than the surrounding minerals, due to the compositionally distinct (low FeO) magmas coupled with the shallow depth of the mercurian mantle.

6.3. Role of Graphite in Magmatic Evolution of Mercury

It has been suggested that Mercury differentiated through a magma ocean event in which substantial heating and melting of the planet took place [*Brown and Elkins-Tanton*, 2009; *Riner et al.*, 2009] (Figure 5a). On the Moon, we see evidence of a global lunar

magma ocean through the presence of a primary anorthositic crust. According to existing lunar magma ocean crystallization models, plagioclase began to crystallize after about 75% crystallization [*Snyder et al.*, 1992] and was buoyant with respect to the FeO-rich residual melt, leading to plagioclase floatation and the formation of a primary anorthositic floatation crust [*Jolliff et al.*, 2000]. The low FeO content and limited density range of mercurian melts prohibits nearly all rock-forming minerals from forming a primary floatation crust on Mercury with the exception of graphite (Figures 3–4); therefore, it is the only candidate mineral that could have composed a primary floatation crust on Mercury.

The volatile-rich nature of Mercury's silicate portion, as determined by elevated K/Th and near chondritic K/Cl ratios [*Evans et al.*, 2014; *Peplowski et al.*, 2011; *Peplowski et al.*, 2012a; *Peplowski et al.*, 2014] lends support to the idea of volatile-rich phases in the mercurian mantle. Consequently, Mercury may be enriched in carbon compared to other terrestrial planets [*Murchie et al.*, 2015; *Peplowski et al.*, 2015]. Elemental carbon phases, including diamond and graphite, occur in a wide variety of planetary materials from Earth, Moon, Mars, and asteroids [*Hirschmann and Withers*, 2008; *Shirey et al.*, 2013; *Steele et al.*, 2010; *Warren and Kallemeyn*, 1992] so it is not unreasonable to postulate the existence of elemental carbon on Mercury. The density difference between graphite and diamond in Mercury's interior, however, is of critical importance in the assessment of a possible floatation crust because only graphitic carbon would have a sufficiently low density to float in a mercurian magma ocean. Mercury's shallow mantle results in a limited *P-T* profile that does not span into the diamond stability field (Figure 6). Graphite is therefore the stable phase of elemental carbon

throughout the silicate portion of Mercury, which is a primary pre-requisite to a graphite floatation crust. Elemental carbon has yet to be definitively detected on the mercurian surface by the MESSENGER GRS [*Peplowski et al.*, 2015] and it is beyond the detection capabilities of MESSENGER's XRS. There is also absence of diagnostic spectral absorption features that suggest the presence of C in reflectance spectra. If primary elemental carbon is present on Mercury, it will primarily be in the form of graphite and not diamond, although diamond could be present via formation by secondary processes such as impact or addition through late accretion.

The existence of graphite within the silicate portion of Mercury is dependent upon many factors, some of which are difficult to constrain. These include the initial C content of bulk Mercury, the distribution of C between Mercury's core and mantle, and whether or not Mercury's core was initially C-saturated. Consequently, we look to both theoretical and empirical evidence to support or refute the idea of a primary floatation crust of graphite on Mercury. Although carbon likely represents one of the light elements incorporated into Mercury's core, metal-silicate partitioning studies of C at the specific P-T-fO_2 conditions of core formation on Mercury have not been determined. This remains the primary limiting factor to making estimates of the C abundances in the bulk silicate portion of Mercury. Regardless, at least some C would be incorporated into the silicate portion of Mercury as dissolved C-O, C-H, or carbonyl species or as a solid phase if the outer core and silicate liquid were C-saturated [*Dasgupta*, 2013]. Carbon solubility in silicate melts is exceedingly low under highly reducing conditions [*Dasgupta et al.*, 2013], so graphite saturation would occur fairly early after the onset of magma ocean crystallization, and once formed, buoyancy forces would drive this graphite towards the

surface of the magma ocean (Figure 5b). If Mercury's magma ocean had elevated hydrogen abundances, the magma ocean liquid would have a higher C solubility [*Ardia et al.*, 2013], which would delay the inevitable formation of graphite.

Assuming a graphite floatation crust formed on Mercury, the thickness and extent of that crust would be dictated by the amount of C allocated to the silicate portion of the planet and the efficiency of graphite floatation. Although we do not know how much carbon was originally in the mantle of Mercury, we can model the thickness of a graphite floatation crust as a function of the C abundance in the bulk silicate portion of the planet (Figure 7) using the parameters listed in Table 5 and the equations that follow. Assuming the entire inventory of carbon, C, in the silicate portion of Mercury floats to the surface due to buoyancy factors to produce a crust of homogeneous thickness over the entire surface of the planet, the thickness of that graphite floatation crust can be calculated by the following equation:

$$T = R - \left(\frac{\left(\frac{4}{3}\pi R^3 - \frac{wt_C}{\rho_C} \right) * \frac{3}{4}}{\pi} \right)^{\frac{1}{3}} \quad (5)$$

where T is the thickness of a graphite floatation crust in m, R is the radius of Mercury in m, wt_C is the weight of carbon in the mantle in kilograms, and ρ_c is the density of graphite in kg/m^3. wt_C is defined as:

$$wt_C = \rho_m V_m \left(\frac{C}{100} \right) \quad (6)$$

where ρ_m is the density of the mantle in kg/m^3, V_m is the volume of Mercury's mantle in m^3, and C is the weight percent of carbon in the mantle. $V_m$is defined as:

$$V_m = \left(\left(\frac{4}{3} \right) \pi R^3 \right) - \left(\left(\frac{4}{3} \right) \pi {R_c}^3 \right) \quad (7)$$

where R_c is the radius of Mercury's core in m.

From this model, we have estimated the upper limit of the thickness of a graphite floatation crust using the abundances of C in carbonaceous chondrites, as Mercury is unlikely to have superchondritic abundances of C. *Lodders and Fegley* [1998] report a range of C abundances in carbonaceous chondrites with CI chondrites containing the most C (3.45 wt%) and CK chondrites containing the least C (0.22 wt%). Using these values, we have estimated that Mercury could have a primary floatation crust of graphite as thick as ~1–21 km if its bulk silicate had as much C as carbonaceous chondrites. However, even if Mercury had much less C, similar to the abundances estimated to be in the mantles of Earth or Mars, Mercury could still have had a primary graphite floatation crust that was 1-100 m in thickness (Figure 7). Once the carbon concentration in the bulk silicate portion of Mercury is better constrained, through future exploration and/or experimental studies, a more robust estimate of the thickness of this graphite floatation crust can be made using equations 5–7 and the results of this model depicted in Figure 7.

A primary graphite floatation crust on Mercury, albeit exotic, is supported by the dark color of Mercury's surface and the existence of low reflectance material covering at least 15 % of its surface (> 4 million km^2 [*Denevi et al.*, 2009]). If quartz and anorthite were primary components of Mercury's floatation crust [*Brown and Elkins-Tanton*, 2009], neither would produce a darkening effect. In fact, one would expect the surface of Mercury to approach the brightness of the lunar highlands with the addition of these two constituents, which is not consistent with MESSENGER data nor telescopic observations and analyses of the mercurian surface. It has been suggested that this low reflectance material could be composed of opaque minerals, namely iron metal, iron-titanium oxides,

graphite, and sulfides [*Denevi et al.*, 2009; *Robinson et al.*, 2008; *Xiao et al.*, 2013]. However, Fe-Ti oxides were ruled out as the source of the low reflectance material mainly due to the low abundance of Fe and Ti from MESSENGER XRS and GRS data [*Nittler et al.*, 2011; *Riner et al.*, 2010; *Riner et al.*, 2011]. Furthermore, sulfides and iron metal have been largely ruled out as the darkening agent because both of these materials redden the UV-VIS spectrum while darkening, whereas the slope of UV-VIS spectra from Mercury are blue [*Blewett et al.*, 2013; *Murchie et al.*, 2015]. In contrast, nanophase Fe metal particles may not cause reddening and therefore cannot be ruled out as a darkening agent [*Lucey and Riner*, 2011]. By the process of elimination, *Murchie et al.* [2015] concluded that the low reflectance material on Mercury may be composed of coarse grained graphite, which would act as a darkening agent without reddening the slope. The source of this graphite, as well as the overall dark appearance of Mercury's surface, can be explained by a primary floatation crust on Mercury composed of graphite that was subsequently mixed with secondary materials by impact gardening (Figure 5d).

7. Conclusion

Following planetary differentiation and the formation of a primary crust on Mercury, partial melting in the mantle along with subsequent volcanism has resurfaced the majority of the planet (Figure 5c) [*Denevi et al.*, 2009; *Denevi et al.*, 2013; *Head et al.*, 2011]. Given the low and limited range of density of mercurian melts (Figure 3), as well as the absence of density crossovers between these melts and possible mantle minerals (Figure 4), there are no restrictions on the depth of origin for these lavas. Therefore, eruptive volcanic products could have originated from as deep as the core-mantle boundary of Mercury. Additionally, partial melts of the mercurian interior would

be less likely to stall during ascent, indicating Mercury may have erupted a greater percentage of its partial melts in comparison to other terrestrial planets. Consequently, Mercury's extreme mantle composition and exceptionally shallow mantle may have led to exotic primary and secondary crust production, including a possible primary graphite floatation crust that was subsequently covered by secondary magmas derived from depths of melting as deep as the core-mantle boundary (Figure 5c). The primary crust, secondary crust, and upper mantle have since been excavated and mixed by impact processes [*Rivera-Valentin and Barr*, 2014], as evidenced by the large number of craters observed on Mercury's surface [*Fassett et al.*, 2011], leading to the complex, chemically enigmatic, darkened surface that is observed today (Figure 5d).

Acknowledgements

All data used in this manuscript, including EPMA analyses, can be requested by contacting Kathleen Vander Kaaden (kvander@unm.edu). The authors would like to thank Whitney McCutcheon for assisting in FTIR analyses and Alison Santos for helpful discussions and assisting in Multi-Anvil runs. We also thank the MESSENGER Science Team for fruitful discussions regarding the interpretation of MESSENGER data. Additionally, the authors thank Nancy Chabot, Shoshana Weider, and an anonymous reviewer whose comments helped to substantially improve this manuscript. Steven Hauck, II (executive editor) and Justin Filiberto (associate editor) are also thanked for their additional comments and for their editorial handling of this manuscript. This work was funded by a NASA Cosmochemistry Grant NNX11AG76G to FMM and New Mexico Space Grant Consortium Fellowship to KEVK.

References

Agee, C. B., and D. Walker (1988), Static compression and olivine flotation in ultrabasic silicate liquid, *Journal of Geophysical Research-Solid Earth and Planets*, *93*(B4), 3437-3449.

Agee, C. B., and D. Walker (1993), Olivine Flotation in Mantle Melt *Earth and Planetary Science Letters*, *114*(2-3), 315-324.

Agee, C. B., et al. (1995), Pressure-temperature phase diagram for the Allende meteorite, *Journal of Geophysical Research-Solid Earth*, *100*(B9), 17725-17740.

Agee, C. B. (1998), Crystal-liquid density inversions in terrestrial and lunar magmas, *Physics of the Earth and Planetary Interiors*, *107*(1-3), 63-74.

Agee, C. B. (2008), Static compression of hydrous silicate melt and the effect of water on planetary differentiation, *Earth and Planetary Science Letters*, *265*(3-4), 641-654.

Anderson, W. W., and T. J. Ahrens (1994), An equation of state for liquid iron and implications for the Earth's core, *Journal of Geophysical Research*, *99*(B3), 4273-4284.

Angel, R. J. (2004), Equations of state of Plagioclase Feldspars, *Contributions to Mineralogy and Petrology*, *146*(4), 506-512.

Ardia, P., et al. (2013), Solubility of CH_4 in a synthetic basaltic melt, with applications to atmosphere-magma ocean-core partitioning of volatiles and to the evolution of the Martian atmosphere, *Geochimica et Cosmochimica Acta*, *114*, 52-71.

Berger, J. A. (2012), Effect of halite and calcite coatings on thermal infrared spectra with implications for Mars exploration, *M.S. Thesis, University of New Mexico*.

Berthet, S., et al. (2009), Melting of the Indarch meteorite (EH4 chondrite) at 1 GPa and variable oxygen fugacity: Implications for early planetary differentiation processes, *Geochimica Et Cosmochimica Acta*, *73*(20), 6402-6420.

Bertka, C. M., and Y. Fei (1997), Mineralogy of the Martian interior up to core-mantle boundary pressures, *Journal of Geophysical Research*, *102*(B3), 5251-5264.

Birch, F. (1947), Finite elastic strain of cubic crystals, *Physical Review*, *71*, 809-824.

Blewett, D. T., et al. (2013), Mercury's hollows: Constraints on formation and composition from analysis of geological setting and spectral reflectance, *Journal of Geophysical Research-Planets*, *118*, 1-20.

Boyd, F. R., et al. (1964), Effects of pressure on melting + polymorphism of enstatite $MgSiO_3$, *Journal of Geophysical Research*, *69*(10), 2101-2109.

Brown, S. M., and L. T. Elkins-Tanton (2009), Compositions of Mercury's earliest crust from magma ocean models, *Earth and Planetary Science Letters*, *286*(3-4), 446-455.

Bundy, F. P., et al. (1961), Diamond-graphite equilibrium line from growth and graphitization of diamond, *Journal of Chemical Physics*, *35*(2), 383-391.

Bundy, F. P., et al. (1996), The pressure-temperature phase and transformation diagram for carbon; Updated through 1994, *Carbon*, *34*(2), 141-153.

Burkemper, L. K., et al. (2012), Constraints on core formation from molybdenum solubility in silicate melts at high pressure, *Earth and Planetary Science Letters*, *335–336*(0), 95-104.

Byrne, P. K., et al. (2014), Mercury's global contraction much greater than earlier estimates, *Nature Geoscience*, *7*, 301-307.

Chabot, N. L., et al. (2014), Experimental constraints on Mercury's core composition, *Earth and Planetary Science Letters*, *390*, 199-208.

Charlier, B., et al. (2013), Phase equilibria of ultramafic compositions on Mercury and the origin of the compositional dichotomy. , *Earth and Planetary Science Letters*, *363*, 50-60.

Circone, S., and C. B. Agee (1996), Compressibility of molten high-Ti mare glass: Evidence for crystal-liquid density inversions in the lunar mantle, *Geochimica Et Cosmochimica Acta*, *60*(14), 2709-2720.

Clausing, R. (1997), Diamond morphology, in *Handbook of Industrial Diamonds and Diamond Films*, edited by M. Prelas, et al., pp. 19-45, Kluwer Academic Publishers.

Colonna, F., et al. (2011), High-pressure high-temperature equation of state of graphite from Monte Carlo simulations, *Carbon 49*, 364-368.

Conrad, P. G., et al. (1999), The high-pressure, single-crystal elasticity of pyrope, grossular, and andradite, *American Mineralogist*, *84*(3), 374-383.

Dasgupta, R. (2013), Ingassing, storage, and outgassing of terrestrial carbon through geologic time, *Reviews in Mineralogy and Geochemistry*, *75*, 183-229.

Dasgupta, R., et al. (2013), Carbon solution and partitioning between metallic and silicate melts in a shallow magma ocean: Implications for the origin and distribution of terrestrial carbon *Geochimica et Cosmochimica Acta*, *102*, 191-212.

Denevi, B. W., et al. (2009), The Evolution of Mercury's Crust: A Global Perspective from MESSENGER, *Science*, *324*(5927), 613-618.

Denevi, B. W., et al. (2013), The distribution and origin of smooth plains on Mercury, *Journal of Geophysical Research-Planets*, *118*(5), 891-907.

Dewaele, A., et al. (2008), High pressure-high temperature equations of state of neon and diamond, *Physical Review*, *B 77*, 094106.

Dziewonski, A. M., and D. L. Anderson (1981), Preliminary reference Earth model, *Physics of the Earth and Planetary Interiors*, *25*(4), 297-256.

Evans, L. G., et al. (2012), Major-element abundances on the surface of Mercury: Results from the MESSENGER Gamma-Ray Spectrometer, *Journal of Geophysical Research-Planets*, *117*, E00L07.

Evans, L. G., et al. (2014), Chlorine on the surface of Mercury: Implications for Mercury's surface evolution, paper presented at 45th Lunar and Planetary Science Conference, The Woodlands, TX.

Fassett, C. I., et al. (2011), The global population of large craters on Mercury and comparison with the Moon, *Geophysical Research Letters*, *38*, L10202.

Fei, Y. (1995), Thermal Expansion, in *Mineral Physics and Crystallography: A Handbook of Physical Constants*, edited by T. J. Ahrens, AGU Reference Shelf, Washington, D.C.

Fried, L. E., et al. (2002), EXP6: A New Equation of State Library for High Pressure Thermochemistry, paper presented at 12th International Symposium on Detonation, US Naval Research Office, San Diego, CA.

Gessmann, C. K., et al. (2001), Solubility of silicon in liquid metal at high pressure: implications for the composition of the Earth's core, *Earth and Planetary Science Letters*, *184*, 367-376.

Graham, E. K., et al. (1988), The Pressure and Temperature-Dependence of the Elastic Properties of Single-Crystal Fayalite Fe_2SiO_4 *Physics and Chemistry of Minerals*, *16*(2), 186-198.

Green, D. H., and W. Hibberson (1970), The instability of plagioclase in peridotite at high pressure, *Lithos*, *3*(3), 209-221.

Guo, X., et al. (2013), The density and compressibility of CaO-FeO-SiO_2 liquids at one bar: Evidence for four-coordinated Fe^{2+} in the $CaFeO_2$ component. , *Geochimica et Cosmochimica Acta*, *120*(206-219).

Guo, X., et al. (2014), Density and sound speed measurements on model basalt (An-Di-Hd) liquids at one bar: New constraints on the partial molar volume and compressibility of the FeO component. , *Earth and Planetary Science Letters*, *388*, 283-292.

Hauck II, S. A., et al. (2013), The curious case of Mercury's internal structure, *Journal of Geophysical Research - Planets*, *118*, 1204-1220.

Hazen, R. M. (1977), Effects of Temperature and Pressure on Crystal-Structure of Ferromagnesian Olivine *American Mineralogist*, *62*(3-4), 286-295.

Head, J. W., et al. (2011), Flood Volcanism in the Northern High Latitudes of Mercury Revealed by MESSENGER, *Science*, *333*(6051), 1853-1856.

Herzberg, C., and J. Z. Zhang (1996), Melting experiments on anhydrous peridotite KLB-1: Compositions of magmas in the upper mantle and transition zone, *Journal of Geophysical Research-Solid Earth*, *101*(B4), 8271-8295.

Hirschmann, M. M., and A. C. Withers (2008), Ventilation of CO_2 from a reduced mantle and consequences for the early martian greenhouse, *Earth and Planetary Science Letters*, *270*(1-2), 147-155.

Hugh-Jones, D. (1997), Thermal expansion of $MgSiO_3$ and $FeSiO_3$ ortho- and clinopyroxenes *American Mineralogist*, *82*(7-8), 689-696.

HughJones, D. A., and R. J. Angel (1994), A Compressional Study of $MgSiO_3$ Orthoenstatite Up to 8.5-GPa *American Mineralogist*, *79*(5-6), 405-410.

Isaak, D. G., et al. (1993), The Elastic Properties of Single-Crystal Fayalite as Determined by Dynamical measurement Techniques *Pure and Applied Geophysics*, *141*(2-4), 393-414.

Jacobs, M. H. G., and B. de Jong (2007), Placing constraints on phase equilibria and thermophysical properties in the system MgO-SiO_2 by a thermodynamically consistent vibrational method, *Geochimica Et Cosmochimica Acta*, *71*(14), 3630-3655.

Javoy, M., et al. (2010), The chemical composition of the Earth: Enstatite chondrite models, *Earth and Planetary Science Letters*, *293*, 259-268.

Jolliff, B. L., et al. (2000), Major lunar crustal terranes: Surface expressions and crust-mantle origins, *Journal of Geophysical Research-Planets*, *105*(E2), 4197-4216.

Kennedy, C. S., and G. C. Kennedy (1976), Equilibrium boundary between graphite and diamond, *Journal of Geophysical Research*, *81*(14), 2467-2470.

Knoche, R., and R. W. Luth (1996), Density measurements on melts at high pressure using the sink/float method: Limitations and possibilities, *Chemical Geology*, *128*(1-4), 229-243.

Lange, R. A., and I. S. E. Carmichael (1987), Densities of Na_2O-K_2O-CaO-MgO-FeO-Fe_2O_3-Al_2O_3-TiO_2-SiO_2 liquids: New measurements and derived partial molar properties, *Geochimica et Cosmochimica Acta*, *51*(11), 2931-2946.

Li, J., and C. B. Agee (2001), Element partitioning constraints on the light element composition of the Earth's core, *Geophysical Research Letters*, *28*(1), 81-81.

Liu, Q., and R. A. Lange (2001), The partial molar volume and thermal expansivity of TiO_2, in alkali silicate melts: Systematic variation with Ti coordination, *Geochimica Et Cosmochimica Acta*, *65*(14), 2379-2393.

Liu, W., and B. Li (2006), Thermal equation of state of $(Mg_{0.9}Fe_{0.1})_2SiO_4$ olivine *Physics of the Earth and Planetary Interiors*, *157*, 188-195.

Lodders, K., and B. Fegley (1998), *The Planetary Scientist's Companion*, Oxford University Press, New York.

Lucey, P. G., and M. A. Riner (2011), The optical effects of small iron particles that darken but do not redden: Evidence of intense space weathering on Mercury, *Icarus*, *212*(2), 451-462.

Malavergne, V., et al. (2010), Highly reducing conditions during core formation on Mercury: Implications for internal structure and the origin of a magnetic field, *Icarus*, *206*(1), 199-209.

Mandeville, C. W., et al. (2002), Determination of molar absorptivities for infrared absorption bands of H2O in andesitic glasses, *American Mineralogist*, *87*(7), 813-821.

McCubbin, F. M., et al. (2008), Compositional diversity and stratification of the martian crust: Inferences from crystallization experiments on the picrobasalt Humphrey from Gusev Crater, Mars., *Journal of Geophysical Research-Planets*, *113*, E11013.

McCubbin, F. M., et al. (2012), Is Mercury a volatile-rich planet?, *Geophysical Research Letters*, *39*.

McCubbin, F. M., et al. (2015), Magmatic volatiles (H, C, N, F, S, Cl) in the lunar mantle, crust, and regolith: Abundances, distributions, processes, and reservoirs, *American Mineralogist*.

Misawa, K. (2004), The Yamato 980459 olivine-phyric shergottite consortium, *Antarct. Meteroite Res.*, *17*, 1-12.

Murchie, S. L., et al. (2015), Orbital multispectral mapping of Mercury using the MESSENGER Mercury Dual Imaging System: Evidence for the origins of plains units and low-reflectance material, *Icarus*.

Neal, C. R. (2001), Interior of the Moon: The presence of garnet in the primitive deep lunar mantle, *Journal of Geophysical Research*, *106*(E11), 27,865-827,885.

Nishida, K., et al. (2011), Density measurement of liquid FeS at high pressures using synchrotron X-ray absorption, *American Mineralogist*, *96*, 864-868.

Nittler, L. R., et al. (2011), The Major-Element Composition of Mercury's Surface from MESSENGER X-ray Spectrometry, *Science*, *333*(6051), 1847-1850.

Ochs, F. A., and R. A. Lange (1999), The density of hydrous magmatic liquids, *Science*, *283*(5406), 1314-1317.

Peplowski, P. N., et al. (2011), Radioactive Elements on Mercury's Surface from MESSENGER: Implications for the Planet's Formation and Evolution, *Science*, *333*(6051), 1850-1852.

Peplowski, P. N., et al. (2012a), Variations in the abundances of potassium and thorium on the surface of Mercury: Results from the MESSENGER Gamma-Ray Spectrometer, *Journal of Geophysical Research - Planets*, *117*(E00L04).

Peplowski, P. N., et al. (2012b), Aluminum abundance on the surface of Mercury: Applications of a new background-reduction technique for the analysis of gamma-ray spectroscopy data, *Journal of Geophysical Research*, *117*, E00L10.

Peplowski, P. N., et al. (2014), Enhanced sodium abundance in Mercury's north polar region revealed by the MESSENGER Gamma-Ray Spectrometer, *Icarus*.

Peplowski, P. N., et al. (2015), Constraints on the abundance of carbon in near-surface materials on Mercury: Results from the MESSENGER Gamma-Ray Spectrometer, *Planetary and Space Science*.

Presnall, D. C., and M. J. Walter (1993), Melting of forsterite, Mg_2SiO_4, from 9.7 to 16.5 GPa, *Journal of Geophysical Research-Solid Earth*, *98*(B11), 19777-19783.

Ramsey, W. H., and P. M. S. Blackett (1948), On the constitution of the terrestrial planets, *Monthly Notices of the Royal Astronomical Society*, *108*(5), 406-413.

Ricolleau, A., et al. (2011), Oxygen and silicon contents of Earth's core from high pressure metal-silicate partitioning experiments, *Earth and Planetary Science Letters*, *310*(3-4), 409-421.

Riner, M. A., et al. (2009), Nature of opaque components on Mercury: Insights into a Mercurian magma ocean, *Geophysical Research Letters*, *36*.

Riner, M. A., et al. (2010), Mercury surface composition: Integrating petrologic modeling and remote sensing data to place constraints on FeO abundance, *Icarus*, *209*(2), 301-313.

Riner, M. A., et al. (2011), Constraints on Mercury's surface composition from MESSENGER neutron spectrometer data, *Earth and Planetary Science Letters*, *308*(1-2), 107-114.

Ringwood, A. E. (1966), Chemical Evolution of the Terrestrial Planets, *Geochimica et Cosmochimica Acta*, *30*, 41-104.

Ringwood, A. E. (1975), *Composition and Petrology of the Earth's Mantle*, 618 pp., New York: McGraw-Hill.

Rivera-Valentin, E. G., and A. C. Barr (2014), Impact-induced compositional variations on Mercury, *Earth and Planetary Science Letters*, *391*, 234-242.

Robinson, M. S., et al. (2008), Reflectance and color variations on Mercury: Regolith processes and compositional heterogeneity, *Science*, *321*(5885), 66-69.

Schutt, D. L., and C. E. Lesher (2006), Effects of melt depletion on the density and seismic velocity of garnet and spinel lherzolite, *Journal of Geophysical Research*, *11*, B05401.

Shirey, S. B., et al. (2013), Diamonds and the Geology of Mantle Carbon, *Reviews in Mineralogy and Geochemistry*, *75*, 355-421.

Skinner, B. J. (1966), Thermal Expansion, in *Handbook of Physical Constants. Revides Edition*, edited by J. S. P. Clark, The Geological Society of America, Inc.

Smith, D. E., et al. (2012), Gravity Field and Internal Structure of Mercury from MESSENGER, *Science*.

Smith, J. R., and C. B. Agee (1997), Compressibility of molten "green glass" and crystal-liquid density crossovers in low-Ti lunar magma, *Geochimica Et Cosmochimica Acta*, *61*(10), 2139-2145.

Smith, J. V., et al. (1970), A petrologic model for the Moon based on petrogenesis, experimental petrology, and physical properties, *Journal of Geology*, *78*(4), 381-405.

Smyth, J. R. (1975), High-Temperature Crystal-Chemistry of Fayalite *American Mineralogist*, *60*(11-1), 1092-1097.

Snyder, G. A., et al. (1992), A Chemical-Model for Generating the Sources of Mare Basalts - Combined Equilibrium and Fractional Crystallization of the Lunar Magmasphere, *Geochimica Et Cosmochimica Acta*, *56*(10), 3809-3823.

Solomon, S. C., et al. (2001), The MESSENGER mission to Mercury: scientific objectives and implementation, *Planetary and Space Science*, *49*, 1445-1465.

Steele, A., et al. (2010), Graphite in an Apollo 17 impact melt breccia, *Science*, *329*(5987), 51-51.

Sumino, Y., and O. L. Anderson (1984), Elastic constants of minerals, in *CRC Handbook of the Physical Properties of Rocks*, edited by S. Carmichael, CRC Press, Boca Raton, FL.

Suzuki, A., et al. (1998), Density and thermal expansion of a peridotite melt at high pressure, *Physics of the Earth and Planetary Interiors*, *107*(1-3), 53-61.

Suzuki, I. (1975), Thermal expansion of periclase and olivine, and their anharmonic properties. , *Journal of Physics of the Earth*, *23*, 145-159.

Suzuki, I., et al. (1981), Thermal expansion of fayalite, Fe_2SiO_4, *Physics and Chemistry of Minerals*, *7*(2), 60-63.

Tsuno, K., et al. (2013), Simultaneous partitioning of silicon and oxygen into the Earth's core during early Earth differentiation, *Geophysical Research Letters*, *40*, 66-71.

van Kan Parker, M., et al. (2011), Compressibility of molten Apollo 17 orange glass and implications for density crossovers in the lunar mantle, *Geochimica Et Cosmochimica Acta*, *75*(4), 1161-1172.

Vander Kaaden, K. E., et al. (2015), Density and compressibility of the molten lunar picritic glasses: Implications for the roles of Ti and Fe in the structures of silicate melts, *Geochimica Et Cosmochimica Acta*, *149*, 1-20.

Warren, P. H., and G. W. Kallemeyn (1992), Explosive volcanism and the graphite-oxygen fugacity buffer on the parent asteroid(s) of the urelite meteorites, *Icarus*, *100*, 110-126.

Warren, P. H., et al. (1996), Compositional-petrologic investigations of Eucrites and the QUE94201 Shergottie, paper presented at Proc. NIPR Sym. Antarctic Meteorites, Nat. Inst. Polar Res., Tokyo.

Weider, S. Z., et al. (2012), Chemical heterogeneity on Mercury's surface revealed by the MESSENGER X-Ray Spectrometer, *Journal of Geophysical Research - Planets*, *117*(E00L05).

Weider, S. Z., et al. (2014a), Geochemical terranes on the innermost planet: Possible origins of Mercury's high-magnesium region, paper presented at 45th Lunar and Planetary Science Conference, The Woodlands, TX.

Weider, S. Z., et al. (2014b), Variations in the abundance of iron on Mercury's surface from MESSENGER X-Ray Spectrometer observations, *Icarus*, *235*, 170-186.

Weider, S. Z., et al. (2015), Evidence for geochemical terranes on Mercury: The first global mapping of major elements on the surface of the innermost planet, *Earth and Planetary Science Letters*.

Wood, J. A., et al. (1970), Lunar anorthosites and a geophysical model of the Moon, *Proceedings of the Apollo 11 Lunar Science Conference*, *1*, 965-988.

Xiao, Z., et al. (2013), Dark spots on Mercury: A distinctive low-reflectance material and its relation to hollows. , *Journal of Geophysical Research - Planets*, *118*, 1-14.

Zhang, L., et al. (1999), Single-crystal hydrostatic compression of synthetic pyrope, almandine, spessartine, grossular and andradite garnets at high pressures, *Physics and Chemistry of Minerals*, *27*(1), 52-58.

Zolotov, M. Y., et al. (2013), The redox state, FeO content, and origin of sulfur-rich magmas on Mercury, *Journal of Geophysical Research-Planets*, *118*(1).

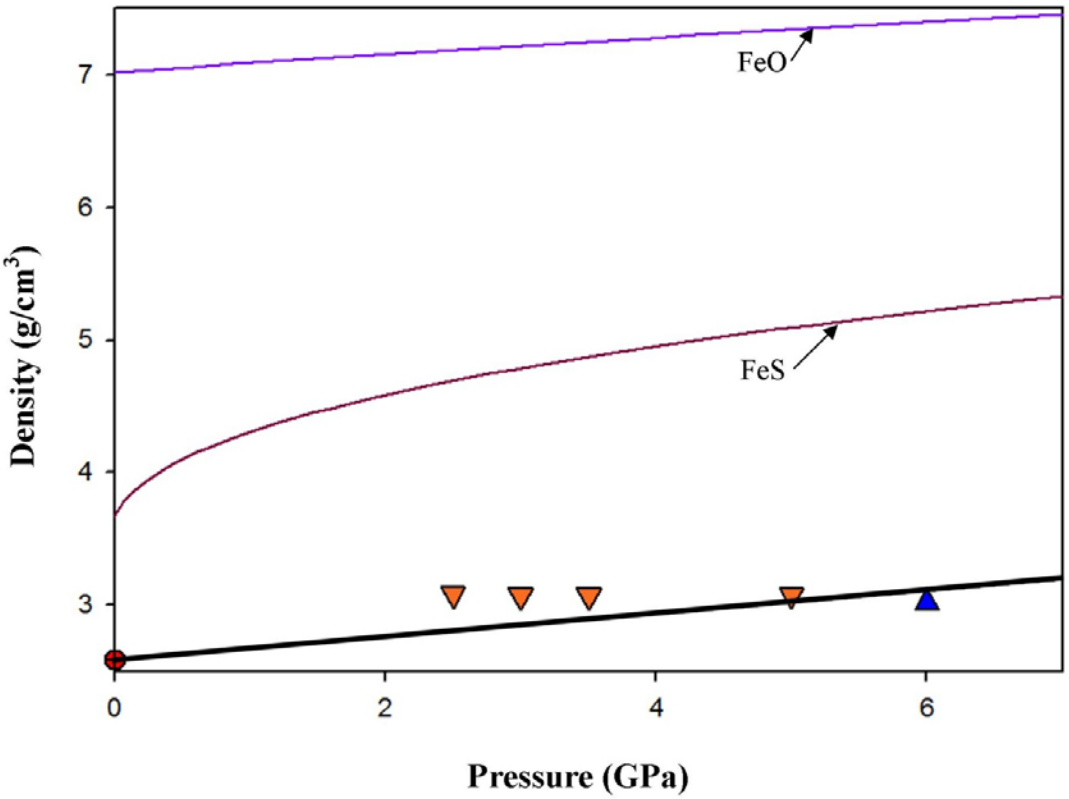

Figure 1. Comparison of the density of the northern volcanic plains composition with FeO and FeS melts. The maroon line is FeS melt [*Nishida et al.*, 2011] and the purple line is FeO melt [*Anderson and Ahrens*, 1994]. The density of the NVP melt (same as Figures 2 and 3) is shown by the bold black line. The calculated 1-bar density (red crossed circle) for this composition at 1450 °C is 2.58 g/cm^3 [*Lange and Carmichael*, 1987; *Ochs and Lange*, 1999]. Downward facing orange triangles represent sinking of Fo_{100} spheres and the upward pointing blue triangle represents floating of Fo_{100} spheres. The addition of S into our mixture would decrease the density of our melt, confirming that the volatile-free composition is an upper estimate of melt density on Mercury.

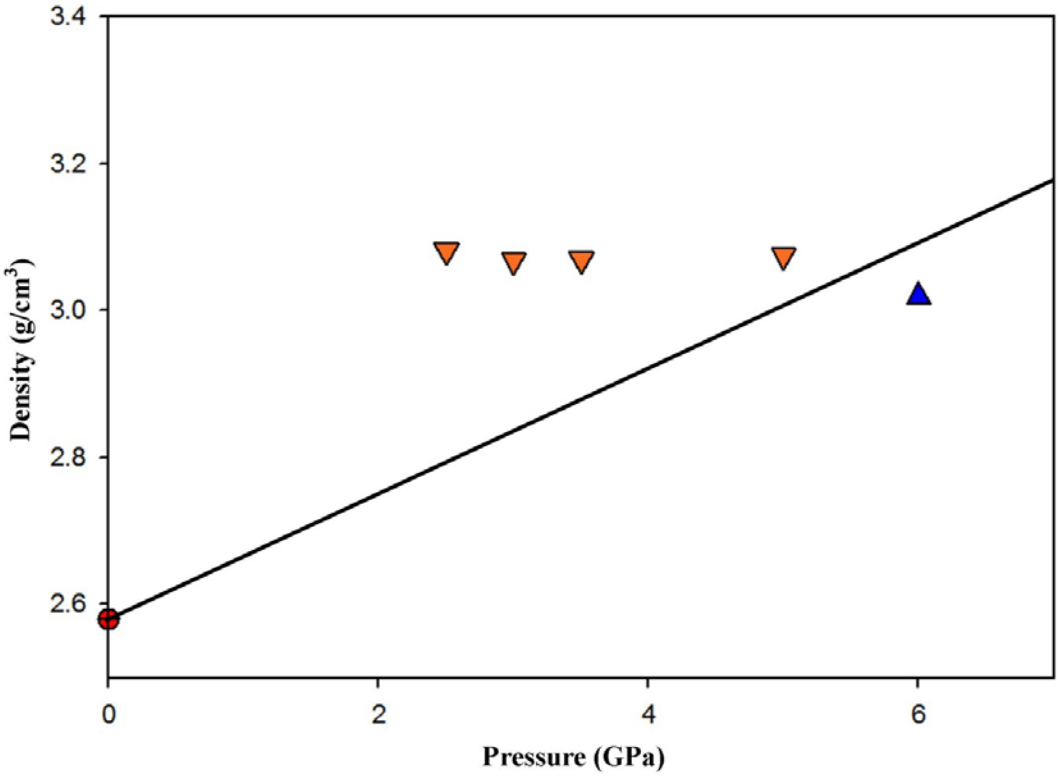

Figure 2. Experimental sink-float results for the NVP melt composition at T=1450 °C. The solid black line represents the best fit straight line to these data. Symbols are the same as in Figure 1.

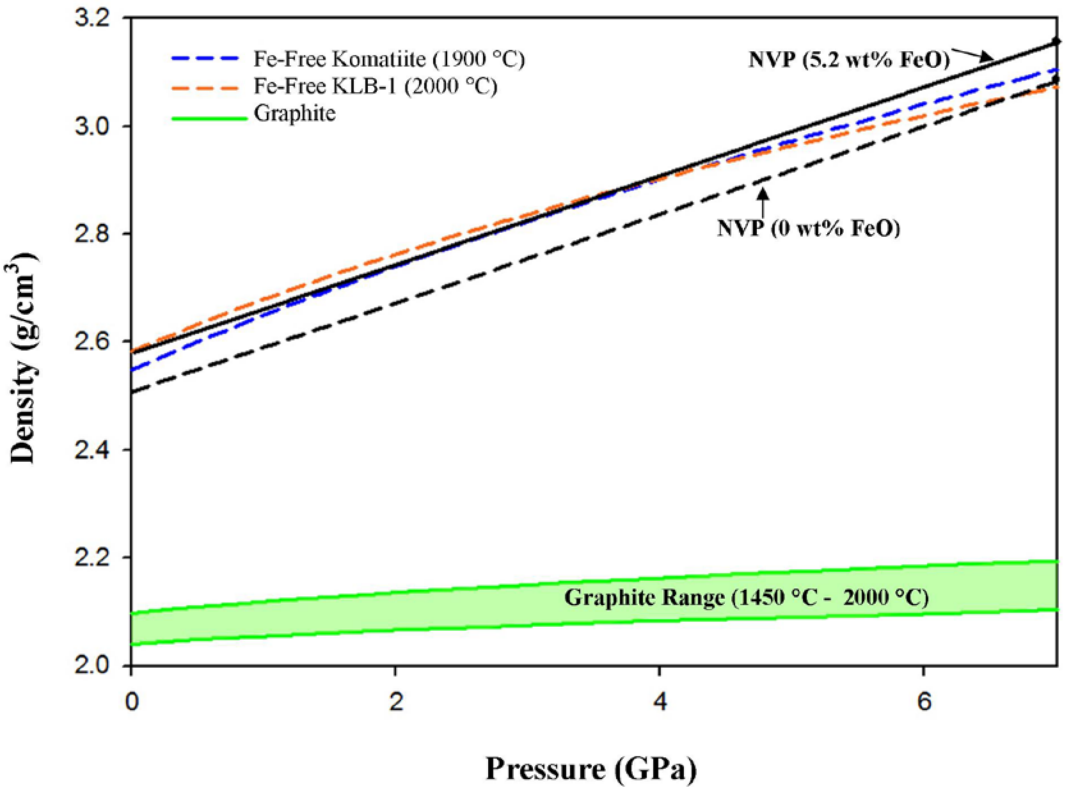

Figure 3. Comparison of the densities of possible mercurian magma ocean melts. The NVP (black solid line) has been plotted using the data from Figure 2 as a maximum density end-member and removing all of the iron (black dashed line) for a minimum density end-member. Terrestrial analog melts including a FeO-free komatiite (blue dashed line) [*Agee and Walker*, 1993] and FeO-free KLB-1 peridotite (orange dashed line) [*Agee and Walker*, 1993] are shown. The FeO-free melts were plotted by calculating the 1-bar densities for the normalized FeO-free versions of each composition and constructing a parallel offset based on the density differences with the FeO-bearing compositions. All curves are plotted at their respective liquidus temperatures. The shaded region in Figure 4 was constructed using the highest and lowest densities of these lines as the outer boundaries over the given pressure range. Although we do not know an exact composition of a mercurian magma ocean, this data shows that graphite (green shaded region) will be buoyant relative to the molten bulk silicate of the mercurian mantle. One-bar densities were calculated using *Lange and Carmichael* [1987].

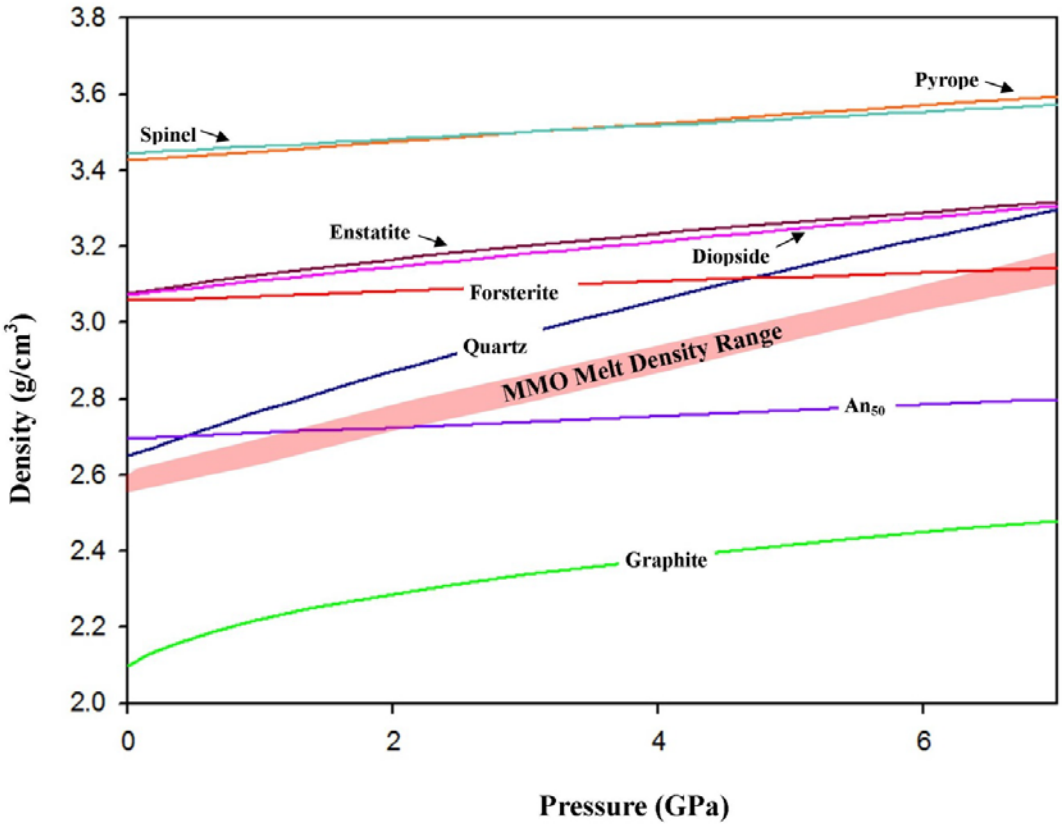

Figure 4. Comparison of the densities of possible mercurian magma ocean (MMO) melts to common rock-forming minerals, including graphite (green line), An_{50} (purple line), quartz (blue line), forsterite (red line), diopside (pink line), enstatite (maroon line), pyrope (orange line), and spinel (turquoise line). All mineral density lines are derived from 3rd-order Birch-Murnaghan equations of state at 1450 °C. The density of the possible mercurian magma ocean melt range refers to the melt region outlined in Figure 3.

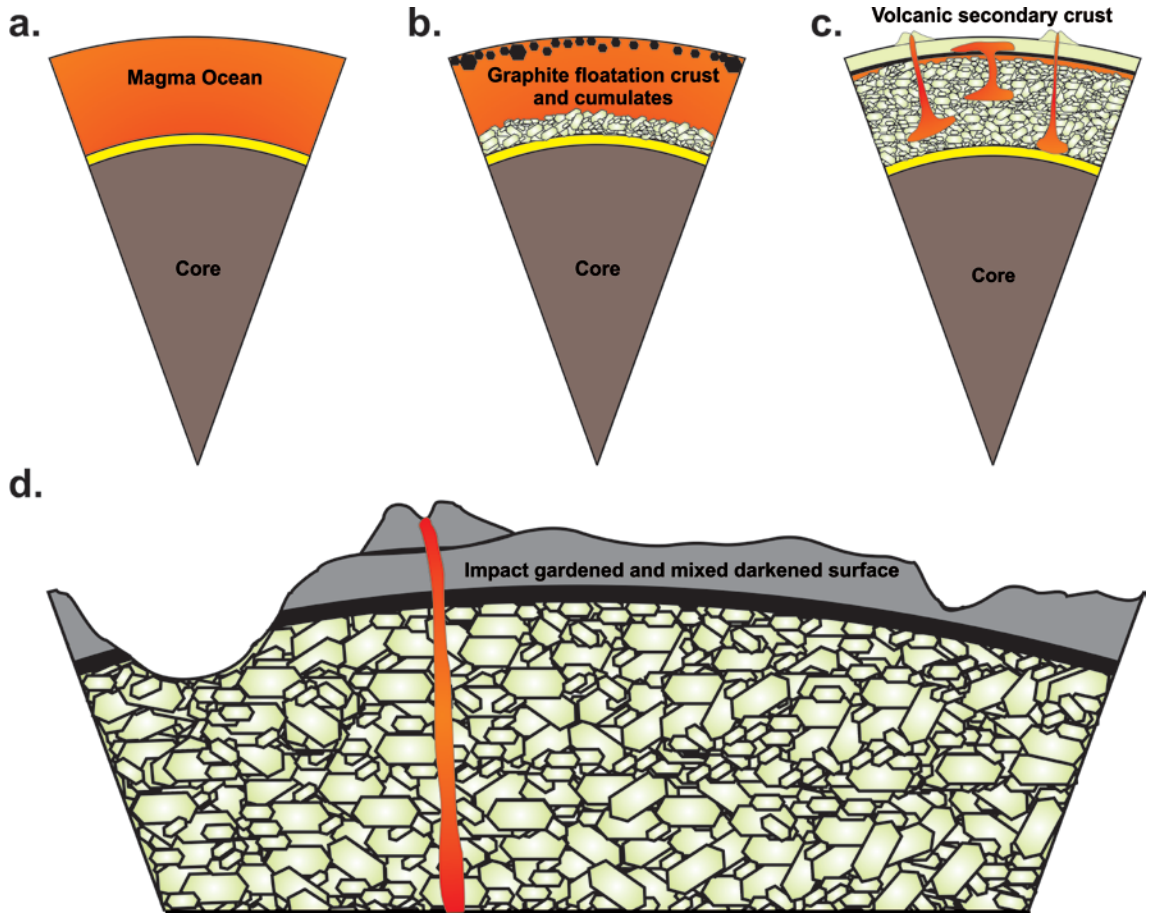

Figure 5. Cartoon illustrating the stages of a mercurian magma ocean and subsequent primary and secondary crust formation. a) Molten mantle (orange) and formation of the core (gray) and hypothesized FeS layer (yellow) at the base of the mantle. b) Crystallization of the magma ocean continues with low-FeO cumulates sinking to the base of the mantle (light green) and the formation of a primary graphite floatation crust (black). c) Continued crystallization followed by subsequent partial melting (orange) and volcanism to produce a secondary crust (light green). d) Impacts to the planet have exposed portions of the mantle (green), as well as mixed the primary (black) and secondary crusts (dark gray), resulting in a darkened and spectrally neutral surface observed on Mercury today. The thickness of the graphite floatation crust is presently unknown, but it can be estimated as a function of the C abundance of the bulk silicate portion of Mercury (Figure 7). The thickness of the graphite floatation crust has been exaggerated for the purposes of this cartoon and does not appear in realistic proportions relative to the size of Mercury's core, mantle, and secondary crust.

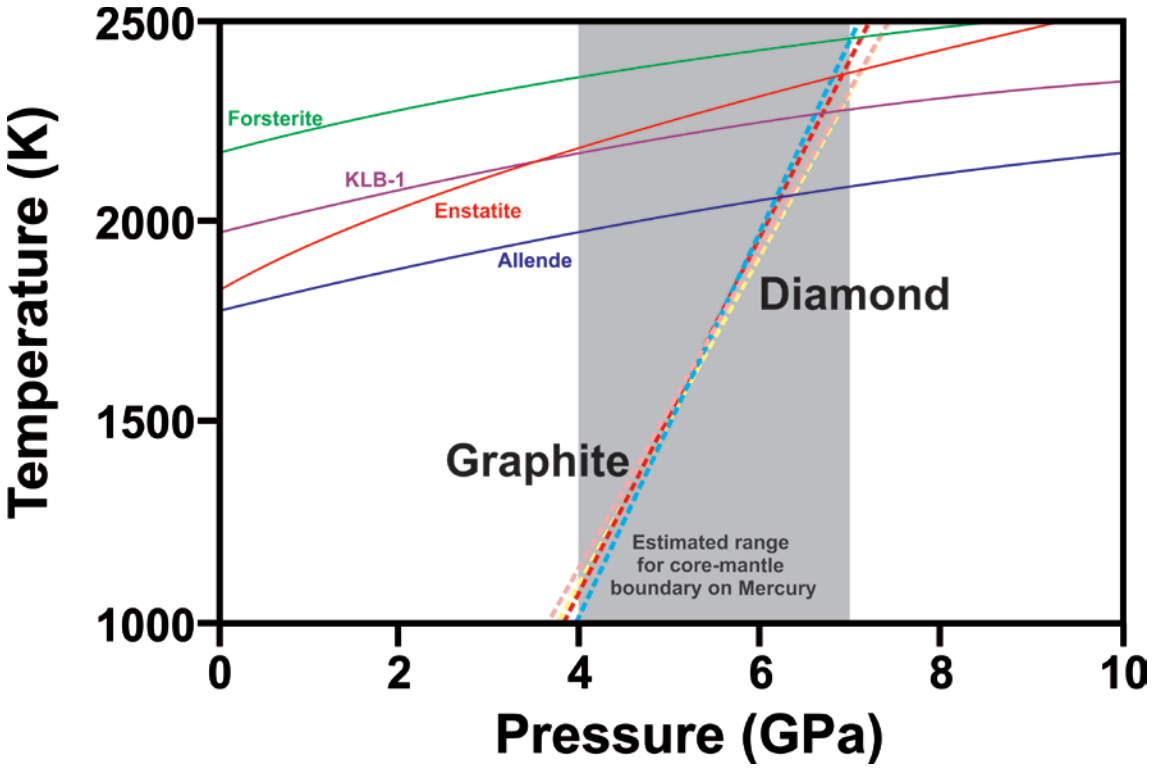

Figure 6. *P-T* phase diagram for carbon, displaying the phase boundary between graphite and diamond, the pressure range of the mercurian core-mantle boundary (gray regions taken, according to *Hauck et al.*, [2013]), and liquidus curves for forsterite, terrestrial peridotite (KLB-1), enstatite, and a CV3 carbonaceous chondrite (Allende). The dashed lines represent various experimentally determined phase boundaries between graphite and diamond. The pink dashed line comes from *Clausing* [1997], the red dashed line comes from *Bundy et al.* [1961], the yellow dashed line is from *Kennedy and Kennedy* [1976], and the blue dashed line is from *Bundy et al.* [1996]. Data for each of the liquidus curves come from the following sources, forsterite (green) is from *Presnall and Walter* [1993], KLB-1 (purple) is from *Herzberg and Zhang* [1996], enstatite (red) is from *Boyd et al.* [1964], and Allende (dark blue) is from *Agee et al.* [1995].

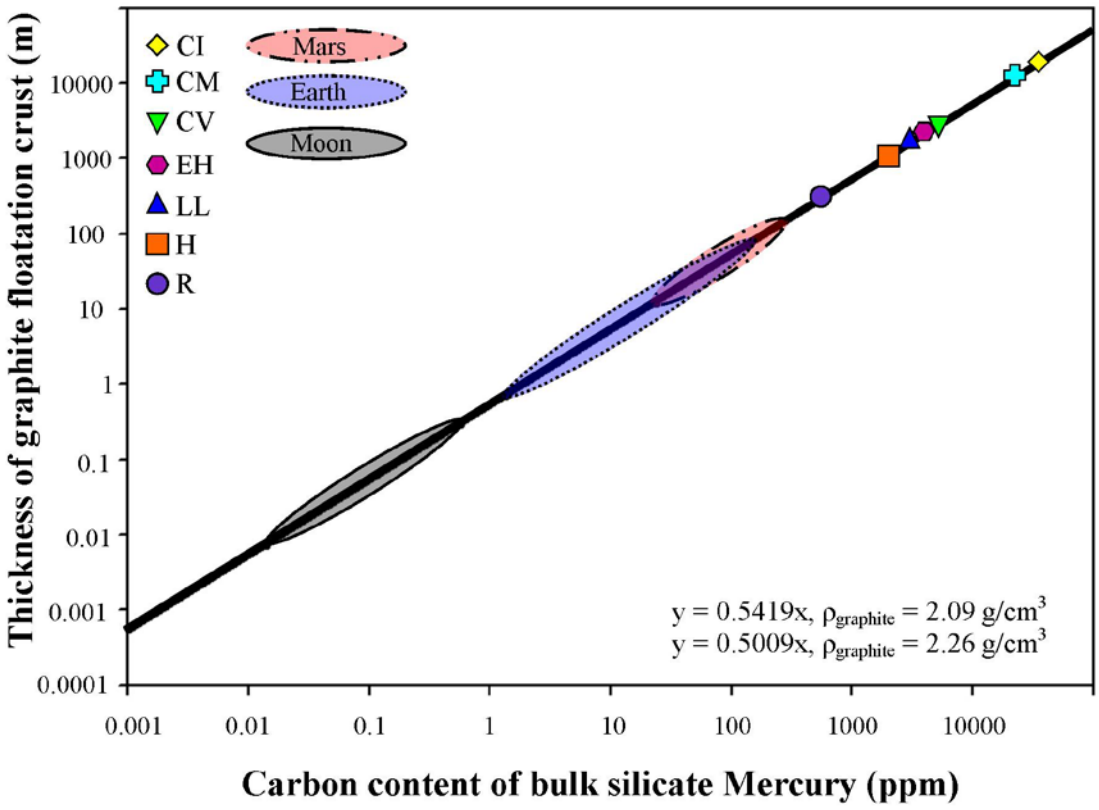

Figure 7. Thickness of possible graphite floatation crust (meters) as a function of carbon content (ppm) in the bulk silicate portion of Mercury. The model was computed using the parameters in Table 5 but assuming an average mantle density of 3.2 g/cm^3. The thickness of the line represents the range of graphite density (2.09 g/cm^3 to 2.26 g/cm^3) used in the calculation. Since the abundance of carbon in the bulk silicate portion of Mercury is unknown, the carbon content of various meteorites [*Lodders and Fegley*, 1998] as well as ranges for carbon in the silicate portions of the Moon [*McCubbin et al.*, 2015], the Earth [*Lodders and Fegley*, 1998], and Mars [*Hirschmann and Withers*, 2008] are plotted for comparison.

Table 1. Composition of the ideal northern volcanic plains (S- and alkali-free) and the starting composition of our mixture in weight percent determined from a superliquidus experiment. Ideal composition calculated and normalized from XRS data in *Nittler et al.* [2011] and *Weider et al.* [2012].

Run Number	**Ideal Composition**	**NVP-1**
Capsule		Graphite
Pressure (GPa)		3.0
Temperature (°C)		1750
Oxides (Wt%)		
SiO_2	57.71	56.67
TiO_2	1.35	1.22
Al_2O_3	13.46	14.40
Cr_2O_3	0.79	0. 37
FeO	5.20	5.16
MgO	15.20	14.43
MnO	0.70	0.68
CaO	5.59	5.26
Total	100.00	98.19

Table 2. Equation of state parameters for calculating sphere density, mantle mineral density, and melt density. Adapted from *Circone and Agee* [1996] and *van Kan Parker et al.* [2011]. [a] *Jacobs and De Jong* [2007], [b] *Liu and Li* [2006], [c] *Suzuki* [1975], [d] *Graham et al.* [1988], [e] *Isaak et al.* [1993], [f] *Suzuki et al.* [1981], [g] *Smyth* [1975], [h] *Hazen* [1977] [i] *Conrad et al.* [1999], [j] *Sumino and Anderson* [1984], [k] *Skinner* [1966], [l] *Zhang et al.* [1999], [m] *Hugh-Jones and Angel* [1994] –valid up to 4 GPa, [n] Calculated from *Hugh-Jones* [1997], [o] *Schutt and Lesher* [2006], [p] *Fried et al.* [2002], [q] *Angel* [2004], [r] *Fei* [1995], [s] *Colonna et al.* [2011], [t] *Dewaele et al.* [2008], [u] *Nishida et al.* [2011], [v] *Anderson and Ahrens* [1994].

	K_{298} (GPa)	dK/dT (GPa/K)	K'	α_0 (E-05) (K^{-1})	α_1 (E-09) (K^{-1})	α_2 (K^{-1})	ρ_{298} (g/cm^3)
Mg_2SiO_4	127.5[a]	-0.02[b]	4.8[a]	3.034	7.422	-5.381E-01[c]	3.229 X_{Fo}[h]
Fe_2SiO_4	134.6[d]	-0.024[d]	5.2[e]	0.2386	11.53	-0.518E-01[f,g,h]	4.417 X_{Fa}[h]
$Mg_2Al_2Si_3O_{12}$	171.32[i]	-0.0258[j]	3.22[i]	2.311	5.956	-4.538E-01[k]	
$MgSiO_3$	95.8[m]	-0.0274[n]	14.9[m]	2.947	2.694	-0.5588[K]	
$MgCaSi_2O_6$[o]	110.5	-0.0205	4.8	2.32	18.8	0	
$MgAl_2O_4$[o]	198	-0.015	5.05	1.85	9.75	-0.365	
SiO_2[p]	27.02	-0.0041	3.8				
$(CaAl_2Si_2O_6)_{0.5}(NaAlSi_2O_8)_{0.5}$	271.85[q]	-0.0408[q]	3.2[q]	1.39[r]	0.597[r]	0[r]	
C (Graphite)[s]	87.08		31.52				
C (Diamond)[t]	444.5		4.18				
FeS[u] **liquid**	2.5	-0.0036	24				
FeO[v] **liquid**	109.7	-0.043	4.66				

Table 3. Experimental run conditions for northern volcanic plains sink-float experiments. This table gives the experimental run number, the sphere used in the experiment, the pressure (P) and temperature (T) of the experiment, the experimental sink-float result, and the number of EPMA analyses (n) conducted on each melt. The number in parentheses represents one standard deviation of the analyzed value. Also given are the average EPMA oxide compositions (wt%) and totals, the densities of the liquids from each experimental charge at the *P-T* conditions of each experiment (ρ_{liq}), the densities of the ideal liquids at each *P-T* ($\rho_{ideal\ liq}$), the densities of the individual spheres (ρ_{sphere}), and the calculated densities at 1450 °C.

Run Number	**NVP-2**	**NVP-7**	**NVP-3**	**NVP-4**	**NVP-11**
Capsule	Graphite	Molybdenum	Graphite	Molybdenum	Molybdenum
Sphere	Fo_{100}	Fo_{100}	Fo_{100}	Fo_{100}	Fo_{100}
P (GPa)	2.5	3.0	3.5	5.0	6.0
T (°C)	1700	1775	1775	1950	2050
Result	Sink	Sink	Sink	Sink	Float
n	8	21	15	23	19
SiO_2	55.85 (1.33)	56.42 (0.45)	55.68 (1.47)	55.80 (0.89)	55.95 (1.36)
TiO_2	1.14 (0.05)	1.20 (0.04)	1.14 (0.10)	1.17 (0.05)	1.18 (0.10)
Al_2O_3	14.56 (0.64)	13.75 (0.52)	13.41 (0.70)	14.06 (0.93)	12.47 (0.70)
Cr_2O_3	0.67 (0.05)	0.67 (0.01)	0.69 (0.05)	0.71 (0.05)	0.66 (0.02)
FeO	4.83 (0.18)	5.07 (0.07)	4.76 (0.27)	5.03 (0.27)	4.93 (0.13)
MgO	16.05 (1.18)	14.93 (0.27)	17.59 (2.39)	16.47 (1.95)	16.89 (0.92)
MnO	0.63 (0.03)	0.67 (0.02)	0.63 (0.04)	0.65 (0.05)	0.64 (0.02)
CaO	5.00 (0.15)	4.85 (0.09)	4.80 (0.49)	5.06 (0.34)	4.82 (0.16)
MoO_2	0.00 (0.00)	0.52 (0.23)	0.00 (0.02)	1.22 (0.51)	1.20 (1.86)

Total	98.73 (0.44)	98.07 (0.29)	98.70 (0.40)	100.19 (0.49)	98.72 (0.72)
ρ_{liq}	2.55	2.54	2.55	2.54	2.56
$\rho_{ideal\ liq}$	2.55	2.54	2.54	2.51	2.50
ρ_{sphere}	3.05	3.05	3.04	3.03	3.00
$\rho_{ideal\ 1450C}$	2.58	2.58	2.58	2.58	2.58
$\rho_{sphere1450C}$	3.08	3.09	3.07	3.08	3.02

Table 4. One-bar densities of planetary melts (T at 1450°C)

Planetary body (reference)	**1-bar density (g/cm^3) [calculated from *Guo et al.*, 2013; *Guo et al.*, 2014; *Lange and Carmichael*, 1987; *Liu and Lange*, 2001; *Ochs and Lange*, 1999]**	**Total range of melt density at 1 bar ($\rho_{max} - \rho_{min}$) (g/cm^3)**
Mercury (this study)	2.51–2.58	0.07
Earth [*Agee and Walker*, 1993; *Agee*, 1998]	2.64–2.83	0.19
Moon [*Vander Kaaden et al.*, 2015]	2.75–3.08	0.33
Mars [*Bertka and Fei*, 1997; *Misawa*, 2004; *Warren et al.*, 1996]	2.78–2.91	0.13

Table 5. Input parameters used to calculate thickness of graphite floatation crust using equations 5–7.

Parameter	Value	Reference
Radius of Mercury (R)	2440 km	*Hauck et al.* [2013]
Radius of Mercury Core (R_c)	2020 km	*Hauck et al.* [2013]
Mantle Density (ρ_m) (min)	2800 kg/m^3	*Hauck et al.* [2013]
Mantle Density (ρ_m) (max)	3600 kg/m^3	*Hauck et al.* [2013]
Carbonaceous Chondrite Carbon Abundance (C) (min)	0.2 wt%	*Lodders and Fegley* [1998]
Carbonaceous Chondrite Carbon Abundance (C) (max)	3.45 wt%	*Lodders and Fegley* [1998]
Density of Graphite (ρ_c) (min)	2090 kg/m^3	
Density of Graphite (ρ_c) (max)	2260 kg/m^3	

Chapter 3

The origin of boninites on Mercury: An experimental study of the northern volcanic plains lavas

In collaboration with

Francis M. McCubbin[1,2]

[1]Institute of Meteoritics, Department of Earth & Planetary Sciences, University of New Mexico, Albuquerque, NM 87131, USA. [2]NASA Johnson Space Center, Mailcode XI2, 2101 NASA Parkway, Houston, TX 77058, USA.

Citation: Vander Kaaden, K.E., and McCubbin, F.M. (2016) The origin of boninites on Mercury: An experimental study of the northern volcanic plains lavas. *Geochimica et Cosmochimica Acta*, **173**, 246–263, doi: 10.1016/j.gca.2015.10.016

Abstract

Phase equilibrium experiments were conducted on a synthetic rock composition matching that of the northern volcanic plains of Mercury as measured by the MErcury Surface, Space ENvironment, GEochemistry and Ranging spacecraft (MESSENGER). The northern volcanic plains are smooth plains of suspected volcanic origin that cover more than 6% of the surface area of Mercury. The northern volcanic plains are less cratered than their surroundings and reported to be the product of flood volcanism, making them a prime candidate for experimental study. The bulk composition of the northern volcanic plains is that of an alkali-rich boninite and represents the first silica-enriched crustal terrain identified on an extraterrestrial planet from orbital data. Phase equilibrium experiments were conducted over the pressure range of the mercurian mantle (0.5–5 GPa) at very low oxygen fugacity (~ΔIW0 to -7) using a piston-cylinder apparatus (P 0.5–1.7 GPa) and a Walker-style multi-anvil device (P ≥ 2.5 GPa). Our results indicate

the origin of the northern volcanic plains lavas (boninites) are best explained by high degrees of partial melting of an olivine-dominant, pyroxene- and plagioclase-bearing mantle source at low pressure (≤1.4 GPa) and does not require hydrous melting to achieve the silica-enriched melt composition. The formation mechanism for boninites on Mercury contrasts substantially with terrestrial boninites, which typically occur in oxidized and hydrous arc environments associated with subduction zones. Instead, mercurian boninites form at exceptionally low oxygen fugacity and do not require melting of hydrated source materials. The NVP lavas represent a novel mechanism by which planetary bodies can form silica-enriched secondary crusts without the aid of water.

Key Words: MESSENGER, northern volcanic plains, phase equilibria, oxygen fugacity

1. Introduction

With the recent estimates of Mercury's surface composition from the X-Ray Spectrometer (XRS) and Gamma-Ray Spectrometer (GRS) onboard the MErcury Surface, Space ENvironment, GEochemistry and Ranging (MESSENGER) spacecraft, we now have our first opportunity to directly investigate the compositions of lavas from the planet Mercury and indirectly investigate the chemical make-up of Mercury's interior (Coffin and Eldholm, 1994; Evans et al., 2015; Evans et al., 2012; Nittler et al., 2013; Nittler et al., 2011; Peplowski et al., 2014; Peplowski et al., 2012; Weider et al., 2015; Weider et al., 2014; Weider et al., 2012). Recent compositional information from Mercury's surface indicates high amounts of sulfur (up to 4 wt%) and relatively low amounts of iron (≤ 4 wt%) (Nittler et al., 2011; Peplowski et al., 2012; Riner et al., 2010;

Weider et al., 2012), consistent with magmatism occurring under highly reducing conditions [i.e. 7 to 3 $\log_{10}$ units below the iron-wüstite (IW) buffer] (McCubbin et al., 2012; Zolotov et al., 2013). Under such reducing conditions, one would expect the majority of the Fe within the planet to partition into the core. Although Fe has been detected on the surface of Mercury, the low oxygen fugacity could indicate that the bulk of the iron on the surface is in the form of metallic iron and/or sulfides. XRS and GRS measurements of Mercury's surface from MESSENGER commonly have footprints that overlap several geologic terrains, so determining an appropriate melt composition for experimental study is a complicated process; however, the northern volcanic plains (NVP) on Mercury may represent an important exception.

The NVP are smooth plains of suspected volcanic origin that cover more than 6–7% of the surface area of Mercury (Head et al., 2011; Ostrach et al., 2015). Spanning a 4.7×10^6 to 10^7 km^3 region of Mercury, this unit is less cratered than its surroundings and purported to be the product of flood volcanism (Head et al., 2011; Ostrach et al., 2015). Although there is some evidence that suggests this unit is not completely homogeneous (Peplowski et al., 2012; Weider et al., 2015), it is the largest volcanic province that has been assessed from orbit by MESSENGER. On Earth, flood volcanism is generally produced by partial melting of mantle material that is erupted onto the surface of the planet. The NVP region has previously been described as being similar to flood basalts and komatiites on Earth, based on similar Mg/Si, Al/Si, and Ca/Si ratios (Weider et al., 2012). The estimated volume of magma that composes the NVP (determined in Head et al., 2011; Ostrach et al., 2015) falls within the volume estimated for the terrestrial Deccan Lavas ($3–8.5 \times 10^6$ km^3) and the Siberian Traps (4×10^6 km^3), but the volume of the NVP

is much greater than other large volcanic fields on Earth including the Karoo-Ferrar Province (0.3 x 10^6 km^3) and the Columbia River Basalts (0.175–1.3 x 10^6 km^3) (Coffin and Eldholm, 1994; Fedorenko et al., 2000; Fedorenko et al., 1996; Hooper and Hawkesworth, 1993; Peate, 1997; Sen, 2001; Takahahshi et al., 1998). A schematic comparison of the average relative volumes of magma from each terrestrial flood volcanic province along with the NVP on Mercury is provided in Figure 1. Flood volcanic provinces on Earth are generally tholeiitic in composition, require high degrees of partial melting, and melted at low pressure (2–4 GPa) (Coffin and Eldholm, 1994; Fedorenko et al., 2000; Fedorenko et al., 1996; Hooper and Hawkesworth, 1993; Peate, 1997; Sen, 2001; Takahahshi et al., 1998), although it is not yet clear whether these characteristics are applicable to flood volcanism on Mercury. In the present study, we experimentally investigate the high pressure phase equilibria of the NVP lavas to gain insight into their petrogenetic history, including source region mineralogy and possible depth and temperature of melting. However, before we conduct experimental work on the NVP lavas, we must first determine an appropriate composition for the NVP lavas as well as an appropriate petrologic characterization of that composition using the most recent XRS and GRS results from MESSENGER for the NVP region.

1.1 Composition and Petrologic Classification of the Northern Volcanic Plains Lavas

The most recent XRS and GRS footprints published by the MESSENGER team that specifically targeted the NVP region were used to determine an average composition of the NVP lavas. Specifically we used Mg/Si, Al/Si, Ca/Si, Fe/Si, and S/Si values from XRS reported in Weider et al. (2014), Na/Si values from GRS corresponding to 80–90 °N latitude reported in Peplowski et al. (2014), and K values from GRS reported in

Peplowski et al. (2012). The abundances of Ti, Mn, and Cr have not been reported for the NVP lavas; therefore we used the XRS detection limits for these elements reported by Nittler et al. (2011) as the upper limit concentrations of these elements.

In order to determine the composition of the NVP lavas from the elemental ratios reported by XRS, the absolute abundance of Si is required; however, the uncertainty on Si abundance measurements from GRS on Mercury is prohibitively high for determining precise surface compositions (i.e., 24.6 ± 7%; Evans et al., 2012); therefore a model abundance of approximately 25% Si has typically been used (Nittler et al., 2011; Weider et al., 2014; Weider et al., 2012), which is within the uncertainty of GRS measurements of Si (Evans et al., 2012). Next, the valence of each element is assigned (i.e., Si^{4+}, Ti^{4+}, Al^{3+}, Cr^{2+}, Fe^{2+}, Mn^{2+}, Mg^{2+}, Ca^{2+}, Na^{+}, K^{+}, S^{2-}) and a corresponding abundance of O^{2-} is determined such that the resulting composition is charge balanced. If the assumptions are valid and no major constituent elements were excluded, the resulting sum of oxides/sulfides should be near 100 wt%. However, the oxide/sulfide totals for the northern volcanic plains are low, even when the upper limit concentrations for Mn, Ti, and Cr are included (~95 wt%). Carbon and chlorine could make up some of this deficit given recently reported detections (or high minimum-detection limits in the case of C; Peplowski et al., 2015) from the MESSENGER GRS/NS instrument (Evans et al., 2015; Murchie et al., 2015; Peplowski et al., 2015); however there are no targeted analyses for C in the NVP region, and Cl abundances are approximately 0.35 ± 0.13 wt% in the region of 80–90° N, which does little to make up the deficit in totals. Unless C abundances are at or near its three-sigma detection limit of 4.1 wt% in the NVP (Peplowski et al., 2015), it is unlikely that the deficiency in totals can be explained by any missing major elements in

the NVP composition, so there is either a problem with the valence assignments or the model value for Si. Given that Mercury is a highly reduced planet, we first consider the valence assignments. Fe, Cr, and Ti all experience a change in valence state over the oxygen fugacity range exhibited by Mercury (Chabot et al., 2014; McCubbin et al., 2012; Papike et al., 2005); however, if Cr or Ti were assigned a lower valence, consistent with highly reducing conditions (Cr^{1+} and Ti^{3+}), the oxide/sulfide totals for the NVP lavas would only become lower. Furthermore, if Fe, Cr, and Ti are present as a metallic phase, they would not be a component in the silicate lavas, and the totals would be lower still. Additionally, metals exhibit limited solubility in silicate liquids and the large density contrast between metals and silicate liquids prohibits efficient transport of metals in silicate melts. Therefore, we rule out valence state assignments as the reason for low oxide/sulfide totals for the NVP lavas. Consequently, we have identified the calculated assumption of ~25 wt% Si as the reason for the low totals; therefore, we normalized the composition of the NVP lavas to 100%, while maintaining the measured Mg/Si, Al/Si, Ca/Si, Fe/Si, Na/Si, S/Si ratios. The resulting composition yielded computed Si abundances for the NVP of 26.2–26.8 wt% Si, which is within the measured value from MESSENGER GRS data of 24.6 ± 7% from Evans et al., (2012). We also computed an NVP composition without upper-limit estimates of Ti, Mn, and Cr, which will be implemented later when discussing possible sulfide mineralogy of the NVP lavas. Both NVP compositions are provided in Table 1.

The resulting bulk composition of the NVP lavas (Table 1) was classified petrologically according to International Union of Geological Sciences (IUGS) classification protocols (Le Bas, 2000; Le Bas and Streckeisen, 1991; Le Maitre, 1984;

Le Maitre et al., 2002). This classification takes into account over three decades of consideration by an IUGS Subcommission to ensure consistent terms are used across disciplines and planetary bodies when describing the chemical makeup of an igneous rock. We caution the reader that the classification determined here is based solely on chemical composition of the NVP lavas and it should not be used, *a priori*, to infer geologic processes or settings. The NVP lavas are metaluminous compositions with Mg#'s of ~96, an alkalinity index of 0.86, and ratio of non-bridging oxygen to tetrahedrally coordinated ions of 0.74–0.78, indicating a relatively high polymerization state of these melts (Mysen, 1987). Using SiO_2 and total alkali content, both NVP compositions are intermediate trachyandesites on a total alkali vs. silica diagram (Le Maitre, 1984; Figure 2). However, this diagram is not applicable to rocks with high MgO contents (MgO > 8 wt%, Le Bas and Streckeisen, 1991); consequently, in order to place further constraints on this classification, the High-Mg classification diagram (Figure 2 in Le Bas, 2000) was employed. The average NVP composition plots in the boninite field with more than 8 wt% MgO and higher than 52 wt% SiO_2. However, since this classification was constructed for terrestrial systems, the total alkali content only extends to 4 wt%. Therefore, similar to alkali rich boninites on Earth, we have termed this composition an "alkalic boninite". It is important to note that this composition does not fall in the komatiite field (MgO > 18 wt%, TiO_2 < 1 wt%, SiO_2 < 52 wt%, and alkalis < 1 wt%), which was also noted previously by Stockstill-Cahill et al. (2012), although their NVP composition included a lower estimated total alkali abundance (0.44 wt%).

CIPW (Cross, C.W., Iddings, J.P, Pirsson, L.W., and Washington, H.S.) norm calculations (Cross et al., 1903) were computed to determine the normative mineralogy of

the NVP lavas (Table S1). The NVP lavas are nepheline normative and dominated by normative plagioclase, olivine, and pyroxene. The normative mineralogy was projected into the quartz, alkali feldspar, plagioclase feldspar, feldspathoid diagram for volcanic rock classification (Le Bas and Streckeisen, 1991), which classifies this composition as a basalt/andesite. Based on terrestrial criteria presented here, the NVP lavas can be classified as either Mg-rich trachyandesites or alkali-rich boninites. Importantly, this classification strongly depends on the amount of Si because this is the main element used to distinguish various rock types. Given the abundance of S in the NVP lavas, sulfide mineralogy cannot be determined from classical CIPW norm calculations, so we will rely on the experimental results in the present study to determine the relative partitioning of elements between the silicate and sulfide melt components and compute sulfide mineralogy prior to calculating CIPW norms on the residual, sulfide-removed compositions.

The presence of a geologic terrane on Mercury composed of rocks classified as either Mg-rich trachyandesites or alkali-rich boninites represents the first example of a silica-enriched crustal terrane that has been identified on the surface of an extraterrestrial body by remote sensing techniques. Although evolved lithologies have been identified from the Moon (Jolliff et al., 1991,1999; Seddio et al., 2013), Mars (Stolper et al., 2013; Sautter et al., 2015; Santos et al., 2015), and asteroids (Day et al., 2009), these features have not been observed on scales that can be identified from orbit. On Earth, evolved crustal terranes, such as the continental crust, are reported to be a direct consequence of plate tectonics and the presence of H_2O (Campbell and Taylor, 1983); however plate tectonics is unlikely to have ever started on Mercury (Byrne et al., 2014), and the low

oxygen fugacity of the planet (McCubbin et al., 2012; Zolotov et al., 2013) would have resulted in H existing primarily as H_2 rather than H_2O (Sharp et al., 2013). The presence of the NVP on Mercury indicates that there are geologic processes that have operated to form silica-enriched crustal terranes in our Solar System that are unique from those that formed evolved crustal terranes on Earth. One of the goals of this study is to identify the geologic processes or conditions that led to the formation of such a silica-enriched crustal terrane on Mercury.

2. Experimental Methods and Motivation

The primary goal of this experimental study is to use high pressure and temperature (*P-T)* phase relations of the best estimate of a melt composition from the mercurian surface to determine basic information about the planet's interior. Importantly, we stress that this kind of investigation has significant limitations given the methods by which the melt composition was determined. Although geologic evidence from remote observations supports the NVP lavas as a continuous unit of flood volcanism (Denevi et al., 2013; Head et al., 2011; Ostrach et al., 2015), we cannot assess, *a priori*, whether the lavas represent a primary unfractionated melt or a fractionated melt that was modified by earlier crystallization, which is typically assessed prior to experimental study. Furthermore, it has been recently suggested that the NVP lavas may not be homogeneous (Peplowski et al., 2012; Weider et al., 2015). Nevertheless, given that these experiments represent some of the first laboratory investigations of a suspected mercurian lava composition, these data will provide important first-order estimates of minimum average pressures and temperatures of melting as well as mantle mineralogy of Mercury, which is largely, at present, unconstrained. It will be difficult to use the experimental results here

to provide firm constraints on the physical and chemical characteristics of the mercurian interior, so the results will be used to construct possible scenarios for the origin of the NVP lavas as well as possible characteristics of the mercurian interior. Fortunately, the shallow depth of Mercury's mantle (≤420±30 km; Hauck II et al., 2013) provides a fairly limited pressure range (≤5 GPa) over which experiments need to be conducted. Consequently, we were able to investigate the entire *P-T* parameter space of the NVP phase diagram that is relevant to Mercury.

Experiments were conducted in the high pressure laboratory at the Institute of Meteoritics (IOM) at the University of New Mexico (UNM). Experiments in the pressure range of ~0.5–1.7 GPa were run in a 13 mm Depths of the Earth Quickpress^{TM} non-end loaded piston cylinder (PC). A Walker style multi-anvil (MA) device was used for pressures from 2.5 to 5 GPa. Early reports from the MESSENGER team placed the sodium abundance on Mercury's surface at 2.9 ±0.1 wt% Na (Evans et al., 2012). Additional data collection efforts have yielded better coverage of the planet and higher resolution measurements for Na, revealing substantial variations in Na across the surface of the planet. Peplowski et al. (2014) reported a range in Na content from ~5 wt% Na (i.e., 6.7 wt% Na_2O) in the high northern latitudes on Mercury to ~2.6 wt% Na (i.e., 3.5 wt% Na_2O) near the equatorial regions. This large variation in Na will have important implications for the mineralogy of the mercurian surface because it's an important factor as to which side of the plane of critical silica saturation a melt composition lies (Irvine and Baragar, 1971; Peplowski et al., 2014; Yoder and Tilley, 1962). Consequently, in addition to the alkali- and S-bearing NVP composition (NAS_B) from Table 1, we also investigated a second melt composition with negligible alkalis and sulfur (NAS_F) (Table

1) to determine the effect on phase mineralogy if the elevated abundances of alkalis and S in the NVP were a consequence of thermal redistribution, which was initially proposed by Evans et al. (2013) but has since been ruled unlikely by Peplowski et al., (2014). The data from this alkali and sulfur free composition will also allow for extrapolation of our dataset to areas on Mercury that are not as high in alkali and S components as the NVP. However, since recent MESSENGER results suggest high abundances of alkalis and S, we primarily focus here on the phase equilibrium results from the NAS_B composition from Table 1, although the experimental results on the NAS_F composition are also provided and discussed where relevant.

2.1 Starting Materials

The synthetic starting materials (Table 1) for the two NVP compositions (NAS_F and NAS_B) investigated in this study were prepared at the IOM using high-purity reagent grade powdered oxides, silicates, and sulfides, which were mixed sequentially by increasing volume and ground under ethanol using an automated agate mortar and pestle. For the NAS_F mix, all the Fe was added as FeO in the form of synthetic fayalite. The reader is referred to Vander Kaaden et al. (2015) for details regarding the preparation of the synthetic fayalite. For the NAS_B, all the Fe was added as FeS. The starting materials were allowed to dry completely and kept in either a desiccator or a drying oven at 100 °C before use in each experiment.

2.2 Phase Equilibrium Experiments

2.2.1 Capsule materials and oxygen fugacity

The NAS_F experiments did not present the same challenges as the NAS_B composition in terms of determining an appropriate capsule material. Without the worry

of S to react with metal, these experiments were run in molybdenum capsules, which control the oxygen fugacity to within a few $\log_{10}$ units of the iron-wüstite (IW) buffer over the *P-T* range of our experiments (Burkemper et al., 2012; O'Neill, 1986). Although the oxygen fugacity of the NAS_F experiments is not as low as the mercurian interior or the NAS_B experiments, it is sufficiently low to assess the mineralogical differences between the two starting compositions. However, we caution that temperatures and pressures of multiple saturation points determined from the NAS_F composition should shift slightly if run at more appropriate oxygen fugacity, which has been demonstrated experimentally in lunar magma compositions (i.e., Krawczynski and Grove, 2012).

Careful consideration of capsule material was required for running the NAS_B experiments because we needed a capsule that would not react with the melt components, including sulfur, so many metal capsule materials (Mo^0 and Fe^0) were ruled out due to their demonstrated affinity for sulfur (e.g. Tauster et al., 1980). Additionally, sulfur solubility increases in silicate melts with decreasing oxygen fugacity (Beermann et al., 2011; Berthet et al., 2009; Holzheid and Grove, 2002; Malavergne et al., 2007; Malavergne et al., 2014; Mavrogenes and O'Neill, 1999; McCoy et al., 1999; Moune et al., 2009; Zolotov et al., 2013), so the experiments were run under low oxygen fugacity to promote S-dissolution into the silicate melt. Furthermore, McCubbin et al. (2012) and Zolotov et al. (2013) have shown the oxygen fugacity of Mercury is between 7 and 3 $\log_{10}$ units below the IW buffer, so highly reducing conditions provide a more realistic representation of the interior of Mercury. Graphite minimally reacts with silicate liquids especially under reducing conditions (Ardia et al., 2013), so it was chosen as the capsule material for the NAS_B experiments. Graphite capsules are incapable of controlling

oxygen fugacity much below the graphite-CO buffer, so we needed to add an additional component to the experiments to promote reducing conditions. Consequently, oxygen fugacity was lowered in each experimental charge by adding Si metal to the bottom of each capsule in an ~ 1:2 mixture of Si metal:silicate starting material (Table 1), similar to the procedure of Siebert et al. (2004) and Rose-Weston et al. (2009). Therefore, these experiments were within a $\log_{10}$ unit of the Si-SiO_2 oxygen fugacity buffer, which is within the range reported for Mercury over the temperature range of our experiments.

2.2.2 Piston Cylinder Experiments

Experiments for pressures ≤1.0 GPa were run in the PC using the procedures, parts, and calibrations described previously in Vander Kaaden et al. (2015) and McCubbin et al. (2015), although we briefly summarize the setup here. The loaded capsules were placed within salt-pyrex cells, which were used as a pressure medium, with crushable MgO parts and a graphite furnace. Exceptions to the procedure include using run durations from 4–21 hours and using a Type B ($Pt_{30}Rh_{70}$/ Pt_6Rh_{94}) thermocouple and Eurotherm (2416) controller to control and monitor temperature throughout the duration of each run. Each experiment was quenched by shutting off power to the furnace and slowly decompressing the run. Experiments on the NAS_F composition were run at 0.57 GPa and 1.2 GPa in the temperature range of 1300 °C – 1450 °C, with run durations of 0.25–4 hours. NAS_B experiments were run at pressures of 0.57–1.7 GPa between 1100 °C – 1480 °C, with run durations of 4–21 hours. When possible, charges were taken to superliquidus temperatures for 3–20 minutes, depending on the stability of the assembly at a given temperature and pressure before dropping to the crystallization temperature.

2.2.3 Multi-Anvil Experiments

Experiments run at pressures between 2.5 and 5 GPa were performed in a MA using procedures that are identical to those described in Vander Kaaden et al. (2015), including a ceramic octahedron, Al_2O_3 inner parts, and 8 mm truncation-edge-length of tungsten carbide cubes. The reader is referred to Agee et al. (1995) for our MA pressure calibration data and procedures. At the termination of each run, the charge was quenched and slowly decompressed in the same manner as the PC experiments. Experiments on the NAS_F composition were run at pressures from 3.5 GPa to 5 GPa in the temperature range of 1350 °C – 2000 °C, with run durations of 1–3 hours. NAS_B experiments were run at pressures ranging from 2.5 GPa to 5 GPa between 1600 °C and 1950 °C, with run durations of 4 hours. Similarly to PC experiments, charges were taken to superliquidus temperatures when possible for 3.5–18 minutes, depending on the stability of the assembly at a given temperature and pressure before dropping to the crystallization temperature.

2.2.4 Approach to a steady-state

Under the highly reducing conditions of our experimental runs, typical exchange coefficients for Mg and Fe in olivine and liquid $\left(K_D{}_{Ol-Liq}^{Mg-Fe}\right)$ cannot be accurately calculated to assess equilibrium within these experiments due to the low amount of Fe in our starting composition. Furthermore, the majority of the Fe in our starting materials partitions into the metal or sulfide phases resulting in low FeO (0.02–0.24 wt%) in the melt. The homogeneous nature of each experimental charge, however, does suggest that our experiments approached a steady-state during our 2–24 hour run durations. Furthermore, there were no inconsistencies in our data to suggest the experimental

charges required additional time to equilibrate, and all of the olivine present are consistently Fo_{100}.

In order to provide an additional check on steady-state conditions, we performed a time series using the NAS_B + Si metal compositions. Care was taken when filling the capsules to ensure equal portions of the NAS_B silicate starting composition and Si metal were loaded into each capsule so the experiments could be directly compared. Experiments were run at 1 GPa and 1425 °C for 0.3, 1.5, 4, 11, and 22 hours. Analyses of these experiments show an increase in SiO_2 with increasing run time (Figure S1). There is little difference between the 1.5 and 4 hour run durations for SiO_2, however, there is a >1 wt% increase in SiO_2 after holding the run for 11 hours and >6 wt% increases after holding for 22 hours when compared with the 4 hour run duration. A crystalline SiO_2 phase was present in the time-series runs that were held for 11 and 22 hours, indicating that our system was susceptible to O diffusion into the capsule, which reacted with the Si metal to raise the SiO_2 content of the melt. Evidence of O diffusion was also observed in a subset of experiments with similar starting materials not included in this work (Figure 3B) where olivine cores were present within pyroxene grains for experiments longer than 4–10 hours. Consequently, caution was taken for any interpretations of our data that were highly dependent on silica activity, including the olivine-opx cotectic point along the liquidus, which we verified using shorter ($\leq$ 4 hour) run durations. The FeO content in the melt decreased until 4 hours and remained fairly constant in the longer run durations (Figure S1) indicating that redox equilibrium was reached by 4 hours. TiO_2 content also decreased over time and S^{2-} increased with increasing run duration.

We also compared the run products from experiments with and without a super-liquidus step as an additional check on whether or not our experiments reached a steady-state. Experiment NSA-34 was taken directly to its crystallization temperature of 1300 °C and held for 4 hours. This experiment consisted of olivine and melt. We then ran experiment NSA-59, which was first taken to a superliquidus temperature of 1425 °C for ~ 20 minutes before being dropped to the crystallization temperature of 1300 °C, and it was held for 24 hours. The results of NSA-59 also consisted of olivine and melt, although the melt composition of NSA-59 had slightly higher SiO_2, which was expected from the O diffusion problem discussed above. The results of these experiments as well as the homogeneous nature of our run products and lack of discrepancies along our phase diagram support our experiments reaching a steady state within the duration of the runs.

3. Analytical Techniques

Each experimental charge was ground and polished to expose the maximum surface area and all phases present. All NAS_F run products were polished using water as the lubricating material. However, Murthy et al. (2003) have shown loss of K from the FeS phase within their run products when using oil- or water-based lubricants during polishing. Furthermore, we analyzed multiple NAS_B experiments by electron probe microanalysis (EPMA) before and after treatment with water and acetone, and the silicate glasses had lower abundances (0.2-1.2 wt%) of volatile elements (mainly Na_2O, S^{2-}, and Cl^-) after treatment (Figure S2). Therefore, all of our NAS_B experimental charges were polished dry using hexagonal boron nitride as a lubricant, which we mixed with various grit sizes of alumina powder. All experimental charges were polished to a 0.3 µm finish.

3.1 Electron Probe Microanalysis

All phases present in each experiment were analyzed using a JEOL JXA 8200 electron microprobe housed in the IOM at UNM. Silicates, metals, and sulfides were analyzed using an accelerating voltage of 15 KeV. A beam current of 15 nA was used for silicates whereas metals and sulfides were analyzed using a beam current of 20 nA. A broad beam (10–20 μm) was used for glass analyses and a focused beam (1–5 μm) was used for silicate minerals, metals, and sulfides. The standards albite (for Na), almandine (Al, Fe), augite (Si, Al, Ca, Mg), olivine (Mg, Si, Fe), orthoclase (K), pyrope (Cr, Mg, Ca), titanite (Ti), and spessartine (Mn) were used to analyze our quenched melt and silicate minerals. A sodalite standard was used to determine the amount of Cl^- contamination and a synthetic $CaMoO_4$ was used to determine the amount of MoO_2 contamination in the glasses for the NAS_F runs. Metal and sulfide standards included Al-metal, albite (for Na), Cr-metal, orthoclase (K), Si metal, pyrite and troilite (S), Mg-metal, spessartine (Mn), augite (Ca), Fe-metal, Ti-metal, and sodalite (Cl). Peak positions were checked on the silicate standards used for metal and sulfide analyses and compared with the peak position of the experimental charge to ensure that analyses were conducted at the correct peak position. Peak count times ranged from 30–60 seconds and background count times ranged from 15–30 seconds, respectively. Analyses in the proximity of Si-rich metal typically suffered from substantial secondary fluorescence of Si, resulting in elevated totals and elevated abundances of Si, so care was taken to measure glass that was ≥ 200 μm from the Si metal.

3.2 Micro-Fourier Transform Infrared Spectroscopy (FTIR)

The presence of H_2O can substantially depress the liquidus temperature of basaltic melts (e.g., Médard and Grove, 2008), so quantitative infrared spectroscopic

measurements were conducted on the experimental glass products of numerous experimental charges at room temperature in transmittance mode with a Nicolet Nexus 670 Fourier Transform Infrared Spectrometer in the IOM at UNM to determine the amount of H_2O present in the "dry" runs from this study. Transmittance IR spectra were collected from doubly polished wafers of the run products over the mid-IR range (400–4000 cm^{-1}) using a Continuum microscope with a Globar source, XT-KBr beamsplitter, and a MCT/A detector over a 100 × 100 μm area with a 4 cm^{-1} resolution. Thicknesses for each sample were obtained by focusing a reflected aperture on the top surface of the sample first then the bottom surface of the sample and recording the z-axis position of the mapping stage in the Atlus software. These arbitrary units were converted to μm using a previous calibration (Berger, 2012). Background spectra were collected under the same conditions before each analysis. Total dissolved water concentrations were determined for each glass from the intensity of the broad band at 3570 cm^{-1} after the calculation scheme of Mandeville et al. (2002) and Dixon et al. (1995). One thousand and twenty four scans were performed for each IR spectrum acquired. The reader is referred to Vander Kaaden et al. (2015) for full details on this procedure.

4. Calculations of Oxygen Fugacity

The oxygen fugacity of all experiments that were sulfur and alkali free (NAS_F) was controlled through the starting material composition as well as the molybdenum capsule that was used in each experiment. Due to the low solubility of MoO_2 in silicate melts (Table S2 and Burkemper et al., 2012) and the presence of the Mo capsule, we can constrain the fO_2 of each experiment to being at or below the Mo-MoO_2 buffer. In order to attempt to quantify the fO_2 of each experimental run product after the analysis of each

experiment by EPMA, the oxygen fugacity of the charge was calculated using the melt phase present in the experiment and assuming an activity of one for Fe metal. This approach gives us a minimum value for the fO_2 of each experiment relative to the IW buffer. Using these two phases, the oxygen fugacity of the charge was calculated relative to the IW buffer using equation (1)

$$\Delta IW = 2log\left(\frac{x_{FeO}^{silicate} * \gamma_{FeO}^{silicate}}{x_{Fe}^{metal} * \gamma_{Fe}^{metal}}\right) \quad (1)$$

where $x_{FeO}^{silicate}$ is the mole fraction of FeO in the silicate, $\gamma_{FeO}^{silicate}$ is the activity coefficient of FeO in the silicate, x_{Fe}^{metal} is the mole fraction of Fe in the metal, and γ_{Fe}^{metal} is the activity coefficient of Fe in the metal. To begin, we assume ideality to make a first-order approximation of the oxygen fugacity (see also below). Since we are assuming that a pure Fe-metal phase is present, the activity of Fe in the metal is fixed at unity. The fO_2 of every NAS_F experiment was calculated, where melt was present, resulting in fO_2 values of 2.24 to 2.76 $\log_{10}$ units below the IW buffer. Since there was not an Fe-metal phase present in any of our experiments, the experimental charges are likely to be more oxidizing than this estimate. Using this constraint on the lower bound of fO_2 and the fact that the Mo-MoO_2 and IW buffer are essentially equal at the *P-T* conditions of interest (Burkemper et al., 2012), the oxygen fugacity of our NAS_F experiments lies somewhere between IW and IW-2.76. The estimated fO_2 of each experiment is given in Table 2.

The oxygen fugacity of all experiments containing sulfur was controlled through the addition of Si metal to each individual capsule. After the analysis of each experiment, the oxygen fugacity of the charge was calculated two different ways. First, the fO_2 was calculated relative to the Si-SiO_2 buffer using equation (2)

$$\Delta Si - SiO_2 = log\left(\frac{x_{SiO_2}^{silicate} * \gamma_{SiO_2}^{silicate}}{x_{Si}^{metal} * \gamma_{Si}^{metal}}\right) \quad (2)$$

where $x_{SiO_2}^{silicate}$ is the mole fraction of SiO_2 in the silicate, $\gamma_{SiO_2}^{silicate}$ is the activity coefficient for SiO_2 in the silicate, x_{Si}^{metal} is the mole fraction of Si in the metal, and γ_{Si}^{metal} is the activity coefficient for Si in the metal. Similar to the method above, we begin by assuming ideality to make a first-order approximation of the oxygen fugacity. However, the presence of Si metal in each experiment fixed the Si activity to unity, so only the activity coefficient for SiO_2 is uncertain. The fO_2 of every NAS_B experiment was calculated, where melt was present, using the melt phase and the Si-rich metal phase resulting in fO_2 values of 0.17 to 0.27 $\log_{10}$ units below the Si-SiO_2 buffer. A second calculation of oxygen fugacity was conducted using the same melt and an Fe-rich metal phase, when present. Using these two phases, the oxygen fugacity of the charge was calculated relative to the iron-wüstite buffer using equation (1). We begin again by assuming ideality to make a first-order approximation of the oxygen fugacity. These calculations resulted in oxygen fugacities between 5.45 and 6.86 $\log_{10}$ units below the IW buffer, which is more reducing than the NAS_F experiments by ~5 to 7 $\log_{10}$ units. Both calculations (using equations 1 and 2) for a given experiment typically agreed within approximately 1 $\log_{10}$ unit, indicating that ideality is a valid assumption for a first-order approximation of the oxygen fugacity. The fO_2 of each experiment is given in Table 2.

We have also gone through the exercise of calculating activity coefficients for FeO (O'Neill and Eggins, 2002), SiO_2 (Beattie, 1993; Carmichael et al., 1970), Fe^0, and Si^0 (Wade and Wood, 2005) and performing the same calculations given in equations (1) and (2). Although the majority of our results shifted only by $\leq$0.5 $\log_{10}$ units in either direction, in a few cases these calculations resulted in values considered to be erroneous

(e.g. ΔIW + 15.91 for NSA-10 and ΔSi-SiO_2 -18.44 for NSA-21). For this reason we have chosen to compute all fO_2 values in this manuscript assuming ideality. This assumption, although not strictly correct, is considered to introduce the least amount of scatter in the precision of our estimates of oxygen fugacity, although there may be up to a 0.5 $\log_{10}$ units uncertainty in accuracy.

5. Results

Table 2 includes a full listing of experiments conducted for NAS_F and NAS_B compositions along with the run conditions, phases present, and estimated oxygen fugacity. The results of each experiment in this study including capsule material, run conditions, run durations, oxygen fugacity, and EPMA data can be found in the Supplementary Materials (Tables S2-S4). Backscattered electron images of representative experimental charges are shown in Figure 3.

5.1 NAS_B phase equilibrium experiments

The phase diagram for the NAS_B composition is shown in Figure 4. SiC was present in most experimental run products at the boundary of the graphite capsule and Si metal, but was much more prominent in MA experiments. Where grains were large enough, analyses were conducted (Table S3) and the carbon abundance was calculated by difference. In this alkali- and sulfur-bearing system, forsterite is the liquidus phase at low pressures (<1.4 GPa) between ~1250 °C and ~1600 °C and albitic plagioclase is present at 0.57 GPa and 1100 °C. A multiple saturation point (MSP) occurs when two or more minerals coexist at the same point in *P-T* space along the liquidus. The first MSP occurs at ~1.4 GPa and ~1460 °C between olivine and orthopyroxene. At pressures between 1.4 GPa and 2.7 GPa, enstatite-rich pyroxene is the liquidus phase. A second MSP occurs at

~ 2.7 GPa and ~1640 °C between orthopyroxene and a jadeite-like pyroxene. The composition of this jadeite-like pyroxene is $En_{89}Wo_{11}$ and has ~3 wt% Na_2O in its structure. At pressures greater than ~3.8 GPa and ~1800 °C, silica appears as a liquidus phase with a jadeite-like pyroxene (~6–7 wt% Na_2O). However, the appearance of SiO_2 on the liquidus is most likely a direct effect of O diffusion into our capsule reacting with the Si metal used to reduce the experiments. Consequently, we cannot confirm the validity of silica on the high pressure liquidus of the NAS_B composition.

The compositions of the residual melts (Table S3) vary as a function of pressure, temperature, and mineral phases present. They are consistently high in SiO_2 (56.86–67.74 wt%), extremely low in FeO (0.02–0.24 wt%), and have a wide range of MgO (4.29–16.67), CaO (3.58–8.50), and Na_2O (3.78–8.06 wt%) abundances. S^{2-} contents range from as low as 0.64 wt% to as high as 4.81 wt%. Additionally, although we did not intentionally include Cl^- in our starting composition, it was present in all runs. We suspect that one of our reagents (most likely FeS) may be contaminated with Cl^-. We have ruled out contamination from the NaCl pressure medium used in the PC experiments as the primary source of Cl^- because the MA experiments, which consist of a Cl^--free ceramic octahedron as a pressure medium, also contain measurable amounts of Cl^- (Table S3). Although the Cl^- may have been present in variable amounts at the start of each experiment, it consistently partitioned entirely into the silicate melt (up to 2.44 wt%), and it was below detection in coexisting sulfide (detection limit 0.01 wt%) and metal (detection limit 0.01 wt%) phases. Micro-FTIR analyses of the glass in two experiments, with sample thicknesses <170 µm, indicate ~1–6 ppm H_2O was present in

these charges which are levels too low to significantly affect phase boundaries (Médard and Grove, 2008) or elemental partitioning (Righter and Drake, 1999).

The addition of Si metal to the bottom of each capsule, as well as higher concentrations of sulfur, led to the formation of numerous metals and sulfides in each experiment. EPMA analyses and stoichiometric compositions of each metal and sulfide phase are given in Table S4. Pure Si metal is present within each experiment, indicating it was not completely consumed during the run. In some cases, the Si metal was veined with a Si-Cr metal mixture. The other metals in these experiments typically consisted of Si, Cr, and Fe with minor amounts of Ti and Mn. The sulfides were dominated by Fe and Cr as well as Ti and Mn. In a few cases, Ca- and Mg-bearing sulfides were present. These results were used to calculate normative sulfides in Table S1 before performing additional CIPW norm calculations on the sulfide-removed residual silicate compositions.

5.2 NAS_F phase equilibrium experiments

SiO_2 is present as a liquidus phase at all pressures investigated in this study for the NAS_F composition. At low pressures, orthopyroxene and SiO_2 are the liquidus phases. The orthopyroxene has an average composition of $En_{90}Fs_8Wo_2$ in all experiments up to 3 GPa (Table 2 and Table S2). At approximately 3 GPa and 1800 °C, garnet appears on the liquidus with orthopyroxene and SiO_2. At pressures greater than 3 GPa, pyrope-rich garnet and SiO_2 are the liquidus phases. Clinopyroxene ($En_{66}Fs_9Wo_{25}$) becomes stable at higher pressures ($\geq$ 2.5 GPa). As expected given the elevated SiO_2 abundances and lack of alkali elements, olivine is not stable at any pressure investigated with this composition (0.5–5 GPa).

EPMA analyses of each melt are provided in Table S2. The melts consistently had high SiO_2 (54.62–59.55 wt%), low MnO (0.65–0.73 wt%), and low Cr_2O_3 (0.20–0.75 wt%). There was a wide range in TiO_2 (1.20–5.70), Al_2O_3 (4.44–17.29), FeO (4.95–9.22), MgO (8.60–15.18) and CaO (5.00–14.17) depending on the silicate phases present in a given run product. Although these experiments were run in molybdenum capsules, there was very little Mo^0 dissolved in the melt. The maximum MoO_2 abundance measured was 1.18 wt%, which most likely reflects a metal bleb that was close to the electron beam during analysis. Micro-FTIR analyses of glasses from four experimental charges from this study indicate an H_2O content typically much less than 0.1 wt% H_2O with one higher value of 0.3 wt%, which are levels too low to significantly affect phase boundaries (Médard and Grove, 2008) or elemental partitioning (Righter and Drake, 1999). Sample thicknesses varied from 48–175 μm.

6. Discussion

6.1 Effect of alkalis on mercurian mineralogy

The mineralogy of Mercury's surface is currently unknown despite the collection of over 4.5 million UV-VIS spectra by the MESSENGER spacecraft (Blewett et al., 2013; Ernst et al., 2010; Holsclaw et al., 2010; Izenberg et al., 2014). Consequently, the mineralogy of the mercurian surface has typically been inferred (e.g., Charlier et al., 2013; Stockstill-Cahill et al., 2012) using chemical compositions of the surface determined by the XRS and GRS instruments onboard MESSENGER (Evans et al., 2012; Nittler et al., 2013; Nittler et al., 2011; Peplowski et al., 2011; Peplowski et al., 2014; Peplowski et al., 2012; Weider et al., 2015; Weider et al., 2012). As stated previously, one of the most surprising results returned from MESSENGER was the elevated

abundances of Na on the surface of the planet (global average of 3.5 wt% Na_2O), particularly at the high northern latitudes (average of 6.7 wt% Na_2O), that has been interpreted as being a geochemical feature of the lavas in the NVP (Peplowski et al., 2014). Consequently, we can compare and contrast the results of our high pressure phase equilibrium data for the two starting compositions (NAS_F and NAS_B), which have over a 5 wt% difference in Na_2O. Importantly, there are numerous differences between the two compositions we investigated as shown in Figure 4, Figure S3, and Table 1. In addition to an ~5 wt% difference in Na_2O abundance, there is also an ~5 wt% difference in FeO abundance that is related to the differences in oxygen fugacity, up to ~6 $\log_{10}$ units, between the two sets of experiments (Tables 1–2). If the NAS_F experiments were run under the low oxygen fugacity conditions of the NAS_B experiments, it would have resulted in a net decrease in the amount of FeO in the NAS_F experiments, which would have caused a net increase in the silica activity by increasing the ratio of Si to other melt components in the NAS_F composition. This enhancement in silica activity in the NAS_F experiments would have caused even further displacement of the NAS_F composition from the olivine stability field.

The addition of alkali elements like Na to silicate melts results in a reduction of silica activity by reducing the number of Si-O-Si linkages in the melt, eventually leading to the stabilization of olivine over pyroxene (Charlier et al., 2013; Hirschmann et al., 1998; Mysen, 1987). Because our low pressure observation is that olivine is the liquidus phase in the NAS_B experiments and pyroxene is the liquidus phase for the NAS_F experiments, we contend that the mineralogical differences between the two compositions can be largely attributed to the differences in Na rather than the differences

in oxygen fugacity between the NAS_F and NAS_B compositions. Furthermore, the NAS_F composition may not actually be representative of a mercurian composition, so we limited the number of experiments that were conducted to characterize the phase diagram for the NAS_F composition. Therefore, we present the experimental data for the experiments on the NAS_F composition, as is, without interpretation of the liquidus or mineral-in and mineral-out curves for lack of experimental constraints (Figure S3). In order to construct these curves accurately, additional experiments are needed.

As expected, the addition of alkalis depresses the liquidus of the melt and displaces the stability field of SiO_2 to higher pressures. SiO_2 is a liquidus phase at 0.4 GPa in the NAS_F composition, but it does not hit the liquidus until pressures greater than 3.5 GPa when alkali elements are present (NAS_B). Furthermore, the appearance of SiO_2 on the high pressure liquidus of the NAS_B composition may be an artifact of O diffusion into our capsules, which reacts with Si metal to increase the SiO_2 content of our experiments. When alkali elements are present, pyroxene and SiO_2 are replaced on the liquidus at low pressures by forsteritic olivine. The stability field of pyroxene is also extended at high pressure in the NAS_B composition compared to the NAS_F composition by the destabilization of garnet. Importantly, this pyroxene composition can have up to 7 wt% Na_2O in its structure. Based on the mineralogical differences between the NAS_F and NAS_B compositions, we conclude that the expected mantle and surface mineralogy of Mercury will be strongly dependent on the abundances of alkali elements present.

Although we have not yet conducted 1-bar experiments, the results of our lowest pressure phase equilibrium experiments can be combined with the CIPW norm calculations of the NVP composition from MESSENGER data (Table S1) as well as the

experimental results from Charlier et al. (2013) to infer the surface mineralogy of Mercury. Charlier et al., (2013) conducted 1-bar crystallization experiments at elevated oxygen fugacity (at the fayalite-magnetite-quartz buffer) on two different mercurian surface compositions and showed orthopyroxene, plagioclase, as well as minor olivine, clinopyroxene, and tridymite should be present on the mercurian surface. The results from our lowest pressure phase equilibrium experiments indicate that olivine, low-calcium, low-iron pyroxene, as well as plagioclase are likely to be primary silicate minerals on the surface of Mercury. However, if there are regions on the surface with low Na_2O (i.e. NAS_F composition) and SiO_2 abundances similar to the NVP, we expect the disappearance of olivine and the appearance of SiO_2. We also expect the presence of Fe-Mn-Ti-Cr sulfides as the dominant sulfides on Mercury, with minor Mg- or Ca-sulfides. The results from our two experimental starting compositions and the two compositions examined by Charlier et al. (2013) yield similar mineralogical results for 3 distinct regions on Mercury. Therefore, one can expect similar mineralogy across the surface of the planet if the melt compositions have the same general characteristics as those already studied experimentally (i.e. low Fe, high Si, and high S). Crystallization experiments on these and similar compositions at 1-bar over a range of oxygen fugacities are needed in order to confirm this predicted mineralogy.

6.2 Models for the origin of the NVP lavas

Partial melts in the Earth's upper mantle are typically controlled by eutectic melting of olivine and pyroxene. The point (in *P-T* space) on a phase diagram of a primary melt composition that corresponds to multiple saturation on the liquidus with the minerals expected to have remained in the source after melting (i.e., olivine and pyroxene

in Earth's upper mantle) is indicative of the average depth at which the melt separated from its source and rose to the surface (Asimow and Longhi, 2004). However, we do not have any insights into the expected mineralogy of the NVP source region, so we do not necessarily expect the *P*-*T* origin of the NVP lavas to correspond to one of the MSP's in the phase diagram (Figure 4). In fact, the sheer volume of lava that was erupted supports the possibility of high degrees of partial melting, which might favor melting out all but the dominant mantle mineral phase.

Additional insights into the interpretation of the phase equilibrium data for the NAS_B composition could be determined based on the elevated abundance of Na in the NVP lavas. Na is an incompatible large-ion lithophile element, and so its distribution within Mercury's interior is predictable for a given set of hypothetical scenarios for the thermal and magmatic evolution of Mercury. The formation mechanism of Mercury is unknown at present, but there are two end-member possibilities that we consider for predicting the distribution of incompatible lithophile elements in Mercury's interior. If the silicate portion of Mercury never fully melted, Mercury's full inventory of incompatible elements would be dispersed throughout its interior, probably in nearly chondritic abundances. This model for the evolution of Mercury's mantle and crust is analogous to studies that have used partial melting experiments of enstatite chondrite as an analogue for the melting of Mercury's interior (Malavergne et al., 2010; McCoy et al., 1999), where Mercury's mantle is assumed to have the composition of an enstatite chondrite. This model would be one way to explain the presence of alkalis at depth, which would support the possibility of the NVP forming from low degrees of partial melting deep within the mercurian mantle; however, we dismiss this model because it

would require that Mercury's mantle is composed of undifferentiated enstatite chondrite material, which is not consistent with Mercury's highly differentiated state. Consequently, this scenario is not well supported in the literature, so we consider it only as an end-member where Na is present throughout Mercury's mantle (enstatite chondrites typically have ~5800–6900 ppm Na; Lodders and Fegley, 1998).

It is generally accepted that Mercury experienced some form of a magma ocean event (Brown and Elkins-Tanton, 2009; Charlier et al., 2013; Riner et al., 2009). A mercurian mantle that experienced a magma ocean would likely host much of its inventory of incompatible elements near the surface of the planet, similar to what is generally expected for the lunar magma ocean (de Vries et al., 2010; Elardo et al., 2011; Elkins-Tanton et al., 2011; Rapp and Draper, 2012; Warren, 1985). Unlike the Moon, however, the low FeO content of Mercury's mantle would have prohibited the formation of a floatation crust consisting of silicate minerals (Vander Kaaden and McCubbin, 2015). Therefore, the last minerals to form during a crystallizing mercurian magma ocean would be concentrated near the surface of the planet instead of at the base of the primary crust as is the case for the Moon (de Vries et al., 2010; Elardo et al., 2011; Elkins-Tanton et al., 2011; Rapp and Draper, 2012; Warren, 1985). Furthermore, the low total FeO content of Mercury's mantle results in only minor density contrasts throughout the cumulate mantle (Vander Kaaden and McCubbin, 2015) and hence gravitational overturn of the mantle is unlikely to have occurred. Consequently, this inferred stratigraphy of incompatible elements concentrated towards the upper mantle/crust would be a permanent geochemical feature of a post magma ocean Mercury.

In the magma ocean scenario, the elevated abundance of Na in the NVP lavas is consistent with a shallow magmatic source region. Given that the first MSP in the NAS_B phase diagram is at 1.4 GPa, which corresponds to approximately one-quarter the depth of the mercurian mantle, we infer that the source for the NVP lavas had to be shallower than the first-observed MSP, and hence the low-pressure liquidus phase (olivine) was the only mineral left in the source during the partial melting event that produced the NVP lavas. This scenario is consistent with high degrees of partial melting (e.g., 15–30% melting for the Deccan Traps; Sen, 2001), which is potentially a common characteristic between flood volcanism on Mercury and flood volcanism on Earth (Coffin and Eldholm, 1994; Fedorenko et al., 2000; Fedorenko et al., 1996; Hooper and Hawkesworth, 1993; Peate, 1997; Sen, 2001; Takahahshi et al., 1998). In addition, a low pressure source region corresponds to the stability field of albitic plagioclase (Green and Hibberson, 1970), which could explain the elevated Na abundances even with high degrees of partial melting. The albitic plagioclase would have completely melted during partial melting to form the NVP lavas. The nepheline-normative characteristics of the NVP lavas, coupled with their elevated Cl^- abundances (Evans et al., 2015), indicate that sodalite may have also been a minor phase in the NVP source region. The primary shortcoming of this model is the source of heat for melting the upper mantle of Mercury at about 4.0 Ga (Thomas et al., 2014), although other small terrestrial bodies in the Solar System have demonstrably circumnavigated this problem, as shown in the number of igneous lunar samples from approximately the same period of time and younger (Elardo et al., 2014; Hiesinger et al., 2003; Hiesinger et al., 2000; Nyquist and Shih, 1992). This process could have been aided by a thermal boost from increased concentrations of incompatible

lithophile heat-producing elements in the upper mantle, although they could have also been sequestered in a putative FeS layer (McCubbin et al., 2012; Smith et al., 2012).

Alternatively, the NVP lavas could have formed by low degrees of partial melting, which would likely require that at least two phases remained in the mantle source after partial melting. In this scenario, we look to the 1.4 GPa MSP between olivine and orthopyroxene as being the probable depth of origin. In this scenario, the elevated Na abundance of the NVP lavas is a consequence of low degrees of partial melting and the preferential incorporation of Na into the partial melt. The primary shortcoming of this model comes in producing such a large volume of magma from low degrees of partial melting deep within the mercurian interior; however we do not see any reason to exclude this scenario from contention.

We can rule out the other MSPs as the average depth of melting based on mineralogical considerations. In a scenario where the average depth of melting is 2.7 GPa, jadeite and orthopyroxene remain in the source region after partial melting. This scenario requires the presence of a large amount of Na deep within the mercurian interior to stabilize a major Na-bearing phase. This would require that Mercury has a highly non chondritic silicate composition with a preponderance of Na, regardless of whether Mercury experienced a magma ocean. This scenario is too unlikely to be seriously considered and would require too many unrealistic caveats to pursue further. Consequently, this MSP is not likely to have any petrogenetic meaning for the NVP lavas or the mercurian interior in general. Therefore, our results favor the origin of the NVP lavas by high degrees of partial melting of an olivine-dominant, pyroxene- and albitic plagioclase-bearing mantle source at low pressure.

If the source region for the northern volcanic plains lavas is in fact dominated by forsteritic olivine, it calls into question models for Mercury's bulk composition that have used CB and enstatite chondrite bulk compositions (e.g., Brown and Elkins-Tanton, 2009; Malavergne et al., 2010; Morgan and Anders, 1980; Taylor and Scott, 2004), which indicate that Mercury's upper mantle is predominantly pyroxene as opposed to olivine. It is unclear to what extent the results from the present study can be applied to the bulk mineralogy of Mercury's upper mantle; however additional data are needed to constrain the bulk composition of Mercury, which is highly unconstrained at this time.

6.3 Partitioning of elements under highly reducing conditions

The reducing nature of Mercury has raised many questions regarding the geochemical behavior of lithophile elements in magmas at low oxygen fugacity on Mercury as well as other reducing bodies in the Solar System. In fact, interpretations of magmatic processes on Mercury are difficult at present because the number of experimental studies relevant to the extremely low fO_2 and high sulfur content of Mercury are very limited (Chabot et al., 2015, Chabot et al., 2014; Liu et al., 2007; Malavergne et al., 2007; Malavergne et al., 2004; McCoy et al., 1999; Ricolleau et al., 2011; Rose-Weston et al., 2009). At such reducing conditions, elements are likely to deviate from their typical geochemical behavior displayed at higher oxygen fugacity (e.g., Foley et al., 2005; McCoy et al., 1999; McCubbin et al., 2012). For example, lithophile elements such as Mg and Ca display chalcophile behavior in some highly reduced chondrites and achondrites forming the minerals oldhamite [(Ca,Mg,Fe,)S] and niningerite [(Mg,Fe,Mn)S] (McCoy et al., 1999). Other than the highly reduced enstatite chondrites and achondrites, we do not have many natural examples of what to expect

with respect to element behavior in such oxygen-starved systems. Fortunately, a number of experimental studies have reported on the distributions of elements among various phases at a range of oxygen fugacities, so it is possible to make some predictions about how, and under what conditions, certain elements would lose their lithophile behavior. Rose-Weston et al. (2009) looked at the effect of pressure, temperature, and oxygen fugacity on metal-silicate partitioning of numerous elements, including S, and observed that S becomes more siderophile with increasing *P* and less siderophile with increasing *T*. More recently, Chabot et al. (2015; 2014) have examined partitioning behavior in the Fe-S and Fe-S-O system. These studies, conducted between 1 atm and 9 GPa over the temperature range 1050–1600 °C, lead to three main conclusions: 1) pressure affects solid metal/liquid metal partitioning, 2) most elements show O-avoidance similar to their S-avoidance tendencies, and 3) none of the experiments were able to match the MESSENGER results for the Fe and S on Mercury's surface. Each of these studies has advanced our understanding of sulfur solubility and elemental partitioning during planetary differentiation; however, they have not explored highly reducing, sulfur bearing conditions that are as extreme as those observed on Mercury.

Experiments run using the NAS_B composition resulted in silicate, metal, and sulfide phases (Table 2). Although there is a wide range in *P-T-*fO_2 space of the experimental charges, we have calculated metal-silicate and sulfide-silicate partition coefficients for each charge, when applicable, using equation (3) below:

$$D^{A-B} = \frac{X_A}{X_B} \qquad (3)$$

where X_A is the mole fraction of element X in phase A (metal or sulfide) and X_B is the mole fraction of element X in phase B (silicate). Figure 5 shows the average D values for

each element in our experimental charges. The D values for Cl were calculated using the detection limit of Cl in our metals and sulfides, therefore providing an upper limit estimate for Cl. The error bars of each element represent the minimum and maximum D values across all of our NAS_B experiments. The geochemical affinity of a particular element is determined by the quadrant in which the average D value plots in Figure 5.

Our results indicate Al, Na, K, Mg, Ca, and Cl remain lithophile at all pressures and temperatures we investigated. However, Ca, Mg, and Na display limited chalcophile behavior over that of siderophile. Si does not display any evidence of chalcophile behavior, but it is both lithophile and siderophile. S remains chalcophile but also displays lithophile behavior at these conditions that out-competes its siderophile character. Ti, Mn, and Cr display chalcophile behavior at the fO_2 conditions we investigated. Ti and Cr are more siderophile than lithophile but Mn is more lithophile than siderophile. Our results also indicate that Fe loses its lithophile character at the conditions we investigated, and it is more siderophile than chalcophile. MESSENGER XRS data indicates a positive correlation between S and Ca abundances on the mercurian surface, leading to inferences that oldhamite is the dominant sulfide phase (Weider et al., 2014). Based on our experimental results, Ca and Mg would not be substantial components in sulfides on Mercury unless the abundance of Fe, Cr, Mn, and Ti were insufficient relative to available sulfide components in the system.

7. Conclusion

The surface of Mercury lacks spectral absorption features that can be used to definitively determine surface mineralogy by UV-VIS spectroscopy; however, our phase equilibrium results, previous mercurian phase equilibrium results (Charlier et al., 2013),

as well as CIPW norm calculations can be used to infer the mineralogy of Mercury's surface. The surface is likely dominated by forsteritic olivine, enstatitic pyroxene, and plagioclase. For regions of the surface with lower sodium and elevated SiO_2, orthopyroxene, plagioclase, and quartz or tridymite can be expected as stable surface minerals. Under the highly reducing conditions of Mercury, typically lithophile elements like Cr, Mn, and Ti become chalcophile and partition into sulfide phases. Consequently, Fe-, Cr-, Mn-, and Ti-bearing sulfides can be expected on the surface of Mercury with possible Mg- and Ca-bearing sulfides if Fe, Cr, Mn, and Ti are not present to bond with S^{2-}.

Partial melting of the mercurian interior resulted in flood volcanism that produced lavas with a bulk composition similar to terrestrial boninites, with notably higher abundances of alkalis. On Earth, boninites typically form in oxidized arc environments associated with subduction zones (Cameron et al., 1983; Hickey and Frey, 1982; Polat et al., 2002; Sobolev and Danyushevsky, 1994), but this is certainly not the case for the origin of mercurian boninites. Instead, our phase equilibrium results indicate they formed through partial melting of the shallow mercurian interior from a source region that consisted primarily of forsteritic olivine, orthopyroxene, and albitic plagioclase. Such a phase assemblage does not require the aid of water or oxidizing conditions to form boninitic melt compositions. Consequently, a new and novel boninite-formation mechanism within the Solar System may operate on Mercury. Furthermore, this process would represent a previously unrecognized mechanism for producing SiO_2-rich, secondary crustal materials on a planet without the aid of water or plate tectonics. The

results from this study further support Mercury as an endmember among the rocky planets in the Solar System.

Acknowledgements

Data reported in this paper including EPMA analyses of experimental charges are available in the Supporting Materials. The authors would like to thank Whitney McCutcheon for assisting in FTIR analyses and Alison Santos for helpful discussions and assisting in Multi-Anvil runs. We also thank the MESSENGER Science Team, with special thanks to the MESSENGER Geochemistry Discipline Group, for fruitful discussions regarding the interpretation of MESSENGER data. The authors also thank Rachel Klima for providing an estimate for the number of UV-VIS spectra collected by the MESSENGER spacecraft. We are appreciative of comments from Michael Toplis (A.E.), as well as reviewers Nancy Chabot, Karen Stockstill-Cahill, and an anonymous reviewer which helped to improve this manuscript. This work was funded by a NASA Cosmochemistry Grant NNX14AK43G to FMM. This work was also supported by a New Mexico Space Grant Consortium Fellowship and by NASA Headquarters under the NASA Earth and Space Science Fellowship Program-Grant NNX15AQ80H both awarded to KEVK.

References

Agee, C.B., Li, J., Shannon, M.C., and Circone, S. (1995) Pressure-temperature phase diagram for the Allende meteorite. J. Geophys. Res. Solid Earth, 100, 17725–17740.

Ardia, P., Hirschmann, M.M., Withers, A.C. and Stanley, B.D. (2013) Solubility of CH_4 in a synthetic basaltic melt, with applications to atmosphere-magma ocean-core partitioning of volatiles and to the evolution of the Martian atmosphere. Geochimica et Cosmochimica Acta 114, 52–71.

Asimow, P.D. and Longhi, J. (2004) The significance of multiple saturation points in the context of polybaric near-fractional melting. Journal of Petrology 45, 2349–2367.

Beattie, P. (1993) Olivine-melt and orthopyroxene-melt equilibria. Contributions to Mineralogy and Petrology 115, 103–111.

Beermann, O., Botcharnikov, R.E., Holtz, F., Diedrich, O. and Nowak, M. (2011) Temperature dependence of sulfide and sulfate solubility in olivine-saturated basaltic magmas. Geochimica et Cosmochimica Acta 75, 7612–7631.

Berger, J.A. (2012) Effect of halite and calcite coatings on thermal infrared spectra with implications for Mars exploration. M.S. Thesis, University of New Mexico.

Berthet, S., Malavergne, V. and Righter, K. (2009) Melting of the Indarch meteorite (EH4 chondrite) at 1 GPa and variable oxygen fugacity: Implications for early planetary differentiation processes. Geochimica et Cosmochimica Acta 73, 6402–6420.

Blewett, D.T., Vaughan, W.M., Xiao, Z., Chabot, N.L., Denevi, B.W., Ernst, C.M., Helbert, J., D'Amore, M., Maturilli, A., Head, J.W. and Solomon, S.C. (2013) Mercury's hollows: Constraints on formation and composition from analysis of geological setting and spectral reflectance. Journal of Geophysical Research-Planets 118, 1013–1032.

Brown, S.M. and Elkins-Tanton, L.T. (2009) Compositions of Mercury's earliest crust from magma ocean models. Earth and Planetary Science Letters 286, 446–455.

Burkemper, L.K., Agee, C.B. and Garcia, K.A. (2012) Constraints on core formation from molybdenum solubility in silicate melts at high pressure. Earth and Planetary Science Letters 335–336, 95–104.

Byrne, P.K., Klimczak, C., Sengor, A.M.C., Solomon, S.C., Watters, T.R., and Hauck, S.A., II (2014) Mercury's global contraction much greater than earlier estimates. Nature Geoscience 7, 301–307.

Cameron, W.E., McCulloch, M.T. and Walker, D.A. (1983) Boninite Petrogenesis: Chemical and Nd-Sr isotopic constraints. Earth and Planetary Science Letters 65, 75–89.

Campbell, I.H. and Taylor, S.R. (1983) No water, no granites, no oceans, no continents. Geophysical Research Letters 10, 1061–1064.

Carmichael, I.S.E., Nicholls, J. and Smith, A.L. (1970) Silica Activity in Igneous Rocks. The American Mineralogist 55, 246–263.

Chabot, N.L., Wollack, E.A. and Humayun, M. (2015) The effect of oxygen as a light element in metallic liquids on partitioning behavior. Meteoritics & Planetary Science 50(4), 530–546.

Chabot, N.L., Wollack, E.A., Klima, R.L. and Minitti, M.E. (2014) Experimental constraints on Mercury's core composition. Earth and Planetary Science Letters 390, 199–208.

Charlier, B., Grove, T.L. and Zuber, M.T. (2013) Phase equilibria of ultramafic compositions on Mercury and the origin of the compositional dichotomy. Earth and Planetary Science Letters 363, 50–60.

Coffin, M.F. and Eldholm, O. (1994) Large igneous provinces: Crustal structure, dimensions, and external consequences. Reviews of Geophysics 32, 1–36.

Cross, W., Iddings, J.P., Pirsson, L.V. and Washington, H.S. (1903) Quantitative classification of igneous rocks. University of Chicago Press.

Day, J.M.D., Ash, R.D., Liu, Y., Bellucci, J.J., Rumble, D., III, McDonough, W.F., Walker, R.J., and Taylor, L.A. (2009) Early formation of evolved asteroidal crust. Nature 457, 179–182.

de Vries, J., van den Berg, A. and van Westrenen, W. (2010) Formation and evolution of a lunar core from ilmenite-rich magma ocean cumulates. Earth and Planetary Science Letters 292, 139–147.

Denevi, B.W., Ernst, C.M., Meyer, H.M., Robinson, M.S., Murchie, S.L., Whitten, J.L., Head, J.W., Watters, T.R., Solomon, S.C., Ostrach, L.R., Chapman, C.R., Byrne, P.K., Klimczak, C. and Peplowski, P.N. (2013) The distribution and origin of smooth plains on Mercury. Journal of Geophysical Research-Planets 118, 891–907.

Dixon, J.E., Stolper, E.M. and Holloway, J.R. (1995) An experimental study of water and carbon dioxide solubilities in mid ocean ridge basaltic liquids .1. Calibration and solubility models. Journal of Petrology 36, 1607–1631.

Elardo, S.M., Draper, D.S. and Shearer, C.K. (2011) Lunar magma ocean crystallization revisited: Bulk composition, early cumulate mineralogy, and the source regions of the highlands Mg-suite. Geochimica et Cosmochimica Acta 75, 3024–3045.

Elardo, S.M., Shearer, C.K., Fagan, A.L., Borg, L.W., Gaffney, A.M., Burger, P.V., Neal, C.R., Fernandes, V.A. and McCubbin, F.M. (2014) The origin of young mare basalts inferred from lunar meteorites Northwest Africa 4734, 032, and LaPaz Icefield 02205. Meteoritics & Planetary Science 49, 261–291.

Elkins-Tanton, L.T., Burgess, S. and Yin, Q.Z. (2011) The lunar magma ocean: Reconciling the solidification process with lunar petrology and geochronology. Earth and Planetary Science Letters 304, 326–336.

Ernst, C.M., Murchie, S.L., Barnouin-Jha, O.S., Robinson, M.S., Denevi, B.W., Blewett, D.T., Head, J.W., Izenberg, N.R. and Solomon, S.C. (2010) Exposure of spectrally distinct material by impact craters on Mercury: Implications for global stratigraphy. Icarus 209, 210–223.

Evans, L.G., Peplowski, P.N., Killen, R.M., Potter, A.E. and Sprague, A.L. (2013) Variable Sodium on the Surface of Mercury: Implications for Surface CHemistry and the Exosphere., 44th Lunar and Planetary Science Conference, The Woodlands, TX, p. # 2033.

Evans, L.G., Peplowski, P.N., McCubbin, F.M., McCoy, T.J., Nittler, L.R., Zolotov, M.Y., Ebel, D.S., Lawrence, D.J., Starr, R.D., Weider, S.Z. and Solomon, S.C. (2015) Chlorine on the surface of Mercury: MESSENGER Gamma-Ray measurements and implications for the planet's formation and evolution. Icarus 257, 417–427.

Evans, L.G., Peplowski, P.N., Rhodes, E.A., Lawrence, D.J., McCoy, T.J., Nittler, L.R., Solomon, S.C., Sprague, A.L., Stockstill-Cahill, K.R., Starr, R.D., Weider, S.Z., Boynton, W.V., Hamara, D.K. and Goldsten, J.O. (2012) Major-element abundances on the surface of Mercury: Results from the MESSENGER Gamma-Ray Spectrometer. Journal of Geophysical Research-Planets 117, E00L07.

Fedorenko, V., Czamanske, G., Zen'ko, T., Budahn, J. and Siems, D. (2000) Field and Geochemical Studies of the Melilite-Bearing Arydzhangsky Suite, and an Overall Perspective on the Siberian Alkaline-Ultramafic Flood-Volcanic Rocks. International Geology Review 42, 769–804.

Fedorenko, V., Lightfoot, P.C., Czamanske, G.K., Hawkesworth, C.J., Wooden, J.L. and Ebel, D.S. (1996) Petrogenesis of the Siberian Flood-Basalt Sequence at Noril'sk. International Geology Review 38, 99–135.

Foley, C.N., Wadhwa, M., Borg, L.E., Janney, P.E., Hines, R. and Grove, T.L. (2005) The early differentiation history of Mars from W-182-Nd-142 isotope systematics in the SNC meteorites. Geochimica et Cosmochimica Acta 69, 4557–4571.

Green, D.H. and Hibberson, W. (1970) The instability of plagioclase in peridotite at high pressure. Lithos 3, 209–221.

Hauck II, S.A., Margot, J.L., Solomon, S.C., Phillips, R.J., Johnson, C.L., Lemoine, F.G., Mazarico, E., McCoy, T.J., Padovan, S., Peale, S.J., Perry, M.E., Smith, D.E. and Zuber, M.T. (2013) The curious case of Mercury's internal structure. Journal of Geophysical Research - Planets 118, 1204–1220.

Head, J.W., Chapman, C.R., Strom, R.G., Fassett, C.I., Denevi, B.W., Blewett, D.T., Ernst, C.M., Watters, T.R., Solomon, S.C., Murchie, S.L., Prockter, L.M., Chabot, N.L., Gillis-Davis, J.J., Whitten, J.L., Goudge, T.A., Baker, D.M.H., Hurwitz, D.M., Ostrach, L.R., Xiao, Z., Merline, W.J., Kerber, L., Dickson, J.L., Oberst, J., Byrne, P.K., Klimczak, C. and Nittler, L.R. (2011) Flood Volcanism in the Northern High Latitudes of Mercury Revealed by MESSENGER. Science 333, 1853–1856.

Hickey, R.L. and Frey, F.A. (1982) Geochemical characteristics of boninite series volcanics: Implications for their source. Geochimica et Cosmochimica Acta 46, 2099–2115.

Hiesinger, H., Head, J.W., Wolf, U., Jaumann, R. and Neukum, G. (2003) Ages and stratigraphy of mare basalts in Oceanus Procellarum, Mare Nubium, Mare Cognitum, and Mare Insularum. Journal of Geophysical Research-Planets 108.

Hiesinger, H., Jaumann, R., Neukum, G. and Head, J.W. (2000) Ages of mare basalts on the lunar nearside. Journal of Geophysical Research-Planets 105, 29239–29275.

Hirschmann, M.M., Baker, M.B., and Stolper, E.M. (1998) The effect of alkalis on the silica content of mantle-derived melts. Geochimica et Cosmochimica Acta 62, 883–902.

Holsclaw, G.M., McClintock, W.E., Robinson, M.S., Domingue, D.L., Izenberg, N.R., Blewett, D.T. and Sprague, A.L. (2010) A comparison of ultraviolet to near-infrared spectral properties of Mercury and the Moon as observed by MESSENGER. Icarus 209, 179–194.

Holzheid, A. and Grove, T.L. (2002) Sulfur saturation limits in silicate melts and their implications for core formation scenarios for terrestrial planets. American Mineralogist 87, 227–237.

Hooper, P.R. and Hawkesworth, C.J. (1993) Isotopic and Geochemical Constraints on the Origin and Evolution of the Columbia River Basalt Journal of Petrology 34, 1203–1246.

Irvine, T.N. and Baragar, W.R.A. (1971) A Guide to the Chemical Classification of the Common Volcanic Rocks. Canadian Journal of Earth Sciences 8(5), 523–548.

Izenberg, N.R., Klima, R.L., Murchie, S.L., Blewett, D.T., Holsclaw, G.M., McClintock, W.E., Malaret, E., Mauceri, C., Vilas, F., Sprague, A.L., Helbert, J., Domingue, D.L., Head, J.W., Goudge, T.A., Solomon, S.C., Hibbitts, C.A. and Dyar, M.D. (2014) The low-iron, reduced surface of Mercury as seen in spectral reflectance by MESSENGER. Icarus 228, 364–374.

Jolliff, B.L. (1991) Fragments of quartz monzodiorite and felsite in Apollo 14 soil particles. Proceedings of Lunar and Planetary Science 21, 101–118.

Jolliff, B.L., Floss, C., McCallum, I.S., and Schwartz, J.M. (1999) Geochemistry, petrology, and cooling history of 14161,7373: A plutonic lunar sample with textural evidence of granitic-fraction separation by silicate-liquid immiscibility. American Mineralogist 84, 821–837.

Krawczynski, M.J. and Grove, T.L. (2012) Experimental investigation of the influence of oxygen fugacity on the source depths for high titanium lunar ultramafic magmas. Geochimica et Cosmochimica Acta 79, 1–19.

Le Bas, M.J. (2000) IUGS Reclassification of the High-Mg and Picritic Volcanic Rocks. Journal of Petrology 41, 1467–1470.

Le Bas, M.J. and Streckeisen, A.L. (1991) The IUGS systematics of igneous rocks. Journal of the Geological Society, London 148, 825–833.

Le Maitre, R.W. (1984) A proposal by the IUGS Subcommission on the Systematics of Igneous Rocks for a chemical classification of volcanic rocks based on the total alkali silica (TAS) diagram. Australian Journal of Earth Sciences 31, 243–255.

Le Maitre, R.W., Streckeisen, A., Zanettin, B., Le Bas, M.J., Bonin, B., Bateman, P., Bellieni, G., Dudek, A., Efremova, S., Keller, J., Lameyre, J., Sabine, P.A., Schmid, R., Sorensen, H. and Woolley, A.R. (2002) Igneous Rocks: A Classification and Glossary of Terms. Cambridge University Press, New York, 236 pages.

Liu, Y., Samaha, N.-T. and Baker, D.R. (2007) Sulfur concentration at sulfide saturation (SCSS) in magmatic silicate melts. Geochimica et Cosmochimica Acta 71, 1783–1799.

Lodders, K. and Fegley, B. Jr. (1998) The Planetary Scientist's Companion, Oxford University Press, 400 pages, ISBN-13:978-0195116946.

Malavergne, V., Berthet, S. and Righter, K. (2007) Formation of CaS-MgS in enstatite chondrites and achondrites as a function of redox conditions and temperature: constraints on their evolution in a planetesimal and in a proto-planet 38th Lunar and Planetary Science Conference. Lunar and Planetary Institute, Houston, TX, p. Abstract #1737.

Malavergne, V., Cordier, P., Righter, K., Brunet, F., Zanda, B., Addad, A., Smith, T., Bureau, H., Surblé, S., Raepsaet, C., Charon, E. and Hewins, R.H. (2014) How Mercury can be the most reduced terrestrial planet and still store iron in its mantle. Earth and Planetary Science Letters 394, 186–197.

Malavergne, V., Siebert, J., Guyot, F., Gautron, L., Combes, R., Hammouda, T., Borensztajn, S., Frost, D. and Martinez, I. (2004) Si in the core? New high-pressure

and high-temperature experimental data. Geochimica et Cosmochimica Acta 68, 4201–4211.

Malavergne, V., Toplis, M.J., Berthet, S. and Jones, J. (2010) Highly reducing conditions during core formation on Mercury: Implications for internal structure and the origin of a magnetic field. Icarus 206, 199–209.

Mandeville, C.W., Webster, J.D., Rutherford, M.J., Taylor, B.E., Timbal, A. and Faure, K. (2002) Determination of molar absorptivities for infrared absorption bands of H2O in andesitic glasses. American Mineralogist 87, 813–821.

Mavrogenes, J.A. and O'Neill, H.S.C. (1999) The relative effects of pressure, temperature and oxygen fugacity on the solubility of sulfide in mafic magmas. Geochimica et Cosmochimica Acta 63, 1173–1180.

McCoy, T.J., Dickinson, T.L. and Lofgren, G.E. (1999) Partial melting of the Indarch (EH4) meteorite: A textural, chemical, and phase relations view of melting and melt migration. Meteoritics & Planetary Science 34, 735–746.

McCubbin, F.M., Riner, M.A., Vander Kaaden, K.E. and Burkemper, L.K. (2012) Is Mercury a volatile-rich planet? Geophysical Research Letters 39.

McCubbin, F.M., Vander Kaaden, K.E., Tartese, R., Boyce, J.W., Mikhail, S., Whitson, E.S., Bell, A.S., Anand, M., Franchi, I.A., Wang, J. and Hauri, E.H. (2015) Experimental investigation of F, Cl, and OH partitioning between apatite and Fe-rich basaltic melt at 1.0–1.2 GPa and 950–1000 °C. American Mineralogist 100, 1790–1802.

Médard, E. and Grove, T.L. (2008) The effect of H_2O on the olivine liquius of basaltic melts: experiments and thermodynamic models. Contributions to Mineralogy and Petrology 155, 417–432.

Morgan, J.W. and Anders, E. (1980) Chemical composition of Earth, Venus, and Mercury. Proceedings of the National Academy of Sciences of the United States of America 77, 6973–6977.

Moune, S., Holtz, F. and Botcharnikov, R.E. (2009) Sulphur solubility in andesitic to basaltic melts: implications for Hekla volcano. Contributions to Mineralogy and Petrology 157, 691–707.

Murchie, S.L., Klima, R.L., Denevi, B.W., Ernst, C.M., Keller, M.R., Domingue, D.L., Blewett, D.T., Chabot, N.L., Hash, C., Malaret, E., Izenberg, N.R., Vilas, F., Nittler, L.R. and Head, J.W. (2015) Orbital multispectral mapping of Mercury using the MESSENGER Mercury Dual Imaging System: Evidence for the origins of plains units and low-reflectance material. Icarus.

Murthy, V.M., van Westrenen, W. and Fei, Y.W. (2003) Experimental evidence that potassium is a substantial radioactive heat source in planetary cores. Nature 423, 163–165.

Mysen, B.O. (1987) Magmatic silicate melts: Relations between bulk composition, structure, and properties, in: Mysen, B.O. (Ed.), Magmatic Properties: Physicochemical Principles. Geochemical Society, University Park, PA, pp. 375–400.

Nittler, L., Weider, S. and Solomon, S.C. (2013) The Composition of Mercury's Crust from MESSENGER Observations. Mineralogical Magazine 77, 1856.

Nittler, L.R., Starr, R.D., Weider, S.Z., McCoy, T.J., Boynton, W.V., Ebel, D.S., Ernst, C.M., Evans, L.G., Goldsten, J.O., Hamara, D.K., Lawrence, D.J., McNutt, R.L.,

Schlemm, C.E., Solomon, S.C. and Sprague, A.L. (2011) The Major-Element Composition of Mercury's Surface from MESSENGER X-ray Spectrometry. Science 333, 1847–1850.

Nyquist, L.E. and Shih, C.Y. (1992) The isotopic record of lunar volcanism. Geochimica et Cosmochimica Acta 56, 2213–2234.

O'Neill, H.S.C. (1986) Mo-MoO_2 (MOM) oxygen buffer and the free energy of formation of MoO_2. American Mineralogist 71, 1007–1010.

O'Neill, H.S.C. and Eggins, S.M. (2002) The effect of melt composition on trace element partitioning: an experimental investigation of the activity coefficients of FeO, NiO, CoO, MoO_2 and MoO_3 in silicate melts. Chemical Geology 186, 151–181.

Ostrach, L.R., Robinson, M.S., Whitten, J.L., Fassett, C.I., Strom, R.G., Head, J.W. and Solomon, S.C. (2015) Extent, age, and resurfacing history of the northern smooth plains on Mercury from MESSENGER observations. Icarus 250, 602–622.

Papike, J.J., Karner, J.M. and Shearer, C.K. (2005) Comparative planetary mineralogy: Valence state partitioning of Cr, Fe, Ti, and V among crystallographic sites in olivine, pyroxene, and spinel from planetary basalts. American Mineralogist 90, 277–290.

Peate, D.W. (1997) The Parana-Etendeka Province, Large Igneous Provinces: Continental, Oceanic, and Planetary Flood Volcanism. The American Geophysical Union, pp. 217–245.

Peplowski, P.N., Evans, L.G., Hauck, S.A., McCoy, T.J., Boynton, W.V., Gillis-Davis, J.J., Ebel, D.S., Goldsten, J.O., Hamara, D.K., Lawrence, D.J., McNutt, R.L., Nittler, L.R., Solomon, S.C., Rhodes, E.A., Sprague, A.L., Starr, R.D. and Stockstill-Cahill, K.R. (2011) Radioactive Elements on Mercury's Surface from MESSENGER: Implications for the Planet's Formation and Evolution. Science 333, 1850–1852.

Peplowski, P.N., Evans, L.G., Stockstill-Cahill, K.R., Lawrence, D.J., Goldsten, J.O., McCoy, T.J., Nittler, L.R., Solomon, S.C., Sprague, A.L., Starr, R.D. and Weider, S.Z. (2014) Enhanced sodium abundance in Mercury's north polar region revealed by the MESSENGER Gamma-Ray Spectrometer. Icarus 228, 86–95.

Peplowski, P.N., Lawrence, D.J., Evans, L.G., Klima, R.L., Blewett, D.T., Goldsten, J.O., Murchie, S.L., McCoy, T.J., Nittler, L.R., Solomon, S.C., Starr, R.D. and Weider, S.Z. (2015) Constraints on the abundance of carbon in near-surface materials on Mercury: Results from the MESSENGER Gamma-Ray Spectrometer. Planetary and Space Science 108, 98–107.

Peplowski, P.N., Lawrence, D.J., Rhodes, E.A., Sprague, A.L., McCoy, T.J., Denevi, B.W., Evans, L.G., Head, J.W., Nittler, L.R., Solomon, S.C., Stockstill-Cahill, K.R. and Weider, S.Z. (2012) Variations in the abundances of potassium and thorium on the surface of Mercury: Results from the MESSENGER Gamma-Ray Spectrometer. Journal of Geophysical Research - Planets 117, E00L04.

Polat, A., Hofmann, A.W. and Rosing, M.T. (2002) Boninite-like volcanic rocks in the 3.7–3.8 Ga Isua greenstone belt, West Greenland: geochemical evidence for intra-oceanic subduction zone processes in the early Earth. Chemical Geology 184(3–4), 231–254.

Rapp, J.F. and Draper, D.S. (2012) Experimental fractional crystallization of the lunar magma ocean Lunar and Planetary Science Conference XLIII. Lunar and Planetary Institute, Woodlands, TX, p. 2048.

Ricolleau, A., Fei, Y., Corgne, A., Siebert, J. and Badro, J. (2011) Oxygen and silicon contents of Earth's core from high pressure metal-silicate partitioning experiments. Earth and Planetary Science Letters 310, 409–421.

Righter, K. and Drake, M.J. (1999) Effect of water on metal-silicate partitioning of siderophile elements: a high pressure and temperature terrestrial magma ocean and core formation. Earth and Planetary Science Letters 171, 383–399.

Riner, M.A., Lucey, P.G., Desch, S.J. and McCubbin, F.M. (2009) Nature of opaque components on Mercury: Insights into a Mercurian magma ocean. Geophysical Research Letters 36(2), .

Riner, M.A., McCubbin, F.M., Lucey, P.G., Taylor, G.J., and Gillis-Davis, J.J. (2010) Mercury surface composition: Integrating petrologic modeling and remote sensing data to place constraints on FeO abundance. Icarus 209, 301–313.

Rose-Weston, L., Brenan, J.M., Fei, Y.W., Secco, R.A. and Frost, D.J. (2009) Effect of pressure, temperature, and oxygen fugacity on the metal-silicate partitioning of Te, Se, and S: Implications for earth differentiation. Geochimica et Cosmochimica Acta 73, 4598–4615.

Santos, A.R., Agee, C.B., McCubbin, F.M., Shearer Jr, C.K., Burger, P.V., Tartèse, R. and Anand, M. (2015) Petrology of igneous clasts in Northwest Africa 7034: Implications for the petrologic diversity of the martian crust. Geochimica et Cosmochimica Acta 157, 56–85.

Sautter, V., Toplis, M.J., Wiens, R.C., Cousin, A., Fabre, C., Gasnault, O., Maurice, S., Forni, O., Lasue, J., Ollila, A., Bridges, J.C., Mangold, N., Le Mouelic, S., Fisk, M., Meslin, P.Y., Beck, P., Pinet, P., Le Deit, L., Rapin, W., Stolper, E.M., Newsom, H., Dyar, D., Lanza, N., Vaniman, D., Clegg, S. and Wray, J.J. (2015) In situ evidence for continental crust on early Mars. Nature Geoscience 8, 605–609.

Seddio, S.M., Jolliff, B.L., Korotev, R.L. and Zeigler, R.A. (2013) Petrology and geochemistry of lunar granite 12032,366–19 and implications for lunar granite petrogenesis. American Mineralogist 98, 1697–1713.

Sen, G. (2001) Generation of Deccan Trap Magmas. Proc. Indian Acad. Sci. (Earth Planet. Sci.) 110, 409–431.

Sharp, Z.D., McCubbin, F.M. and Shearer Jr, C.K. (2013) A hydrogen-based oxidation mechanism relevant to planetary formation. Earth and Planetary Science Letters 380, 88–97.

Siebert, J., Malavergne, V., Guyot, F., Combes, R. and Martinez, I. (2004) The behaviour of sulphu in metal-silicate core segregation experiments under reducing conditions. Physics of the Earth and Planetary Interiors 143–144, 433–443.

Smith, D.E., Zuber, M.T., Phillips, R.J., Solomon, S.C., Hauck, S.A., Lemoine, F.G., Mazarico, E., Neumann, G.A., Peale, S.J., Margot, J., Johnson, C.L., Torrence, M.H., Perry, M.E., Rowlands, D.D., Goossens, S., Head, J.W. and Taylor, A.H. (2012) Gravity Field and Internal Structure of Mercury from MESSENGER. Science.

Sobolev, A.V. and Danyushevsky, L.V. (1994) Petrology and geochemistry of boninites from the north termination of the Tonga Trench: Constraints on the generation

conditions of primary high-Ca boninite magmas. Journal of Petrology 35, 1183–1211.

Stockstill-Cahill, K.R., McCoy, T.J., Nittler, L.R., Weider, S.Z. and Hauck, S.A., III (2012) Magnesium-rich crustal compositions on Mercury: Implications for magmatism from petrologic modeling. Journal of Geophysical Research 117, E00L15.

Stolper, E.M., Baker, M.B., Newcombe, M.E., Schmidt, M.E., Treiman, A.H., Cousin, A., Dyar, M.D., Fisk, M.R., Gellert, R., King, P.L., Leshin, L., Maurice, S., McLennan, S.M., Minitti, M.E., Perrett, G., Rowland, S., Sautter, V., Wiens, R.C. and Team, M.S.L.S. (2013) The Petrochemistry of Jake_M: A Martian Mugearite. Science 341.

Takahahshi, E., Nakajima, K. and Wright, T.L. (1998) Origin of the Columbia River basalts: melting model of a heterogeneous plume head. Earth and Planetary Science Letters 162, 63-80.

Tauster, S.J., Pecoraro, T.A. and Chianelli, R.R. (1980) Structure and properties of molybdenum sulfide: Correlation of O_2 chemisorption with hydrosulfurization activity. Journal of Catalysis 63, 515–519.

Taylor, G.J. and Scott, E.R.D. (2004) Mercury, in: Davis, A.M. (Ed.), Treatise on Geochemistry: Meteorites, Comets, and Planets. Elsevier, Amsterdam, The Netherlands, pp. 477–485.

Thomas, R.J., Rothery, D.A., Conway, S.J. and Anand, M. (2014) Long-lived explosive volcanism on Mercury. Geophysical Research Letters 41, 6084–6092.

Vander Kaaden, K.E., Agee, C.B. and McCubbin, F.M. (2015) Density and compressibility of the molten lunar picritic glasses: Implications for the roles of Ti and Fe in the structures of silicate melts. Geochimica et Cosmochimica Acta 149, 1–20.

Vander Kaaden, K.E. and McCubbin, F.M. (2015) Exotic Crust Formation on Mercury: Consequences of a Shallow, FeO-poor Mantle. Journal of Geophysical Research – Planets 120, 195–209.

Wade, J. and Wood, B.J. (2005) Core formation and the oxidation state of the Earth. . Earth and Planetary Science Letters 236, 78–95.

Warren, P.H. (1985) The magma ocean concept and lunar evolution. Annual Review of Earth and Planetary Sciences 13, 201–240.

Weider, S.Z., Nittler, L.R., Starr, R.D., Crapster-Pregont, E.J., Peplowski, P.N., Denevi, B.W., Head, J.W., Byrne, P.K., Hauck II, S.A. and Solomon, S.C. (2015) Evidence for geochemical terranes on Mercury: The first global mapping of major elements on the surface of the innermost planet. Earth and Planetary Science Letters 416, 109–120.

Weider, S.Z., Nittler, L.R., Starr, R.D., McCoy, T.J. and Solomon, S.C. (2014) Variations in the abundance of iron on Mercury's surface from MESSENGER X-Ray Spectrometer observations. Icarus 235, 170–186.

Weider, S.Z., Nittler, L.R., Starr, R.D., McCoy, T.J., Stockstill-Cahill, K.R., Byrne, P.K., Denevi, B.W., Head, J.W. and Solomon, S.C. (2012) Chemical heterogeneity on Mercury's surface revealed by the MESSENGER X-Ray Spectrometer. Journal of Geophysical Research - Planets 117.

Yoder, H.S. and Tilley, C.E. (1962) Origin of basalt magmas: an experimental study of natural and synthetic rock systems. Journal of Petrology 3, 342–532.

Zolotov, M.Y., Sprague, A.L., Hauck, S.A., Nittler, L.R., Solomon, S.C. and Weider, S.Z. (2013) The redox state, FeO content, and origin of sulfur-rich magmas on Mercury. Journal of Geophysical Research-Planets 118.

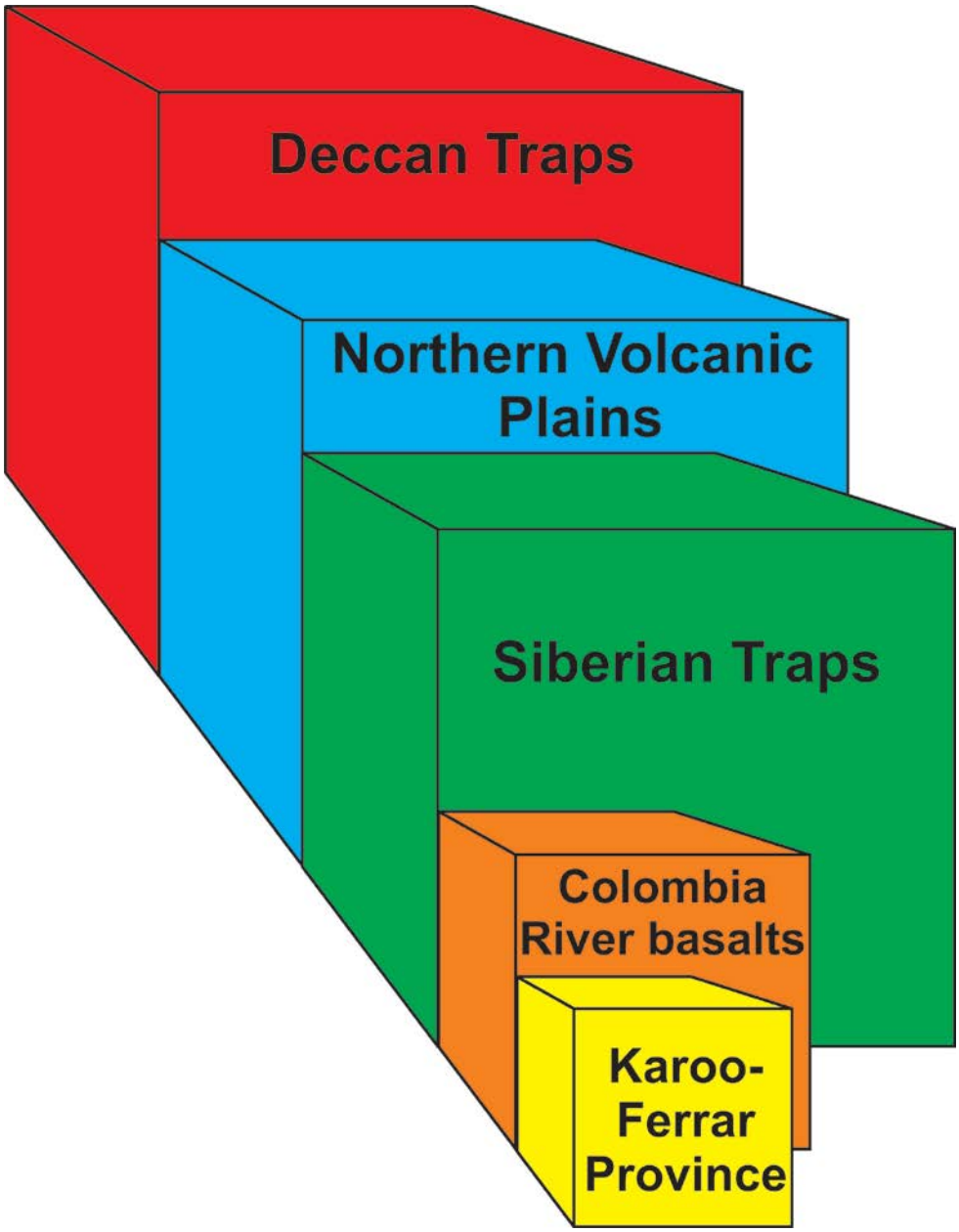

Figure 1. Volume of lava produced from the northern volcanic plains magma compared to common voluminous terrestrial magmas (Fedorenko et al., 2000; Fedorenko et al., 1996; Hooper and Hawkesworth, 1993; Peate, 1997; Sen, 2001; Takahahshi et al., 1998). Boxes are to scale for the average amount of lava produced (refer to text).

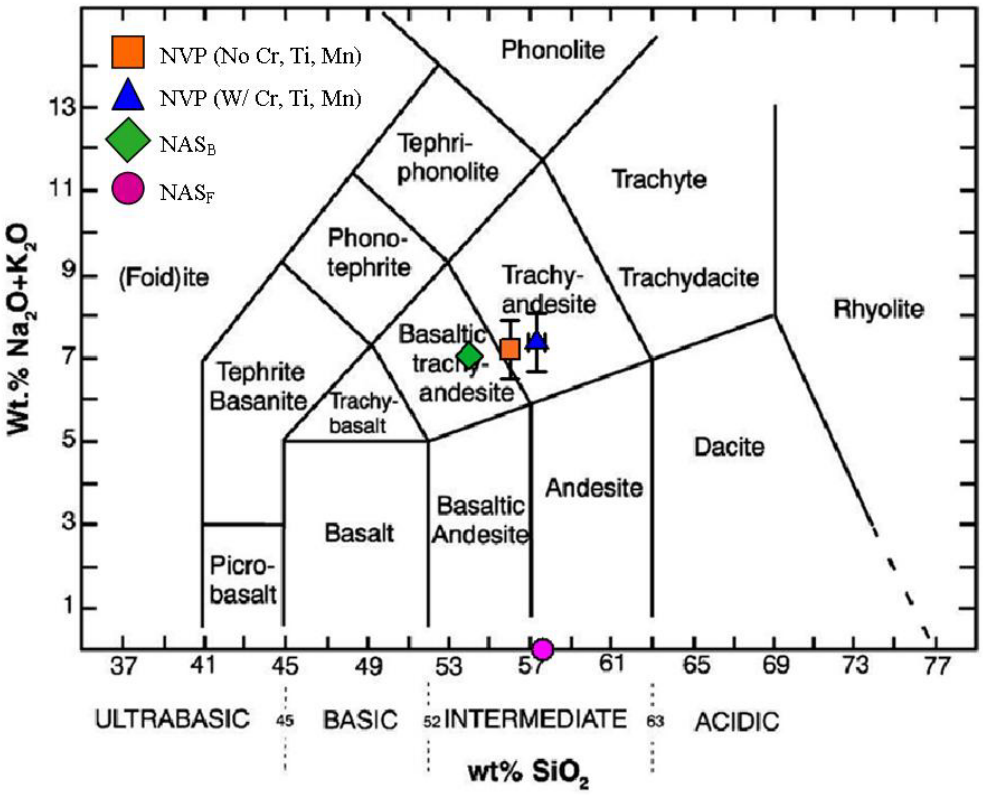

Figure 2. Total alkali vs. silica diagram for the calculated NVP compositions as well as the experimental starting material used in this study.

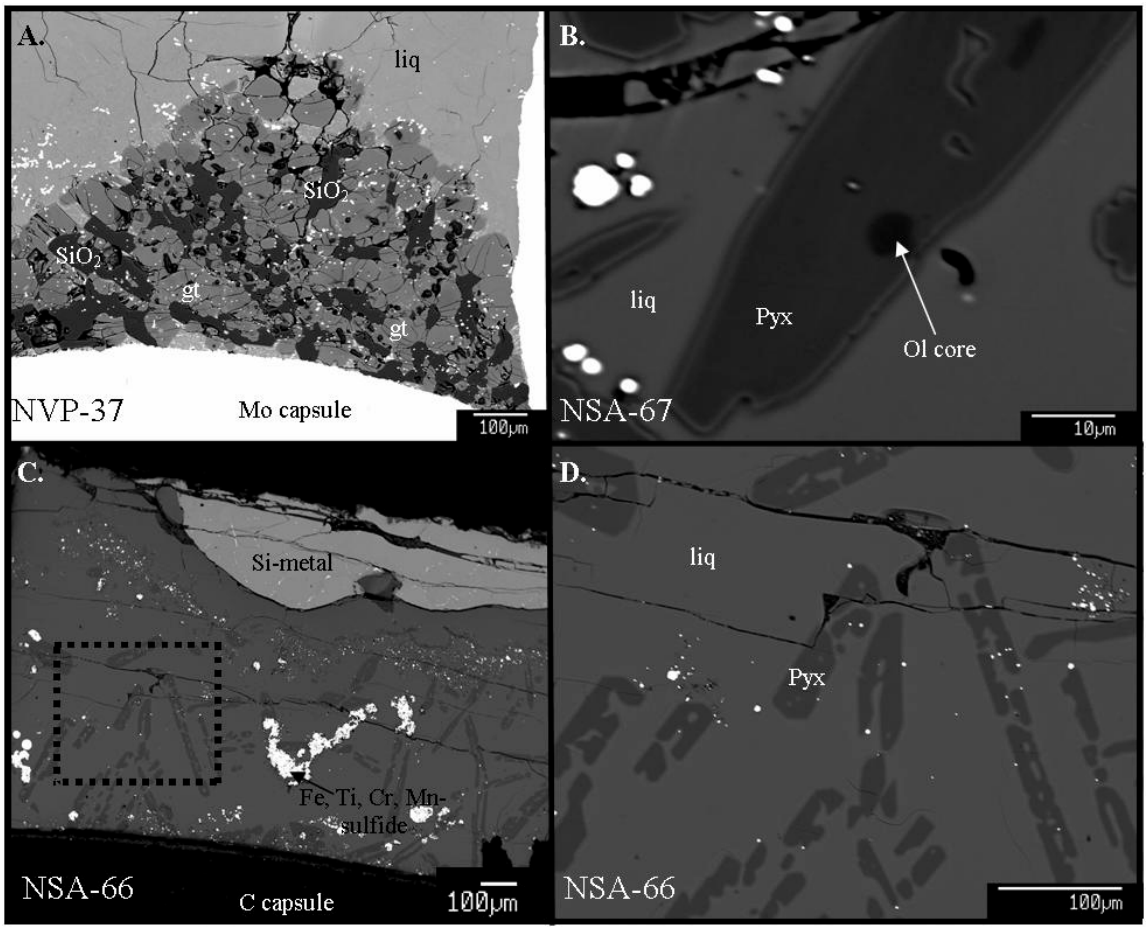

Figure 3. Backscattered electron images of select experimental run products. A) Experimental charge from the NAS_F composition (5 GPa, 1975 °C, 2 hours). B) Experimental charge from a subset of experiments not included in this study showing the result of oxygen diffusion into the capsule for experiments with run durations of longer than 4 hours (0.9 GPa, 1300 °C, 5 hours). C) Experimental charge from the NAS_B composition (1.7 GPa, 1360 °C, 4 hours). D) A zoomed in image of the dotted rectangular box in Figure 3C. Liq: liquid, SiO_2: silica phase, gt: garnet, pyx: pyroxene, ol: olivine, Mo: molybdenum capsule, C: graphite capsule.

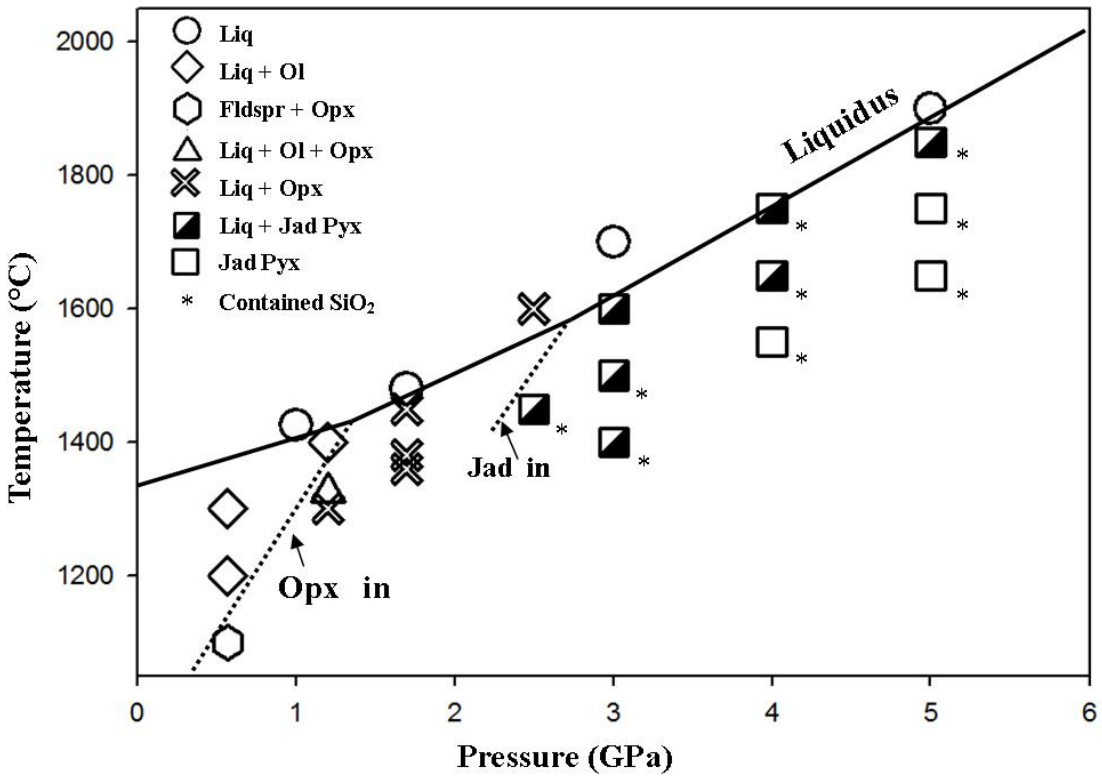

Figure 4. Experimental phase diagram for the NAS_B composition. The solid black line is the liquidus for this composition. The dotted lines are estimated mineral in lines. Each phase is given by a different symbol. There is a multiple saturation point between olivine and orthopyroxene at ~1.4 GPa and a multiple saturation point between orthopyroxene and jadeite-like pyroxene at ~2.7 GPa. The appearance of SiO_2 is most likely the result of O diffusion into our capsule reacting with Si metal.

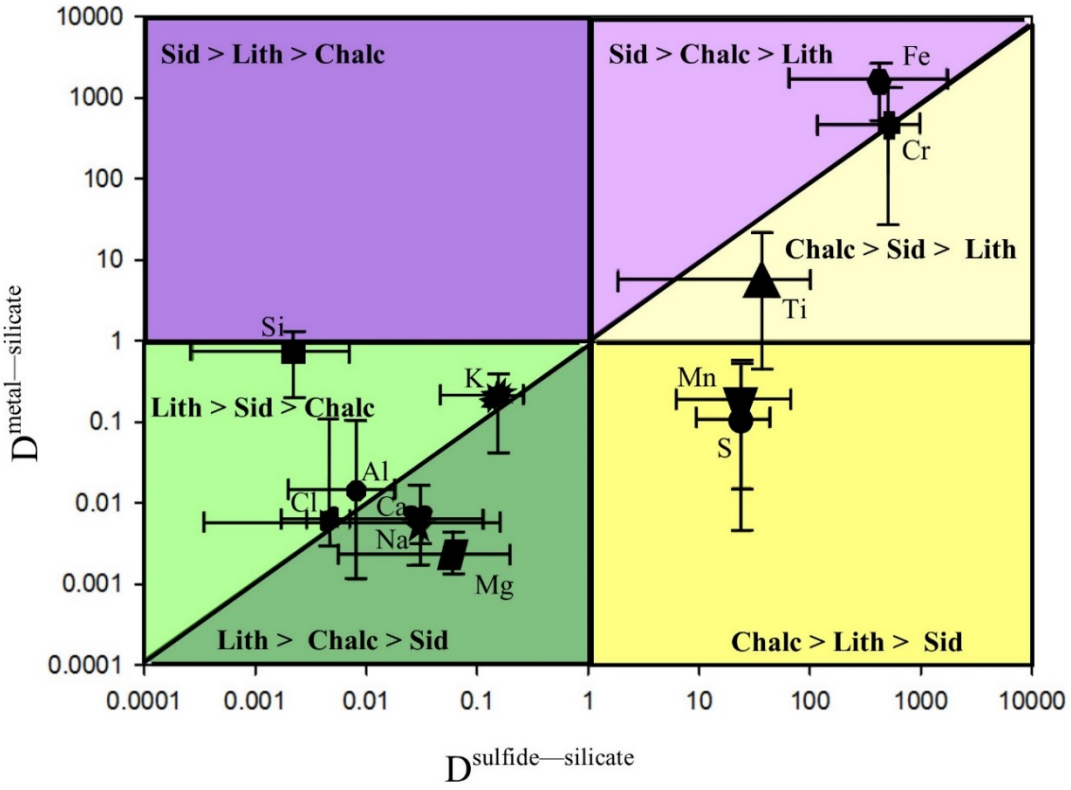

Figure 5. Elemental partitioning of elements from NAS_B experiments. The symbol for each element is the average D value from all of the experiments in Table S3-S4. The error bars represent the maximum and minimum D values from all experimental charges. The D values for Cl were calculated using the EPMA detection limits in the metals and sulfides. The affinity of an element is depicted by which region of the graph it falls in. Sid: Siderophile, Lith: Lithophile, Chalc: Chalcophile.

Table 1. Composition of the silicate starting materials used in this study in wt% (Nittler et al., 2013; Nittler et al., 2011; Peplowski et al., 2014; Weider et al., 2012).

	Average NVP*	Average NVP**	Alkali- and Sulfur-Free (NAS_F)	Alkali- and Sulfur-Bearing (NAS_B)	Equilibrated Starting Material (NSA-64)
SiO_2	57.37	56.11	57.76	54.09	57.03
TiO_2	0.00	0.81	1.35	1.26	1.14
Al_2O_3	13.98	13.68	13.47	12.61	11.63
CrO	0.00	0.69	0.71	0.66	0.11
FeO	1.03	1.01	5.21	0.00	0.06
MgO	15.56	15.22	15.22	14.26	16.67
MnO	0.00	0.68	0.69	0.65	0.52
CaO	4.20	4.11	5.58	5.23	5.90
Na_2O	7.16	7.01	0.00	6.82	5.03
K_2O	0.22	0.22	0.00	0.25	0.17
FeS	0.00	0.00	0.00	4.16	0.00
S^{2-}	0.94	0.92	0.00	0.00	1.31
Cl^-	0.00	0.00	0.00	0.00	1.40
^-O=S+Cl	0.46	0.47	0.00	0.00	0.97
Total	100.00	100.00	100.00	100.00	100.00

***Average composition without Cr, Ti, Mn.**
****Average composition using upper limits for Cr, Ti, Mn**

Table 2. Table of experimental run conditions and results.

Run	Capsule	P (GPa)	Superliq (°C)	Superliq (min)	T (°C)	Duration (Hours)	Phase Assemblage	ΔIW*	ΔSi-SiO_2 †
NVP-45	Mo^0	0.57	----	----	1300	2	Lq, $En_{90}Fs_8Wo_2$, SiO_2	-2.67^	----
NVP-40	Mo^0	0.57	----	----	1360	0.375	Lq, $En_{91}Fs_7Wo_2$, SiO_2	-2.71^	----
NVP-42	Mo^0	0.57	----	----	1375	1.05	Lq	-2.73^	----
NVP-20	Mo^0	1.2	----	----	1350	2	Lq, $En_{89}Fs_9Wo_2$, SiO_2	-2.66^	----
NVP-10	Mo^0	3	----	----	1700	1	Lq, $En_{90}Fs_2Wo_8$, SiO_2, $Py_{82}Al_{11}Gr_7$	-2.69^	----
NVP-14	Mo^0	3	----	----	1800	1	Liq	-2.75^	----
NVP-44	Mo^0	3.5	----	----	1350	3	$En_{87}Fs_{10}Wo_3$, SiO_2, $Py_{69}Al_{17}Gr_{14}$	----	----
NVP-27	Mo^0	3.5	----	----	1800	2	Lq, $Py_{82}Al_{11}Gr_7$, SiO_2	-2.56^	----
NVP-29	Mo^0	3.5	----	----	1875	2	Lq, $Py_{85}Al_{10}Gr_5$, SiO_2	-2.72^	----
NVP-21	Mo^0	4	----	----	1800	2	Lq, $Py_{82}Al_{11}Gr_7$, SiO_2	-2.55^	----
NVP-26	Mo^0	4	----	----	1850	2	Lq, $Py_{84}Al_{10}Gr_6$, SiO_2	-2.65^	----
NVP-31	Mo^0	4	----	----	1900	2	Lq, $Py_{85}Al_{10}Gr_5$, SiO_2	-2.66^	----
NVP-35	Mo^0	4	----	----	1950	2	Lq	-2.74^	----
NVP-15	Mo^0	5	----	----	1850	2	Lq, $En_{66}Fs_9Wo_{25}$, $Py_{74}Al_{13}Gr_{13}$, SiO_2	-2.24^	----
NVP-17	Mo^0	5	----	----	1950	2	Lq, $Py_{85}Al_{10}Gr_6$, SiO_2	-2.70^	----
NVP-37	Mo^0	5	----	----	1975	2	Lq, $Py_{81}Al_{11}Gr_8$, SiO_2	-2.62^	----
NVP-22	Mo^0	5	----	----	2000	2	Liq	-2.76^	----
NSA-11	C	0.57	1300	18	1100	4	Plg, En-rich, Mtl, Sfd	----	----
NSA-14	C	0.57	1350	4	1200	24	Lq, Fo_{100}, SiC, Mtl, Sfd	-6.57	-0.20
NSA-34	C	0.57	----	----	1300	4	Lq, $Fo_{99.5}Fa_{0.5}$, Mtl, Sfd	----	-0.21
NSA-64	C	1.0	----	----	1425	4	Lq, Mtl	----	-0.27
NSA-23	C	1.2	----	----	1300	21.7	Lq, $En_{96}Fs_1Wo_3$, Mtl, Sfd	----	-0.21
NSA-25	C	1.2	----	----	1325	8	Lq, Fo_{100}, $En_{97}Fs_0Wo_3$, SiC, Mtl	-6.86	-0.23
NSA-27	C	1.2	----	----	1400	4	Lq, Fo-rich, SiC, Mtl	-6.94	-0.21
NSA-66	C	1.7	1450	60	1360	4	Lq, $En_{97}Fs_1Wo_2$, Mtl, Sfd	----	-0.24
NSA-65	C	1.7	1450	0.3	1380	24	Lq, $En_{97}Fs_1Wo_2$, Mtl, Sfd	----	-0.21
NSA-71	C	1.7	----	----	1450	4	Lq, $En_{97}Fs_1Wo_2$, Mtl	-5.29	-0.26
NSA-70	C	1.7	----	----	1480	4	Lq, Mtl, Sfd		-0.22
NSA-36	C	2.5	----	----	1450	4	Lq, $En_{85}Fs_2Wo_{13}$, SiO_2, Mtl, Sfd	-5.66	-0.15
NSA-29	C	2.5	----	----	1600	4	Lq, $En_{97}Fs_0Wo_3$, SiC, Mtl	-6.33	-0.19
NSA-13	C	3	1700	10	1400	4	Lq, $En_{85}Fs_0Wo_{15}$, SiO_2, SiC, Mtl, Sfd	----	-0.13
NSA-21	C	3	1750	10	1600	4	Lq, $En_{89}Fs_0Wo_{11}$, SiC, Mtl	-6.34	-0.18
NSA-10	C	3	1700	10	1500	4	Lq, $En_{88}Fs_0Wo_{12}$, $En_{81}Fs_0Wo_{19}$, SiO_2, SiC, Mtl, Sfd	-5.28	-0.13
NSA-17	C	3	1800	3.5	1700	4	Lq , SiC, Mtl	-5.75	-0.18
NSA-9	C	4	1750	10	1550	4	$En_{82}Fs_0Wo_{18}$, SiO_2, SiC, Mtl, Sfd	----	0.00
NSA-8	C	4	1750	10	1650	4	Lq, $En_{79}Fs_2Wo_{19}$, SiO_2, SiC, Mtl, Sfd	----	0.00

NSA-15	C	4	1950	10	1750	4	Lq, $En_{82}Fs_{0}Wo_{18}$, SiO_2, SiC, Mtl, Sfd	-7.05	-0.19
NSA-12	C	5	1850	10	1650	4	$En_{78}Fs_{3}Wo_{19}$, SiO_2 , Mtl, Sfd	----	0.00
NSA-24	C	5	1850	10	1750	4	$En_{80}Fs_{2}Wo_{18}$, SiO_2, SiC, Mtl, Sfd	----	0.00
NSA-28	C	5	1900	10	1850	4	Lq, $En_{81}Fs_{1}Wo_{18}$, SiO_2, SiC, Mtl, Sfd	----	0.00
NSA-18	C	5	1900	3.5	----	----	Lq , SiC, Mtl	-6.79	-0.22

Abbreviations are as follows: Liquid (lq), Plagioclase (Plg), Olivine (ol) Pyroxene (pyx), Garnet (gt), Silicon Carbide (SiC), Metals (Mtl), Sulfides (Sfd).
***Oxygen fugacity calculated using Fe-rich metal.**
†Oxygen fugacity calculated using Si-rich metal.
^Oxygen fugacity is more oxidizing than this value.

10. Appendix A: Supplementary Materials

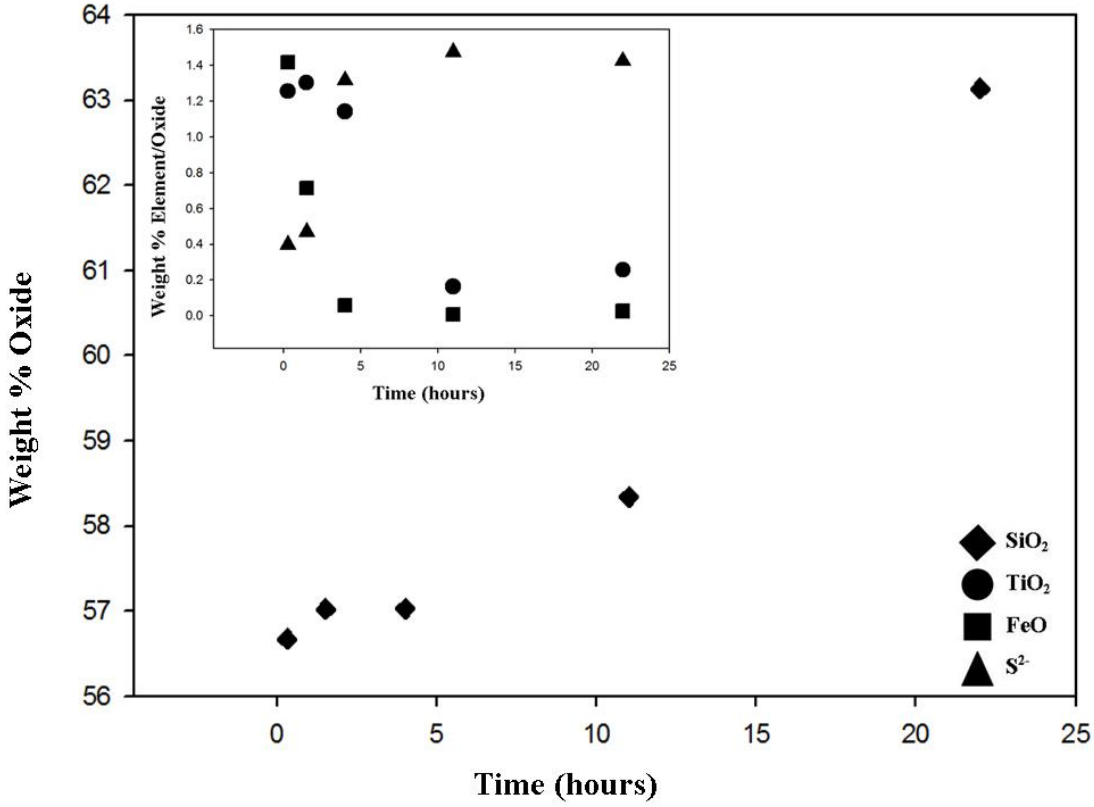

Figure S1. Experimental results for certain oxides and elements of interest in the silicate melt. Each element/oxide is given by a different symbol. The reader is referred to Section 2.2.4 for full discussion of this figure.

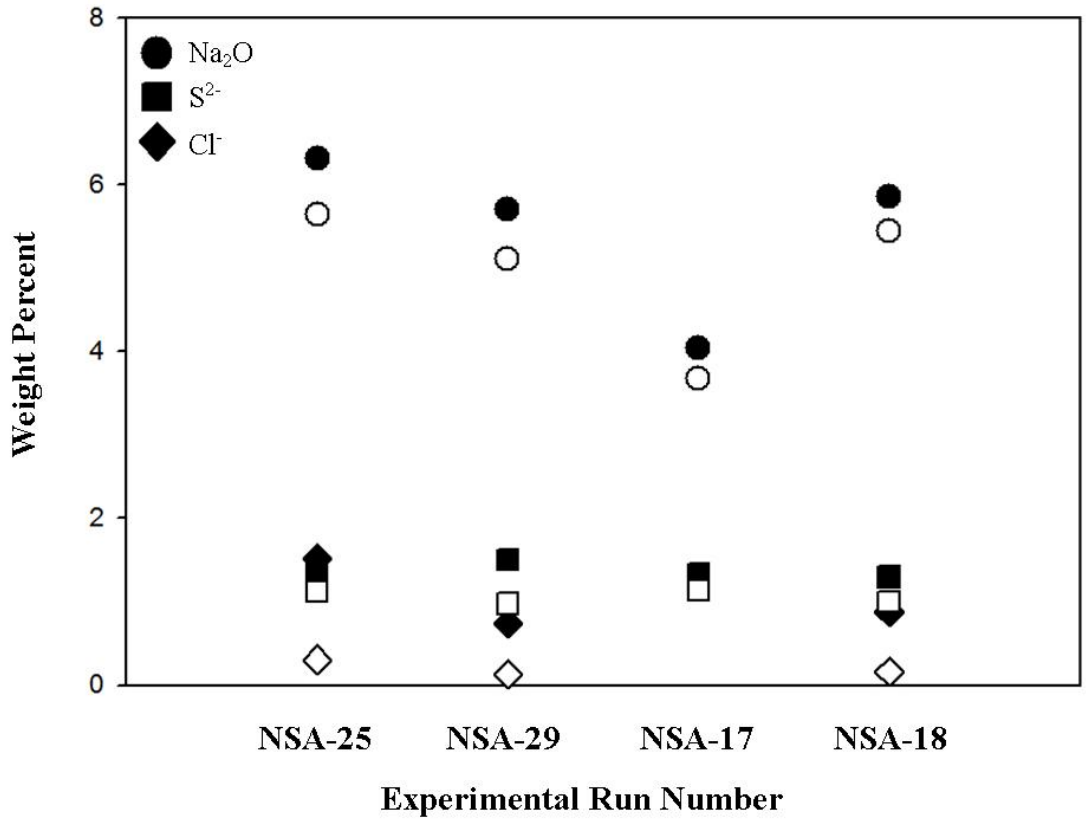

Figure S2. The effect of water and acetone on volatile elements in the silicate melt. The filled symbols represent results from samples polished using only hexagonal boron nitride and the open symbols represent results from samples polished using water and rinsed in acetone prior to FTIR analysis.

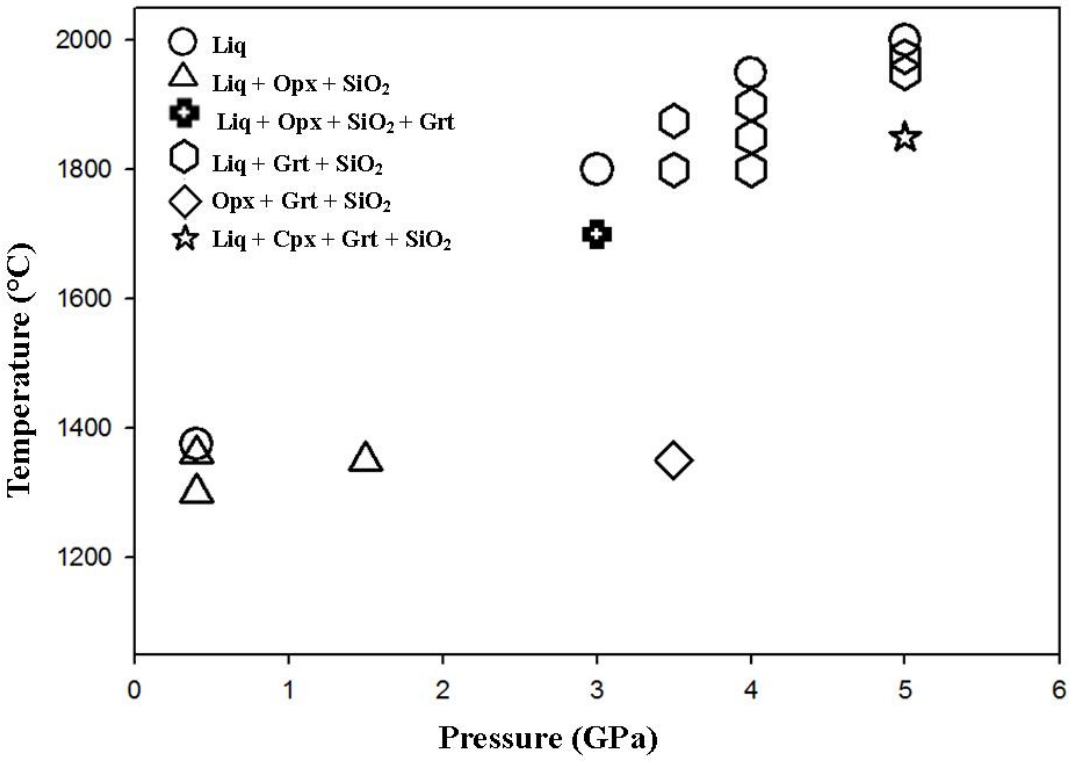

Figure S3. Experimental phase diagram for the NAS_F composition. Each phase is given by a different symbol. The liquidus and mineral in lines have been omitted due to lack of experimental constraints. Orthopyroxene and SiO_2 are the liquidus phases at low pressure. Garnet replaces orthopyroxene on the liquidus at pressures >3 GPa.

Table S1. CIPW norm calculations for Northern Volcanic Plains Compositions

Composition without Cr, Mn, or Ti		**Composition with Cr, Mn, or Ti**	
Phase	***wt %***	***Phase***	***wt %***
FeS	1.26	FeS	1.26
MgS	0.41	CrS	0.65
CaS	0.54	MnS	0.62
Plagioclase	59.06	Plagioclase	57.24
Orthoclase	1.3	Orthoclase	1.3
Nepheline	3.73	Nepheline	3.91
Diopside	10.43	Diopside	10.16
Olivine	23.26	Olivine	23.44
		Ilmenite	0.39
		Perovskite	1.03

Table S2.

This table can be downloaded from the Electronic Annex 2: Supplementary Tables File http://www.sciencedirect.com/science/article/pii/S0016703715005980

Table S3.

This table can be downloaded from the Electronic Annex 2: Supplementary Tables File http://www.sciencedirect.com/science/article/pii/S0016703715005980

Table S4.

This table can be downloaded from the Electronic Annex 2: Supplementary Tables File http://www.sciencedirect.com/science/article/pii/S0016703715005980

Chapter 4

Sulfur Solubility in Silicate Melts Under Highly Reducing Conditions as Seen on Mercury

In collaboration with

Francis M. McCubbin[1,2]

[1]Institute of Meteoritics, Department of Earth & Planetary Sciences, University of New Mexico, Albuquerque, NM 87131, USA. [2]NASA Johnson Space Center, Mailcode XI2, 2101 NASA Parkway, Houston, TX 77058, USA.

Abstract

Since the return of data from the MErcury Surface, Space ENvironment, GEochemistry and Ranging spacecraft (MESSENGER), the surface of Mercury has been shown to have elevated abundances of magmatic volatiles, including sulfur. In order to determine the sulfide concentration at sulfide saturation (SCSS) in mercurian-like melts, sulfide solubility experiments in silicate melts were conducted on a synthetic rock composition matching that of the northern volcanic plains on Mercury as well as a synthetic diopside composition for comparison with a simpler system. SCSS piston-cylinder experiments were run at 0.5 GPa and 1.0 GPa in the temperature range of 1300 °C – 1600 °C, with run durations of 2–22 hours. SCSS multi-anvil experiments on the NVP and diopside compositions were run at 4 GPa in the temperature range of 1750 °C – 2050 °C, with run durations of 0.025–4 hours. The addition of Si-metal to each experimental charge set the oxygen fugacity of these experiments between ΔIW-3.4 and ΔIW-7.1, consistent with estimates of the oxygen fugacity of Mercury. The SCSS in the silicate portion of the experimental charges ranged from 1.23 wt% S to 17.02 wt% S, showing an increase in S-solubility with decreasing oxygen fugacity. Furthermore, our experimental results show sulfide solubility in silicate melts is dependent on pressure,

temperature and, to a lesser extent, melt composition. If the reducing conditions determined by the mercurian surface compositions were present during the planets formation, these experimental results are consistent with transport of S towards the surface because of the high carrying capacity for S in reduced melts and the incompatibility of S in rock-forming silicates.

Key Words: MESSENGER, northern volcanic plains, solubility, oxygen fugacity

1. Introduction

Prior to the return of data from the MErcury Surface, Space ENvironment, GEochemistry and Ranging (MESSENGER) spacecraft, the planet Mercury was thought to be depleted in volatile elements mainly due to its close proximity to the sun (Albarede, 2009). Flybys from the Mariner 10 mission confirmed the presence of atmospheric H, He, and O (Broadfoot et al., 1974; Broadfoot et al., 1976). Ground-based discoveries enhanced our knowledge about Na, K, and Ca in the atmosphere (Bida et al., 2000; Potter and Morgan, 1985, 1986) as well as polar volatiles found in radar-reflective deposits (Harmon and Slade, 1992; Slade et al., 1992). Although there was some evidence for the presence of volatiles on the surface of the planet and in the exosphere, it was not until the return of data from MESSENGER that we discovered just how volatile rich Mercury is (Evans et al., 2015; Murchie et al., 2015; Nittler et al., 2011; Peplowski et al., 2014; Peplowski et al., 2016; Peplowski et al., 2015; Peplowski et al., 2012; Weider et al., 2012).

New data from the X-Ray Spectrometer (XRS) and Gamma-Ray Spectrometer (GRS) onboard the MESSENGER spacecraft has shown the surface of the planet has elevated abundances of magmatic volatiles including S (Nittler et al., 2011; Weider et al., 2012), K (Peplowski et al., 2012), Na (Peplowski et al., 2014), C (Murchie et al., 2015; Peplowski et al., 2016; Peplowski et al., 2015), and Cl (Evans et al., 2015). Furthermore, MESSENGER XRS data has shown that the surface of the planet is depleted in Fe (Nittler et al., 2011; Weider et al., 2012). Although the presence of all volatiles on the surface of the planet has important implications for the thermal and magmatic evolution of Mercury, the volatile of importance for the current study is sulfur.

Sulfur contents on the mercurian surface have been measured to be ~ 4 wt% (Nittler et al., 2011), which far exceeds the solubility of S^{2-} in silicate liquids in terrestrial systems (e.g., Wallace and Carmichael, 1992; Wallace and Edmonds, 2011; Wykes et al., 2015). On Earth, sulfur contents in silicate liquids are typically less than 1 wt% with no clear trend between basaltic and rhyolitic melts (Wallace and Edmonds, 2011). Instead, the main driver of S concentration in silicate melts appears to be the amount of FeO in the melt (Wallace and Edmonds, 2011; Wykes et al., 2015). With 8–10 wt% FeO, typical MORB pillow rim glasses and melt inclusions contain 800–1300 ppm S (Wallace and Edmonds, 2011 and references therein). Increasing the amount of FeO to 15–16 wt% in these glasses and melt inclusions results in S abundances of 2000–2400 ppm (Wallace and Edmonds, 2011 and references therein). In comparison, basaltic arc magmas contain 900–2500 ppm S on average, with values extending to as high as 7000 ppm as measured in olivine-hosted melt inclusions (Wallace and Edmonds, 2011 and references therein). The concentrations of S present in the source regions of these materials range from 250–

500 ppm S for mafic arc magmas (de Hoog et al., 2001; Metrich et al., 1999), 150–190 ppm S for MORB (Saal et al., 2002 and references therein), and 70–240 ppm S for primitive mantle (Lorand et al., 2003; Palme and O'Neill, 2004). In contrast to the conditions typically observed on Earth, it has also been shown that sulfide solubility in silicate melts increases with decreasing oxygen fugacity (fO_2) (Berthet et al., 2009; Holzheid and Grove, 2002; Malavergne et al., 2007; Mavrogenes and O'Neill, 1999; McCoy et al., 1999). This fact, coupled with the high S content and low Fe contents has resulted fO_2 estimates of Mercury to be approximately 3 to 7 $\log_{10}$ units below the IW buffer (ΔIW-3 to ΔIW-7) (McCubbin et al., 2012; Zolotov et al., 2013), orders of magnitude lower than the fO_2 on the Earth, Moon, and Mars (i.e., Sharp et al., 2013). Much of our geochemical understanding of elements in natural systems comes from empirical observations of terrestrial rocks and other planetary bodies, which may not apply to a planet as reduced as Mercury. Any broad geochemical interpretations that are rooted in these empirical observations may be misguided when applied to Mercury because at such reducing conditions, elements are likely to deviate from their typical geochemical behavior displayed at higher oxygen fugacity as shown by Vander Kaaden and McCubbin (2016).

On Mercury, sulfur is likely to play an extremely different role in magmatic systems than what is seen on Earth as it will display both lithophile and chalcophile tendencies. Our investigation will focus on the controls of sulfide solubility in silicate melts under highly reducing conditions. We will explore S solubility using the composition of the northern volcanic plains (NVP) lavas which are smooth plains covering 12 % of the surface area of the northern hemisphere of Mercury and are less cratered than their

surroundings, suggesting they are volcanic in origin (Head et al., 2011; Ostrach et al., 2015). These lavas are the most likely example of a lava that can be compositionally assessed from orbit making them the best candidate to study S solubility experimentally. The role of S during planetary differentiation on Mercury will be inferred by investigating S concentrations at sulfide saturation (SCSS) in silicate magmas as a function of pressure, temperature, and oxygen fugacity.

2. Methods

2.1 Starting Materials

The synthetic starting materials (Table 1) used to investigate SCSS in this study were prepared at the Institute of Meteoritics (IOM) at the University of New Mexico (UNM) using high-purity reagent grade powdered oxides, silicates, and sulfides, which were mixed sequentially by increasing volume and ground under ethanol using an automated agate mortar and pestle. All of the Fe in each experiment was added as FeS. The starting materials were allowed to dry completely and kept in either a desiccator or a drying oven at 100 °C before use in each experiment.

2.2 Capsule Material and Oxygen Fugacity

Careful consideration of capsule material was required for running all experiments in this study because capsules that would not react with the melt components, including sulfur and Si metal, was required, so many metal capsule materials (Mo^0 and Fe^0) were ruled out due to their demonstrated affinity for sulfur (e.g., Tauster et al., 1980). Additionally, sulfide solubility increases in silicate melts with decreasing oxygen fugacity (Beermann et al., 2011; Berthet et al., 2009; Holzheid and Grove, 2002; Malavergne et al., 2007; Malavergne et al., 2014; Mavrogenes and O'Neill, 1999; McCoy

et al., 1999; Moune et al., 2009; Zolotov et al., 2013), so the experiments were run under low oxygen fugacity to promote S-dissolution into the silicate melt for the SCSS experiments. Furthermore, McCubbin et al. (2012) and Zolotov et al. (2013) have shown the oxygen fugacity of Mercury is between 7 and 3 $\log_{10}$ units below the IW buffer, so highly reducing conditions provide a more realistic representation of the interior of Mercury. Graphite minimally reacts with silicate liquids especially under reducing conditions (Ardia et al., 2013) and has not demonstrated an affinity for S, so it was chosen as the capsule material for all SCSS experiments conducted in this study.

Graphite capsules are incapable of controlling oxygen fugacity much below the graphite-CO buffer, so we needed to add an additional component to the experiments to promote reducing conditions. Consequently, oxygen fugacity was lowered in each SCSS experimental charge by adding Si metal to the bottom of each capsule, similar to the procedure of Siebert et al. (2004), Rose-Weston et al. (2009), and Vander Kaaden and McCubbin (2016). Therefore, the SCSS experiments were conducted within a $\log_{10}$ unit of the Si-SiO_2 oxygen fugacity buffer, which is within the range reported for Mercury over the temperature range of our experiments.

2.3 Piston Cylinder (PC) Experimental Methods

Experiments for pressures ≤1.0 GPa were run in the PC using the procedures, parts, and calibrations described previously in Vander Kaaden et al. (2015) and McCubbin et al. (2015), although we briefly summarize the setup here. Each experiment began by first packing Si-metal, FeS, and the NVP silicate starting material or diopside starting material (Table 1) into the capsule in an ~ 2:2:3 mixture. As discussed above, the Si-metal was added to each capsule in order to set the oxygen fugacity of the experiment to mercurian

conditions and allow the S to dissolve into the silicate melt. The FeS was added to ensure sulfide saturation during each experimental run. The loaded graphite capsules were placed within salt-pyrex cells, which were used as a pressure medium, with crushable MgO parts and a graphite furnace. Exceptions to the procedure in Vander Kaaden et al. (2015) and McCubbin et al. (2015) include using run durations from 2–21.7 hours and using a Type B ($Pt_{30}Rh_{70}$/ Pt_6Rh_{94}) thermocouple and Eurotherm (2416) controller to control and monitor temperature throughout the duration of each run. Each experiment was quenched by shutting off power to the furnace and slowly decompressing the run. Experiments were run at 0.50 GPa and 1.0 GPa in the temperature range of 1300 °C – 1600 °C.

2.4. Multi-Anvil (MA) Experimental Methods

Experiments run at the IOM at 4.0 GPa were performed in a MA using procedures that are identical to those described in Vander Kaaden et al. (2015), including a ceramic octahedron, Al_2O_3 inner parts, and 8 mm truncation-edge-length of tungsten carbide cubes. The reader is referred to Agee et al. (1995) for our MA pressure calibration data and procedures. Capsules for the SCSS experiments were prepared the same way they were for the PC runs. At the termination of each run, the charge was quenched and slowly decompressed in the same manner as the PC experiments. Experiments on the NVP and diopside compositions to assess SCCS were run at 4 GPa in the temperature range of 1750 °C – 2050 °C, with run durations of 0.025–4 hours.

2.5 Analysis of SCSS Experiments

All run products were polished using hexagonal boron nitride powder as a lubricant instead of water to ensure no volatile phases were lost from the experimental charges

(Murthy et al., 2003). All phases for the SCSS experiments, including silicate glass, metals, and sulfides, were analyzed using a JEOL 8200 superprobe at the University of New Mexico. An accelerating voltage of 15 KeV were used for all analyses. A beam current of 15 nA was used for silicate analyses, whereas metals and sulfides were analyzed using a beam current of 20 nA. A broad beam (10–20 μm) was used for glass analyses and a focused beam (1–5 μm) was used for silicate minerals, metals, and sulfides. The standards albite (for Na), almandine (Al, Fe), augite (Si, Al, Ca, Mg), olivine (Mg, Si, Fe), orthoclase (K), pyrope (Cr, Mg, Ca), titanite (Ti), and spessartine (Mn) were used to analyze our quenched melt and silicate minerals. A sodalite standard was used to determine the amount of Cl^- contamination. Metal and sulfide standards included Al-metal, albite (for Na), Cr-metal, orthoclase (K), Si metal, pyrite and troilite (S), Mg-metal, spessartine (Mn), augite (Ca), Fe-metal, Ti-metal, and sodalite (Cl). Peak positions were checked on the silicate standards used for metal and sulfide analyses and compared with the peak positions in the experimental charge to ensure that analyses were conducted at the correct peak position. Peak count times ranged from 30–60 seconds and background count times ranged from 15–30 seconds, respectively. Analyses in the proximity of Si-rich metal typically suffered from substantial secondary fluorescence of Si, resulting in elevated totals and elevated abundances of Si, so care was taken to measure glass that was ≥ 200 μm from the Si metal, however, this did not completely solve the issue and some experimental charges still resulted in high totals, mainly due to excess measurements of Si.

2.6 Micro-Fourier Transform Infrared Spectroscopy (FTIR) of SCSS Experiments

Quantitative infrared spectroscopic measurements were conducted on the experimental glass products of numerous experimental charges at room temperature in transmittance mode with a Nicolet Nexus 670 Fourier Transform Infrared Spectrometer in the IOM at UNM to determine the amount of H_2O present in the "dry" runs from this study. The techniques used in this study were identical to Vander Kaaden and McCubbin (2015). Transmittance IR spectra were collected from doubly polished wafers of the run products over the mid-IR range (400–4000 cm^{-1}) using a Continuum microscope with a Globar source, XT-KBr beamsplitter, and a MCT/A detector over a 100 × 100 µm area with a 4 cm^{-1} resolution. Thicknesses for each sample were obtained by focusing a reflected aperture on the top surface of the sample first then the bottom surface of the sample and recording the z-axis position of the mapping stage in the Atlus software. These arbitrary units were converted to µm using a previous calibration (Berger, 2012). Background spectra were collected under the same conditions before each analysis. Total dissolved water concentrations were determined for each glass from the intensity of the broad band at 3570 cm^{-1} after the calculation scheme of Mandeville et al. (2002) and Dixon et al. (1995). One thousand and twenty four scans were performed for each IR spectrum acquired.

2.7 Calculations of Oxygen Fugacity

After the analysis of each experiment, the oxygen fugacity of the charge was calculated using the silicate melt and an Fe-rich metal phase, relative to the iron-wüstite buffer using equation (1).

$$\Delta IW = 2log\left(\frac{x_{FeO}^{silicate} * \gamma_{FeO}^{silicate}}{x_{Fe}^{metal} * \gamma_{Fe}^{metal}}\right) \quad (1)$$

where $x_{FeO}^{silicate}$ is the mole fraction of FeO in the silicate, $\gamma_{FeO}^{silicate}$ is the activity coefficient of FeO in the silicate, x_{Fe}^{metal} is the mole fraction of Fe in the metal, and γ_{Fe}^{metal} is the activity coefficient of Fe in the metal. Given the uncertainty in activity coefficients, we assumed ideality to make a first-order approximation of the oxygen fugacity in all calculations.

3. Results

For the SCSS experiments, in terms of silicates, a few experiments resulted in both silicate melt and minerals, although most experiments were run at superliquidus temperatures resulting in a single silicate melt phase. Sulfides were present in all experimental charges, ensuring sulfide saturation during the run. Furthermore, Si-metal was present at the end of each experiment, so we can verify that it was not consumed during the duration of the run and the low fO_2 was maintained. An example of an experimental run product is given in Figure 1. In few cases, two immiscible melts were produced. In the experimental charges that contained a rhyolitic and basaltic composition, the basaltic composition was considered for all data interpretation. EPMA data for the 11 SCSS runs is given in Table 2. The addition of Si-metal to each experimental charge set the oxygen fugacity of these experiments between ΔIW-3.39 and ΔIW-7.12. The SCSS in the silicate portion of the experimental charges ranged from 1.23 wt% S to 17.02 wt% S. These experimental results are shown in Figure 2A in comparison to previously published data (Beermann et al., 2011; Berthet et al., 2009; Holzheid and Grove, 2002; Malavergne et al., 2007; Mavrogenes and O'Neill, 1999; McCoy et al., 1999; Moune et al., 2009). Consistent with mercurian melt compositions, the FeO in all charges was less than 1.5 wt%. Due to the wide range in melt compositions used (Table 1), as expected, the

experimental charges resulted in a wide range of melt compositions from diopside in nature to a reduced version of the NVP composition, where the majority of the iron has been partitioned into the metal phase.

4. Discussion

4.1 Effect of capsule setup on SCSS

When combining silicates, sulfides, and metals for an experimental study, there are typically two ways to do so: 1) combine all phases in the appropriate proportions and mix them together before putting them into the capsule, or 2) layer the starting materials in the capsule and allow them to combine at high *PT* conditions. When we attempted to run the SCSS experiments by combining all phases prior to putting them in the capsule, this resulted in extremely heterogeneous run products with many phases too small to analyze using EPMA. Therefore, all SCSS experiments were setup by layering the starting materials. To determine if there was an effect on the order of the layers, we ran two experiments at 1300 °C, 1 GPa.

For the experiment where the capsule was loaded with a layer of Si-metal at the base, followed by a layer of the NVP starting composition, topped with a layer of FeS, two immiscible melts were produced (Figure 1). This experiment was run for four hours. One immiscible melt contained high SiO_2, and Na_2O, (closest to Si-metal), and one with high Al_2O_3, MgO and CaO. This experiment also produced a region of pyroxene and a region of olivine suggesting perhaps a gradational silica activity across the capsule with the melt against the Si-metal having the highest silica activity. Furthermore, some pyroxenes do contain olivine cores (XD), indicating O diffusion into our capsule during the experiments, the effects of which were obvious after 4 to 10 hours.

For the experiment where the capsule was loaded with a layer of Si-metal at the base, followed by a layer of FeS, topped with a layer of the NVP starting composition (Figure 3), this produced two immiscible melts as well. This experiment was held at elevated *PT* conditions for 24 hours. One of the immiscible melts again contained high SiO_2, Na_2O, and S^{2-} (closest to Si-metal), and the other immiscible melt again contained high Al_2O_3, MgO and CaO. The addition of FeS also decreased the pressure of the multiple saturation point for this composition as olivine is typically the liquidus phase at these *PT* conditions. However, some pyroxenes do contain olivine cores (XB), suggesting Ol reacted out to form orthopyroxene. We attribute this reaction to the long duration of the run and O diffusion into the capsule, similar to the previous experiment. Since both layering techniques produced similar results, for consistency purpose, all of the SCSS experiments were layered with Si-metal at the base, followed by a layer of FeS, and topped with a layer of the silicate starting material (Table 1). Furthermore, in order to minimize O diffusion into the capsule, the majority of our experiments were held at *PT* conditions for two hours or less.

4.2 Implications for S concentration on the surface of Mercury

The SCSS results obtained in this study further support an increase in sulfide solubility in silicate melts with decreasing oxygen fugacity (Figure 2A). Furthermore, including data from McCoy et al. (1999), SCSS increases with increasing temperature from 0.0001–4 GPa (Figure 2B); however, the slope of the temperature effect on SCSS varies as a function of pressure. The slope of the temperature effect on SCSS from 0.5–4 GPa is much steeper, and also fairly similar, than the 0.0001 GPa data from (McCoy et al., 1999). Although SCSS increases as a function of temperature at all pressures, the

temperature effect on SCSS correlates more strongly with the amount of super-heating above the liquidus temperature rather than absolute temperature. This point is illustrated in Figure 2B where lower temperature melts at 1 GPa have higher SCSS values than higher temperature melts at 4 GPa, but both sets of experiments display similar increasing trends in SCSS as a function of *T*. We interpret this behavior to indicate that silicate melt structure, or melt viscosity, may also play a role in controlling SCSS at these reducing conditions. At 0.5 and 1 GPa, the diopside melt compositions, which were run at higher temperature, form an extension for the slope of the corresponding 0.5 and 1 GPa data on the NVP melt composition, so melt composition may play a subordinate role on SCSS to temperature. Similarly, for our only overlapping temperature (1400 °C), SCSS increases with increasing pressure, at least between 0.5 and 1 GPa (Figure 2C).

These results indicate that the elevated abundances of sulfur on Mercury's surface can be explained by transport within highly reduced silicate magmas, which have a much higher carrying capacity for sulfide than moderately reduced to oxidizing magmas. In addition to oxygen fugacity, both pressure and temperature will have a strong effect on the carrying capacity of silicate melts during partial melting in Mercury's interior. In order to determine the role of viscosity on sulfide solubility an investigation into much simpler silicate systems including pure SiO_2 melt as well as a diopside ($CaMgSi_2O_6$) melt are warranted.

5. Conclusion

The role that volatiles played in the thermal and magmatic evolution of Mercury are critical to understanding the present day planet that has been investigated by Mariner 10 and MESSENGER. The current study aimed to examine the role of S in silicate melts

and its impact on the thermal and magmatic evolution of Mercury. From our data, SCSS in silicate melts is highly dependent on oxygen fugacity, pressure, and temperature and less dependent on melt composition. If Mercury formed under the highly reducing conditions that are currently reflected on the surface, the silicate melts that were produced would have had a higher carrying capacity for sulfur, bringing it to the surface within melts. Once cooled on the surface, sulfides crystallized, most likely with Cr-Mn-Ti-bearing sulfides first and Mg-Ca-bearing sulfides following (Vander Kaaden and McCubbin, 2016). This process is reflected in the MESSENGER data by both the high S content on the surface as well as the correlation between Ca and S on the surface measured by XRS (Nittler et al., 2011). Understanding the role of all of the volatiles present on Mercury is imperative to our understanding of these complex and unique processes.

Acknowledgements

The authors would like to thank Whitney McCutcheon for assisting in FTIR analyses and Alison Santos for helpful discussions and assisting in laboratory procedures. We also thank the MESSENGER Science Team, with special thanks to the MESSENGER Geochemistry Discipline Group, for fruitful discussions regarding the interpretation of MESSENGER data. This work was funded by a NASA Cosmochemistry Grant NNX14AK43G to FMM.

References

Agee, C.B., Li, J., Shannon, M.C. and Circone, S. (1995) Pressure-temperature phase diagram for the Allende meteorite. Journal of Geophysical Research-Solid Earth 100, 17725-17740.

Albarede, F. (2009) Volatile accretion history of the terrestrial planets and dynamic implications. Nature 461, 1227-1233.

Ardia, P., Hirschmann, M.M. and Withers, A.C. (2013) Solubility of methane in a synthetic basaltic melt, with applications to atmosphere-magma coean-core partitioning of volatiles and to the evolution of the martian atmosphere. Geochimica Et Cosmochimica Acta 114, 52-71.

Beermann, O., Botcharnikov, R.E., Holtz, F., Diedrich, O. and Nowak, M. (2011) Temperature dependence of sulfide and sulfate solubility in olivine-saturated basaltic magmas. Geochimica Et Cosmochimica Acta 75, 7612-7631.

Berger, J.A. (2012) Effect of halite and calcite coatings on thermal infrared spectra with implications for Mars exploration. M.S. Thesis, University of New Mexico.

Berthet, S., Malavergne, V. and Righter, K. (2009) Melting of the Indarch meteorite (EH4 chondrite) at 1 GPa and variable oxygen fugacity: Implications for early planetary differentiation processes. Geochimica Et Cosmochimica Acta 73, 6402-6420.

Bida, T.A., Killen, R.M. and Morgan, T.H. (2000) Discovery of calcium in Mercury's atmosphere. Nature 404, 159-161.

Broadfoot, A.L., Kumar, S., Blelton, M.J.S. and McElroy, M.B. (1974) Mercury's atmosphere from Mariner 10: preliminary results. Science 185, 166-169.

Broadfoot, A.L., Shemansky, D.E. and Kumar, S. (1976) Mariner 10: Mercury atmosphere. Geophysical Research Letters 3, 577-580.

de Hoog, J.C.M., Mason, P.R.D. and van Bergen, M.H. (2001) Sulfur and chalcophile elements in subduction zones: Constraints from a laser ablation ICP-MS study of melt inclusions from Galunggung Volcano, Indonesia. Geochimica Et Cosmochimica Acta 65, 3147-3164.

Dixon, J.E., Stolper, E.M. and Holloway, J.R. (1995) An experimental study of water and carbon dioxide solubilities in mid ocean ridge basaltic liquids .1. Calibration and solubility models. Journal of Petrology 36, 1607-1631.

Evans, L.G., Peplowski, P.N., Killen, R.M., Potter, A.E. and Sprague, A.L. (2013) Variable Sodium on the Surface of Mercury: Implications for Surface CHemistry and the Exosphere., 44th Lunar and Planetary Science Conference, The Woodlands, TX, p. # 2033.

Evans, L.G., Peplowski, P.N., McCubbin, F.M., McCoy, T.J., Nittler, L.R., Zolotov, M.Y., Ebel, D.S., Lawrence, D.J., Starr, R.D., Weider, S.Z. and Solomon, S.C. (2015) Chlorine on the surface of Mercury: MESSENGER Gamma-Ray measurements and implications for the planet's formation and evolution. Icarus 257, 417-427.

Harmon, J.K. and Slade, M.A. (1992) Radar mapping of Mercury: full-disk images and polar anomalies. Science 258, 640-642.

Head, J.W., Chapman, C.R., Strom, R.G., Fassett, C.I., Denevi, B.W., Blewett, D.T., Ernst, C.M., Watters, T.R., Solomon, S.C., Murchie, S.L., Prockter, L.M., Chabot,

N.L., Gillis-Davis, J.J., Whitten, J.L., Goudge, T.A., Baker, D.M.H., Hurwitz, D.M., Ostrach, L.R., Xiao, Z., Merline, W.J., Kerber, L., Dickson, J.L., Oberst, J., Byrne, P.K., Klimczak, C. and Nittler, L.R. (2011) Flood Volcanism in the Northern High Latitudes of Mercury Revealed by MESSENGER. Science 333, 1853-1856.

Holzheid, A. and Grove, T.L. (2002) Sulfur saturation limits in silicate melts and their implications for core formation scenarios for terrestrial planets. American Mineralogist 87, 227-237.

Lorand, J.P., Alard, O., Luguet, A. and Keays, R.R. (2003) Sulfur and selenium systematics of the subcontinental lithospheric mantle: inferences from the Massif Central xenolith suite (France). Geochimica Et Cosmochimica Acta 21, 4137-4151.

Malavergne, V., Berthet, S. and Righter, K. (2007) Formation of CaS-MgS in enstatite chondrites and achondrites as a function of redox conditions and temperature: constraints on their evolution in a planetesimal and in a proto-planet 38th Lunar and Planetary Science Conference. Lunar and Planetary Institute, Houston, TX, p. Abstract #1737.

Malavergne, V., Cordier, P., Righter, K., Brunet, F., Zanda, B., Addad, A., Smith, T., Bureau, H., Surblé, S., Raepsaet, C., Charon, E. and Hewins, R.H. (2014) How Mercury can be the most reduced terrestrial planet and still store iron in its mantle. Earth and Planetary Science Letters 394, 186-197.

Mandeville, C.W., Webster, J.D., Rutherford, M.J., Taylor, B.E., Timbal, A. and Faure, K. (2002) Determination of molar absorptivities for infrared absorption bands of H2O in andesitic glasses. American Mineralogist 87, 813-821.

Mavrogenes, J.A. and O'Neill, H.S.C. (1999) The relative effects of pressure, temperature and oxygen fugacity on the solubility of sulfide in mafic magmas. Geochimica Et Cosmochimica Acta 63, 1173-1180.

McCoy, T.J., Dickinson, T.L. and Lofgren, G.E. (1999) Partial melting of the Indarch (EH4) meteorite: A textural, chemical, and phase relations view of melting and melt migration. Meteoritics & Planetary Science 34, 735-746.

McCubbin, F.M., Riner, M.A., Vander Kaaden, K.E. and Burkemper, L.K. (2012) Is Mercury a volatile-rich planet? Geophysical Research Letters 39.

McCubbin, F.M., Vander Kaaden, K.E., Tartese, R., Boyce, J.W., Mikhail, S., Whitson, E.S., Bell, A.S., Anand, M., Franchi, I.A., Wang, J. and Hauri, E.H. (2015) Experimental investigation of F, Cl, and OH partitioning between apatite and Fe-rich basaltic melt at 1.0-1.2 GPa and 950-1000 °C. American Mineralogist 100, 1790-1802.

Metrich, N., Schiano, P., Clocchiatti, R. and Maury, R.C. (1999) Transfer of sulfur in subduction settings: an example from Batan Island (Luzon volcanic arc, Philippines). Earth and Planetary Science Letters 167, 1-14.

Moune, S., Holtz, F. and Botcharnikov, R.E. (2009) Sulphur solubility in andesitic to basaltic melts: implications for Hekla volcano. Contributions to Mineralogy and Petrology 157, 691-707.

Murchie, S.L., Klima, R.L., Denevi, B.W., Ernst, C.M., Keller, M.R., Domingue, D.L., Blewett, D.T., Chabot, N.L., Hash, C., Malaret, E., Izenberg, N.R., Vilas, F., Nittler, L.R. and Head, J.W. (2015) Orbital multispectral mapping of Mercury using

the MESSENGER Mercury Dual Imaging System: Evidence for the origins of plains units and low-reflectance material. Icarus.
Murthy, V.M., van Westrenen, W. and Fei, Y.W. (2003) Experimental evidence that potassium is a substantial radioactive heat source in planetary cores. Nature 423, 163-165.
Nittler, L.R., Starr, R.D., Weider, S.Z., McCoy, T.J., Boynton, W.V., Ebel, D.S., Ernst, C.M., Evans, L.G., Goldsten, J.O., Hamara, D.K., Lawrence, D.J., McNutt, R.L., Schlemm, C.E., Solomon, S.C. and Sprague, A.L. (2011) The Major-Element Composition of Mercury's Surface from MESSENGER X-ray Spectrometry. Science 333, 1847-1850.
Ostrach, L.R., Robinson, M.S., Whitten, J.L., Fassett, C.I., Strom, R.G., Head, J.W. and Solomon, S.C. (2015) Extent, age, and resurfacing history of the northern smooth plains on Mercury from MESSENGER observations. Icarus 250, 602-622.
Palme, H. and O'Neill, H.S.C. (2004) Cosmochemical estimates of mantle composition., Treatise on Geochemistry. Elsevier, Amsterdam, pp. 1-38.
Peplowski, P.N., Evans, L.G., Stockstill-Cahill, K.R., Lawrence, D.J., Goldsten, J.O., McCoy, T.J., Nittler, L.R., Solomon, S.C., Sprague, A.L., Starr, R.D. and Weider, S.Z. (2014) Enhanced sodium abundance in Mercury's north polar region revealed by the MESSENGER Gamma-Ray Spectrometer. Icarus 228, 86-95.
Peplowski, P.N., Klima, R.L., Lawrence, D.J., Ernst, C.M., Denevi, B.W., Frank, E.A., Goldsten, J.O., Murchie, S.L., Nittler, L.R. and Solomon, S.C. (2016) Remote sensing evidence for an ancient carbon-bearing crust on Mercury. Nature Geoscience.
Peplowski, P.N., Lawrence, D.J., Evans, L.G., Klima, R.L., Blewett, D.T., Goldsten, J.O., Murchie, S.L., McCoy, T.J., Nittler, L.R., Solomon, S.C., Starr, R.D. and Weider, S.Z. (2015) Constraints on the abundance of carbon in near-surface materials on Mercury: Results from the MESSENGER Gamma-Ray Spectrometer. Planetary and Space Science.
Peplowski, P.N., Lawrence, D.J., Rhodes, E.A., Sprague, A.L., McCoy, T.J., Denevi, B.W., Evans, L.G., Head, J.W., Nittler, L.R., Solomon, S.C., Stockstill-Cahill, K.R. and Weider, S.Z. (2012) Variations in the abundances of potassium and thorium on the surface of Mercury: Results from the MESSENGER Gamma-Ray Spectrometer. Journal of Geophysical Research - Planets 117.
Potter, A.E. and Morgan, T.H. (1985) Discovery of sodium in the atmosphere of Mercury. Science 229, 651-653.
Potter, A.E. and Morgan, T.H. (1986) Potassium in the atmosphere of Mercury. Icarus 67, 336-340.
Rose-Weston, L., Brenan, J.M., Fei, Y.W., Secco, R.A. and Frost, D.J. (2009) Effect of pressure, temperature, and oxygen fugacity on the metal-silicate partitioning of Te, Se, and S: Implications for earth differentiation. Geochimica Et Cosmochimica Acta 73, 4598-4615.
Saal, A.E., Hauri, E.H., Langmuir, C.H. and Perfit, M.R. (2002) Vapour undersaturation in primitive mid-ocean-ridge basalt and the volatile content of Earth's upper mantle. Nature 419, 451-455.

Siebert, J., Malavergne, V., Guyot, F., Combes, R. and Martinez, I. (2004) The behaviour of sulphur in metal-silicate core segregation experiments under reducing conditions. Physics of the Earth and Planetary Interiors 143-144, 433-443.

Slade, M.A., Butler, B.J. and Muhleman, D.O. (1992) Mercury radar imaging: evidence for polar ice. Science 258, 635-640.

Tauster, S.J., Pecoraro, T.A. and Chianelli, R.R. (1980) Structure and properties of molybdenum sulfide: Correlation of O2 chemisorption with hydrodesulfurization activity. Journal of Catalysis 63, 515-519.

Vander Kaaden, K.E., Agee, C.B. and McCubbin, F.M. (2015) Density and compressibility of the molten lunar picritic glasses: Implications for the roles of Ti and Fe in the structures of silicate melts. Geochimica Et Cosmochimica Acta 149, 1-20.

Vander Kaaden, K.E. and McCubbin, F.M. (2015) Exotic Crust Formation on Mercury: Consequences of a Shallow, FeO-poor Mantle. Journal of Geophysical Research - Planets 120, 195-209.

Vander Kaaden, K.E. and McCubbin, F.M. (2016) The origin of boninites on Mercury: An experimental study of the northern volcanic plains lavas. Geochimica Et Cosmochimica Acta 173, 246-263.

Wallace, P. and Carmichael, I.S.E. (1992) Sulfur in Basaltic Magmas. Geochimica Et Cosmochimica Acta 56, 1863-1874.

Wallace, P.J. and Edmonds, M. (2011) The Sulfur Budget in Magmas: Evidence from Melt Inclusions, Submarine Glasses, and Volcanic Gas Emissions. Reviews in Mineralogy & Geochemistry 73, 215-246.

Weider, S.Z., Nittler, L.R., Starr, R.D., McCoy, T.J., Stockstill-Cahill, K.R., Byrne, P.K., Denevi, B.W., Head, J.W. and Solomon, S.C. (2012) Chemical heterogeneity on Mercury's surface revealed by the MESSENGER X-Ray Spectrometer. Journal of Geophysical Research - Planets 117.

Wykes, J.L., O'Neill, H.S.C. and Mavrogenes, J.A. (2015) The Effect of FeO on the Sulfur Content at Sulfide Saturation (SCSS) and the Selenium Content at Selenide Saturation of Silicate Melts. Journal of Petrology 56, 1407-1424.

Zolotov, M.Y., Sprague, A.L., Hauck, S.A., Nittler, L.R., Solomon, S.C. and Weider, S.Z. (2013) The redox state, FeO content, and origin of sulfur-rich magmas on Mercury. Journal of Geophysical Research-Planets 118.

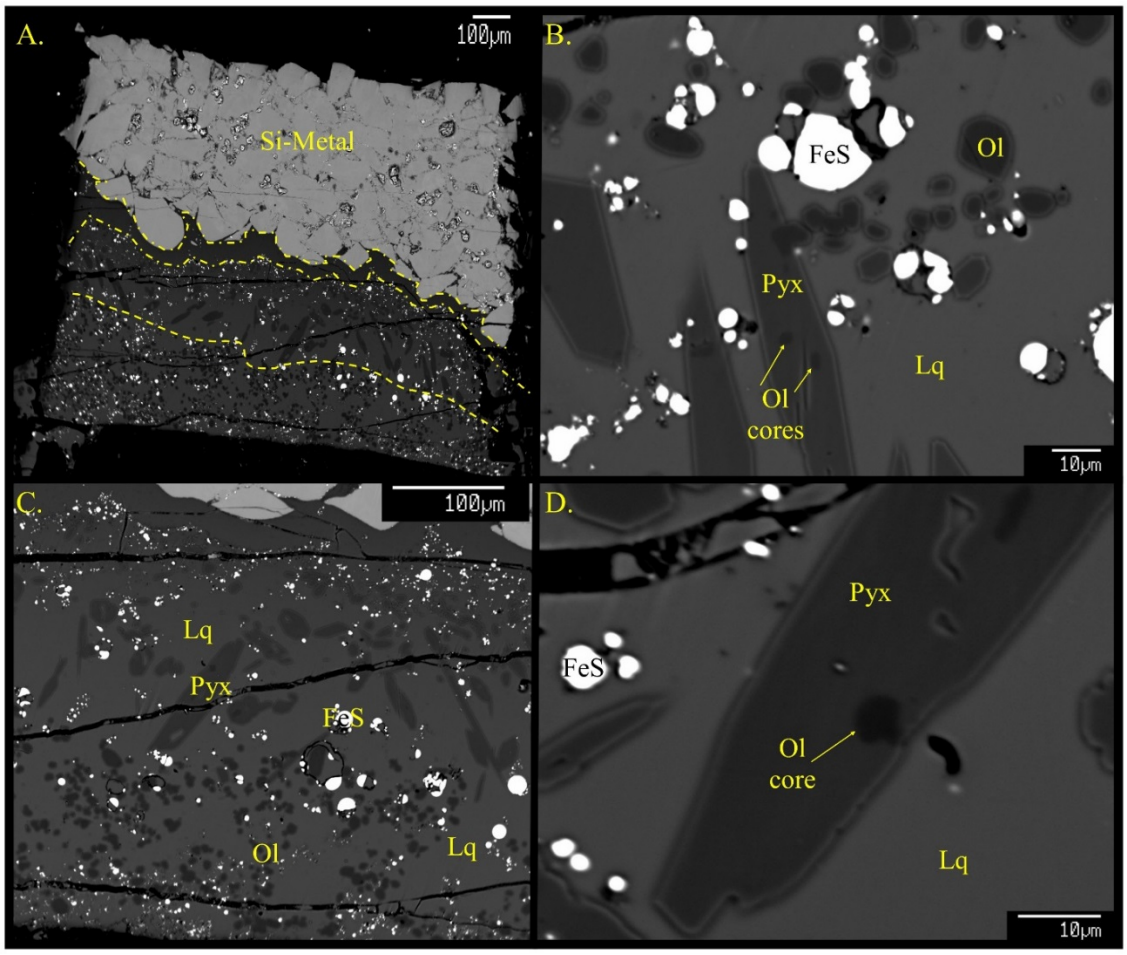

Figure 1. BSE image of an SCSS experimental run product from 1300 °C, 1.0 GPa, 4 hours. Ol = olivine, Pyx = pyroxene, Lq = liquid (melt). See text for full details.

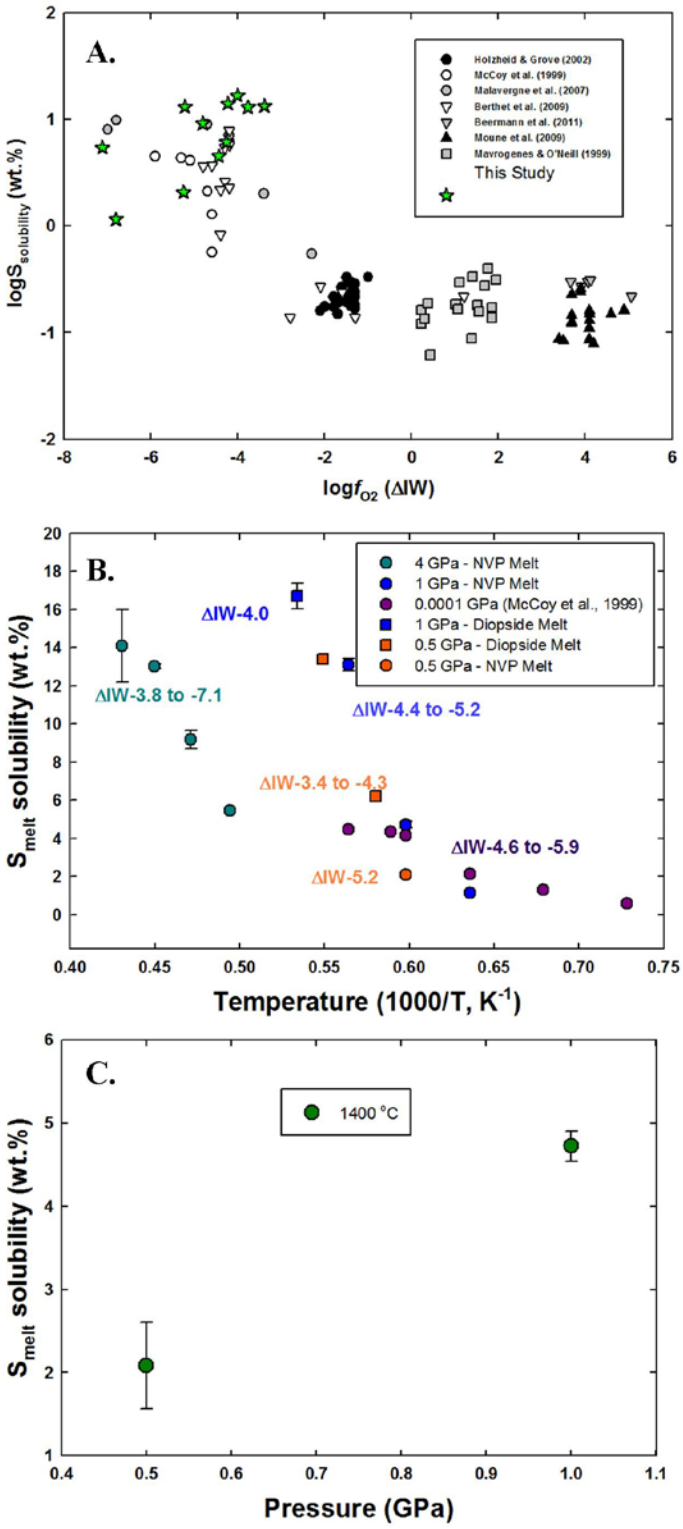

Figure 2. SCSS (wt%) in silicate melt as a function of oxygen fugacity (A), temperature (B), and pressure (C). The smaller error bars indicate a more homogeneous melt. For the NVP compositions that produced immiscible melts, the basaltic endmember was used for these plots.

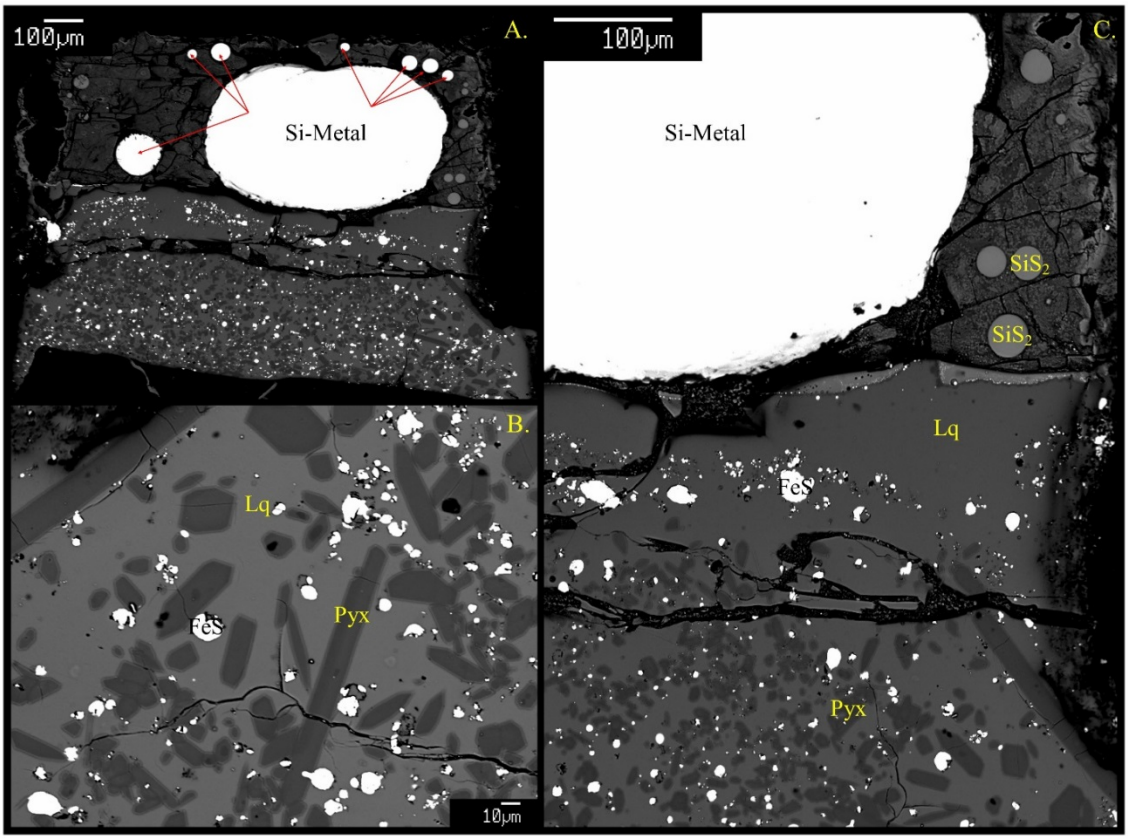

Figure 3. Experimental run product from 1300 °C, ~1.0 GPa, 24 hours. Labels are the same as Figure 1. See text for full details.

Table 1. Composition of the silicate starting materials used in the SCSS study. All values are in wt%. Average NVP composition derived from MESSENGER data (Evans et al., 2013; Nittler et al., 2011; Peplowski et al., 2014; Peplowski et al., 2012; Weider et al., 2012).

	Average NVP	Alkali- and Sulfur-Bearing	Diopside
SiO_2	56.07	54.05	55.49
TiO_2	0.81	1.26	-------
Al_2O_3	13.67	12.60	-------
Cr_2O_3	0.77	0.74	-------
FeO	1.01	-------	-------
MgO	15.21	14.25	18.61
MnO	0.68	0.65	-------
CaO	4.11	5.23	25.90
Na_2O	7.00	6.81	-------
K_2O	0.22	0.25	-------
FeS	0	4.16	-------
S	0.92	-------	-------
$^{-}O=S$	0.47	-------	-------
Total	100.00	100.00	100.00

Table 2. EPMA data for SCSS experiments (wt%). The standard deviations are listed parenthetically. *contained a superliquidus step at 1950 °C for 10 minutes. N=number of analyses included in average.

Run	SSD-2	SSD-3	NSA-42	SSD-1	NSA-43	NSA-50	NSA-23	NSA-44	NSA-45	NSA-47	NSA-15*
P (GPa)	0.5	0.5	0.5	1	1	1	1	4	4	4	4
T(°C)	1550	1450	1400	1600	1400	1500	1300	1850	1950	2050	1750
Run Time (Hr)	2	2	2	2	2	2	21.7	0.667	2	0.025	4
ΔIW	-3.39	-4.26	-5.25	-4.01	-4.44	-5.22	-6.81	-4.81	-3.77	-4.23	-7.12
n	11	12	7	7	2	12	9	16	12	5	7
SiO_2	55.79 (1.43)	59.07 (0.80)	57.47 (4.45)	52.87 (0.73)	62.37 (0.46)	51.43 (1.99)	62.71 (3.17)	66.22 (0.59)	58.76 (0.32)	60.00 (1.38)	65.16 (0.50)
TiO_2	0.04 (0.02)	0.05 (0.02)	1.10 (0.17)	0.05 (0.01)	0.28 (0.02)	0.32 (0.04)	1.15 (0.16)	0.54 (0.14)	0.37 (0.14)	0.07 (0.01)	0.28 (0.02)
Al_2O_3	0.89 (0.04)	0.93 (0.05)	14.22 (0.38)	0.90 (0.05)	13.32 (0.14)	6.35 (0.24)	16.54 (0.61)	13.05 (0.28)	20.16 (0.24)	15.41 (0.45)	12.51 (0.77)
Cr_2O_3	0.00 (0.00)	0.00 (0.01)	0.09 (0.04)	0.01 (0.01)	0.03 (0.01)	0.02 (0.01)	0.07 (0.02)	0.07 (0.02)	0.08 (0.03)	0.04 (0.01)	0.06 (0.01)
FeO	1.44 (0.18)	0.53 (0.13)	0.17 (0.04)	1.00 (0.06)	0.30 (0.05)	0.25 (0.07)	0.14 (0.02)	0.22 (0.09)	0.88 (0.55)	0.64 (0.21)	0.02 (0.02)
MnO	0.06 (0.01)	0.03 (0.01)	0.17 (0.05)	0.06 (0.01)	0.06 (0.02)	0.10 (0.03)	0.22 (0.03)	0.30 (0.09)	0.26 (0.02)	0.16 (0.04)	0.12 (0.01)
MgO	15.43 (1.30)	17.60 (0.27)	16.44 (2.95)	18.07 (0.45)	13.90 (0.46)	20.52 (1.42)	8.97 (1.10)	11.84 (0.37)	9.12 (0.11)	14.05 (0.78)	9.98 (0.72)
CaO	18.49 (1.30)	18.76 (0.25)	5.22 (0.68)	19.89 (0.53)	4.37 (0.18)	6.44 (0.53)	6.50 (0.92)	3.84 (0.11)	3.46 (0.02)	3.10 (0.11)	6.08 (0.15)
Na_2O	1.20 (0.12)	0.21 (0.01)	5.17 (0.85)	0.21 (0.03)	4.99 (0.11)	5.56 (0.28)	8.18 (0.32)	5.34 (0.19)	4.57 (0.09)	3.89 (0.15)	6.86 (0.38)
K_2O	0.07 (0.01)	0.07 (0.01)	0.15 (0.15)	0.09 (0.02)	0.15 (0.00)	0.23 (0.03)	0.25 (0.03)	0.08 (0.01)	0.07 (0.01)	0.05 (0.01)	0.66 (0.06)
S	13.37 (0.50)	6.16 (0.17)	2.13 (0.03)	17.02 (0.67)	4.66 (0.01)	12.99 (0.31)	1.23 (0.05)	9.81 (0.47)	13.64 (0.13)	14.79 (1.88)	5.82 (0.79)
Cl	0.09 (0.02)	0.04 (0.00)	0.93 (0.09)	0.14 (0.01)	0.77 (0.01)	1.74 (0.18)	1.63 (0.05)	0.34 (0.01)	0.25 (0.01)	0.18 (0.01)	2.60 (0.36)
S + Cl = -O	6.69	3.08	1.27	8.52	2.50	6.87	0.98	4.97	6.86	7.42	3.49
Total	100.18	100.37	101.98	101.79	102.69	99.08	106.61	106.69	104.76	104.97	106.67

Chapter 5

Carbon Solubility in Si-Fe-Bearing Metals During Core Formation on Mercury

In collaboration with

Francis M. McCubbin[1,2]
D. Kent Ross[3,4]

[1]Institute of Meteoritics, Department of Earth & Planetary Sciences, University of New Mexico, Albuquerque, NM 87131, USA. [2]NASA Johnson Space Center, Mailcode XI2, 2101 NASA Parkway, Houston, TX 77058, USA. [3]Jacobs JETS, NASA Johnson Space Center, 2101 NASA Parkway, Houston TX 77058, [4]University of Texas at El Paso-CASSMAR

Abstract

Recent results from the MErcury Surface, Space ENvironment, GEochemistry and Ranging spacecraft (MESSENGER) have shown elevated abundances of carbon on the surface of Mercury as well as ample evidence, including high S contents and low FeO contents, suggesting Mercury formed under reducing conditions, approximately 3 to 7 $\log_{10}$ units below the IW buffer. At such highly reducing conditions, the behavior of elements may differ from what is typically seen on Earth (i.e. C has the potential to be a light element in the core). To investigate the effect of light elements on Mercury's core composition we conducted carbon solubility experiments in Fe-rich metals with various amounts of Si (ranging from 5 to 35 wt% Si) to determine the amount of C that would be soluble in the core of Mercury as a function of core composition and temperature. Carbon concentration at graphite saturation (CCGS) experiments were run at 1.0 GPa in the temperature range of 1300 °C – 1800 °C, with run durations of 8–24 hours, with the exception of the sole 1800 °C experiment that was held for ~1.25 hours. Analysis of the

CCGS experiments resulted in a range of C abundances from 0.6–4.1 wt%. In general, C abundances decreased with increasing Si in the metal and temperature has minimal effect on CCGS. If the reducing conditions determined by the mercurian surface compositions were present during core formation, these experimental results are consistent with low C contents in the mercurian core due to the elevated Si abundances in Fe-rich metal under such reducing conditions. Therefore, the majority of the C on the planet would preferentially partition into the mantle. However, given the low solubility of C in silicate melts under highly reducing conditions, saturation of C would occur quickly in the mercurian mantle. Therefore, the likely production of graphite further supports the possibility of a graphite floatation crust on Mercury.

Key Words: MESSENGER, carbon, core, oxygen fugacity

1. Introduction

Recent results from the MErcury Surface, Space ENvironment, GEochemistry and Ranging (MESSENGER) spacecraft have shown elevated abundances of carbon on the surface of Mercury (Murchie et al., 2015; Peplowski et al., 2016; Peplowski et al., 2015). Furthermore, the X-Ray Spectrometer on board MESSENGER measured elevated abundances of S and low abundances of FeO (Nittler et al., 2011; Weider et al., 2012), suggesting the planets oxygen fugacity is several $\log_{10}$ units below the Iron-Wüstite buffer (McCubbin et al., 2012; Zolotov et al., 2013). Similar to the role of other volatiles (e.g. sulfur) on highly reducing planetary bodies, carbon is expected to behave differently in an oxygen starved environment than it does in an oxygen enriched environment. As

discussed by Nittler et al. (2011) and Hauck et al. (2013), under such highly reducing conditions, the majority of the iron available on the planet partitions into the core. On Mercury, this resulted in a relatively large core and a thin mantle (Hauck et al., 2013; Smith et al., 2012). Using a composition similar to the largest volcanic field on the planet (the northern volcanic plains), Vander Kaaden and McCubbin (2015) conducted sink-float experiments to determine the density of melts and minerals on Mercury. From their investigation, they showed that graphite would be the only buoyant mineral in a mercurian magma ocean. Therefore, Vander Kaaden and McCubbin (2015) suggested the presence of a possible primary floatation crust on the planet composed of graphite. Concurrently, Peplowski et al. (2015) used GRS data from MESSENGER to show an average northern hemisphere abundance of C on the planet of 1.4 ± 0.9 wt%. However, as this result was only at the one-sigma detection limit, possible carbon abundances at the three-sigma detection limit for Mercury ranged from 0 to 4.1 wt% carbon. Additionally, Murchie et al. (2015) investigated the possible darkening agent on Mercury and concluded that coarse-grained graphite could darken high reflectance plains to the low reflectance material. To further test the possibility of elevated abundances of carbon in Mercury's crust, Peplowski et al. (2016) used the low-altitude MESSENGER data to show that carbon is the only material that is consistent with both the visible to near-infrared spectra and the neutron measurements of low reflectance material on Mercury, confirming that C is the primary darkening agent on Mercury. The confirmation of carbon on the planet leads to many unanswered questions regarding the role of carbon during the differentiation and evolution of Mercury.

Given the elevated abundances of both S and C on Mercury's surface, it begs the question, what is the core composition of the planet? Both S and C are believed to be light elements in planetary cores, but the enrichment in these elements at the surface of Mercury may preclude the core as their primary reservoir. Although no definitive conclusion has been reached, previous studies have made advances towards answering this question. Riner et al. (2008) and Chen et al. (2008) looked at Fe-S systems and implemented various crystallization and layered core scenarios to try to determine the composition and structure of Mercury's core. Malavergne et al. (2010) examined core crystallization scenarios in the presence of S and Si. Hauck et al. (2013) used the most recent geophysical constraints from the MESSENGER spacecraft to model the internal structure of Mercury, including the core, in a Fe-S-Si system. Furthermore, Chabot et al. (2014) conducted a series of metal-silicate partitioning experiments in a Fe-S-Si system. These results showed the core of Mercury has the potential to contain more than 15 wt% Si. However, with the newest results from MESSENGER's low altitude campaign, carbon is another potential light element that could be incorporated into Mercury's core that has not yet been considered experimentally.

For our examination of C, we will use Fe-Si mixtures (up to 35 wt% Si) to simulate simplified mercurian core compositions. Questions regarding the role C during planetary differentiation on Mercury will be answered by investigating C concentration at graphite saturation (CCGS) in metallic liquids with varying proportions of Fe and Si, as a function of temperature.

2. Methods

2.1 Starting Materials

The synthetic starting materials (Table 1) used to investigate CCGS were prepared at the Institute of Meteoritics, University of New Mexico (UNM) using high-purity Fe and Si metal powders that were hand mixed in a glass vial for several hours to ensure homogeneity throughout the powder. The ratio of Fe:Si metal was chosen in order to examine a range of possible Si-contents in the mercurian core. The Low Si (5 wt% Si) and Int-High Si (22 wt% Si) compositions were chosen based on the thermal minima on the liquidus temperatures along the Fe-Si metallic-binary join. The Int-High Si composition is also close to the upper limit described in Chabot et al. (2014) for the upper limit of Si in a mercurian core. The Low-Int Si and High Si compositions were chosen to expand the range of possible core compositions on Mercury to be examined.

2.2 PC Experimental Methods

With the exception of the 1300 °C experiments, which were conducted at UNM using the procedures outlined in Vander Kaaden and McCubbin (2016), all PC CCGS experiments were conducted in the high pressure laboratory at Johnson Space Center (JSC). Each experiment began by first packing one of the Si-Fe metal mixtures into a graphite capsule using a Teflon coated spatula and wooden tamper to minimize Fe-loss due to magnetization with the spatula/tamper. The main difference between the UNM setup and the JSC setup is the pressure medium used and how the temperature is measured and monitored throughout an experiment. For the CCGS experiments at JSC, the loaded graphite capsules were placed within barium carbonate ($BaCO_3$) cells, which were used as a pressure medium, with crushable MgO parts and a graphite furnace. A hard fired alumina disk was placed between the top of the thermocouple wire and the graphite capsule to ensure no contact during the run that could result in oxidation or

corrosion of the thermocouple wire. A Type C ($W_5Re_{95}/W_{26}Re_{74}$) thermocouple was used to monitor temperature throughout the run and was controlled by a Love controller throughout the duration of each run. Each experiment was quenched by shutting off power to the furnace and slowly decompressing the run. Experiments were run at 1.0 GPa in the temperature range of 1300 °C – 1800 °C, with run durations of 8–24 hours, with the exception of the sole 1800 °C experiment that was held for ~1.25 hours.

2.3 Approach to a steady state

In order to determine the length of time required to allow a single atom of carbon to diffuse from the graphite capsule across the entirety of the experimental sample, the longest dimension of the capsule was first measured (typically ~0.24 cm). From here, various diffusion coefficients for C in Fe-metal were taken from the literature (Tibbetts, 1980; Wert, 1950). The time it took for the diffusion of carbon across the entirety of the capsule was then calculated. At 1500 °C, it takes an average of 0.71 hours for C to diffuse across the longest dimension of the graphite capsule with a maximum time of 1.11 hours. At higher temperatures of 1800 °C however, it only takes, on average, 0.18 hours for C to diffuse across the longest dimension of the graphite capsule with a maximum of 0.28 hours. Additionally, a time series was conducted on the Int-High composition at 1 GPa and 1500 °C. The time series consisted of experiments run at 1 hour, 4 hours, and 8 hours to assure the calculated times using carbon diffusion coefficients was accurate for approaching a steady state in these experiments. The results of the time series analyses are shown in Figure 1. This data shows that carbon, iron, and silicon remain constant, within error, after run durations of 1 hour. Therefore, all experiments conducted for longer than 1 hour were considered in this study.

2.4 Analysis of CCGS Experiments

All run products were polished using hexagonal boron nitride powder as a lubricant instead of water to ensure no volatile phases were lost from the experimental charges (Murthy et al. 2003). All phases for the CCGS experiments were analyzed using a JEOL 8530F microprobe at NASA's JSC. Each sample was painted with Pelco® colloidal silver liquid from the capsule to the edge of the 1-inch round epoxy plug to ensure overlap and electrical contact with the sample holder. To minimize charging effects during analyses, the edges of the capsule were also surrounded by silver paint. Since each experiment only contained metal, there was no need to coat the samples in a conductive material. All analyses were collected at 15 keV and 30 nA while using the cold finger on the microprobe to increase the vacuum and minimize contamination. The cold finger was filled with liquid nitrogen prior to the beginning of each session, allowed to cool for approximately 1 hour while the vacuum on the microprobe regained its high vacuum state, and then filled periodically throughout each analytical session.

Si, Fe, and C were analyzed in each experiment. Si and Fe were analyzed using the TAP and LIFH crystals, respectively. They were standardized on pure metals that have been synthesized in the piston cylinder at JSC. C was analyzed using the LDE2 crystal and was standardized using a synthetic Fe_3C standard made in the piston cylinder apparatus at JSC. The composition of the synthetic cohenite standard was confirmed using the Transmission Electron Microscope (TEM) at JSC under the direction of Dr. Lindsay Keller. Due to the wide peaks on this crystal as well as an interference between the backgrounds of C and Si, an optimal background was chosen to ensure this overlap was avoided. Peak and background counts for major elements were 30 and 15 seconds,

respectively whereas peak and background counts for carbon were 60 and 30 seconds, respectively. All data was corrected using the phi-rho-z correction method, which is ideal when analyzing light elements (Merlet, 1994).

3. Results

Each CCGS experiment resulted in two phases upon quench (Figure 2A). However, this liquid metal was a single phase at the *PT* conditions of our runs and typically quenched to a dendritic texture of Si-Fe rich, C-poor dendrites surrounded by C-rich, Fe-Si metal. Although present throughout the experimental charge, higher concentrations of dendrites are typically found near the edges of the capsules or around graphite grains suggesting they are nucleating on the C-rich surfaces available. In the experiments containing ≥ 22 wt% Si, the interstitial melt was typically too small to analyze accurately using EPMA. Future analyses will include TEM work to determine accurately the metallic melt compositions in these charges. In some experimental charges, vermicular intergrowths of graphite were present (Figure 2B). According to the 1-bar Fe-Si phase diagram, the runs at 1300 °C in the Si_5Fe_{95} and $Si_{35}Fe_{65}$ should have remained solid. However, the addition of C into the Fe-Si system must have depressed the liquidus of these metals as evidenced by the quenched dendritic texture in these runs (Figure 2A), which clearly indicate these compositions were liquid at the *PT* conditions of the experiment. The ability of C to depress the liquidus apparently out-competed the effect of P to raise the liquidus temperatures, indicating that C has a strong effect on liquidus depression in the Fe-Si-C system.

In order to characterize fully each experimental charge, we analyzed the samples using both broad beam analyses (~15–20 μm) across the entire sample and spot analyses

(~1–5 μm) on the dendrites and surrounding regions. Assuming the resulting experimental charge was one phase during the run, as evidenced by the dendritic texture in the experimental charges, EPMA analyses are given in Table 2. The broad beam analyses, representative of the average sample at the experimental *PT* conditions, both quenched melt and dendritic phases, show a range in C abundances from 0.6–4.1 wt%. Additionally, the broad beam analyses show the samples contain ~4.5–22.6 wt% Si and ~79.1–92.8 wt% Fe, indicative of the wide range in starting compositions that were used in this study (Table 1). However, in an attempt to see if the dendritic textures forced by the quenching of our experiments showed any additional information, EPMA analyses for the dendrites are given in Table 3 and were conducted using a 1–5 μm beam diameter, depending on the size of the phase in a given experiment. These analyses resulted in carbon abundances in the dendrites ranging from 0.4–1.4 wt%, Si values of 4.5–32 wt%, and Fe abundances of 68.2–94.7 wt%. EPMA analyses for the liquids surrounding the dendrites are given in Table 4 and were also conducted using a 1–5 μm spot. These analyses show carbon abundances in the surrounding quenched liquid phases ranging from 3.1–5.0 wt%, Si values of 3.7–16.3 wt%, and Fe abundances of 82.13–93.19 wt%.

4. Implications for the carbon content of Mercury's core

Although we do not currently know the composition of the core at the time of formation of Mercury, the data from this study can place some constraints on the role of carbon in the mercurian core. Figures 3–7 show that temperature has little to no effect on CCGS. Carbon solubility is highest in the most Fe-rich metal and decreases with increasing Si content in the metal. However, experiments CSM-984, CS-2, and CSM-996 all have ~79.75 wt% Fe in the liquid metal (Table 2). Carbon contents range from 0.63

wt% to 1.04 wt% with the lower C content corresponding to higher Si (22.6 wt%) and the higher C content corresponding to lower Si (18.45 wt%), suggesting Si has a stronger control on C solubility than Fe in an Fe-Si-C system. Furthermore, Figure 7 shows that composition has a much stronger effect on CCGS than temperature, at least a 1 GPa. Additionally, Figure 6 represents the dendritic metal-surrounding quenched liquid metal pairs that were present in a given experiment. From this data, the surrounding quenched liquid metal is consistently higher in C than the dendritic metal exsolved during the quenching of the experiment. However, since these phases were likely a single melt phase at the *PT* conditions, the broad beam analyses (Figure 3, Table 2) are used to discuss the implications for carbon contents in the mercurian core.

Given the surface composition measured by the MESSENGER spacecraft, it is likely that the planet formed under highly reducing conditions (McCubbin et al., 2012; Zolotov et al., 2013). The geochemical behavior of elements under these highly reducing conditions will differ from what is generally seen in more oxidizing conditions, like Earth (Vander Kaaden and McCubbin, 2016). At conditions as reducing as IW-3 to IW-7, Si is expected to partition into the core of the planet (Chabot et al., 2014). Based on the experimental results in the present study, the more Si that partitions into an iron-rich core of the planet, the less carbon that will partition into it. Although a molten core could contain substantial amounts of carbon (up to ~4 wt% in an Fe-Si-C system), as the core cools and crystallizes, the amount of C in the core could decrease, as suggested by the dendrites present in our experiments. However, additional experiments to examine solid metal-liquid metal c-bearing core compositions are warranted.

Our experiments indicate that if Mercury has a Si-rich core (having more than ~5

wt% silicon), it would have saturated in carbon at low C abundances. If Mercury's volatile-rich nature (Evans et al., 2015; Murchie et al., 2015; Nittler et al., 2011; Peplowski et al., 2014; Peplowski et al., 2016; Peplowski et al., 2015; Peplowski et al., 2012; Weider et al., 2012) also holds true for carbon, a substantial proportion of the carbon in Mercury would have been excluded from the metallic portion of the planet. Furthermore, carbon solubility in silicate melts is exceptionally low under highly reducing conditions, so it would have been excluded from the silicate portion of the planet as well (Ardia et al., 2013). Therefore, if carbon is excluded from the core and the silicate portion of the planet, it indicates that graphite saturation in bulk Mercury is able to happen at lower C abundances than other planets that have higher capacities for C in the core and mantle. Consequently, graphite is likely to be an early phase that forms during the primary differentiation of Mercury, as the core-mantle boundary is above the diamond stability field (Bundy et al., 1996; Bundy et al., 1961; Clausing, 1997; Kennedy and Kennedy, 1976). Based on the work of Vander Kaaden and McCubbin (2015), this graphite would float to the surface of the planet during differentiation in a magma ocean and could have composed a primary floatation crust. Therefore, the results from our CCGS experiments suggest that core formation under highly reducing conditions on Mercury is conducive to the formation of a primary floatation crust of graphite.

5. Conclusion

The current study aimed to examine the role of C in the mercurian core. If Mercury formed under the highly reducing conditions that are currently reflected on the surface, we would expect a large core to form with increasing amounts of Si. While liquid, the Si-Fe-rich core could contain substantial amounts of carbon. The liquid outer

core has the potential to store higher amounts of carbon, at carbon saturation, which would occur early on in the differentiation of Mercury. Therefore any graphite that forms while the core mantle boundary is above the diamond stability field, would have floated through the liquid core and up to the surface forming a primary graphite floatation crust in a magma ocean scenario (Vander Kaaden and McCubbin, 2015), similar to the anorthositic crust seen on the Moon. With continued cooling, followed by partial melting, the surface of the planet is covered by secondary volcanism, burying the clear evidence of a graphite floatation crust. With continued bombardment of the mercurian surface, the graphite floatation crust is then exposed within impact basins. This process is reflected in the MESSENGER data by the newest analyses of C in the low reflectance material (Peplowski et al., 2016). The highly reducing nature of Mercury as well as its enrichment in volatiles has lead to an extremely complex and exotic thermal and magmatic evolution. Understanding the role of all of the volatiles present on Mercury is imperative to our understanding of these complex and unique processes.

Acknowledgements

The authors would like to thank Lisa Danielson, Kellye Pando, and Jenny Rapp for helpful discussions and assisting in laboratory procedures. Carbon analyses could not have been accomplished without the help of D. Kent Ross, which we are extremely grateful for. We also thank the MESSENGER Science Team, with special thanks to the MESSENGER Geochemistry Discipline Group, for fruitful discussions regarding the interpretation of MESSENGER data. This work was funded by a NASA Cosmochemistry Grant NNX14AK43G to FMM. This work was also supported by NASA Headquarters

under the NASA Earth and Space Science Fellowship Program-Grant NNX15AQ80H both awarded to KEVK.

References

Ardia, P., Hirschmann, M.M. and Withers, A.C. (2013) Solubility of methane in a synthetic basaltic melt, with applications to atmosphere-magma coean-core partitioning of volatiles and to the evolution of the martian atmosphere. Geochimica Et Cosmochimica Acta 114, 52-71.

Bundy, F.P., Bassett, W.A., Weathers, M.S., Hemley, R.J., Mao, H.U. and Goncharov, A.F. (1996) The pressure-temperature phase and transformation diagram for carbon; Updated through 1994. Carbon 34, 141-153.

Bundy, F.P., Bovenkerk, H.P., Strong, H.M. and Wentorf, R.H. (1961) Diamond-Graphite Equilibrium Line from Growth and Graphitization of Diamond. Journal of Chemical Physics 35, 383-391.

Chabot, N.L., Wollack, E.A., Klima, R.L. and Minitti, M.E. (2014) Experimental constraints on Mercury's core composition. Earth and Planetary Science Letters 390, 199-208.

Chen, B., Li, J. and Hauck II, S.A. (2008) Non-ideal liquidus curve in the Fe-S system and Mercury's snowing core. Geophysical Research Letters 35.

Clausing, R. (1997) Diamond morphology, in: al., M.P.e. (Ed.), Handbook of Industrial Diamonds and Diamond Films. Kluwer Academic Publishers, pp. 19-45.

Evans, L.G., Peplowski, P.N., McCubbin, F.M., McCoy, T.J., Nittler, L.R., Zolotov, M.Y., Ebel, D.S., Lawrence, D.J., Starr, R.D., Weider, S.Z. and Solomon, S.C. (2015) Chlorine on the surface of Mercury: MESSENGER Gamma-Ray measurements and implications for the planet's formation and evolution. Icarus 257, 417-427.

Hauck II, S.A., Margot, J.L., Solomon, S.C., Phillips, R.J., Johnson, C.L., Lemoine, F.G., Mazarico, E., McCoy, T.J., Padovan, S., Peale, S.J., Perry, M.E., Smith, D.E. and Zuber, M.T. (2013) The curious case of Mercury's internal structure. Journal of Geophysical Research - Planets 118, 1204-1220.

Kennedy, C.S. and Kennedy, G.C. (1976) Equilibrium boundary between graphite and diamond. Journal of Geophysical Research 81, 2467-2470.

Malavergne, V., Toplis, M.J., Berthet, S. and Jones, J. (2010) Highly reducing conditions during core formation on Mercury: Implications for internal structure and the origin of a magnetic field. Icarus 206, 199-209.

McCubbin, F.M., Riner, M.A., Vander Kaaden, K.E. and Burkemper, L.K. (2012) Is Mercury a volatile-rich planet? Geophysical Research Letters 39.

Murchie, S.L., Klima, R.L., Denevi, B.W., Ernst, C.M., Keller, M.R., Domingue, D.L., Blewett, D.T., Chabot, N.L., Hash, C., Malaret, E., Izenberg, N.R., Vilas, F., Nittler, L.R. and Head, J.W. (2015) Orbital multispectral mapping of Mercury using the MESSENGER Mercury Dual Imaging System: Evidence for the origins of plains units and low-reflectance material. Icarus.

Murthy, V.M., van Westrenen, W. and Fei, Y.W. (2003) Experimental evidence that potassium is a substantial radioactive heat source in planetary cores. Nature 423, 163-165.

Nittler, L.R., Starr, R.D., Weider, S.Z., McCoy, T.J., Boynton, W.V., Ebel, D.S., Ernst, C.M., Evans, L.G., Goldsten, J.O., Hamara, D.K., Lawrence, D.J., McNutt, R.L., Schlemm, C.E., Solomon, S.C. and Sprague, A.L. (2011) The Major-Element

Composition of Mercury's Surface from MESSENGER X-ray Spectrometry. Science 333, 1847-1850.
Peplowski, P.N., Evans, L.G., Stockstill-Cahill, K.R., Lawrence, D.J., Goldsten, J.O., McCoy, T.J., Nittler, L.R., Solomon, S.C., Sprague, A.L., Starr, R.D. and Weider, S.Z. (2014) Enhanced sodium abundance in Mercury's north polar region revealed by the MESSENGER Gamma-Ray Spectrometer. Icarus 228, 86-95.
Peplowski, P.N., Klima, R.L., Lawrence, D.J., Ernst, C.M., Denevi, B.W., Frank, E.A., Goldsten, J.O., Murchie, S.L., Nittler, L.R. and Solomon, S.C. (2016) Remote sensing evidence for an ancient carbon-bearing crust on Mercury. Nature Geoscience.
Peplowski, P.N., Lawrence, D.J., Evans, L.G., Klima, R.L., Blewett, D.T., Goldsten, J.O., Murchie, S.L., McCoy, T.J., Nittler, L.R., Solomon, S.C., Starr, R.D. and Weider, S.Z. (2015) Constraints on the abundance of carbon in near-surface materials on Mercury: Results from the MESSENGER Gamma-Ray Spectrometer. Planetary and Space Science.
Peplowski, P.N., Lawrence, D.J., Rhodes, E.A., Sprague, A.L., McCoy, T.J., Denevi, B.W., Evans, L.G., Head, J.W., Nittler, L.R., Solomon, S.C., Stockstill-Cahill, K.R. and Weider, S.Z. (2012) Variations in the abundances of potassium and thorium on the surface of Mercury: Results from the MESSENGER Gamma-Ray Spectrometer. Journal of Geophysical Research - Planets 117.
Riner, M.A., Bina, C.R., Robinson, M.S. and Desch, S.J. (2008) Internal structure of Mercury: Implications of a molten core. Journal of Geophysical Research-Planets 113.
Smith, D.E., Zuber, M.T., Phillips, R.J., Solomon, S.C., Hauck, S.A., Lemoine, F.G., Mazarico, E., Neumann, G.A., Peale, S.J., Margot, J., Johnson, C.L., Torrence, M.H., Perry, M.E., Rowlands, D.D., Goossens, S., Head, J.W. and Taylor, A.H. (2012) Gravity Field and Internal Structure of Mercury from MESSENGER. Science.
Tibbetts, G.G. (1980) Diffusivity of carbon in iron and steels at high temperatures. Journal of Applied Physics 51, 4813.
Vander Kaaden, K.E. and McCubbin, F.M. (2015) Exotic Crust Formation on Mercury: Consequences of a Shallow, FeO-poor Mantle. Journal of Geophysical Research - Planets 120, 195-209.
Vander Kaaden, K.E. and McCubbin, F.M. (2016) The origin of boninites on Mercury: An experimental study of the northern volcanic plains lavas. Geochimica Et Cosmochimica Acta 173, 246-263.
Weider, S.Z., Nittler, L.R., Starr, R.D., McCoy, T.J., Stockstill-Cahill, K.R., Byrne, P.K., Denevi, B.W., Head, J.W. and Solomon, S.C. (2012) Chemical heterogeneity on Mercury's surface revealed by the MESSENGER X-Ray Spectrometer. Journal of Geophysical Research - Planets 117.
Wert, C.A. (1950) Diffusion Coefficient of C in alpha-Iron. Physical Review 79, 601-605.
Zolotov, M.Y., Sprague, A.L., Hauck, S.A., Nittler, L.R., Solomon, S.C. and Weider, S.Z. (2013) The redox state, FeO content, and origin of sulfur-rich magmas on Mercury. Journal of Geophysical Research-Planets 118.

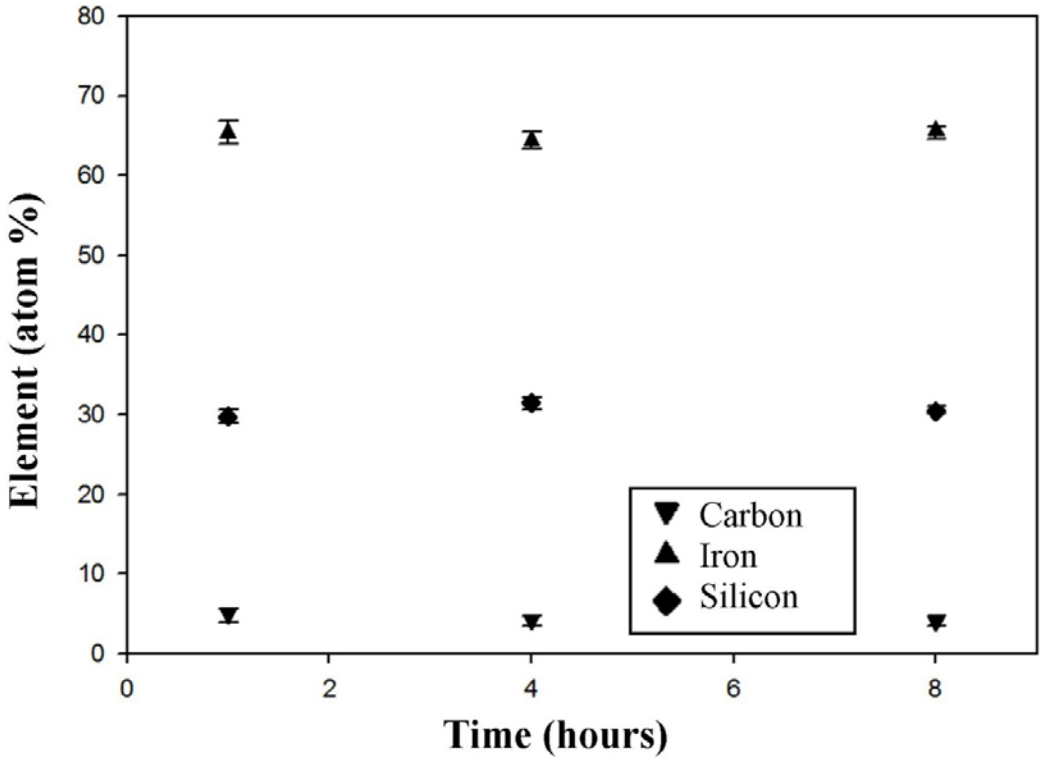

Figure 1. CCGS time series. Symbols correspond to a particular element.

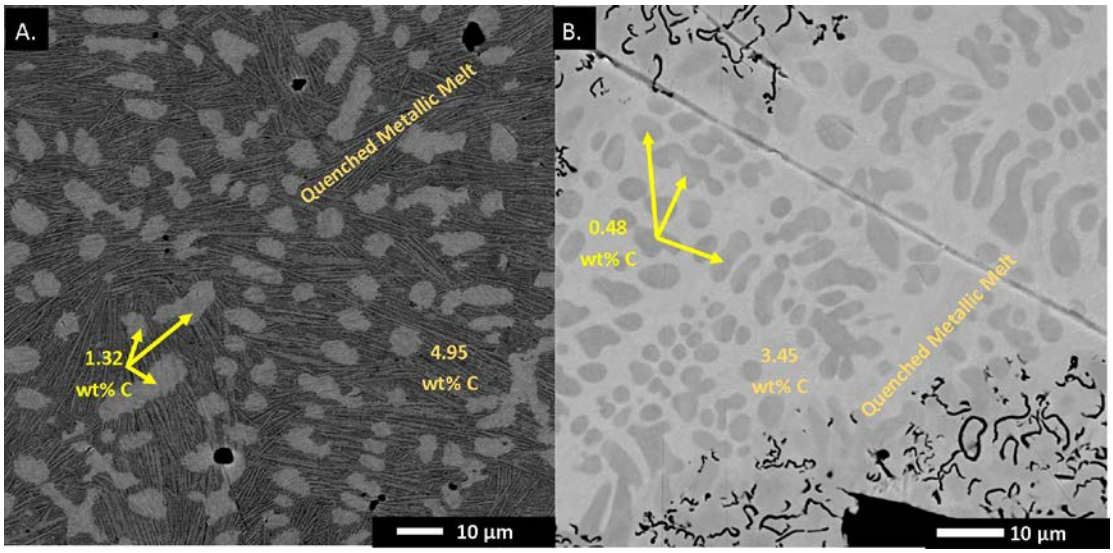

Figure 2. BSE images of CCGS experimental run products in Si_5Fe_{95} metal (A) CS-3 run at 1 GPa and 1300 °C and (B) CSM-997 run at 1 GPa and 1800 °C.

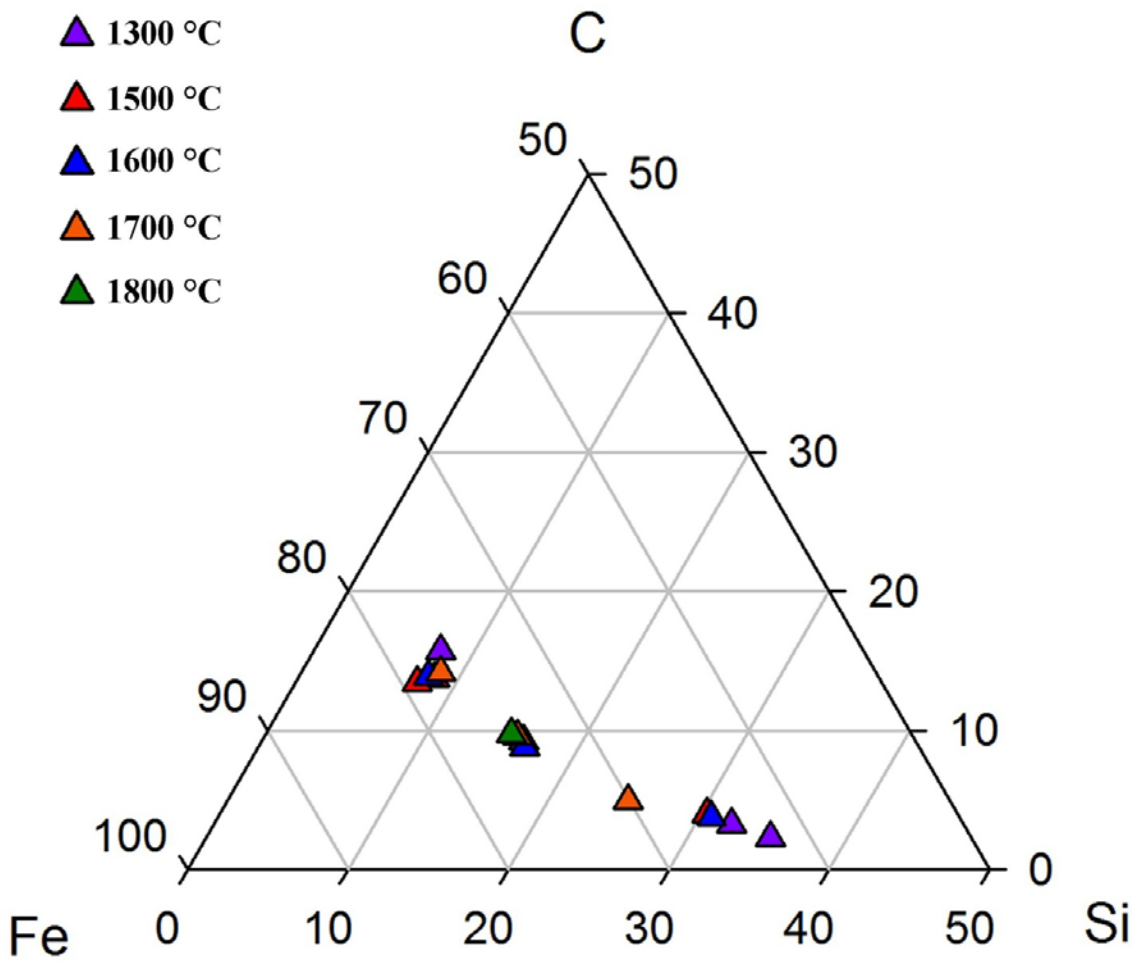

Figure 3. C-Fe-Si ternary containing only broad beam (~15–20 µm) analyses representing the average compositions of all CCGS experimental run products. The color of the symbol corresponds to temperature.

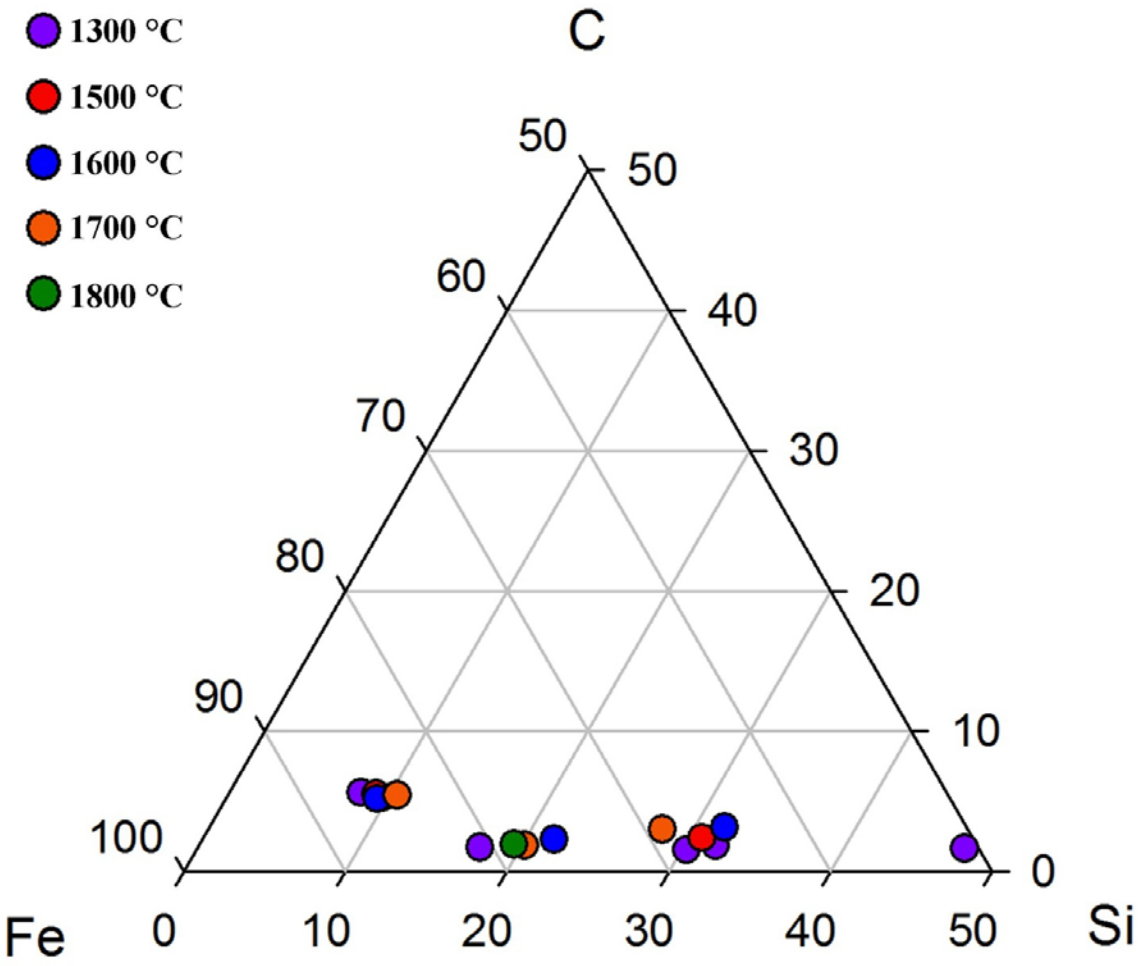

Figure 4. C-Fe-Si ternary containing only spot analyses (~1–5 µm) analyses on the metallic dendrites exsolved during quenching of the CCGS experiments. The color of the symbol corresponds to temperature.

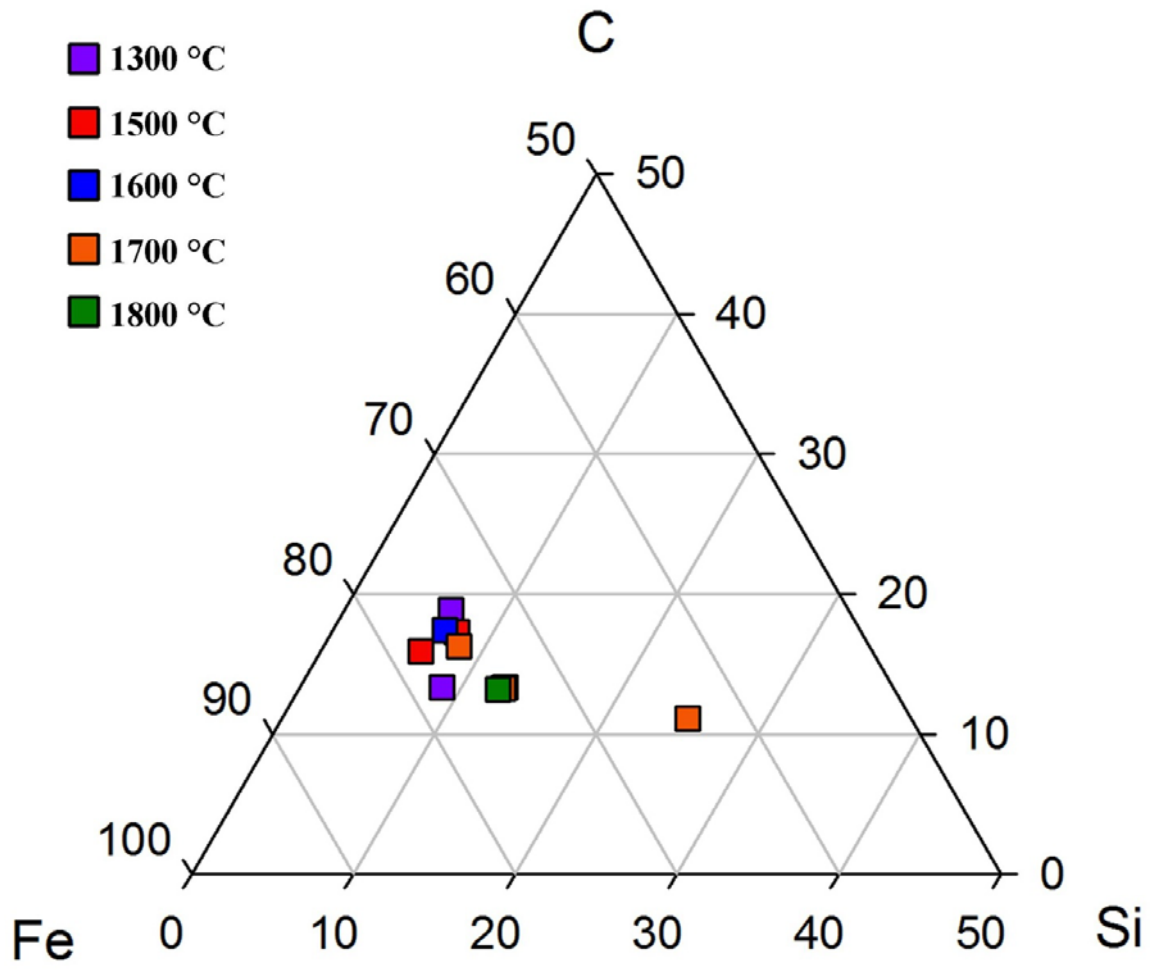

Figure 5. C-Fe-Si ternary containing only spot analyses (~1–5 µm) analyses on the metallic quenched liquid surrounding the dendrites (Figure 4) present upon quenching of the CCGS experiments. The color of the symbol corresponds to temperature.

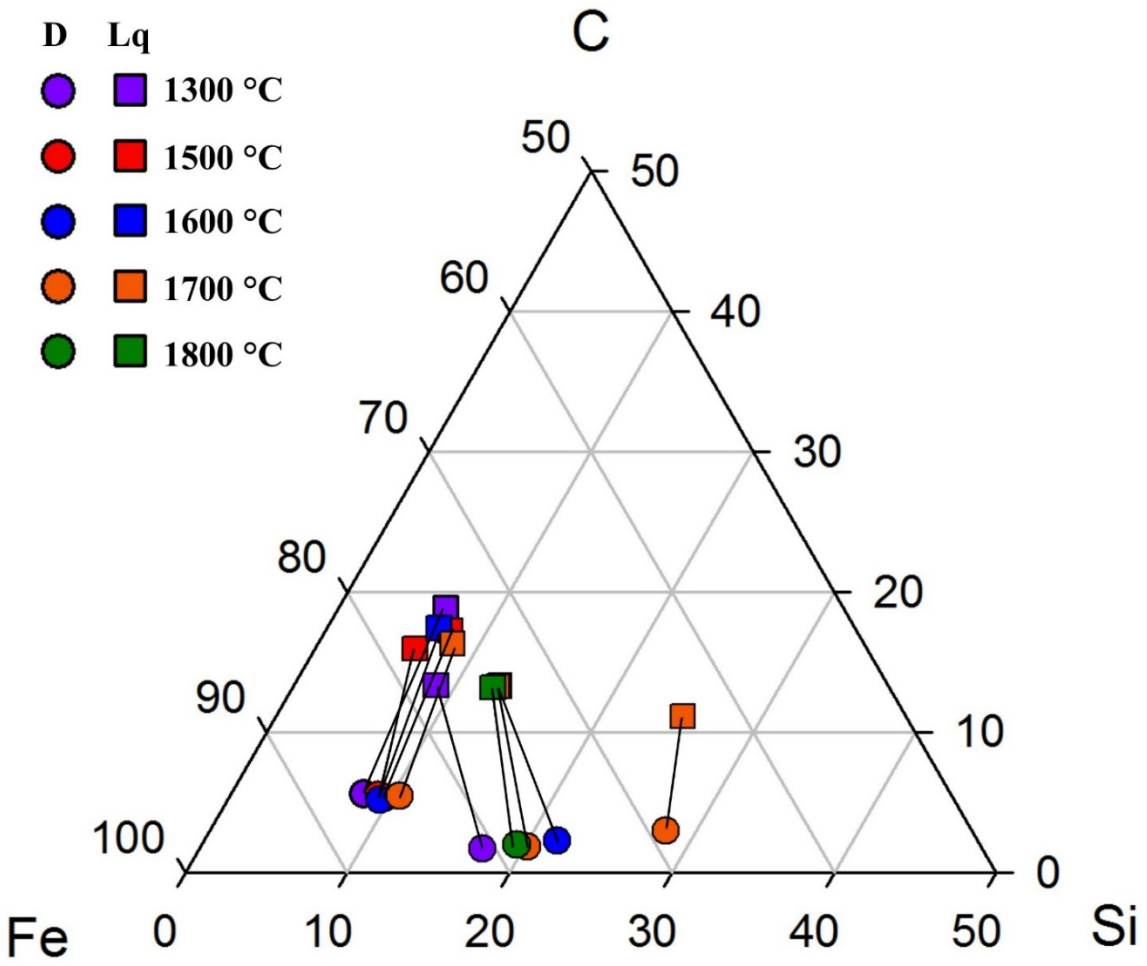

Figure 6. C-Fe-Si ternary containing only spot analyses (~1–5 µm) analyses on the metallic dendritic liquids (D)-surrounding quenched liquid (Lq) pairs present in the CCGS experiments. Tie lies connect the dendrites and surrounding liquid metals from a given experiment. The color of the symbol corresponds to temperature. Squares represent the surrounding liquid metal and circles represent the dendrites.

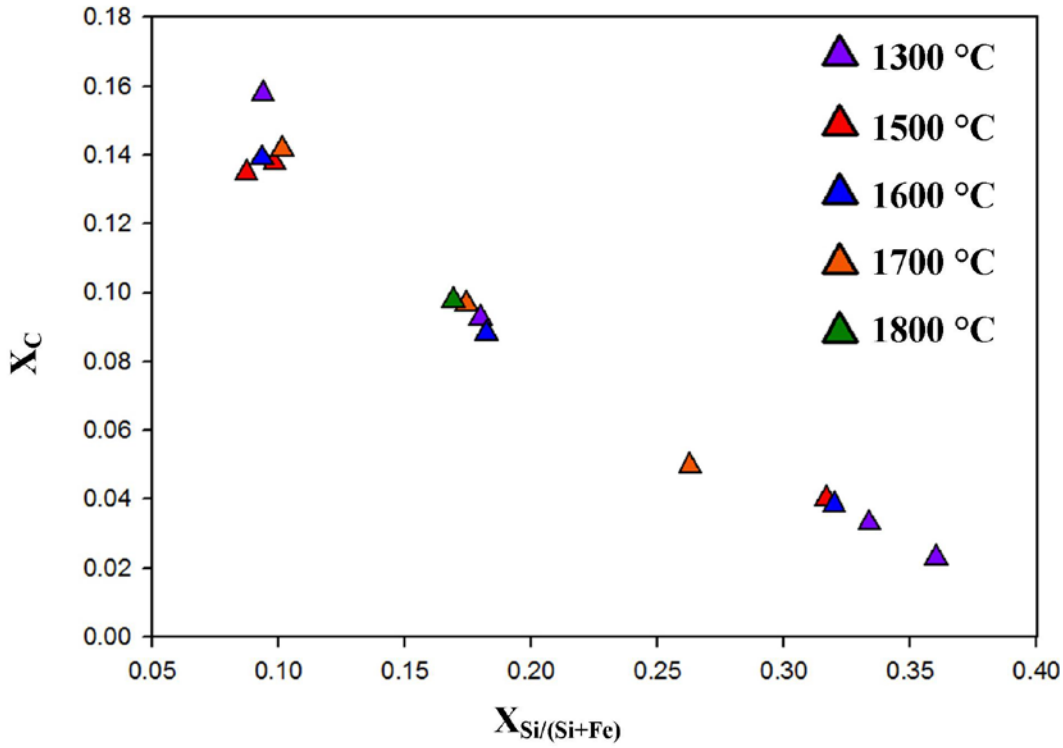

Figure 7. Plot of the mole fraction of Si/(Si +Fe) ($X_{Si/(Si+Fe)}$) vs. the mole fraction of carbon (X_C) as a function of temperature. All analyses represent the same broad beam analyses as Figure 3. The color of the symbol corresponds to temperature.

Table 1. Composition of the metal starting materials used in the CCGS study. All values are in wt%.

	Low Si	Low-Int Si	Int-High Si	High Si
Si	5	10	22	35
Fe	95	90	78	65
Total	100	100	100	100

Table 2. EPMA data for all broad beam (~15–20 µm) analyses on the CCGS experiments (wt%). Std=standard deviation. N=number of analyses included in average.

Exp #	Composition (wt%)	Temperature (°C)	Hold time (Hours)	n	Si	std	C	std	Fe	std	Total
CS-2	$Si_{35}Fe_{65}$	1300	24	17	22.6	1.59	0.63	0.09	79.72	1.54	102.95
CS-3	Si_5Fe_{95}	1300	24	17	4.82	0.1	4.13	0.82	92.55	0.75	101.5
CS-4	$Si_{10}Fe_{90}$	1300	24	20	9.87	0.31	2.4	0.23	89.45	0.23	101.72
CS-5	$Si_{22}Fe_{78}$	1300	24	16	20.42	0.45	0.89	0.11	81.07	0.78	102.38
CSM-982	Si_5Fe_{95}	1500	8	16	5.07	0.11	3.52	0.33	92.5	0.33	101.09
CSM-984	$Si_{22}Fe_{78}$	1500	8	16	18.45	0.14	1.04	0.08	79.14	0.49	98.63
CSM-998	$Si_{10}Fe_{90}$	1500	8	11	4.46	0.4	3.42	0.52	92.83	0.66	100.71
CSM-983	Si_5Fe_{95}	1600	8	11	4.79	0.11	3.54	0.37	92.31	0.83	100.64
CSM-1002	$Si_{10}Fe_{90}$	1600	8	14	9.95	0.68	2.26	0.36	88.79	0.43	101
CSM-996	$Si_{22}Fe_{78}$	1600	8	12	19.02	1.07	1.01	0.1	80.4	1.04	100.43
CSM-1003	$Si_{10}Fe_{90}$	1700	8	13	9.32	0.5	2.45	0.27	87.86	0.34	99.63
CSM-993	Si_5Fe_{95}	1700	8	10	5.2	0.54	3.64	0.88	91.61	0.89	100.45
CSM-995	$Si_{22}Fe_{78}$	1700	8	12	14.97	1.38	1.27	0.16	83.38	0.55	99.62
CSM-997	Si_5Fe_{95}	1800	1.25	13	9.16	0.32	2.51	0.28	49.44	0.6	61.11

Table 3. EPMA data for all spot (~1–5 μm) analyses on the CCGS experiments metallic dendrites only (wt%). Std=standard deviation. N=number of analyses included in average.

Exp #	Composition (wt%)	Temperature (°C)	Hold time (Hours)	n	Si	std	C	std	Fe	std	Total
CS-2	$Si_{35}Fe_{65}$	1300	24	8	19.61	0.67	0.48	0.07	80.64	0.55	100.73
CS-2	$Si_{35}Fe_{65}$	1300	24	7	32.02	0.34	0.47	0.07	68.19	0.1	100.68
CS-3	Si_5Fe_{95}	1300	24	6	4.49	0.21	1.32	0.06	93.88	0.38	99.69
CS-4	$Si_{10}Fe_{90}$	1300	24	5	9.42	0.54	0.39	0.04	86.54	0.3	96.35
CS-5	$Si_{22}Fe_{78}$	1300	24	9	18.2	0.75	0.4	0.03	81.24	0.35	99.84
CSM-982	Si_5Fe_{95}	1500	8	19	5.39	0.09	1.27	0.11	94.72	0.25	101.38
CSM-984	$Si_{22}Fe_{78}$	1500	8	13	18.82	0.44	0.62	0.12	80.93	0.48	100.37
CSM-998	$Si_{10}Fe_{90}$	1500	8	12	5.13	0.35	1.32	0.1	94.46	0.43	100.91
CSM-983	Si_5Fe_{95}	1600	8	17	5.17	0.25	1.43	0.83	94.45	0.89	101.05
CSM-1002	$Si_{10}Fe_{90}$	1600	8	8	12.55	0.94	0.56	0.78	86.9	0.72	100.01
CSM-996	$Si_{22}Fe_{78}$	1600	8	5	19.82	0.71	0.85	0.46	80.25	1.01	100.92
CSM-1003	$Si_{10}Fe_{90}$	1700	8	8	11.52	0.19	0.45	0.03	88.71	0.82	100.68
CSM-993	Si_5Fe_{95}	1700	8	8	5.88	0.38	1.3	0.1	93.73	0.54	100.91
CSM-995	$Si_{22}Fe_{78}$	1700	8	13	17.26	0.46	0.79	0.37	84.07	0.37	102.12
CSM-997	Si_5Fe_{95}	1800	1.25	8	11.18	0.3	0.48	0.04	89.7	0.28	101.36

Table 4. EPMA data for all spot (~1–5 μm) analyses on the CCGS experiments metallic liquids surrounding the dendrites only (wt%). Std=standard deviation. N=number of analyses included in average.

Exp #	Composition (wt%)	Temperature (°C)	Hold time (Hours)	n	Si	std	C	std	Fe	std	Total
CS-3	Si_5Fe_{95}	1300	24	7	4.09	0.34	4.97	0.09	91.4	0.46	100.46
CS-4	$Si_{10}Fe_{90}$	1300	24	5	4.99	0.7	3.23	0.17	87.6	0.59	95.82
CSM-982	Si_5Fe_{95}	1500	8	20	4.81	0.16	4.57	0.22	92.38	0.29	101.76
CSM-998	$Si_{10}Fe_{90}$	1500	8	9	3.74	0.91	4.13	1.11	93.19	0.84	101.06
CSM-983	Si_5Fe_{95}	1600	8	12	4.29	0.33	4.59	0.32	92.77	0.38	101.65
CSM-1002	$Si_{10}Fe_{90}$	1600	8	8	7.78	0.69	3.47	0.13	89.76	0.79	101.01
CSM-1003	$Si_{10}Fe_{90}$	1700	8	12	7.68	0.21	3.45	0.09	89.59	0.48	100.72
CSM-993	Si_5Fe_{95}	1700	8	7	4.99	0.27	4.76	0.18	91.58	0.31	101.33
CSM-995	$Si_{22}Fe_{78}$	1700	8	5	16.25	0.12	3.08	0.23	82.13	0.33	101.46
CSM-997	Si_5Fe_{95}	1800	1.25	14	7.55	0.21	3.45	0.07	90.38	0.15	101.38